CURRENT MECHANISMS IN ZINC DIFFUSION-DOPED SILICON SAMPLES AT T = 300 K

E.U. Arzikulov[a,c]*, M. Radzhabova[a], Xue Cui[c], Liu Teng[c], S.N. Srajev[a], N. Mamatkulov[b], Sh.J. Quvondiqov[a], Vasiliy O. Pelenovich[d,e], B. Yang[f]

[a]*Samarkand State University named after Sharof Rashidov, 140104, 15, University Blvd., Samarkand, Republic of Uzbekistan*
[b]*Samarkand State University Veterinary Medicine, Livestock and Biotechnologies,*
140003, 77, Mirzo Ulug Bek Str., Samarkand, Republic of Uzbekistan
[c]*School of Material Science and Engineering, Shenyang Aerospace University,* 37 Daoyi South Avenue, Shenyang**,** *China*
[d]*The Institute of Technological Sciences, Wuhan University, Wuhan, 430072, China*
[e]*Hubei Key Laboratory of Electronic Manufacturing and Packaging Integration, Wuhan University, Wuhan, 430072, China*
[f]*School of Power and Mechanical Engineering, Wuhan University, Wuhan, 430072, China*
*Corresponding Author e-mail: eshkuvata@gmail.com
Received July 17, 2024; revised September 28, 2024; accepted October 9, 2024

This work is devoted to the study of current flow in diffusion-doped zinc silicon samples in the dark and when illuminated with light with an intensity in the range from 0.6 to 140 lx and at a temperature of 300 K. At T = 300 K and in the dark, the type of the *I–V* characteristic contained all areas characteristic of semiconductors with deep energy levels. It was found that when illuminated with light, the type of *I–V* characteristics of the studied Si samples depended on the value of the applied voltage, the electrical resistivity of the samples, the light intensity, and their number reached up to 6. In this case, linear, sublinear, and superlinear sections were observed, as well as the switching point (sharp current jump) and areas with negative differential conductivities (NDC). The existence of these characteristic areas of the applied voltage and their character depended on the intensity of the light. The experimental data obtained were interpreted in the formation of low dimensional objects with the participation of multiply charged zinc nanoclusters in the bulk of silicon. They changed the energy band structure of single-crystal silicon, which affected generation-recombination processes in Si, leading to the types of *I–V* characteristics observed in the experiment.

Keywords: *Doped silicon; I–V characteristic; Negative differential conductivity; Low dimensional objects; Zinc nanoclusters*
PACS: 72.8-,-r, 72.80. Cw

1. INTRODUCTION

The study of current flow processes in highly compensated (HC) silicon samples doped with zinc in a high non-equilibrium state, at room temperatures and in the presence of illumination, is of important scientific and practical interest. From a scientific point of view, such studies provide more information about the role of a particular center formed by impurity atoms on current flow processes. From a practical point of view, knowledge of the behavior of a sample under various conditions makes it possible to determine the optimal conditions for creating various sensors of external influences based on HC silicon samples.

It is known that zinc in silicon acts as a double acceptor with ionization energies $E_1=E_V+0.31$ and $E_2=E_V+0.50$ eV [1-3]. A study of the surface morphology using an atomic force microscope (AFM) and the photoelectric properties of diffusion zinc-doped silicon samples showed that nano-sized multi-charged clusters are formed in them [4]. These clusters significantly change the structure of the energy states of the zinc atoms in silicon. As a result, instead of the above two acceptor energy levels corresponding to a single zinc atom, other deep energy levels appear with the participation of zinc nanoclusters lying in the range of values $E=E_V+(0.16\div0.617)$ eV, which is consistent with the data [5].

2. EXPERIMENTAL METHODS, RESULTS AND IT'S DISCUSSION

To elucidate the mechanism of current flows in HC samples of silicon diffusion-doped with zinc with different types of conductivity and degrees of compensation, of both n- and p-type conductivities with resistivity lying in the range of $10^2\div10^5$ Ω·cm at T = 300 K were obtained using the high-temperature diffusion method according to the technology described in [6]. Ohmic contacts to the studied samples were created by laser soldering of copper wire with a diameter of 100 μm or by applying conductive silver paste [7].

The measurement of the *I–V* characteristics of diffusion-doped HC Si<P, Zn> samples of both p- and n-types, was carried out according to the method described in the [8]. Samples of p- or n- n-conductivity types in the form of parallelepipeds with dimensions of $10\times5\times0.3$ mm³ were included in a circuit consisting of a series-connected load resistance R_L and a stabilized voltage source. The voltage generator mode ($R_S \gg R_L$) was performed regardless of the current flowing through the sample. An incandescent lamp, powered by direct current, served as a source of lighting.

2.1 Results And Discussion

A study of the *I–V* characteristic of HC silicon samples diffusion-doped with zinc of both n- and p- types of conductivity and with electrical resistivity in the range of $10^2 \div 10^5$ $\Omega \cdot$cm at T = 300 K showed that the *I–V* characteristic in the dark contains three characteristic sections (Figure 1).
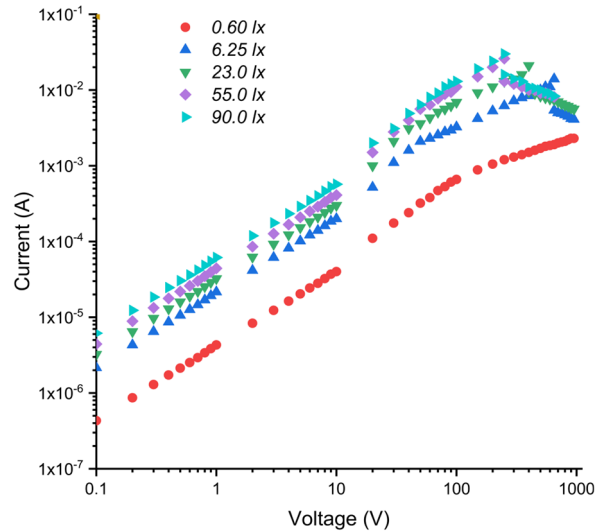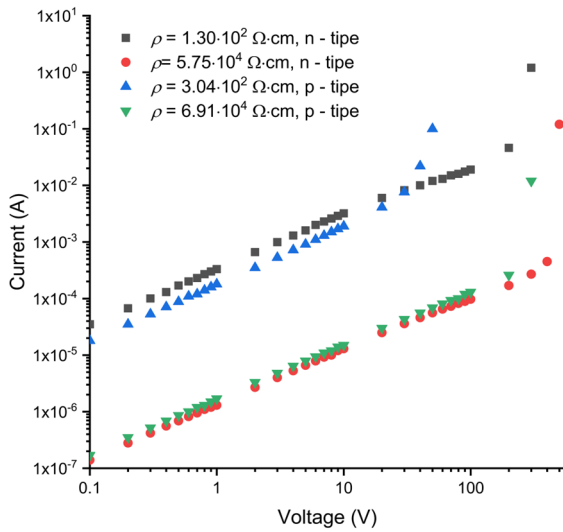


Figure 1. *I–V* characteristics of Si<P, Zn> samples with different specific electrical resistances and types of conductivity in the dark at *T* = 300 K

Figure 2. *I–V* characteristics of n–Si<P, Zn> samples with $\rho = 5.74 \cdot 10^4$ $\Omega \cdot$cm, *T* = 300 K

The first section in the dependence $I = U^\alpha$ is linear (the exponent α lies in the range $0.97 \div 1.03$) for all studied samples whose length in voltage increases approximately 10 times with increasing ρ (for example, $0.1 \div 10$ V for a sample with $\rho = 1.3 \cdot 10^2$ $\Omega \cdot$cm and $0.1 \div 100$ V for a sample with $\rho = 6.91 \cdot 10^4$ $\Omega \cdot$cm). The second section is superlinear (the exponent is equal to the value $1.28 \div 1.97$). The third section of the *I–V* characteristic is a section of a sharp increase in current from voltage. Here the value reaches up to 25.03. At first glance, the last section looks like an electrical breakdown. However, repeated measurements have shown that the experimental data is repeatable; therefore, we can say there is no electrical breakdown here. It should be noted that the exponent increases sharply in this section with increases of the ρ.

Figure 2 shows the *I–V* characteristics of n–Si<P, Zn> samples, also taken at room temperature and in the presence of illumination with an intensity of 0.6–90 lx.
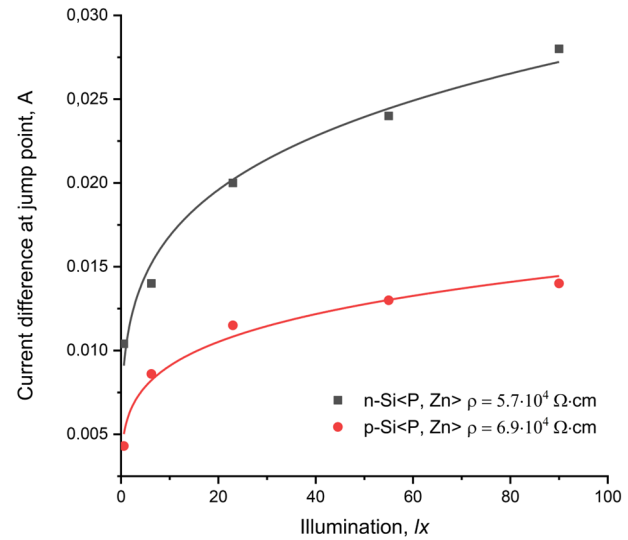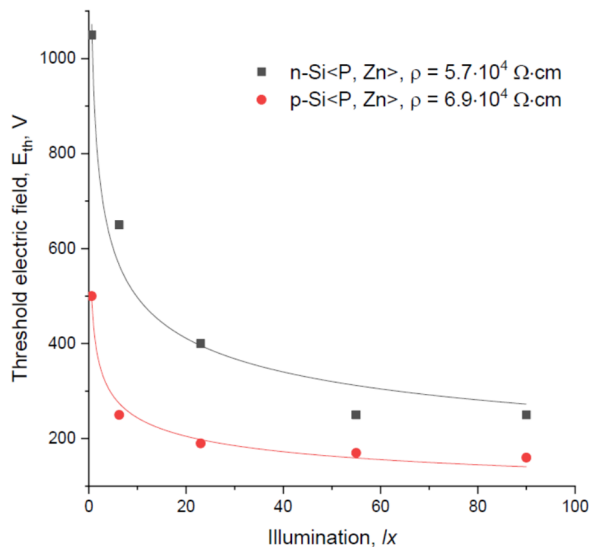

Figure 3. Dependence of the threshold voltage of the current jump on the illumination of the light

Figure 4. Dependence of the magnitude of the current jump on the illumination of the light

As can be seen from Figure 2 the *I–V* Characteristics of n–Si<P, Zn> samples taken at low illumination of light have three characteristic sections [9]. The first almost linear section with the exponent $\alpha = 0.99$ lies in the voltage range $0.10 \div 9$ V, then follows the superlinear section with $\alpha = 1.24$ lying in the voltage range $10 \div 90$ V, then follows the sublinear

section with the exponent $\alpha = 0.554$ lying in the range $100 \div 950$ V [10]. As the light irradiance value (LIV) increases, the number of characteristic areas and the nature of the $I = U^{\alpha}$ dependence changes. So, for example, at 6.25 *lx* the number of characteristic areas reaches six and this number is maintained for all LIV. In this case, the voltage extension of the first ohmic section is preserved for all values of the LIV. The nature of the second section does not change, i.e. it's always super linear. However, the degree of superlinearity increases from the beginning, and having reached a maximum ($\alpha = 1.77$), it decreases ($\alpha = 1.55$). The third section at low LIV is sublinear ($\alpha = 0.68$) and with increasing LIV the sublinearity decreases ($\alpha = 0.75$) with further growth of LIV it first turns into a linear dependence ($\alpha = 0.97$) and then becomes superlinear ($\alpha = 1.15$). The fourth section at relatively low LIV (6.25-23 *lx*) exhibits a superlinear dependence ($\alpha = 1.44 \div 2.04$), then, as in the third section, it first turns almost linear ($\alpha = 1.08$), and then a weak sublinear relationship ($\alpha = 0.90$). The fifth section is a section of a sharp jump in current downward in value. The threshold voltage corresponding to a current surge depends on the LIV. At low LIV, the jump occurs at higher values of voltage applied to the sample. With increasing LIV, the current sharply decreases, and, starting from 23 *lx*, the current jump does not depend on the LIV (Figure 3), but the magnitude of its jump ($\Delta I = I_{max} - I_{min}$) depends on the LIV. At low LIV, the value of ΔI is small and with increasing LIV it increases sharply, and, starting from LIV 23 *lx*, its growth slows down (Figure 4).

Figure 5 shows the *I–V* characteristics of HC samples p–Si<P, Zn> with $\rho = 6.91 \cdot 10^4$ Ω·cm taken at a temperature $T = 300$ K in the presence of illumination with an intensity lying in the range of $0.6 \div 100$ *lx*.
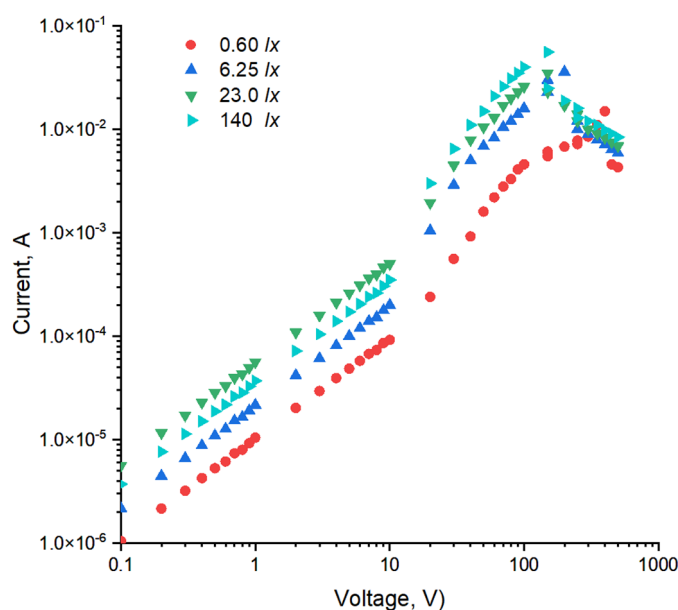
Figure 5. *I–V* characteristics of n–Si<P, Zn> samples with $\rho = 6.91 \cdot 10^4$ Ω·cm, $T = 300$ K

As can be seen from Figure 5, in contrast to n–Si<P, Zn> samples, the *I–V* characteristics of p–Si<P, Zn> taken at $T = 300$ K and low LIV contain 6 characteristic sections (instead of three). These are sections: the first almost linear section with the exponent $\alpha = 0.98$ lies in the voltage range $0.10 \div 9$ V, and this dependence is preserved for all LIV, then follows the second superlinear section with $\alpha = 1.73 \div 2.08$, lying in the voltage range $10 \div 30$ V, followed by the third sublinear section with the exponent $\alpha = 0.42$, lying in the range $40 \div 100$ V. With an increase in the LIV, this section moves to a superlinear dependence with the exponent α, lying in the range $1.27 \div 1.45$. Next comes the fourth superlinear section with $\alpha = 2.55$. With increasing LIV, this dependence becomes sublinear, and the value decreases. The fifth is a section of a sharp jump in current downward in value. The voltage corresponding to the current surge depends on the LIV. At low values of the LIV, the jump occurs at higher values of the voltage applied to the sample. With increasing LIV, the threshold voltage value decreases sharply, and starting from 23 *lx*, as in the case of p–Si<P, Zn> samples, it ceases to be affected by the LIV (Figure 3). In this case, the magnitude of the jump ($\Delta I = I_{max} - I_{min}$) also depends on the LIV. At low LIV, the value of ΔI is small, but with increasing LIV it increases sharply and, starting from LIV 23 *lx*, its growth slows down (Figure 4). It should be noted that in n–Si<P, Zn> both the value of the threshold voltage U_{th} and the value of ΔI are always greater than in p–Si<P, Zn>.

The nonlinearity of the *I–V* characteristic occurs not only in many semiconductor devices, in which the main working element is *p-n* junctions but also in many semiconductor materials in which *p-n* junctions are completely absent [11]. In semiconductor materials, if we exclude the influence of contacts, nonlinearity is most often due to the effects of strong fields. It is known that in strong electric fields, there is a dependence of mobility on the field strength until velocity saturation, NDC, impact ionization, and breakdown. However, in weak electric fields, the manifestation of nonlinearity of the *I–V* characteristic is also possible [12].

In [6], it was shown that in the silicon samples we studied, diffusion-doped with zinc at low voltages, the dependence of the current flowing through the sample on the applied voltage is linear. At higher voltages, nonlinearities appear in the

I–V dependence, which is described by the theory of limited space charge current (SCLC) by trapping holes at levels created by zinc atoms located in the band gap of silicon [13].

However, the exact reasons for the nonlinear nature of the *I–V* characteristics in semiconductors have not yet been unambiguously established [14]. According to [15], the nonlinearity of the relationship between excess carrier concentrations in compensated semiconductors leads to a complex dependence on the parameters that determine the shape of the *I–V* characteristics on the injection level. An important role in the formation of the *I–V* characteristics of the diode structure is played by the bipolar drift mobility and the effective diffusion coefficient. In the expressions that determine the above quantities, there is a function $v(p)=dn/dp$, the form of which is determined by the specific type of the system of deep impurity levels in the compensated semiconductor. At low and high injection levels, when carrier concentrations are related by a linear dependence and the value of $v(p)$ is constant, the influence of equilibrium parameters on the values of mobility and diffusion coefficient has a weak effect. When considering the mechanisms responsible for the behavior of the *I–V* characteristics of a compensated semiconductor, it is necessary to take into account the influence of simultaneous changes in the bipolar drift mobility and the effective diffusion coefficient, which is a difficult task in practice.

In our case, possible reasons for the nonlinearity of the *I–V* characteristics in Si<P, Zn> samples may be the following mechanisms: i) currents limited by space charges; ii) and ionization of impurity centers in strong electric fields [14, 16]. As was shown in [14], when a voltage is applied to samples with high resistance, an injection current appears in the circuit, which obeys the power law $J \sim E^2$. The nonlinear sections of the *I–V* characteristics in such samples containing shallow and deep traps were mainly associated with the possibility of implementing monopolar or double injection.

In the HC Si<P, Zn> samples we studied, there are $r-$ (slow, associated with doubly ionized zinc atoms) and $s-$ (fast, levels arising during high-temperature diffusion) recombination centers, as well as $t-$ trap levels associated with shallow levels [17]. This suggests that in fields where a quadratic dependence $J \sim E^2$ is observed, the *I–V* characteristic exhibits a trap character of conductivity. The experimental data obtained in the corresponding sections of the *I–V* characteristic show that in p- and n-type Si<P, Zn> samples, the transport of charge carriers in electric fields with a strength of less than 10^2 V/cm is mainly due to monopolar injection and is consistent with Lampert's theory [9].

The sections of the *I–V* characteristic with $\alpha < 1$ that we studied for p- and n-type Si<P, Zn> samples can be satisfactorily explained within the framework of the theory of the "injection depletion effect" [13]. The appearance of sublinear sections of the *I–V* characteristic is theoretically possible only in the case of counter-directions of ambipolar diffusion of nonequilibrium current carriers and their ambipolar drift, which in our case is mainly determined by injection modulation of the charge of deep levels [18]. Due to the difference in diffusion coefficients, holes move slowly, and electrons run far ahead, which leads to their separation in space and an electric field arises between them, inhibiting their movement. A decrease in their speed causes a decrease in current, which in turn leads to the appearance of sublinear sections of the *I–V* characteristic.

Analysis of the results of experimental data obtained at relatively high electric field strengths (at E > 10^2 V/cm) shows that the increase in electrical conductivity with increasing E is associated with an increase in the concentration of excess charge carriers. This circumstance allows us to assume that the presence of a region of the sharper current growth in the *I–V* characteristic, where $\alpha > 3$, can be explained by the fact that in Si<P, Zn> p– and n-type samples at such E, depletion (or ionization) occurs traps stimulated by an electric field.

There is another mechanism that also leads to a strong change in the concentration of charge carriers. This may be due to a sharp increase in the degree of ionization of small donors or acceptors when free carriers are heated by an electric field. Such a sharp increase in the degree of ionization can be associated both with an increase in the rate of impact ionization upon heating of charge carriers and with the field dependence of the probability of their capture by similarly charged traps. This is only possible at very low temperatures. In fields of the order of 10^2 V/cm, almost complete release of charge carriers from traps occurs, which leads to sharp superlinearity of the *I–V* characteristic. At present, however, there is still no complete clarity regarding the specific mechanism of origin of the region responsible for NDC [10].

The origin of the fifth region, where a downward current jump is observed at certain values of voltage applied to the sample, is not yet completely clear. Such a current jump may be associated with the "opening" of a new additional recombination channel associated with zinc atoms. In this case, the capture cross section for nonequilibrium charge carriers at the center corresponding to this channel probably depends on the electric field strength. When the threshold voltage value is reached, this channel "opens", which leads to a sharp decrease in the number of current carriers and corresponds to a current jump down in value.

In [19], a model of a semiconductor with quantum dots (QDs) was used to explain the experimental data obtained. It is known that the presence in the band gap of a semiconductor of various traps for charge carriers associated with impurity atoms significantly affects the type of their *I–V* characteristics. This is especially evident in HC semiconductor materials. In this case, *S*- or *N*-shaped sections also appear on the *I–V* characteristic instead of a linear section, followed by quadratic and almost vertical dependencies. *I–V* characteristics with several NDCs or the simultaneous presence of *S*- and *N*-shaped characteristics are also possible [10].

The results obtained can be interpreted in such a way that zinc atoms in silicon, with strong compensation, form not only single deep levels but also an entire band of levels characteristic of nanoclusters (or quantum dots) with large carrier capture cross sections [7].

The value of the electrical resistivity of Si<P, Zn> samples of both n- and p-type conductivity with NC with different charge states, obtained by high-temperature diffusion lies in a wide range ($\rho{\sim}10^2{\div}10^4$ Ω·cm), i.e. they are quite high-resistance. These NCs are deep traps for charge carriers. Unlike conventional traps, where carriers are at a fixed energy level, in NC they are not only bound but can also be at different quantized energy levels with different densities of states and capture cross sections. The nature of their distribution among levels depends on the degree of compensation, on injection, etc., in addition, the process of tunneling between NCs is possible. Therefore, it should be expected that the *I-V* characteristics in such materials should have their characteristics, which were experimentally discovered in the Si<P, Zn> samples with NC we studied [20].

It should also be noted that with a decrease in the resistivity of the samples, the value of the vertical section of the *I–V* characteristic also decreases. Knowing the charge carrier concentrations at a given temperature, we calculated the positions of the Fermi level in these samples at T=300 K, which are F_1=0.35 eV, F_2=0.43 eV, and F_3=0.49 eV, respectively. Therefore, it can be assumed that in these samples the NCs act as traps with different concentrations and ionization energies, which are higher than the Fermi level. We can consider that in the samples under study there are only NCs with different charge multiplicities and assume that the detected energy levels correspond to their different charge states.

3. CONCLUSIONS

Based on the studies of the electrical properties of silicon samples diffusion-doped with zinc, it was established that the *I–V* characteristic consists of several characteristic sections (the number of which can reach up to 6): linear, sublinear, superlinear, switching point, and section with NDC. Their number and voltage ranges depend on the temperature, degree of illumination, and resistivity of the sample.

The sublinear sections of the *I–V* characteristic observed in p- and n-type Si<P, Zn> samples can be satisfactorily explained within the framework of the theory of the injection depletion effect. The observed quadratic dependences $J \sim E^2$ in the *I–V* characteristic can be associated with the influence of traps on conductivity. In the p- and n-type Si<P, Zn> samples we studied, the transfer of charge carriers in electric fields with a strength of less than 10^2 V/cm is mainly due to monopolar injection and is consistent with Lampert's theory.

The presence of a region of sharper current growth in the I–V characteristic, where α >3, can be explained by the fact that in Si<P, Zn> p- and n-type samples at such electric field strengths, emptying (or ionization) of traps occurs, stimulated by the electric field.

The observed features in the *I–V* characteristic are mainly associated with the formation of nano-sized multiply charged clusters, which significantly change the structure of the energy states of zinc atoms in silicon. As a result, instead of the well-known two acceptor energy levels corresponding to atomic zinc, a whole spectrum of deep donor energy levels of zinc nanoclusters appears lying in the range E=E_V+(0.16÷0.4) eV.

ORCID
Eshkuvat U. Arzikulov, https://orcid.org/0000-0001-9179-3402; **Vasiliy O. Pelenovich**, https://orcid.org/0000-0001-8663-3543

REFERENCES
[1] C.S. Fuller, and F.J. Morin, Phys. Rev. **105**, 379 (1957). https://doi.org/10.1103/PhysRev.105.379
[2] E. Merk, J. Hoyman, and E.E. Haller, Solid State Commun. **72**, 851 (1989). https://doi.org/10.1016/0038-1098(89)90412-2
[3] S. Weiss, N. Beckman, and R. Kassing, Appl. Phys. A, **50**, 151 (1990). https://doi.org/10.1007/BF00343410
[4] E.U. Arzikulov, M. Radzhabova, Sh.J. Quvondiqov, G. Gulyamov, East Eur. J. Phys. (3), 400 (2023). https://doi.org/10.26565/2312-4334-2023-3-43
[5] T. Abdulmecit, Turk. J. Phys. **44**(4), 302 (2020). https://doi.org/10.3906/fiz-2007-11
[6] M.K. Bakhadirkhanov, N.F. Zikrillaev, and E.U. Arzikulov, Tech. Phys. Lett. **17**, 1 (1991). (in Russian)
[7] M. Neul, I.V. Sprave, L.K. Diebel, L.G. Zinkl, F. Fuchs, Y. Yamamoto, C. Vedder, *et al*., Phys. Rev. Materials, **8**, 043801 (2024). https://doi.org/10.1103/PhysRevMaterials.8.043801
[8] N.F. Zikrillaev, and E.U. Arzikulov, Report. Uzb. Acad. Sci. **11**, 27 (1991). (in Russian)
[9] M.A. Lampert, and P. Mark, *Current Injection in Solids*, (Electrical Science, 1970).
[10] M.C. Ozdemir, O. Sevgili, I. Orak, and A. Turut, Mater. Sci. Semicond. Process. **125**, 105629 (2021). https://doi.org/10.1016/j.mssp.2020.105629
[11] S. Boughdachi, Y. Badali, Y. Azizian-Kalandaragh, and S. Altindal, J. Elec. Mater. **47**, 12 (2018). https://doi.org/10.1007/s11664-018-6593-y
[12] E. Schöll, *Nonequilibrium Phase Transitions in Semiconductors. Self-Organisation Induced by Generation and Recombination Processes*, (Springer-Verlag, Berlin, Heidelberg, New York, London, Paris, Tokyo, 1987).
[13] V.E. Lashkarev, A.V. Lyubchenko, and M.K. Sheikman, *Nonequilibrium processes in photoconductors*, (Nauk. Dumka, Kiev, 1981). (in Russian)
[14] D. Degler, U. Weimar, and N. Barsan, ACS Sens. **4**, 2228 (2019). https://doi.org/10.1021/acssensors.9b00975
[15] M. Labed, J.Y. Min, A.B. Slim, N. Sengouga, C.V. Prasad, S. Kyoung, and Y.S. Rim, J. Semicond., **44**(7), 072801 (2023). https://doi.org/10.1088/1674-4926/44/7/072801

[16] P. Vivek, J. Chandrasekaran, V. Balasubramani, A. Manimekalai, and T.G.V. Prabhu, Surfaces and Interfaces, **37**, 102689 (2023). https://doi.org/10.1016/j.surfin.2023.102689

[17] H. Chouaib, M. Aouassa, and M. Bouabdellaoui, J. Mater. Sci: Mater. Electron. **34**, 1815 (2023). https://doi.org/10.1007/s10854-023-11171-6

[18] B.I. Shklovsky, and A.L. Efros, *Electronic properties of doped semiconductors*, (Springer-Verlag, Berlin, Heidelberg, New York, Tokyo, 1979).

[19] N.N. Gerasimenko, and Yu.N. Parkhomenko, *Silicon - Nanoelectronics Material*, (Technosphere, Moscow, 2007). (in Russian)

[20] M.A. Rafiq, J. Semicond. **39**, 061002 (2018). https://doi.org/10.1088/1674-4926/39/6/061002

МЕХАНІЗМИ СТРУМУ В ЗРАЗКАХ КРЕМНІЮ, ЛЕГОВАНОГО ДИФУЗІЄЮ ЦИНКУ, ПРИ T = 300 K

Е.С. Арзікулов[a,c], М. Раджабова[a], Сюе Цуй[c], Лю Тенг[c], С.Н. Сраєв[a], Н. Маматкулов[b], Ш.Дж. Гувондіков[a], Василь О. Пеленович[d,e], Б. Янг[f]

[a]Самаркандський державний університет імені Шарофа Рашидова,
140104, Університетський бульвар, 15 Самарканд, Республіка Узбекистан
[b]Самаркандський державний університет ветеринарної медицини, тваринництва та біотехнологій,
140003, вул. Мірзо Улуг Бек, 77, Самарканд, Республіка Узбекистан
[c]Школа матеріалознавства та інженерії Шеньянського аерокосмічного університету,
37 Південна авеню Даої, Шеньян, Китай
[d]Інститут технологічних наук Уханьського університету, Ухань, 430072, Китай
[e]Ключова лабораторія виробництва електроніки та інтеграції упаковки в Хубеї, Уханьський університет, Ухань, Китай
[f]Школа енергетики та машинобудування Уханьського університету, Ухань, Китай

Дана робота присвячена вивченню протікання струму в дифузійно легованих зразках цинкового кремнію в темряві та при освітленні світлом з інтенсивністю в діапазоні від 0,6 до 140 лк і температурі 300 K. При T = 300 K і в темряві вид ВАХ містив усі ділянки, характерні для напівпровідників з глибокими енергетичними рівнями. Встановлено, що при освітленні світлом вид ВАХ досліджуваних зразків кремнію залежав від величини прикладеної напруги, питомого електричного опору зразків, інтенсивності світла, а їх кількість досягала 6. при цьому спостерігалися лінійні, сублінійні та суперлінійні ділянки, а також точка перемикання (різкий стрибок струму) і області з від'ємною диференціальною провідністю (НДП). Наявність цих характерних ділянок прикладеної напруги та їх характер залежали від інтенсивності світла. Отримані експериментальні дані інтерпретовано при формуванні низькорозмірних об'єктів за участю багатозарядних нанокластерів цинку в об'ємі кремнію. Вони змінили енергетичну зонну структуру монокристалічного кремнію, що вплинуло на процеси генерації-рекомбінації в Si, що призвело до типів ВАХ, які спостерігалися в експерименті.

Ключові слова: *легований кремній; ВАХ; негативна диференціальна провідність; малорозмірні об'єкти; нанокластери цинку*

STUDY OF DEFECT STRUCTURE OF SILICON DOPED WITH DYSPROSIUM USING X-RAY PHASE ANALYSIS AND RAMAN SPECTROSCOPY

Khodjakbar S. Daliev[a], Sharifa B. Utamuradova[b], Jonibek J. Khamdamov[b],
Shahriyor B. Norkulov[b]*, Mansur B. Bekmuratov[b]

aBranch of the Federal State Budgetary Educational Institution of Higher Education "National Research University MPEI",
1 Yogdu st., Tashkent, Uzbekistan
bInstitute of Semiconductor Physics and Microelectronics at the National University of Uzbekistan,
20 Yangi Almazar st., Tashkent, 100057, Uzbekistan
*Corresponding Author e-mail: nshb19990@gmail.com

In this paper, the effect of doping silicon with dysprosium (Dy) on its structural and optical characteristics is investigated. Silicon n-Si was doped with dysprosium by thermal diffusion at 1473 K for 50 h. Raman spectroscopy and X-ray diffraction analysis were used for the analysis. The Raman spectroscopy results showed a main peak at 523.93 cm^{-1}, corresponding to n-Si optical phonons, with an increase in the intensity and full width at half maximum (FWHM) in n-Si<Dy> samples, indicating an improvement in the crystallinity of the structure. A decrease in the intensity of the peaks at 127.16 cm^{-1} and 196.24 cm^{-1}, associated with amorphous structures, confirms a decrease in defects. The detection of a new peak at 307.94 cm^{-1} indicates successful deposition of dysprosium as nanocrystallites associated with the 2TA phonon mode in the cubic phase of Dy_2O_3. X-ray diffraction analysis revealed characteristic structural lines indicating the (111) crystalline orientation and the presence of microdistortions in the lattice. Heat treatment and rapid cooling lead to a change in the intensity of structural lines, an increase in the second- and third-order lines, which indicates microstrains and a change in the size of subcrystallites. Doping of silicon with dysprosium improves the crystallinity of the structure, reduces the number of defects and forms polycrystalline layers on the surface consisting of SiO_2 and Dy_2O_3 nanocrystals.

Key words: *Silicon; Defects; Dysprosium; Rare earth element; Raman spectroscopy; Diffusion; Heat treatment; Temperature; Composition; X-ray phase analysis*
PACS: 33.20.Rm, 33.20.Fb

INTRODUCTION

It is known that defect formation processes are significantly affected by various factors [1-6]. The formation efficiency and annealing kinetics of certain defects in the bulk of silicon depend on the presence of various active and inactive uncontrolled impurities, their content and state in the silicon lattice, other specially introduced impurities, the presence of several impurities at once, and many factors. Diffusion is carried out from the oxide film of rare earth elements on the surface of the silicon wafer. Thin-film nanocomposites consisting of crystalline and amorphous Si nanoparticles embedded in silicon oxide layers have been widely studied over the past two decades as suitable materials for non-volatile memory devices, third-generation photovoltaic devices, and other applications. The efficiency of rare earth doping in silicon and the manifestation of optical properties of the structures depend on the spectrum of optically and electrically active centers containing rare earth elements, their total concentration, and the interaction with uncontrolled impurities and thermal defects in the bulk of the material. Recent advances in self-aligned silicide deposition have revived the interest in metal-oxide semiconductor Schottky barrier field-effect transistors (SB-MOSFETs), and devices with outstanding electrical characteristics and high-frequency performance have been fabricated. Metal silicides such as PtSi, $DySi_{2-x}$, $YbSi_{2-x}$, and $ErSi_{2-x}$ have been extensively studied as Schottky barrier source-drain (S/D) contacts due to their low Schottky barrier height on silicon [7-8].

Raman spectroscopy has proven its effectiveness in monitoring the local formation of various technologically important metal silicides (e.g. $CoSi_2$, $TiSi_2$, PtSi and NiSi) [2-9]. The Raman spectrum also provides a unique "fingerprint" of the material: each phonon in the spectrum corresponds to a unique vibrational mode of the crystal lattice. This method provides additional information such as the phase state, strain, nucleation site and grain size of the silicide material.

The aim of this work is to dope n-Si silicon with dysprosium (Dy) by the diffusion method at a temperature of 1473 K and to study the structural and optical characteristics of n-Si silicon samples and the REE oxide film on the surface of n-Si<Dy> silicon wafer using Raman spectroscopy and X-ray diffraction (XRD) analysis.

MATERIALS AND METHODS

In this study, n-Si and its doped n-Si<Dy> sample were analyzed using Raman spectroscopy (RS) and X-ray diffraction (XRD) methods. Control n-Si samples with initial resistance from 0.2 to 100 Ω×cm was selected for the experiment. The doping process with dysprosium (Dy) was carried out by thermal diffusion method. The samples were chemically cleaned and treated with HF solution to remove oxide layers from the surface.

Then Dy (99.999% purity) was deposited on the cleaned silicon surface in a high vacuum environment with a vacuum level of 10^{-6} to 10^{-7} Torr in evacuated quartz ampoules using an oil-free vacuum pump system. Diffusion annealing of the samples was performed at a temperature of 1473 K for 50 hours, followed by rapid and slow cooling to uniformly distribute the material and achieve the maximum concentration of dysprosium in silicon.

Raman spectroscopy was performed on a QE Pro High-Sensitivity Spectrometer Raman microscope at room temperature using a 532 nm laser in the wavelength range from 50 to 1200 cm^{-1}. X-ray diffraction analysis was performed on a MiniFlex II diffractometer (Rigaku, Japan) using CuKα radiation. All diffraction patterns were recorded in the angular range 2θ=3÷120°. The obtained diffraction data were analyzed for the presence of characteristic signals for n-Si<Dy> composites. The presence of elements was determined based on literature data on phases and the ICDD card database for known compounds.

RESULTS AND DISCUSSIONS

To study the physical and chemical structure of the samples, Raman analysis was performed, the obtained spectra are presented in Figure 1.
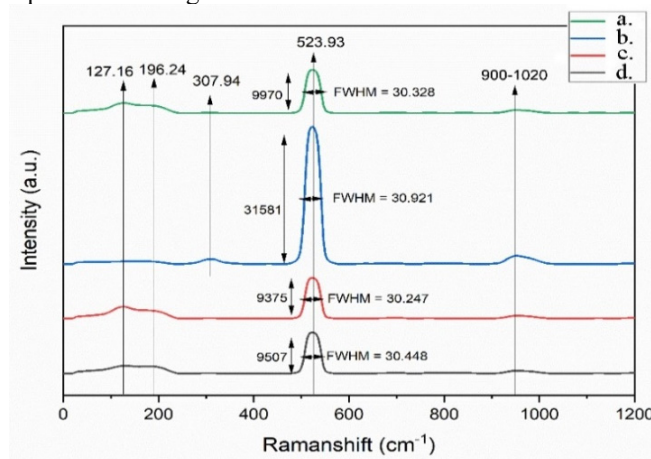
Figure 1. Raman spectra of the studied samples:
a. n-Si doped with dysprosium (<Dy>), heat-treated at 1373 K for 50 hours, followed by rapid cooling and 15 μm depth removal; **b.** n-Si doped with dysprosium (<Dy>), heat-treated at 1373 K for 50 hours, followed by rapid cooling; **c.** n-Si (control), heat-treated at 1373 K for 50 hours, followed by rapid cooling; **d.** n-Si (original material)
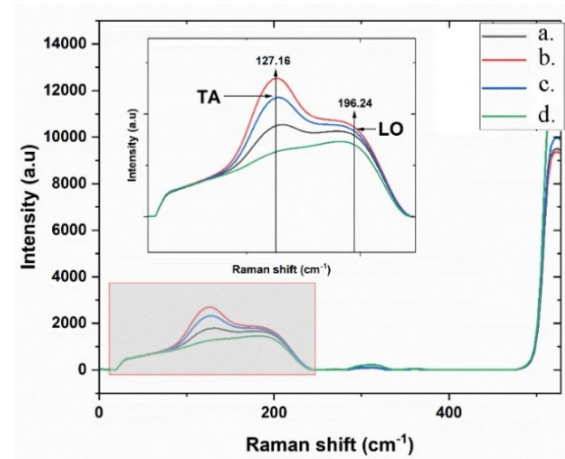
Figure 2. TA and LO peaks of samples:
a. n-Si (as-is). **b.** n-Si (control) heat-treated at 1373 K for 50 h followed by rapid cooling; **c.** n-Si doped with dysprosium (<Dy>) heat-treated at 1373 K for 50 h followed by rapid cooling and 15 μm depth removal; **d.** n-Si doped with dysprosium (<Dy>) heat-treated at 1373 K for 50 h followed by rapid cooling

As shown in Figure 1, the first-order Raman spectrum (G point, k~0) of all single-crystal silicon samples at room temperature is observed at 523.93 cm^{-1} [10, 11]. The peak is formed as a result of optical phonon scattering inside the n-Si nanocrystal, which corresponds to the LO (longitudinal optical) and TO (transverse optical) optical phonon modes of n-Si at the center of the Brillouin zone [12]. It is known that tensile stress causes the Raman peak to shift toward a lower wavenumber, while compressive stress causes the Raman peak to shift toward a higher wavenumber [13]. Figures 1 and 2 show the typical shifts of Raman peaks for amorphous silicon based on the experimental results of references, which are approximately 127.16 cm^{-1} (phonon mode similar to TA-like phonon mode) and 196.24 cm^{-1} (phonon mode similar to LA-like phonon mode) [12, 13, 16].

It is evident from Fig. 1 that the peak intensity and first-order bandwidth at half-maximum for the heat-treated n-Si$_{ht}$ sample are lower than that obtained for the control sample (n-Si). In addition, the higher intensity of the peaks at 127.16 cm^{-1} and 196.24 cm^{-1} appearing in the Raman spectrum of the heat-treated sample indicates that the amorphous silicon with higher concentration of crystal defects is formed during the processing.

According to the Raman spectra of the obtained n-Si<Dy> samples, due to the deposition of dysprosium on the n-Si surface, the peak intensity significantly increased along with the FWHM value at 523.93 cm^{-1}, and the peak intensity of the amorphous structures at 127.16 cm^{-1} and 196.24 cm^{-1} sharply decreased. These observations indicate that the deposition of dysprosium leads to an increase in the crystallinity of the structure and a decrease in the defect sites in the n-Si samples. In addition, a new peak appearing at 307.94 cm^{-1} is associated with the Fg band (2TA phonon mode) in the cubic phase of Dy_2O_3 [17, 18]. The peak position, intensity and width at half maximum are 307.94 cm^{-1}, 1157.84 and 44.15 cm^{-1}, respectively. Thus, using Raman spectroscopy, it is possible to prove the successful deposition of dysprosium (in the form of n-Si<Dy>) on the silicon surface for 50 hours at a temperature of 1473 K under vacuum conditions.

After removing the 15 μm thick surface, it is seen that the intensity of the Dy_2O_3 peak decreases significantly at about 307.94 cm^{-1}, and the intensity of the crystalline and amorphous structure decreases and increases, respectively, compared to n-Si. When analyzing the n-Si<Dy> sample, the removal of the Dy_2O_3 layer from the surface of the silicon wafer was determined.

Fig. 3 shows the secondary phonon range of 15 μm thick samples obtained as a result of mechanical processing by diffusing Dy atoms onto the n-Si surface after heat treatment (phonon mode similar to 2TO) [12.14.15.]. In the range of 900-1020 cm⁻¹, there is a broad peak, which is formed as a result of the superposition of two or more optical modes [19.].
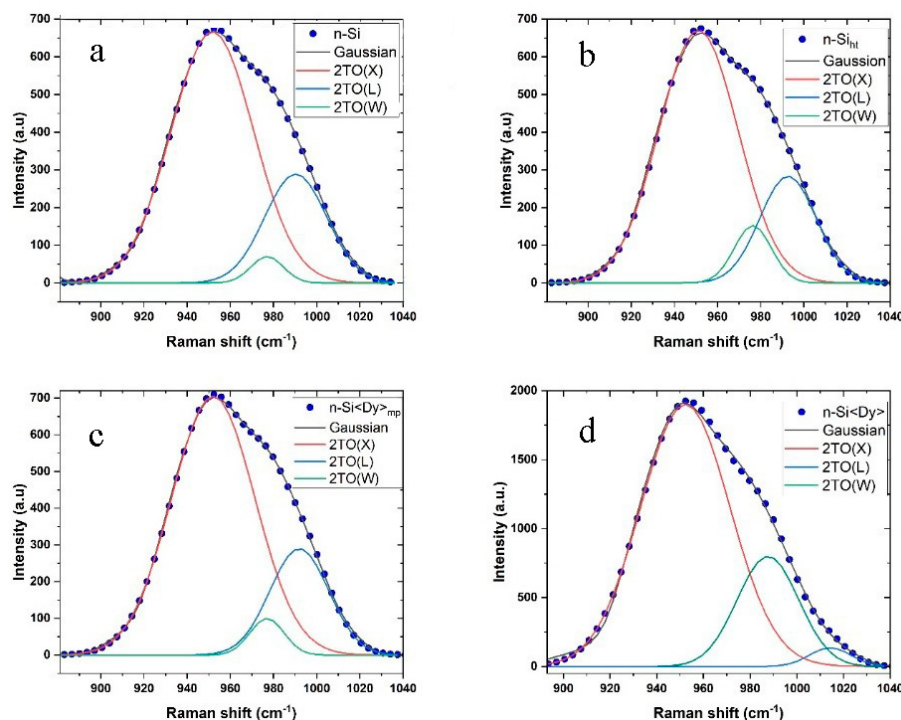
Figure 3. Second-order phonon range of samples:

a. n-Si (as-received material). **b.** n-Si (control) heat-treated at 1373 K for 50 h followed by rapid cooling; **c.** n-Si doped with dysprosium (<Dy>), heat-treated at 1373 K for 50 h followed by rapid cooling and 15 μm depth removal; **d.** n-Si doped with dysprosium (<Dy>), heat-treated at 1373 K for 50 h followed by rapid cooling

For a deep study of the obtained Raman spectra of the samples, work was carried out to separate the obtained signals (3 peaks 2TO(X), 2TO(W) and 2TO(L)) using the Origin Pro and Fityk programs; the obtained data on these peaks are presented in Table 1.

Table 1. Results of the Raman spectra analysis of Si samples.

No	Samples studied	2TO	Center (cm⁻¹)	Area	Height	FWHM
1	**n-Si**	X	951.64	31939.7	666.817	44.9978
		L	990.27	289.095	33.8002	33.8002
		W	977.02	1327.96	70.3974	17.7213
2	**n-Si$_{ht}$**	X	951.16	30764.9	670.615	43.0974
		L	992.65	9270.74	283.238	30.7489
		W	976.35	3285.26	152.592	20.2259
3	**n-Si<Dy>$_{mp}$**	X	952.03	34169.9	705.095	45.5265
		L	991.93	9885.45	290.036	32.0194
		W	976.94	1983.78	99.8088	18.6721
4	**n-Si<Dy>**	X	952.23	91713.8	1901.56	45.1889
		L	1014.27	3032.63	136.081	20.9358
		W	987.64	26456.7	799.234	31.0977

Comparing the obtained Raman spectra data of the samples (Table 1), we can draw a conclusion on the effect of various treatments and additives on the properties of the materials. Below is a comparison of n-Si<Dy> samples with the control n-Si sample:

Change in the 2TO(X) peak shift:

thermally treated n-Siht sample: the area decreased by ~3.7% compared to the control sample (31939.7 versus 30764.9), the height remained virtually unchanged (666.817 versus 670.615), the half-width decreased by ~4.2% (44.9978 versus 43.0974).

sample obtained by decreasing the sample surface area by 15 μm n-Si<Dy>mp: area increase by ~7% (31939.7 vs. 34169.9), height increase by ~5.8% (666.817 vs. 705.095), half-maximum increase by ~1.2% (44.9978 vs. 45.5265). The area and height increase, but the rate of increase is significantly lower than that of the n-Si<Dy> sample.

n-Si<Dy> sample: area increased by ~187% (31939.7 vs. 91713.8), height increased by ~185% (666.817 vs. 1901.56), width at half-maximum increased by ~0.4% (44.9978 vs. 45.1889).

Change in 2TO(L) peak shift:

thermally treated n-Siht sample: area increased by ~3106% (289.095 vs. 9270.74), height increased by ~738% (33.8002 vs. 283.238), width at half-width is ~9% lower (33.8002 vs. 30.7489).

sample obtained by decreasing the sample surface by 15 μm n-Si<Dy>mp: area increased by ~3321% (289.095 vs. 9885.45), height increased by ~758% (33.8002 vs. 290.036), width at half-width is ~5.3% lower (33.8002 vs. 32.0194).

n-Si<Dy> sample: area increased by ~949% (3032.63 vs. 289.095), height increased by ~302% (136.081 vs. 33.8002), FWHM decreased by ~38% (20.9358 vs. 33.8002).

Change in 2TO(W) peak shift:

thermally treated n-Siht sample: area increased by ~147% (1327.96 vs. 3285.26), height increased by ~116% (70.3974 vs. 152.592), FWHM increased by ~14% (17.7213 vs. 20.2259).

sample obtained by decreasing the sample surface area by 15 μm n-Si<Dy>mp: area increased by ~49% (1327.96 vs. 1983.78), height increased by ~42% (70.3974 vs. 99.8088), FWHM increased by ~5.4% (17.7213 vs. 18.6721).

n-Si<Dy> sample: area increased by ~1894% (1327.96 vs. 26456.7), height increased by ~1035% (70.3974 vs. 799.234), FWHM increased by ~75% (17.7213 vs. 31.0977). Raman scattering can also be used to determine the thickness of our silicide films. This is done by measuring the attenuation of Raman scattering on silicon substrate phonons due to the silicide layer. The intensity of the silicon peak is determined by the following equation:

$$I = I_0 e^{-2\alpha d}, \tag{1}$$

where, I_0 is the intensity of the reference silicon wafer without the top layer, a is the absorption coefficient of the top layer, d is the film thickness [17]. To determine the yield thickness, equation (1) can be rewritten as follows:

$$\alpha d = -\frac{1}{2} \ln \left(\frac{I}{I_0} \right). \tag{2}$$

We measured two vibrations of dysprosium monosilicide at wavelengths of 127 and 196 cm^{-1}. To deeply study the physical and chemical structure of both the control n-Si sample and the obtained n-Si<Dy> samples, X-ray phase analysis was performed.

Figure 4 shows the X-ray diffraction pattern of the n-Si sample (initial). It is evident from the data presented in Figure 4 that the X-ray diffraction pattern contains some structural reflections with different intensities (the structural data are presented in Table 2).
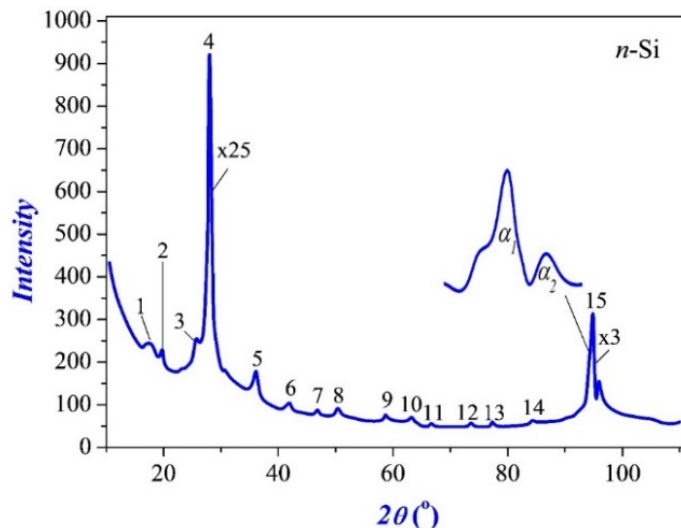
Figure 4. X-ray diffraction pattern of n-Si sample (initial)

Among such structural reflections, the structural line observed at 2θ = 27.99° with d/n = 3188 nm has the highest intensity; it was established based on the experimental analysis that it belongs to the crystallographic orientation (111). The high intensity of this reflection (21779 imp·sec^{-1}) and the half-width (0.01 rad), determined from the experimental results, indicate both a good degree of crystallinity of the studied samples and the fact that most of the constituent atoms are arranged in the crystallographic order (111). According to this structural reflection, its beta (β) component was observed at 2θ = 25.31° with d/n = 3.5096 nm, and its second (222) and third (333) orders were observed at 2θ = 57.9° with d/n = 1.5933 nm and 2θ = 94.68 with d/n = 1.0474, respectively. Usually, the second (222) order reflex is considered to be a forbidden structural line with respect to the crystallographic first order (111), and in most cases it manifests itself in the X-ray diffraction pattern by the presence of microdistortions of the crystal lattice. The ratio of the intensity of the

structural lines to the intensity of the main structural line is I(222)/I(111) = 3.6·10^{-3}, and this value is greater than 10^{-4}, which once again confirms the presence of microdistortions in the crystal lattices of the studied n-Si sample (initial). Such microdistortions of the crystal lattice are formed as a result of the uneven distribution of oxygen atoms from the main background impurities of silicon-based structures. Also, the presence of microdistortions in the crystal lattice is indicated by the fact that the inelastic background level of the X-ray diffraction pattern has a non-monotonic character, i.e. it takes variable values at small, medium and large scattering angles.

In turn, these microdistortions (formed as a result of filling several oxygen atoms in the crystal lattice with unsaturated silicon-oxygen bonds) lead to the formation of a thin layer on the surface of the n-Si plate, belonging to another phase group. Therefore, several structural lines (structural data are given in Table 2), corresponding to silicon dioxide, are observed in the X-ray diffraction pattern at small and medium scattering angles.

Table 2. Structural data of n-Si (initial)

№	Reflexes and background level	Intensive in rel. units	Location 2θ, deg	Interlayer distance. d, Å	Line width, rad	Block size, nm
1	Diffuse. Neg. SiO$_x$; x < 2	247	17.1	5.11	0.05	0.9
2	(100)$_{SiO2}$	233	20.4	4.354	0.009	17.6
3	(111)$_\beta$	231	25,31	3,5096	-	-
4	(111)$_{Si}$	21779	27.997	3,1843	0.01	14.21
5	(210)$_{SiO_2}$	176	35,39	2,45403	0,018	8.44
6	(200)$_{SiO_2}$	99.5	41.66	2.1662	0.017	9.29
7	(220)$_{Si}$	88	46.57	1.9489	0.01	15.3
8	(212)$_{SiO_2}$	99.6	49.84	1.8285	0.015	13.9
9	(222)$_{Si}$	80	57,9	1,5933	Prohibited	
10	(300)$_{SiO_2}$	60.1	64.2	1.451	0.018	9.49
11	(301)$_{SiO_2}$	69	66.2	1.411	0.022	7.92
12	(302)$_{SiO_2}$	74	73.8	1.2828	0.02	8.43
13	(331)$_{Si}$	74	77.14	1.234	0.016	11.56
14	(333,511)$_\beta$	72	83.97	1.1515-	-	-
15	(333,511)$_{Si}$	1221	94.68	1.0474	0.027	7.86
Inelastic background						
Small-angle scattering		259	-	-	-	-
Medium-angle scattering		75	-		-	-
High-angle scattering		58	-	-	-	-

The parameters of the crystal lattices were determined using the experimental values of these structural reflections based on the formulas given in [20], they are equal to a = b = 4.9762 nm and c = 5.4321 nm, respectively. This fact proves that their unit cell belongs to the trigonal crystal lattice and the space group P3$_2$1. Based on the obtained results and their analysis, as well as the values of the SiO$_2$ crystallite sizes presented in Table 2 and their different crystallographic directions, it can be concluded that a polycrystalline layer with a thickness of 1÷2 μm is formed on the surface of the studied n-Si samples. Also, clear splitting by α$_1$ and α$_2$ radiations (having two times differences from each other) of the third (333) structural reflection on the X-ray diffraction pattern indicates that a layer is formed on the surface of the sample under the influence of microstresses.

In addition, the X-ray diffraction pattern at 2θ ≈ 17.1° shows a wide (FWHM = 0.05 rad) diffuse reflection caused by structural fragments of SiO$_x$ in the surface layers with unsaturated bonds. The too wide width of this reflection indicates that the sizes of the structural fragments caused by this reflection are small and there is no long-range order in their arrangement. Consequently, these structural fragments are not SiO$_x$ nanocrystals, but clusters. The characteristic sizes of these clusters were ~ 0.9 nm, respectively.

Based on the experimental values of the main (111) structural reflection, it was determined that the lattice parameter of the n-Si plate under study was a$_{Si}$ = 5.4451 nm.

The samples, the structural values of which were determined above, were subjected to heat treatment at a temperature of 1100°C for 40 hours, and then cooled at a cooling rate of 3000C/s. The surface of such plates was polished using certain technological means. X-ray structural studies of the processed samples were carried out, the experimental results are shown in Fig. 5.

From Fig. 5 it is evident that the X-ray patterns of the processed n-Si plates differ significantly from the X-ray pattern of the original samples (Fig. 4) and an increase in the intensity of structural lines by 13 times is observed in it. However, the scattering angle of the observed main structural reflection (111) remained practically unchanged, and the lattice constant is equal to a$_{Si(pol)}$ = 5.4456 nm with a very small difference (Δa = 0.0005 nm) in values.

Also, the characteristic second (222) and third (333) orders increase by 114 and 377 times, respectively. In most X-ray diffraction patterns of the undistorted diamond-like structure lattice, the second (222) order structural line is not observed (forbidden reflection), and the intensity of the third (333) order structural line is lower than the intensity of the main structural line (111) [21]. In our case, the X-ray diffraction pattern showed high-intensity second (222) and third (333) order structural lines. This, in turn, indicates that certain microdeformations arose in their crystal lattice due to long-

term (40 hours) heat treatment (1100 °C) and subsequent rapid cooling of the samples. In support of our statement, we can cite an example of the ratio I(222)/I(111) of the intensities of the lines of the second (222) order and the main (111) structure, equal to $3.4 \cdot 10^{-2}$. The fact that this value is almost 100 times greater than the value of 10^{-4} indicates the presence of sufficient microstresses in the crystal lattice [22]. In addition, the sharp cooling of the samples caused the disintegration of their subcrystallites, which led to a decrease in their sizes (Table 3). A decrease in the size of the subcrystallites leads to an increase in the number of boundary areas in them, this fact, in turn, causes an increase in the number of defective high-potential regions, i.e. microdistortions at their interfaces [20].
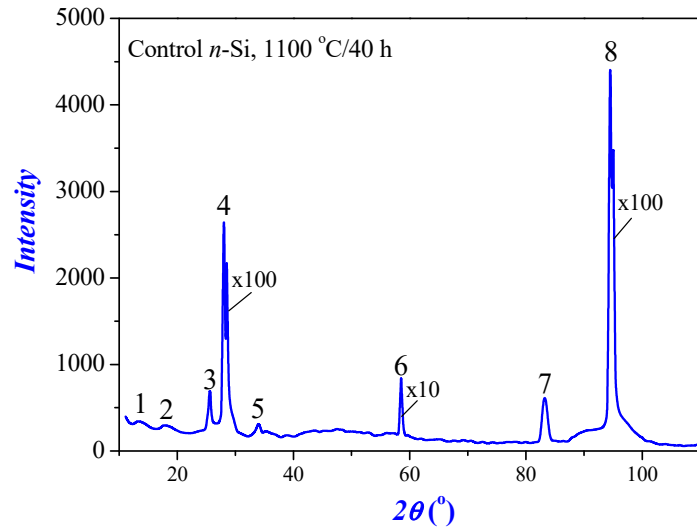

Figure 5. X-ray diffraction pattern of processed n-Si wafers (control)

Table 3. Structural data of processed n-Si wafers (control)

№	Reflexes and background level	Intensive in rel. units	Location 2θ, deg	Interlayer distance. d, Å	Line width, rad	Block size, nm
1	Diffuse. Neg. SiO_x; x < 2	347	13.51	6.5484	0.1473	0.99
2	Diffuse. Neg. SiO_x; x < 2	296	17.84	5.0103	0.1499	0.98
3	$(111)_\beta$	689	25.47	3.4964	-	-
4	$(111)_{Si}$	268610	27.995	3.1846	0.017	8.8
5	$(210)_{SiO_2}$	313	34.14	2.5531	0.024	6.3
6	$(222)_{Si}$	9175	58.47	1.5772	Prohibited	
7	$(333,511)_\beta$	636	83.24	1.1597	-	-
8	$(333,511)_{Si}$	461190	94.5	1.0492	0.017	12.4
Inelastic background						
Small-angle scattering		219	-	-	-	-
Medium-angle scattering		132	-	-	-	-
High-angle scattering		63	-	-	-	-

After heat treatment, the surface of the samples was polished and a 2 μm thick layer was removed. When analyzing the obtained sample, only one structural line was observed on their X-ray diffraction pattern at 2θ = 34.14° with d/n = 2.5531 nm, belonging to silicon dioxide, corresponding to a trigonal crystal lattice (with parameters a = b = 4.9762 nm and c = 5.4321 nm) and space group P321. This, in turn, indicates that under the influence of heat treatment, oxygen atoms form a bond with silicon atoms at a certain depth, and then under the influence of rapid cooling they form crystallites. But due to the ionic radius of oxygen (r_{Si}^{4+} = 1.40 Å), which is greater than the ionic radius of silicon (r_o^{-2} = 0.42 Å), its ions prefer to be located along the unsaturated bond at the boundaries of subcrystallites [23]. This nature of oxygen leads to the formation of structural fragments with low symmetry among subcrystallites consisting of silicon ions with high symmetry, as well as to deformations of the crystal lattice due to the arrangement of its atoms in the nodes. This is evidenced by an increase in the level of the inelastic background at small, medium and large scattering angles of the X-ray diffraction patterns of the studied samples and the observation of two diffuse reflections associated with SiO_x fragments in small-angle scattering (see Fig. 5).

Subsequently, using doping (for 40 hours at a temperature of 1100 °C) with Dy atoms, n-Si<Dy> samples were obtained. The obtained X-ray diffraction data for the samples are shown in Fig. 6.

It is evident that the X-ray diffraction pattern of n-Si<Dy> platinum differs sharply from the X-ray diffraction pattern of the n-Si sample (initial sample, Fig. 4). It is necessary to take into account the fact that the intensity of the main structural line (111) did not change, and the intensity of the structural lines of the second (222) and third (333) orders increased by 1.6 and 82 times, respectively. Observation of the forbidden structural line of the second (222) order and the ratio of its intensity to the intensity of the main (111) reflection is $I(222)/I(111) = 4.8 \cdot 10^{-3}$ and this value is less than 10^{-4}. Also, the intensity of the line of the structure of the third (333) order is 4.5 times greater than the intensity of the main reflection (111). This, in turn, indicates that volume defects were formed at the boundaries of subcrystallites as a result of prolonged heat treatment of the samples and rapid cooling at the end of the process [24]. In addition, in the X-ray diffraction pattern, the main (111) structural line was shifted toward higher-angle scattering ($\Delta\theta = 0.18^o$). Based on the results of experiments on this structural line, it was established that the lattice constant of the sample is $a_{Si<Dy>} = 5.4186$ nm. This, in turn, is associated with the doping of the silicon plate with Dy atoms, and the difference in the ionic radii of the O ($r_o^{-2} = 1.3$ Å) and Dy ($r_{Dy}^{3+} = 0,91$ Å) atoms with Si ($r_{Si}^{4+} = 0.42$ Å and $r_{Si}^{-4} = 2.7$ Å) indicates that a deformation equal to $a_{Si} - a_{Si<Dy>} = 0.026$ nm has formed in the crystal lattice.
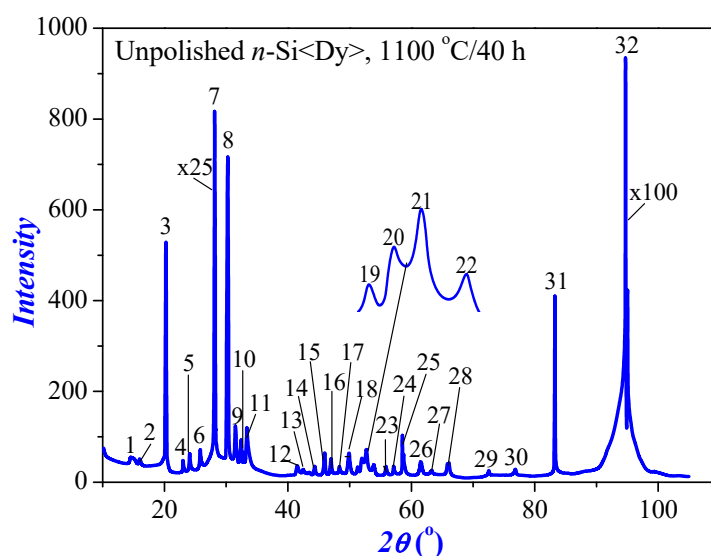

Figure 6. Radiograph of unpolished n-Si<Dy> platins

In addition, a number of structural reflections belonging to other crystallographic orientations are observed in the X-ray diffraction pattern with small- and medium-angle scattering, and their experimental and calculated data are presented in Table 4. Based on the analysis of the obtained results, it was found that these structural reflections are observed as a result of combinations of the mutual order of the SiO_2 and Dy_2O_3 compounds. As a result of long-term heat treatment of the samples, the diffusing Dy atoms combine with oxygen atoms from the main background impurities of silicon to form nanocrystallites. This is evidenced by the fact that the inelastic background level tends to be monotonous in the medium and large-angle scattering in the X-ray diffraction pattern of the obtained n-Si<Dy> sample. Also, after the processes carried out, as a result of sharp cooling of the samples, it was found that nanocrystallites based on SiO_2 and Dy_2O_3 compounds accumulate mainly in the surface areas of the obtained sample and form oxide layers with polycrystalline properties. Based on the experimental results of the study of the formed layer, consisting of nanocrystallites of different crystallographic orientation and size, it was established that such a layer has a monoclinic unit cell with parameters $a = b = 6.4548$ nm and $c = 8.6549$ nm, belonging to the space group $P2_{1/c}$.

However, rapid cooling of the samples leads to the formation of unsaturated bonds due to the absence of oxygen and dysprosium atoms in the ordered arrangement of silicon-oxygen-dysprosium atoms of some nanocrystallites [25, 23]. This, in turn, leads to the formation O of small clusters consisting of a small number of atoms [26]. The small size and close arrangement of such clusters leads to the appearance of diffuse reflection in small-angle scattering X-ray diffraction patterns of the studied samples.

Table 4. Structural data without polished n-Si<Dy> wafers

No	Reflexes and background level	Intensive in rel. units	Location 2θ, deg	Interlayer distance. d, Å	Line width, rad	Block size, nm
1	Diffuse. Neg. $SiDy_xO_x$; x < 2	54	14.56	6.057	0.09	1.6
2	$(110)_{SiO_2+Dy_2O_3}$	51	15.89	5.575	0.0054	27
3	$(200)_{SiO_2+Dy_2O_3}$	535	20.18	4.3964	0.0033	44.5
4	$(111)_{SiO_2+Dy_2O_3}$	48	22.79	3.8989	0.0035	42.1
5	$(210)_{SiO_2+Dy_2O_3}$	67	23.88	3.7264	0.0035	42.3

No	Reflexes and background level	Intensive in rel. units	Location 2θ, deg	Interlayer distance. d, Å	Line width, rad	Block size, nm
6	$(111)_\beta$	86	26.02	3.4207	-	-
7	$(111)_{Si}$	22178	28.13	3.1688	0.003	49.7
8	$(021)_{SiO_2+Dy_2O_3}$	1067	29.41	3.0337	0.0041	36.4
9	$(300)_{SiO_2+Dy_2O_3}$	842	30.74	2.9059	0.0041	36.6
10	$(121)_{SiO_2+Dy_2O_3}$	110	32.25	2.7733	0.0036	41.8
11	$(22\bar{1})_{SiO_2+Dy_2O_3}$	147	33.27	2.6946	0.0037	40.6
12	$(130)_{SiO_2+Dy_2O_3}$	25	40.48	2.2263	0.0053	29.1
13	$(031)_{SiO_2+Dy_2O_3}$	38	41.39	2.1796	0.0062	24.9
14	$(230)_{SiO_2+Dy_2O_3}$	35	44.29	2.0431	0.0053	29.5
15	$(321)_{SiO_2+Dy_2O_3}$	65	45.87	1.9766	0.0053	29.7
16	$(220)_{Si}$	59	46.93	1.938	0.004	39.5
17	$(13\bar{2})_{SiO_2+Dy_2O_3}$	37	48.29	1.8852	0.0017	93.3
18	$(411)_{SiO_2+Dy_2O_3}$	73	49.86	1.8272	0.0074	21.57
19	$(51\bar{1})_{SiO_2+Dy_2O_3}$	40	51.26	1.7808	0.0057	28.17
20	$(500)_{SiO2+Dy2O3}$	62	51.94	1.7588	0.0068	23.68
21	$(41\bar{3})_{SiO_2+Dy_2O_3}$	85	52.65	1.7369	0.0076	21.25
22	$(231)_{SiO_2+Dy_2O_3}$	44	53.8	1.7025	0.0081	20.04
23	$(311)_{Si}$	39	55.73	1.6478	0.0024	68.23
24	$(004)_{SiO_2+Dy_2O_3}$	46	56.94	1.6156	0.0042	39.21
25	$(222)_{Si}$	131	58.46	1.5774	Prohibited	
26	$(24\bar{2})_{SiO_2+Dy_2O_3}$	48	61.27	1.5116	0.007	24
27	$(142)_{SiO_2+Dy_2O_3}$	30	63.29	1.4681	0.0065	46.9
28	$(43\bar{3})_{SiO_2+Dy_2O_3}$	49	65.81	1.4179	0.0072	23.9
29	$(31\bar{5})_{SiO_2+Dy_2O_3}$	29	72.46	1.3031	0.0059	30.4
30	$(350)_{SiO_2+Dy_2O_3}$	31	76.64	1.2422	0.0039	47.3
31	$(333,511)_\beta$	444	83.25	1.1595	-	-
32	$(333,511)_{Si}$	100210	94.68	1.0474	0.0017	125.7
Inelastic background						
Small-angle scattering		31	-	-	-	-
Medium-angle scattering		14	-	-	-	-
High-angle scattering		11	-	-	-	-

Fig. 7 shows an X-ray diffraction pattern after polishing the obtained n-Si samples doped with Dy atoms at a temperature of 1100°C for 40 hours. Significant differences can be seen in the resulting X-ray diffraction pattern compared to the X-ray diffraction patterns of the original samples (Fig. 4).
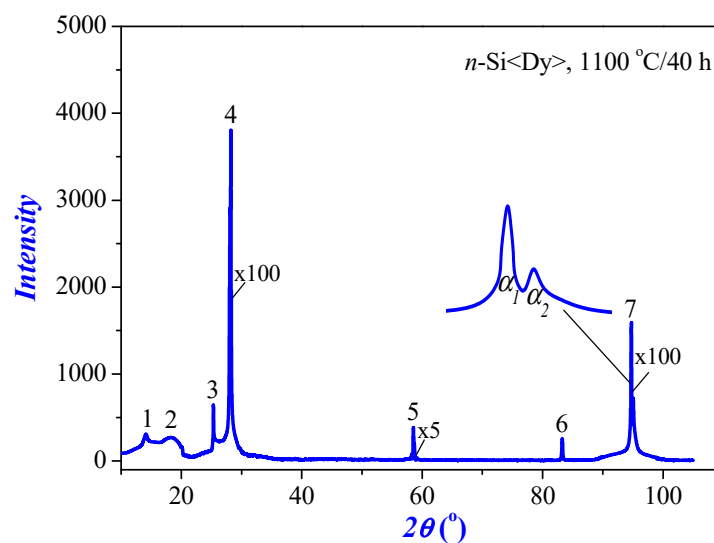

Figure 7. X-ray diffraction pattern of processed n-Si<Dy> samples

It can be seen that the main (111) structural line is 18 times higher than its intensity and is shifted toward higher scattering angles at $\Delta\theta = 0.19°$ (Table 5). This, in turn, indicates that the number of atoms belonging to a certain crystallographic orientation increase, i.e. the degree of monocrystallization increases [22]. But the manifestation shifted toward higher angular scattering reports that the deformation caused by the penetration of Dy atoms into the silicon crystal

lattice resulted in the formation of a_{Si} - $a_{Si(pol)<Dy>}$ = 5.4451 nm – 5.4080 nm = 0.037 nm. This, in turn, leads to the fact that in the X-ray diffraction pattern the radiation intensity of the second (222) (forbidden) order structure increases by 25 times. The intensity ratio of this structural line to the intensity of the main (111) structural line is I(222)/I(111) = 0.005, and this value is greater than 10^{-4} and this indicates the presence of micronutrients under the influence of deformations [27].

When studying the sample (333), the structural line was observed to be two times less intense compared to the intensity of the main structural line (111), and was also clearly split into α1 and α2 components and suggested a ratio of their intensities of $I_{\alpha_1}/I_{\alpha_2} \approx 2$. This, in turn, indicates that Dy atoms cannot be located in bulk crystal nodes due to the difference in the ionic radius of Dy atoms Dy (r_{Dy}^{3+}= 0,91 Å) and Si (r = 0.42 Å and Si (r_{Si}^{4+} = 0.42 Å and r_{Si}^{-4} = 2.7 Å), i.e., they settle on the nodes at the interfaces of subcrystallites and surface areas. This is also evidenced by the fact that the level of the inelastic background of the X-ray diffraction pattern has a monotonic character with medium- and large-angle scattering.

The obtained research data led to the following conclusion: silicon, oxygen and dysprosium atoms form new bonds, forming different crystallites as a result of long-term heat treatment of the samples. Also, sharp cooling of the samples after heat treatment leads to the formation of oxide layers on the surface areas of the formed crystallites. However, as a result of polishing the surface of the samples and removing layers 1÷2 μm thick, no structural lines associated with SiO_2 and Dy_2O_3 compounds were observed in the X-ray diffraction patterns of the n-Si(pol)<Dy> samples. Only in scattering at an angle of 14.05° with d/n = 6.2774 was a structural line associated with the Dy_2O_3 compound observed, which means that oxygen and dysprosium atoms are located in empty sites at the interfaces of the n-Si(pol)<Dy> sample subcrystallites. This allows the formation of small-sized nanocrystallites due to the accumulation of impurity atoms in these places. Based on the experimental results of the structural reflection $(001)_{Dy_2O_3}$, it was established that such nanocrystallites belong to the space group P4m2 and consist of tetragonal unit cells with parameters a = b= 3.8116 nm and c = 5.4933 nm, respectively.

Table 5. Structural data of processed n-Si<Dy> wafers

№	Reflexes and background level	Intensive in rel. units	Location 2θ, deg	Interlayer distance. d, Å	Line width, rad	Block size, nm
1	$(001)_{Dy_2O_3}$	337	14.05	6.2774	0.011	13.2
2	Diffuse. Neg. $SiDy_xO_x$; x < 2	288	18.27	4.8669	0.1297	0.98
3	$(111)_\beta$	4360	25.33	3.5121	-	-
4	$(111)_{Si}$	398650	28.19	3.1626	0.0049	52.3
5	$(222)_{Si}$	2056	58.53	1.5757	Prohibited	
6	$(333,511)_\beta$	261	83.29	1.1591	-	-
7	$(333,511)_{Si}$	193840	94.68	1.04747	0.0071	97.6
Inelastic background						
Small-angle scattering		38	-	-	-	-
Medium-angle scattering		15	-	-	-	-
High-angle scattering		11	-	-	-	-

In addition, at the boundaries of subcrystallite division near the surface areas of the Si(pol)<Dy> sample, the formation of unsaturated bonds with oxygen and dysprosium atoms is observed, and these do not allow the atoms to be located in a long-range order. As a result, diffusion reflection is observed during small-angle scattering of the sample under study.

CONCLUSIONS

The study included a comprehensive assessment of the structural and optical characteristics of dysprosium (Dy) doped silicon using Raman spectroscopy and X-ray diffraction (XRD) analysis. The aim of the work was to study the effects of dysprosium doping of silicon by high-temperature diffusion and their influence on the crystal structure and optical properties of the materials.

Raman spectroscopy showed that doping with dysprosium leads to significant changes in the Raman spectrum. In particular, an increase in the peak intensity at 523.93 cm^{-1} and the appearance of a new peak at 307.94 cm^{-1} associated with the phonon modes of Dy_2O_3 were noted. This indicates successful deposition of dysprosium on the silicon surface and an increase in the crystallinity of the structure, as well as a decrease in the defect concentration. At the same time, the observed decrease in the intensity of the peaks corresponding to amorphous silicon confirms the improvement of the crystalline structure of the samples. X-ray phase analysis confirmed changes in the silicon crystal lattice after doping. In particular, a change in the crystal lattice parameters associated with the introduction of dysprosium is observed. The intensities of the X-ray lines for the samples subjected to heat treatment increased, indicating the formation of new crystalline phases and the possible formation of oxide layers.

Based on the X-ray phase analysis data, the exact crystallographic orientation and change in the lattice parameters depending on the treatment were established. Thus, in the n-Si<Dy> samples, changes were found indicating the presence

of dysprosium dioxides and a change in the crystal structure of silicon, which is confirmed by shifts in the X-ray peaks and changes in the sizes of subcrystallites.

In general, the results of the work show that doping silicon with dysprosium leads to an improvement in the crystal structure and a change in the optical properties. The use of Raman spectroscopy and X-ray phase analysis methods made it possible to better understand the mechanisms of interaction of rare earth elements with silicon and their effect on the properties of semiconductor materials.

ORCID

Khodjakbar S. Daliev, https://orcid.org/0000-0002-2164-6797; **Sharifa B. Utamuradova**, https://orcid.org/0000-0002-1718-1122
Jonibek J. Khamdamov, https://orcid.org/0000-0003-2728-3832 **Shahriyor B. Norkulov**, https://orcid.org/0000-0002-2171-4884;
Mansur B. Bekmuratov, https://orcid.org/0009-0006-3061-1568

REFERENCES

[1]   A.I. Prostomolotov, Yu.B. Vasiliev, and A.N. Petlitsky, "Mechanics of defect formation during growth and heat treatment of single-crystal silicon," (4), 1716–1718 (2011). http://www.unn.ru/pages/e-library/vestnik/19931778_2011_-_4-4_unicode/147.pdf

[2]   Sh.B. Utamuradova, Sh.Kh. Daliyev, J.J. Khamdamov, Kh.J. Matchonov, Kh.Y. Utemuratova, East Eur. J. Phys. (2), 274-278 (2024). https://doi.org/10.26565/2312-4334-2024-2-28

[3]   K.S. Daliev, S.B. Utamuradova, J.J. Khamdamov, and Z.E. Bahronkulov, "Electrophysical properties of silicon doped with lutetium," Advanced Physical Research, **6**(1), 42–49 (2024). https://doi.org/10.62476/apr61.49

[4]   Kh.S. Daliev, Sh.B. Utamuradova, J.J. Khamdamov, and M.B. Bekmuratov, "Structural Properties of Silicon Doped Rare Earth Elements Ytterbium," East Eur. J. Phys. (1), 375-379 (2024). https://doi.org/10.26565/2312-4334-2024-1-37

[5]   K.S. Daliev, S.B. Utamuradova, A. Khaitbaev, J.J. Khamdamov, S.B. Norkulov, and M.B. Bekmuratov, "Defective Structure of Silicon Doped with Dysprosium," East European Journal of Physics, (2), 283-287 (2024). https://doi.org/10.26565/2312-4334-2024-2-30

[6]   S.B. Utamuradova, K.S. Daliev, A.I. Khaitbaev, J.J. Khamdamov, J.S. Zarifbayev, and B.S. Alikulov, "Defect Structure of Silicon Doped with Erbium," East European Journal of Physics, (2), 288-292 (2024). https://doi.org/10.26565/2312-4334-2024-2-31

[7]   S.B. Utamuradova, S.K. Daliev, A. Khaitbaev, J. Khamdamov, U.M. Yuldoshev, and A.D. Paluanova, "Influence of Gold on Structural Defects of Silicon," East European Journal of Physics, (2), 327-335 (2024). https://doi.org/10.26565/2312-4334-2024-2-38

[8]   R.T.-P. Lee, K.-M. Tan, T.-Y. Liow, C.-S. Ho, S. Tripathy, G.S. Samudra, D.-Z. Chi, and Y.-C. Yeo, "Probing the ErSi1.7 Phase Formation by Micro-Raman Spectroscopy," Journal of The Electrochemical Society, **154**(5) H361-H364 (2007). https://doi.org/10.1149/1.2710201

[9]   J. Kedzierski, P. Xuan, E.H. Anderson, J. Bokor, T.J. King, and C. Hu, "Complementary silicide source/drain thin-body MOSFETs for the 20 nm gate length regime," in: *International Electron Devices Meeting 2000. Technical Digest. IEDM (Cat. No.00CH37138)* (San Francisco, CA, USA, 2000), p. 57-60. https://doi.org/10.1109/IEDM.2000.904258

[10] W.-J. Lee, and Y.-H. Chang, "Growth without Postannealing of Monoclinic VO_2 Thin Film by Atomic Layer Deposition Using VCl 4 as Precursor," Coatings, **8**, 431 (2018). https://doi.org/10.3390/coatings8120431

[11] K. Ali, S. Khan, M. Zubir, and M.Z.M. Jafri, "Spin-on doping (SOD) and diffusion temperature effect on re-combinations/ideality factor for solar cell applications," Chalcogenide Letters, **9**, 457–463 (2012). https://www.chalcogen.ro/457_KhuramAli.pdf

[12] V. Mankad, S. Gupta, P. Jha, N. Ovsyuk, and G. Kachurin, "Low-frequency Raman scattering from Si/Ge nanocrystals in different matrixes caused by acoustic phonon quantization," J. Appl. Phys. **112**, 54318 (2012). https://doi.org/10.1063/1.4747933

[13] T. Liu, P. Ge, and W. Bi, "The Influence of Wire Speed on Phase Transitions and Residual Stress in Single Crystal Silicon Wafers Sawn by Resin Bonded Diamond Wire Saw," Micromachines (Basel), **12**, (2021). https://doi.org/10.3390/mi12040429

[14] G.-W. Lee, Y.-B. Lee, D.-H. Baek, J.-G. Kim, and H.-S. Kim, "Raman Scattering Study on the Influence of E-Beam Bombardment on Si Electron Lens," Molecules, **26**, (2021). https://doi.org/10.3390/molecules26092766

[15] K. Adu, M. Williams, M. Reber, R. Jayasingha, H.R. Gutierrez, and G. Sumanasekera, "Probing Phonons in Nonpolar Semiconducting Nanowires with Raman Spectroscopy," J. Nanotechnol. **2012**, 264198 (2012). https://doi.org/10.1155/2012/264198

[16] Y. Gogotsi, C. Baek, and F. Kirscht, "Raman microspectroscopy study of processing-induced phase transformations and residual stress in silicon," Semicond. Sci. Technol. **14**, 936 (1999). https://doi.org/10.1088/0268-1242/14/10/310

[17] D. Casimir, H. Alghamdi, I.Y. Ahmed, R. Garcia-Sanchez, and P. Misra, "Raman Spectroscopy of Graphene, Graphite and Graphene Nanoplatelets," in: *2D Materials*, edited by C. Wongchoosuk, and Y. Seekaew, (IntechOpen, 2019). https://doi.org/10.5772/intechopen.84527

[18] K. Maex, and M. Van Rossum, "Properties of Metal Silicides," Inspec, (The institution of Electrical Engeineers, London, UK, 1995). p. 5. https://api.semanticscholar.org/CorpusID:92679751

[19] Sh.B. Utamuradova, Kh.J. Matchonov, J.J. Khamdamov, and Kh.Y. Utemuratova, "X-ray diffraction study of the phase state ofsilicon single crystals doped with manganese," New Materials, Compounds and Applications, **7**(2), 93-99 (2023). http://jomardpublishing.com/UploadFiles/Files/journals/NMCA/v7n2/Utamuradova_et_al.pdf

[20] S.Z. Zainabidinov, Sh.B. Utamuradova, *et al*., "Structural Peculiarities of the $(ZnSe)_{1-x-y}(Ge_2)_x(GaAs_{1-\delta}Bi_\delta)_y$ Solid Solution with Various Nanoinclusions," Journal of Surface Investigation: X-ray, Synchrotron and Neutron Techniques, **16**(6), 1130–1134 (2022). https://doi.org/10.1134/S1027451022060593

[21] I.L. Shulpina, R.N. Kyutt, V.V. Ratnikov, I.A. Prokhorov, I.Zh. Bezbakh, M.P. Shcheglov, "Methods of X-ray diffraction diagnostics of heavily doped semiconductor single crystals," Journal of Technical Physics, **80**(4), 105 (2010). https://journals.ioffe.ru/articles/viewPDF/9970

[22] S.Z. Zainabidinov, A.S. Saidov, M.U. Kalanov, and A.Y. Boboev, "Synthesis, Structure and Electro-Physical Properties n-GaAs-p-(-$(GaAs)_{1-x-y}(Ge_2)_x(ZnSe)_y$ Heterostructures," App. Sol. Energy, **55**(5), 291–308 (2019). https://doi.org/10.3103/S0003701X1905013X

[23] K.V. Ravi, *Imperfections and Impurities in Semiconductor Silicon*, (Wiley, New York, 1981).

[24] A.N. Tereshchenko, Dislocation luminescence in silicon with different impurity composition, PhD Thesis, Chernogolovka, 2011.

[25] M.A. Lourenço, Z. Mustafa, W. Luduczak, L. Wong, R.M. Gwilliam, and K.P. Homewood, "High temperature dependence Dy[3+] in crystalline silicon in the optical communication and eye-safe spectral regions," Optics Letters, **38**(18), 3669-3672 (2013). https://doi.org/10.1364/OL.38.003669

[26] I.P. Suzdalev, and P.I. Suzdalev, "Nanoclusters and nanocluster systems. Organization, interaction, properties," Advances in Chemistry, **70**(3), 203-240 (2001). https://doi.org/10.1070/RC2001v070n03ABEH000627

[27] N.V. Gokhfeld, Electron microscopic study of atomically ordered alloys based on Cu-Pd and Cu-Au, subjected to severe plastic deformation and subsequent annealing, PhD Thesis, Ekaterinburg, 2019. http://elar.urfu.ru/handle/10995/95084

ДОСЛІДЖЕННЯ ДЕФЕКТНОЇ СТРУКТУРИ КРЕМНІЮ, ЛЕГОВАНОГО ДИСПРОЗІЄМ, ЗА ДОПОМОГОЮ РЕНТГЕНОФАЗОВОГО АНАЛІЗУ ТА РАМАНІВСЬКОЇ СПЕКТРОСКОПІЇ

Ходжакбар С. Далієв[a], Шаріфа Б. Утамурадова[b], Джонібек Дж. Хамдамов[b], Шахрійор Б. Норкулов[b], Мансур Б. Бекмуратов[b]

[a]*Філія Федерального державного бюджетного навчального закладу вищої освіти «Національний дослідницький університет МПЕІ», вул. Йогду, 1, м. Ташкент, Узбекистан*

[b]*Інститут фізики напівпровідників та мікроелектроніки Національного університету Узбекистану, 100057, Ташкент, Узбекистан, вул. Янги Алмазар, 20*

У даній роботі досліджено вплив легування кремнію диспрозієм (Dy) на його структурні та оптичні характеристики. Кремній n-Si легували диспрозієм методом термодифузії при 1473 К протягом 50 годин. Для аналізу використовували спектроскопію комбінаційного розсіювання та рентгеноструктурний аналіз. Результати раманівської спектроскопії показали головний пік при 523,93 см⁻¹, що відповідає оптичним фононам n-Si, зі збільшенням інтенсивності та повної ширини на половині максимуму (FWHM) у зразках n-Si<Dy>, що вказує на покращення в кристалічність структури. Зменшення інтенсивності піків при 127,16 см⁻¹ і 196,24 см⁻¹, пов'язаних з аморфними структурами, підтверджує зменшення дефектів. Виявлення нового піку при 307,94 см⁻¹ вказує на успішне осадження диспрозію у вигляді нанокристалітів, пов'язаних із фононною модою 2ТА у кубічній фазі Dy_2O_3. Рентгеноструктурний аналіз виявив характерні структурні лінії, що вказують на орієнтацію кристала (111) та наявність мікроспотворень у гратці. Термічна обробка та швидке охолодження призводять до зміни інтенсивності структурних ліній, збільшення ліній другого та третього порядку, що свідчить про мікродеформації та зміну розмірів субкристалітів. Легування кремнію диспрозієм покращує кристалічність структури, зменшує кількість дефектів і формує на поверхні полікристалічні шари, що складаються з нанокристалів SiO_2 і Dy_2O_3.

Ключові слова: *кремній; дефекти; диспрозій; рідкоземельний елемент; Раманівська спектроскопія; дифузія; теплова обробка; температура; композиція; рентгенофазовий аналіз*

ENERGY OF CRYSTAL LATTICE THERMAL OSCILLATIONS IN TlGaS$_2$ SEMICONDUCTOR COMPOUND

Kamala M. Guseinova[a], Fuad A. Mammadov[a], Aynure A. Hadiyeva[b,c*], Vusala I. Eminova[c,d,e]
Cahangir I. Huseynov[f]

aSumgait State University, Sumgait, Azerbaijan
bAzerbaijan State Oil and Industry University, Baku, Azerbaijan
cKhazar University, Baku, Azerbaijan
dMinistry of Science and Education Republic of Azerbaijan, Institute of Physics, Baku, Azerbaijan
eFrench-Azerbaijani University (UFAZ) under Azerbaijan State Oil and Industry University, Baku, Azerbaijan
fAzerbaijan State Pedagogical University, Baku, Azerbaijan
*Corresponding Author e-mail: aynure.hadiyeva9@gmail.com

This article presents the results of a study of the temperature dependences of the coefficients of thermal expansion and isothermal compressibility of the ternary compound TlGaS$_2$. In the studied temperature range (80-400 K), no anomalies were found in the temperature dependences of these properties. The thermal expansion coefficient of the TlGaS$_2$ semiconductor compound is calculated based on empirical formulas including Debye temperature and Debye functions, and the average energy of the crystal lattice is calculated and its temperature dependence is tabulated. It was shown that the energy of the crystal lattice depends on the degree of anharmonicity of the oscillations.

Keywords: *Semiconductor; Thermal expansion; Thermal oscillation; Crystal lattice; Debye temperature; Young's modulus; Anharmonicity*
PACS: 05.70.Ce

INTRODUCTION

The class of thallium chalcogenide compounds of $TlB^{III}C_2^{VI}(B = In, Ga, \quad C = S, Se, Te)$ exhibits a layered-chain structure, is classified as 2D crystals and is characterised by anisotropic physical properties [1]. These compounds are characterized by weak van der Waals bonding between layers and covalent bonding within each layer. The charge carriers in $TlB^{III}C_2^{VI}$ single crystals can move within the layers, while their motion between the layers is restricted by van der Waals interaction. Crystals of this family are of not only scientific but also significant practical interest, since they are optically active, have high photosensitivity in a wide spectral range and, as a result, are promising for use in optoelectronics.

The ternary compound $TlGaS_2$ belongs to a large group of layered crystals of the $TlB^{III}C_2^{VI}$ type exhibiting both semiconductor and ferroelectric properties, and crystallizes into a monoclinic structure in the space group $C_{2h}^h(C\,2/c)$with unit cell parameters $a = 10.299\,Å,\ b = 10.284\,Å,\ c = 15.175\,Å,\ \beta = 99.603°$ [2, 3]. $TlGaS_2$ is a $p-$type wide bandgap layered semiconductor with melting point $T_{melt} = 1165\,K$, possesses a wide range of practically important physical characteristics such as high photo- and X-ray sensitivity. On the temperature dependences of various physical parameters of this compound, sharp peaks are observed. Sharp increases in the values of thermal parameters are often due to the temperature dependence of the Gruneisen parameter in these substances. The role of optical phonons in phonon-phonon scattering increases in these cases [4].

To assess the nature of chemical bonding and the dynamics of thermal oscillations in layered semiconductors, it is important to investigate the temperature dependences of thermal parameters. In complex semiconductor compounds, these dependencies are due to the degree of anharmonicity of crystal lattice vibrations, transverse and longitudinal acoustic phonons, as well as optical phonons.

Analysis of literature data shows that $TlGaS_2$ is a perspective semiconductor material in terms of practical applications [5, 6, 7, 8]. To elucidate the temperature range of applicability of a given material, it is necessary to know the thermal and thermodynamic properties in addition to the electrical properties. The coefficients of thermal expansion and isothermal compressibility are such parameters. These parameters are significant and informative characteristics of solids that are related to the thermodynamic and structural characteristics of the material. The objective of the present work is to investigate the temperature dependences of thermal expansion and isothermal compressibility coefficients of $TlGaS_2$, basing on experimental investigations of thermal properties of crystals to determine the Debye function, the energy of zero-point vibrations in the lattice, the values of average lattice energy and the Debye temperature.

EXPERIMENTAL METHOD

The samples were synthesized from the elements taken in stoichiometric ratios by their direct fusion in quartz ampoules evacuated to $10^{-3}\,Pa$ at $1180 \pm 5\,K$ for 5–7 h. High purity chemical elements were used as initial components: Tl (Tl00), Ga (Ga 5N), S (HP 165). During the synthesis process, the ampoules were shaken frequently to ensure better mixing of the components. The samples based on $TlGaS_2$ were annealed in vacuum at 750 K for 120 h in order to homogenize. Homogenizing annealing of the resulting single-phase samples was carried out in a spectrally pure argon environment. The annealed alloys were cooled to room temperature in a switched-off furnace mode. Completeness of synthesis and homogeneity of the obtained samples, as well as their individuality, were controlled by DTA and XRD methods. The single crystals of materials investigated by us were grown applying a modified Bridgman method – a method of slow cooling at a constant temperature gradient along the ingot. The structural and morphological properties of $TlGaS_2$ thin films were investigated by XRD, SEM and AFM techniques.

The angular positions of the diffraction spectrum lines of the synthesized $TlGaS_2$ samples were recorded on a Bruker D8 ADVANCE X-ray diffractometer in $40\,kV$, $40\,mA$ mode with CuK_α -radiation ($\lambda = 1.5406$ Å) on a 450K TTC type temperature chamber. Samples for measurements were prepared by grinding crystals and their subsequent pressing in a special holder. Diffraction reflections were recorded in the range 2θ 0–$90°$, indexed by the TOPAS program, and crystallographic parameters refined by using EVA program. To study the morphology and microcomposition of the sample surface, a scanning electron microscope of Japanese brand JEOL JSM6610-LV was used.

Cleavage along the basal plane (001) $TlGaS_2$ was carried out immediately before the experiments. Electron diffraction patterns and micrographs were taken on freshly cleaved surfaces. AFM surface micrographs were obtained for 3-5 samples, from which the clearest images reflecting the general trend were selected.

Measurements of the coefficient of thermal expansion (α_L) and isothermal compressibility (Tχ) were carried out using the dilatometric setup described in [9, 10]. For these measurements, cylindrical samples with a length of $0.03\,m$ and a diameter of $0.005\,m$ were made from synthesized ingots. The measurements were carried out in a direction perpendicular to the layers. The relative measurement error was 0.5%.

RESULTS AND DISCUSSION

The X-ray pattern of $TlGaS_2$ recorded at offset angle 2θ in the range of 0–$90°$, is depicted in Figure 1a). Analysis of the intensities of X-ray reflections shows the presence of a predominant direction in the crystal, as well as that the investigated sample consists of a single phase. It is evident that the diffraction peaks in the control pattern of the sample appeared at $2\theta = 24.35°, 36.15°$ and $48.45°$. These peaks are associated with the $(400), (-422)$ and (215) planes, respectively. Diffraction patterns recorded from different areas of single crystals corresponded to the monoclinic syngony. The unit cell parameter calculated by the least squares method for the reflections is $a = 10.299$ Å, $b = 10.284$ Å, $c = 15.175$ Å, $\beta = 99.603°$, agreeing satisfactorily with the results of [11, 12].
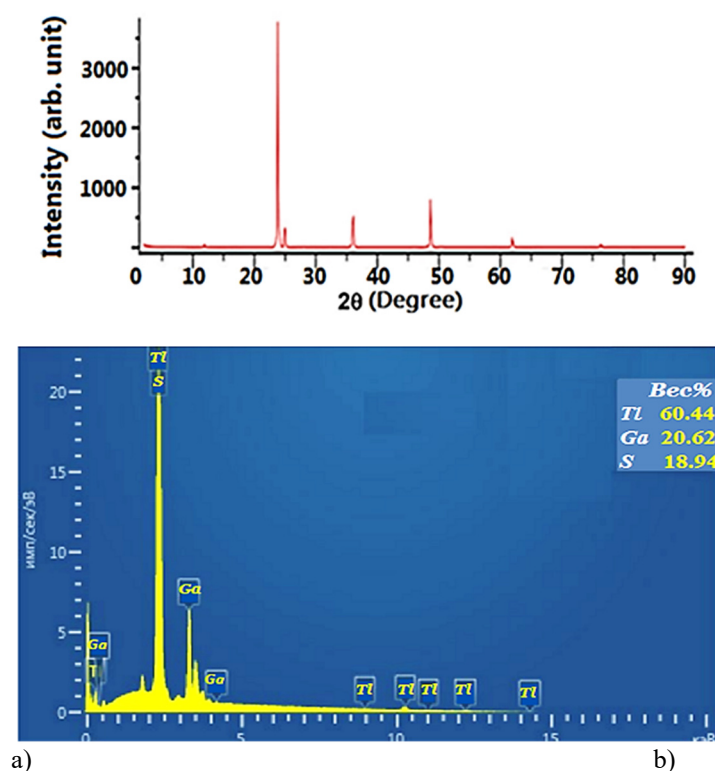

Figure 1. a) X-ray diffraction pattern of the TlGaS$_2$ crystal; b) microanalysis of the crystal surface

Quantitative X-ray microanalysis determined the phase composition and distribution of chemical elements on the surface of the investigated sample (Fig. 1b). Analysis of the obtained results shows the homogeneity of the surface, but with a change in stoichiometry within the homogeneity region $TlGaS_2$ towards the excess of thallium.

The results of microprobe X-ray spectral analysis showed that the content of elements in the grown single crystals corresponds to the formula - $[Tl] : [Ga] : [S] = 1 : 1 : 2$.

A two-dimensional image of $TlGaS_2$ single crystals obtained by magnifying a relatively homogeneous surface area $5 \cdot 10^3 \times 5 \cdot 10^3 nm$ in an atomic force microscope is presented in Fig. 2. a). Fig. 2.b). shows a volumetric description of a part with a relatively uniform relief on the surface of this single crystal. As is clear from the figure, the surface of $TlGaS_2$ single crystal is quite homogeneous and smooth.

Although the $TlGaS_2$ single crystal is a layered crystal, certain irregularities are observed on the natural fracture surface. Analysis of the histogram of the atomic force microscope image shows that the natural surface of the $TlGaS_2$ single crystal is varied in a uniform arrangement of $25\ nm$. The average grain size is $55\ nm$. The observed certain roughness in the boundary layer is most likely associated with the presence of weak van der Waals forces between the layers. In the process of separation, groups of atoms, rather than individual atoms, remain on the crystal surface [13].
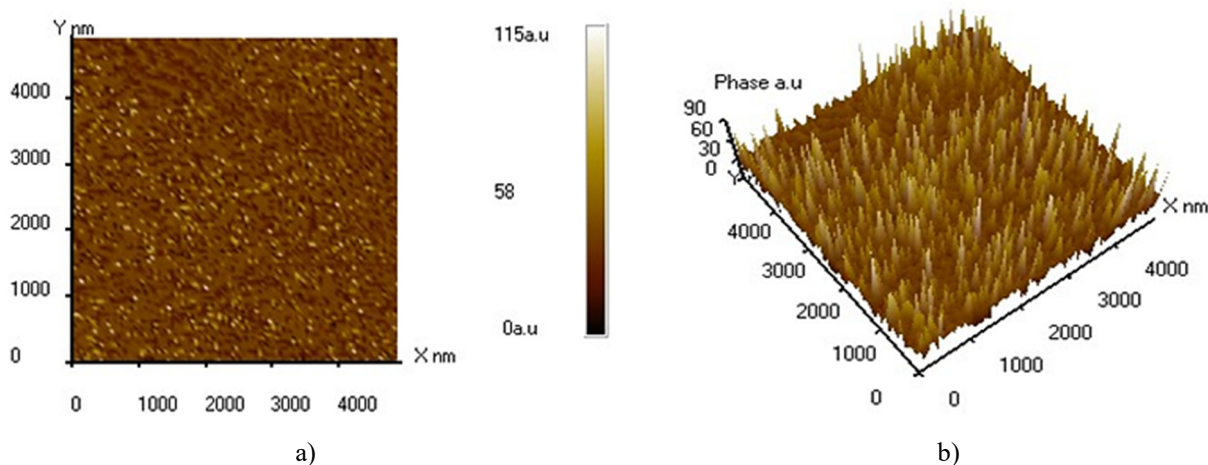

a)   b)

Figure 2. 2D (a) and 3D (b) images of TlGaS$_2$ single crystal surface

The measurement results of the coefficient of linear thermal expansion (CLTE) are presented in Fig. 3. Analysis of the obtained results demonstrates that α_L in the temperature range $80 - 220\ K$ increases sharply from $3.8 \cdot 10^{-6}$ to $9.9 \cdot 10^{-6} K^{-1}$, and above $(260 - 300\ K)$ the growth of α_L slows down and depends weakly on temperature, and with further temperature increase remains almost constant. This behavior of α_L is probably related to the change in the degree of anharmonicity of thermal vibrations of atoms in single crystals of the ternary compound $TlGaS_2$.
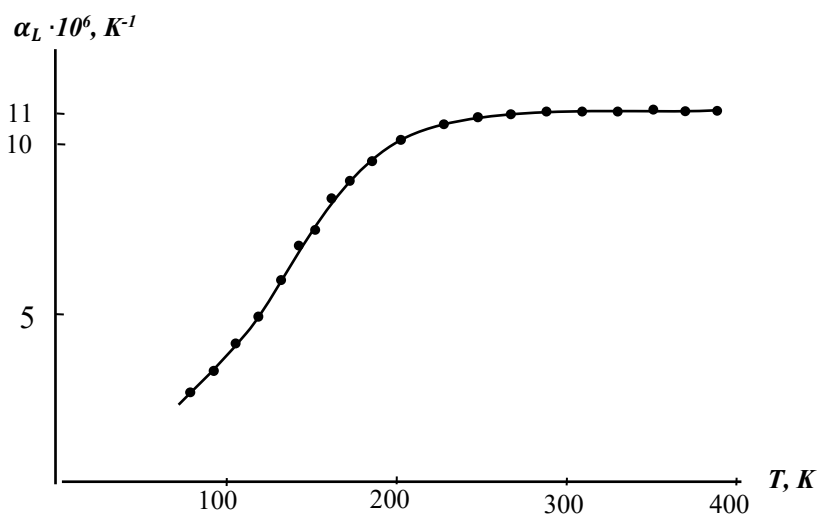

Figure 3. Temperature dependence of the coefficient of thermal expansion of $TlGaS_2$

The CLTE of solids is due to the anharmonicity of the resulting interaction potential of atoms in the crystal lattice. The CLTE is known to be directly proportional to the anharmonicity coefficient [14,15]. Therefore, a sharp increase in

CLTE in the temperature range $80 - 220 K$ and a slight change in its relatively high temperatures is caused by a change in the coefficient of anharmonicity of thermal atomic vibrations in the crystal lattice. Since at low temperatures, the degree of temperature dependence of the vibration coefficient in the $TlGaS_2$ lattice is greater than that at relatively high temperatures. The Gruneisen constant, which is a measure of the anharmonicity of atomic vibrations, decreases with increasing temperature, and starting at a temperature of $\sim 280\,K$, it practically remains constant [16].

The isothermal compressibility measurement results of $TlGaS_2$ in the temperature range of $80 - 400\,K$ are presented in Fig. 4. It is evident from the figure that in the entire investigated temperature range, the isothermal compressibility coefficient χ_T increases slightly from $6.4 \cdot 10^{-12}\frac{m^2}{N}$ to $6.9 \cdot 10^{-12}\frac{m^2}{N}$ as the temperature increases.
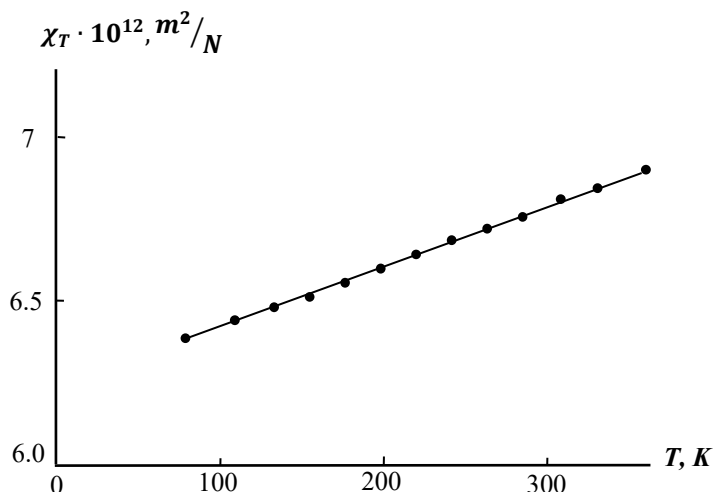

Figure 4. Temperature dependence of the isothermal compressibility coefficient of TlGaS$_2$

A comparison of CLTE and isothermal compressibility shows that changes in CLTE are considerably larger in magnitude than changes in the isothermal compressibility coefficient. In the temperature range 80-400 K, the increase in the isothermal compression coefficient is 8%, and in this range an increase in CLTE of more than 3 times is observed. This significant change of CTLE in the investigated temperature range in comparison with isothermal compressibility is associated with the fact that thermal expansion also changes the amplitude of vibrations of atoms in the crystal lattice, which in turn leads to isothermal compressibility.

It is apparent from Figures 3 and 4 that no anomalies are noticed in the temperature dependences of the coefficient of linear thermal expansion and isothermal compressibility in the analyzed temperature range. This confirms that no phase transformations are present in the indicated temperature range.

As is known, a number of physical properties of crystalline bodies depend greatly on the value of the interaction energy between the atoms and molecules that make up it. As the temperature increases, the vibrational motion of the atoms that make up the crystal lattice also increases, and this, in turn, leads to an increase in the energy of the lattice as a whole. Based on the existing theoretical models, the average energy of the crystal can be calculated with the help of thermodynamic parameters [17].

$$W = \frac{9}{8} N k_0 \theta + 3 k_0 N T D \left(\frac{\theta}{T}\right). \tag{1}$$

Here, $W_0 = \frac{9}{8} N k_0 \theta$ - is the energy of the zero-point oscillations of the lattice, θ - Debye temperature, N - is the Avogadro number, k_0 - is the Boltzmann constant, T - is the absolute temperature, and $D(\theta/T)$ - is the Debye function. The value of the Debye temperature is determined from the expression

$$\theta = \frac{h\nu_{max}}{k_0}. \tag{2}$$

Here h – Planck's constant, ν_{max} – is the maximum frequency of thermal oscillations of atoms. The value of this frequency

$$\nu_{max} = \frac{1}{2\pi}\sqrt{\frac{\beta}{m}}, \tag{3}$$

is determined from the expression. Here β - is the coefficient of the harmonic oscillation limits, m – is the mass of the atom. The value of β can be determined using values of Young's modulus (E) and lattice parameter a_0 [18]. In this case

$$E\frac{\Delta a}{a_0} = \frac{F}{a_0^2}, \tag{4}$$

$$F = -\beta\Delta\alpha, \tag{5}$$

equations are used.

In the existing literature, the values of E, β and ν_{max} have been reported for solids that crystallize in the cubic structure. As a result of the calculations, a value of approximately 10^{13} Hz was obtained for the ν_{max} value, as shown in Einstein's theory. It is interesting from both theoretical and practical point of view how useful these expressions are for complex semiconductor compounds.

In this study, using the values of the Debye characteristic temperature (θ_D) and Young's modulus (E) calculated based on the experimental values of the thermal expansion coefficient for the TlGaS$_2$ semiconductor compound, the energy of the zero-point oscillations of the crystal lattice and the values of the average energy of the lattice as a whole were determined. The Debye characteristic temperature and Young's modulus values were calculated using existing empirical formulas [19, 20].

$$\theta_D = \frac{19.37}{\sqrt{\bar{A}V^{2/3}\alpha}}, \tag{6}$$

and

$$\theta_D = \frac{1.6818 \cdot 10^3 \sqrt{E}}{M^{1/3}\rho^{1/6}}. \tag{7}$$

Here, the value of Young's modulus is given in units of $10\ kg/cm^2$. M - molecular weight, ρ - density, $\bar{A}$ - root mean square atomic mass, V - molar volume, α - coefficient of linear thermal expansion.

It should be noted that the values of θ_D and E calculated from these expressions depend on the temperature according to the change of the value of α.

Since the Debye approximation is used in the reported formula (1), the maximum value of E was taken to find the value of θ. In this case, the calculated zero-point energy for the crystal lattice can be taken as constant. Thus, the average energy of the lattice and its temperature dependence were determined by adding the temperature and the Debye function to this energy each time.

The values of α, $D(\frac{\theta}{T})$, W for the TlGaS$_2$ compound given in the Table 1. The value of the $D(\frac{\theta}{T})$- Debye function corresponding to different temperatures is taken from the literature [20].

Table 1. Thermodynamic parameters and values of Debye function of TlGaS$_2$

T, K	$\alpha, 10^{-6}$ 1/K	$D(\frac{\theta}{T})$	W$_o$, J/mol	W, J/mol	θ_D, K
80	3.85	0.521	1972.71	3009.37	325
90	4.29	0.549	1972.71	3206.24	319
100	4.75	0.590	1972.71	3442.98	302
120	5.24	0.651	1972.71	3916.46	276
140	6.42	0.680	1972.71	4345.07	267
160	6.92	0.725	1972.71	4863.42	258
180	7.28	0.765	1972.71	5404.18	243
200	8.21	0.770	1972.71	5810.36	228
220	9.57	0.812	1972.71	6424.41	225
240	9.76	0.835	1972.71	6966.65	222
260	9.89	0.840	1972.71	7415.22	218
280	10.83	0.848	1972.71	7896.68	215
300	10.86	0.854	1972.71	8352.21	212

As can be seen from the table, with the increase in temperature, both the Debye function, but also the average energy of the lattice increases. These increases can be attributed to the anharmonic oscillation of atoms in the crystal lattice.

To confirm this idea, the ratio of the coefficient (γ) characterizing the degree of anharmonicity of oscillations to the square of the coefficient characterizing the degree of harmonicity (β^2) for the TlGaS$_2$ compound was calculated and presented in the table (Table 2). For this purpose, the formula given in the literature was used [21].

$$\alpha = \frac{\gamma k_0}{a\beta^2}$$

Here, α is the thermal linear expansion coefficient, k_0 is the Boltzmann constant, and α is the lattice parameter.

Table 2. Temperature dependence of the degree of anharmonicity of TlGaS$_2$

T, K	80	90	100	120	140	160	180	200	220	240	260	280	300
$\frac{\gamma}{\beta^2}, 10^7\,N^{-1}$	28.73	31.18	34.53	38.09	46.67	50.31	52.92	62.95	66.57	70.95	72.17	76.73	78.95

As can be seen from the table, the ratio $\frac{\gamma}{\beta^2}$ increases with the increase in temperature. This suggests that the value of the coefficient of thermal expansion is a function $D\left(\frac{\theta}{T}\right)$ and the values of the average energy of the lattice depend on the degree of anharmonic oscillation of atoms.

CONCLUSION

The morphology of natural fracture surfaces of layered $TlGaS_2$ single crystals grown by the Bridgman method has been investigated. Analysis of the data obtained on a scanning probe microscope has revealed that the root mean square roughness of the film surface is 25 nm, and the average grain size is 55 nm. Temperature dependences of the coefficient of linear thermal expansion and isothermal compressibility exhibit no anomalies, showing that there is no phase transition in the investigated temperature range $(80 - 400\,K)$. By calculations based on the experimental values of CLTE, the characteristic Debye temperature decreases with increasing temperature, whereas the value of the average lattice energy and the Debye function increase. It has been shown that these increases are determined by the anharmonicity of vibrations of the atoms of the crystal lattice.

ORCID
Kamala M. Guseinova, https://orcid.org/0009-0004-8950-2900; **Fuad A. Mammadov,** https://orcid.org/0000-0002-1954-6279
Aynure Hadiyeva, https://orcid.org/0000-0001-7238-1066, **Vusala Eminova,** https://orcid.org/0009-0003-6827-9191
Cahangir I. Huseynov, https://orcid.org/0000-0002-4498-2400

REFERENCES

[1] M. Isik, A. Karatay, and N.M. Gasanly, "Structural and optical characteristics of thermally evaporated TlGaSe$_2$ thin films," Optical Materials, **124**, 112018 (2022). https://doi.org/10.1016/j.optmat.2022.112018

[2] W. Henkel, H.D. Hochheimer, C. Carlone, A. Werner, S. Ves, and H.G. Schnering, "High-pressure Raman study of the ternary chalcogenides TlGaS$_2$, TlGaSe$_2$, TllnS$_2$ and TllnSe$_2$," Phys. Rev. B, **26**(6), 3211–3221 (1982). https://doi.org/10.1103/PhysRevB.26.3211

[3] G.E. Delgadoa, A.J. Mora, F.V. Perez, and J. Gonzalez, "Crystal structure of the ternary semiconductor compound thallium gallium sulfide, TlGaS$_2$," Physica B: Condens. Matter. **391**(2), 385–388 (2007). https://doi.org/10.1016/j.physb.2006.10.030

[4] D.I.Huseynov, M.I.Murguzov, Sh.S.Ismailov Thermal conductivity of Er$_x$Sn$_{1-x}$Se ($x \leq 0.025$) solid solutions," Inorganic Materials, **44**, 467–469 (2008). https://doi.org/10.1134/S0020168508050063

[5] X. Xin, F. Liu, X.-Q. Yan, W. Hui, X. Zhao, X. Gao, Z.-B. Liu, and J.-G.Tian, "Two-photon absorption and non-resonant electronic nonlinearities of layered semiconductor TlGaS$_2$," Opt Express, **26**(26), 33895-33905 (2018). https://doi.org/10.1364/OE.26.033895

[6] Y. Fu, D. He, J. He, X. Han, J. Bai, Y. Wang, and H. Zhao, "Photocarrier dynamics in TlGaS2 nanoflakes and van der waals heterostructures with hexagonal boron nitride and WS2 nanoflakes: implications for optoelectronic applications," ACS Applied Nano Materials, **3**, 8702–8707 (2020). https://doi.org/10.1021/acsanm.0c01448

[7] B.A. Ünlü, A. Karatay, E.A. Yildiz, T. Dinçbay, H. Ünver, N. Gasanly, and A. Elmali, "Defect assisted nonlinear absorption and optical limiting in amorphous $TlGaS_{2(1-x)}Se_{2x}(0 \leq x \leq 1)$ thin films," Journal of Luminescence, **241**, 118540 (2022). https://doi.org/10.1016/j.jlumin.2021.118540

[8] S.Delice, M.Isik, N.M. asanly, Thermoluminescence properties and trapping parameters of TlGaS 2 single crystals // Journal of Luminesce, 2022, 244, 118714, https://doi.org/10.1016/j.jlumin.2021.118714

[9] A. Say, D. Adamenko, O. Gomonnai, I. Roman, I. Martynyuk-Lototska, and R. Vlokh, "Anisotropy of thermal expansion of TlGaSe$_2$ crystals," Phase Transitions, **92**(9), 824-830 (2019). https://doi.org/10.1080/01411594.2019.1642475

[10] I. Martynyuk-Lototska, O. Mys, A. Say, et al., "Anisotropy of acoustic and thermal expansion properties of TlInSe2 crystals," Phase Transitions, **92**(1), 23–35 (2019). https://doi.org/10.1080/01411594.2018.1545227

[11] B. Gurkan, and S. Berber, "Structural and electronic properties of layered semiconductor chalcogenide crystals: TIGaSe$_2$, TIGaS$_2$ and TIInS$_2$," J. Indian Chem. Soc. **96**, 1123-1130 (2019). https://doi.org/10.5281/zenodo.5643212

[12] M. Isik, A. Karatay, A.N. Ech-Chergui, and N.M. Gasanly, "Study of the structural and optical properties of thallium gallium disulfide (TlGaS$_2$) thin films grown via thermal evaporation," Physica Scripta, **97**(7), 075808 (2022). https://doi.org/10.1088/1402-4896/ac74f0

[13] Z. Cicek, S. Yakut, D. Deger, D. Bozoglu, S. Mustafaeva, P. Ismailova, A.A. Hasanov, and K. Ulutas, "Thickness dependence of dielectric properties of $TlGaS_2$ thin films," Materials Science in Semiconductor Processing, **166**, 107733 (2023). https://doi.org/10.1016/j.mssp.2023.107733

[14] Y.S. Touloukian, R.K. Kirby, R.E. Taylor, and T.Y.R. Lee, *Thermal Expansion: Nonmetallic Solids (Thermophysical properties of matter*, vol. 13, (IFI/Plenum, New York, 1977).

[15] M.S. Barabashko, A.I. Krivchikov, R. Basnukaeva, O.A. Korolyuk, and A. Jeżowsk, "Proportional correlation between heat capacity and thermal expansion of atomic, molecular crystals and carbon nanostructures," Condensed Matter Physics, **26**(3), 33602 (2023). https://doi.org/10.5488/CMP.26.33602

[16] C. Kittel, *Introduction to Solid State Physics*, 8th ed. (John Wiley & Sons: New York, USA, 2005).

[17] B.M. Askerov, and S.R. Figarova, *Thermodynamics, Gibbs Method and Statistical Physics of Electron Gases*, (Springer-Verlag, Berlin, Heidelberg, 2010).

[18] M.T. Cao-Rial, C. Moreno, and P. Quintela, "Determination of Young modulus by using Rayleigh waves," Applied Mathematical Modelling, **77**, Part 1, 439-455 (2020). https://doi.org/10.1016/j.apm.2019.07.051

[19] O.L. Anderson, "A simplified method for calculating the Debye temperature from elastic constants," Journal of Physics and Chemistry of Solids, **24**(7), 909-917 (1963). https://doi.org/10.1016/0022-3697(63)90067-2

[20] D.C. Wallace, *Thermodynamics of crystals*, (Dover Publications, Wiley, New York, 1998).

[21] O. Madelung, *Introduction to Solid-State Theory*, (Springer Science & Business Media, 1996).

ЕНЕРГІЯ ТЕПЛОВИХ КОЛИВАНЬ КРИСТАЛІЧНОЇ ГРАТКИ В НАПІВПРОВІДНИКОВІЙ СПОЛУЦІ TlGaS$_2$

Камала М. Гусейнова[a], Фуад А. Мамедов[a], Айнур А. Гадієва[b,c], Вусала І. Емінова[c,d,e], Ягандір І. Гусейнов[f]

[a]Сумгаїтський державний університет, Сумгаїт, Азербайджан
[b]Азербайджанський державний університет нафти та промисловості, Баку, Азербайджан
[c]Хазарський університет, Баку, Азербайджан
[d]Міністерство науки і освіти Азербайджанської Республіки, Інститут фізики, Баку, Азербайджан
[e]Французько-Азербайджанський університет (UFAZ) при Азербайджанському державному університеті нафти та промисловості, Баку, Азербайджан
[f]Азербайджанський державний педагогічний університет, Баку, Азербайджан

У статті наведено результати дослідження температурної залежності коефіцієнтів теплового розширення та ізотермічної стисливості потрійної сполуки TlGaS$_2$. У досліджуваному діапазоні температур (80-400 K) аномалій температурних залежності цих властивостей не виявлено. Коефіцієнт теплового розширення напівпровідникової сполуки TlGaS$_2$ розраховано на основі емпіричних формул, включаючи температуру Дебая та функції Дебая, а також розраховано середню енергію кристалічної решітки та її температурну залежність які наведені в таблиці. Показано, що енергія кристалічної решітки залежить від ступеня ангармонійності коливань.

Ключові слова: *напівпровідник; теплове розширення; теплові коливання; кристалічна решітка; температура Дебая; модуль Юнга; ангармонічність*

FACTORS INFLUENCING THE IDEALITY FACTOR OF SEMICONDUCTOR p-n AND p-i-n JUNCTION STRUCTURES AT CRYOGENIC TEMPERATURES

 Jo'shqin Sh. Abdullayev[a]*, **Ibrokhim B. Sapaev[a,b]**

[a]National Research University TIIAME, Department of Physics and Chemistry, Tashkent, Uzbekistan
[b]Western Caspian University, Baku, Azerbaijan
*Corresponding Author e-mail: j.sh.abdullayev6@gmail.com

This article elucidates the dependence of the ideality factor on both internal functional parameters and external factors in semiconductors at low temperatures. We have explored the influence of external factors such as temperature and external source voltage. Through numerical modeling and theoretical analysis, we thoroughly investigate the dependencies of semiconductor material internal functional parameters—including doping concentration, the bandgap of semiconductors, the lifetime of charge carriers, and geometric dimensions ranging from micrometers to nanometers— the ideality factor on p-n and p-i-n junction structures. Our analysis spans cryogenic temperatures from 50 K to 300 K, with intervals of 50 K. To conduct this study, we have focused on p-n and p-i-n junction structures fabricated from Si and GaAs. The selected model features geometric dimensions of a=10 μm, b=8 μm, and c=6 μm. The thickness of the i-layer ranged from 10 μm to 100 μm in 10- μm increments. Increasing the thickness of the i-layer results in a corresponding rise in the ideality factor.

Keywords: *p-n junction; p-i-n junction; SRH recombination; Internal functional parameters; External factors; Ideality factor; Cryogenic temperatures*

PACS: 73.40. Lq, 73.61.Cw, 73.61.Ey, 72.20.Jv

INTRODUCTION

This factor evaluates the ideality of p-n and p-i-n junction structures and assists in assessing the current mechanisms through numerical and theoretical modeling. The attributes and functionality of p-i-n and p-n junction diodes are intimately connected to the conduct of carriers at the interface established between p-type and n-type materials. These junctions serve as the fundamental building blocks for many other electronic devices, and the analytical techniques applied to understand p-i-n and p-n junctions can be extended to solve various electronic problems. The kinetic processes of electrons and holes at p-n and p-i-n junctions are explained through two mechanisms: drift-diffusion and recombination-generation. The ideality factor serves as a distinguishing parameter between these mechanisms, theoretically falling within the range of 1 to 2 [1]. However, several experiments have shown that the ideality factor often exceeds 2 [2-3]. The primary objective of this work is to discuss the relationship between forward voltage, temperature, the thickness of the i-layer, and material parameters, all of which are dependent on the ideality factor. Numerous scientific articles have explored the correlation between the ideality factor and temperature [4-8], although these studies have typically not covered a broad temperature range. Characteristics of thermosensors at cryogenic temperature were studied [9].

While numerous articles [10-12] have investigated the ideality factor, its true nature and the parameters influencing it remain incompletely understood. Variations in ideality factor values across different materials [13] underscore the importance of comprehensively studying the dependence of materials on their functional parameters. To address this gap, this work focuses on studying the ideality factor of p-n and p-i-n junction structures fabricated from Si and GaAs materials. Overall, operating semiconductor devices at cryogenic temperatures is essential for a wide range of scientific and technological applications, enabling advancements in fields such as quantum computing, astrophysics, materials science, and high-energy physics. At cryogenic temperatures, semiconductor devices often exhibit improved electrical characteristics, such as reduced noise, increased carrier mobility, and lower leakage currents. This can lead to enhanced device performance, including higher-speed operation, improved signal-to-noise ratios, and lower power consumption.

Some semiconductor materials, such as certain types of doped silicon and germanium, exhibit superconducting behavior at cryogenic temperatures. Cryogenic temperatures are essential for the operation of many quantum computing architectures, which often rely on semiconductor-based qubits. In astrophysics and space exploration, semiconductor devices operating at cryogenic temperatures are used in instruments such as infrared detectors, spectrographs, and low-noise amplifiers. Cryogenic temperatures are often employed in materials research to investigate the electronic properties of semiconductors, including bandgap engineering, electron mobility, and quantum confinement effects. In experiments conducted at particle accelerators and high-energy physics laboratories, semiconductor detectors cooled to cryogenic temperatures are used to measure the energy and trajectories of charged particles produced in collisions.

MATERIALS AND METHODS

In the ideal scenario, the relationship between the current density and the voltage passing through the p-n and p-i-n junction structures is expressed as follows.

$$J = J_S \left(\exp\left(\frac{qU_{p-n}}{mkT} \right) - 1 \right), \qquad (1)$$

where U_{p-n} is p-n junction voltage, q is the elementary electron charge, J_S is referred to as the saturation current density in the reverse connection, and its value is determined as follows:

$$J_{S1} = qn_i^2 \left(\frac{D_p}{L_p N_D} + \frac{D_n}{L_n N_A} \right). \qquad (2a)$$

Where n_i intrinsic concentration, $D_{p,n}$ and $L_{p,n}$ are diffusion coefficient and length of electrons and holes respectively. N_D and N_A are donors and acceptors. The diffusion length L_D for silicon with resistivity values of 10 Ωcm and 100 Ωcm, and carrier lifetimes of 8µs and 3µs for electrons and holes, respectively, is approximately $L_{p,n} \approx 100$ µm. If the current transport mechanism relies on a drift-diffusion mechanism, then expression (2a) is appropriate. Conversely, if the current transport mechanism is driven by a recombination-generation mechanism, it is determined from expression (2b).

$$J_{S2} = \frac{qn_i \cdot d_{p-n}}{2\tau_{eff}} \qquad (2b)$$

Another crucial aspect of the ideality factor m is its role in determining the recombination mechanism in the p-n junction. Experiment and theoretical calculations indicate that the ideality factor is inversely proportional to temperature as follows expression.

$$m(T) = \frac{q}{kT} \cdot \frac{U_{p-n}}{\ln\left(\frac{I(T,U)}{I_S(T)} + 1 \right)} \qquad (3)$$

We express the ideality factor using expression (4). Through theoretical calculations, we aimed to determine the parameters on which A(T) and C(T) coefficients depend. The coefficients A(T) and C(T) are assumed to represent both the internal functional parameters and external factors of the semiconductor material.

$$m(T) = A(T) + \frac{C(T)}{T} \qquad (4)$$

The expression (4) was employed to analytically ascertain the temperature dependence of the ideality factor for p-n junctions based on Si and GaAs, covering temperatures from 50 K to 300 K with intervals of 50 K. The band gap of the semiconductor depends on the size [14].

The thickness of the i-layer ranged from 10 µm to 100 µm in 10-µm increments. Increasing the thickness of the i-layer results in a corresponding rise in the ideality factor. The thesis chose Si semiconductor materials, incorporating boron doping at a concentration of 3e17 cm^{-3} to create the pSi-layer and phosphorus doping at a concentration of 4e18 cm^{-3} for the nSi-layer. The diffusion length L_D for silicon with resistivity values of 10 Ωcm and 100 Ωcm, and carrier lifetimes of 8µs and 3µs for electrons and holes, respectively, is approximately $L_D \approx 100$ µm.
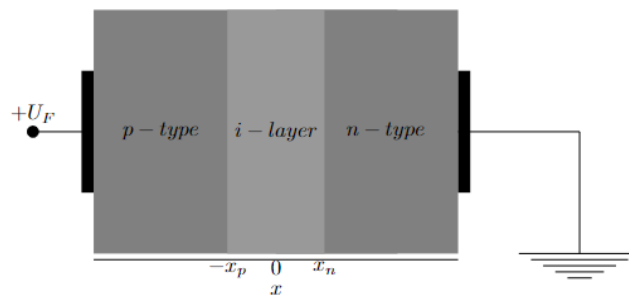

Figure 1. The schematic depicting a 2D cross-section of our model planar p-i-n junction, U_F is forward voltage. The light grey area represents the *i*-layer region, while the dark grey areas represent the quasi-neutral (QNR) fields in the p-type and n-type regions, respectively

The selected model features geometric dimensions of a=10 µm, b=8 µm, and c=6 µm. Within the electrophysical models, certain distinctions are noted: the gap width fluctuates with temperature [15], while the mobility of electrons and holes is influenced by both temperature and concentration [16]. Moreover, variations in Shockley-Read-Hall (SRH) recombination are observed in response to changes in temperature and doping concentration [17]. Recombination in p-n and p-i-n junctions at low temperatures shows distinct characteristics compared to room temperature behavior due to changes in carrier dynamics and material properties. Recombination Mechanisms are mainly three types. Radiative

Recombination, Non-Radiative Recombination, Surface Recombination. The results obtained from the models and samples employed in this section are thoroughly presented and scrutinized in Section RESULTS AND DISCUSSION.

RESULTS AND DISCUSSION

In this section, the results are presented and analyzed. The various current lines observed in Figure 2 at low voltage can be explained as follows. The results are depicted in Figure 2, showcasing both semi-logarithmic (a) and linear (b) I-U characteristics. It is evident from the figures that there is a decrease in current as the layer thickness increases.
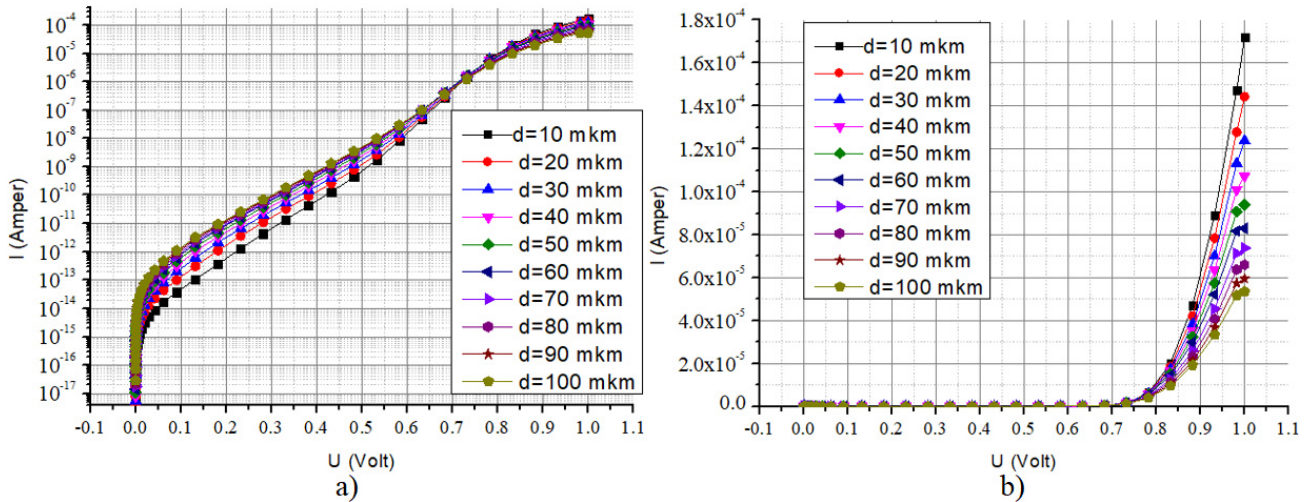
Figure 2. Volt-Amper characteristic of p-i-n junction based on Si a) Semi-logarithmic, b) linear, d is the thickness *i*-layer

Figure 3 (b) illustrates the dependency of the ideality factor (i) on the layer thickness at 0.2, 0.4, 0.6, and 0.8 volts.
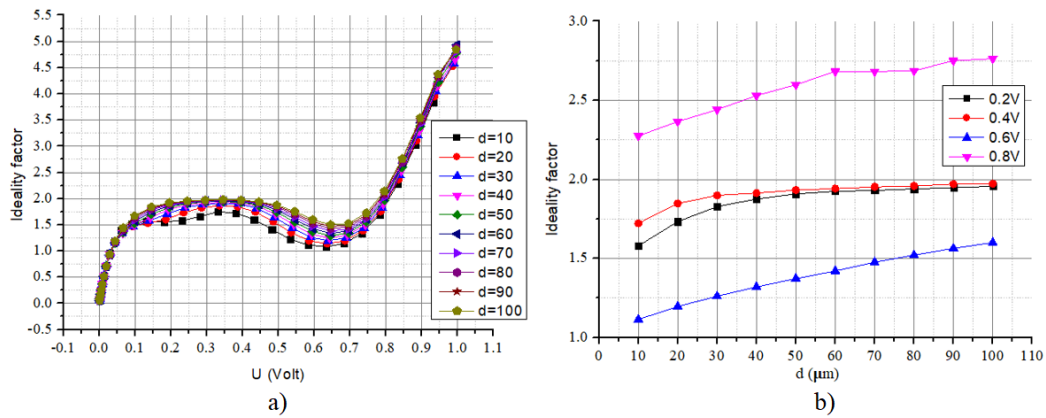
Figure 3. Ideality factor of the p-i-n junction dependent on a) forward voltage, b) the thickness of the i-layer
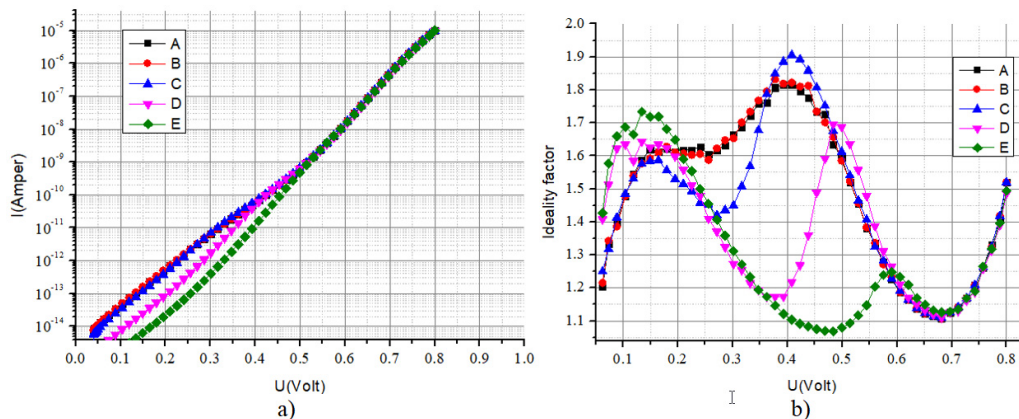
Fig. 4. a) The semi-logarithmic volt-ampere characteristic of a p-i-n junction, b) the ideality factor of the p-i-n junction as a function of forward voltage, across different intrinsic doping concentrations of the i-layer

The I-U characteristic of the p-i-n junction structure made of Si material is provided, wherein the intrinsic field concentration was studied for cases A, B, C, D, and E. The intrinsic concentration of silicon is typically $n_i \approx 10^{10}$ cm^{-3}, however, in this scenario, $n_i = 10^{11}$ cm^{-3} for case A, $n_i = 10^{12}$ cm^{-3} for case B, $n_i = 10^{13}$ cm^{-3} for case C, $n_i = 10^{14}$ cm^{-3} for case D, and $n_i = 10^{15}$ cm^{-3} for case E were observed. From Figure 4, we can see that in the range from 0 volts to 0.5 volts, there are different lines of current strength at different values of doping concentration, and at values greater than 0.5 volts, they almost all overlap. This situation can be explained as follows: recombination processes were observed between 0 and 0.5 volts, while the drift-diffusion mechanism prevailed above 0.5 volts. Recombination processes with different values were observed for different concentration levels. In the case of E, where $n_i = 10^{15}$ cm^{-3}, it is shown that the drift-diffusion current prevails even at low voltages and high concentration values.
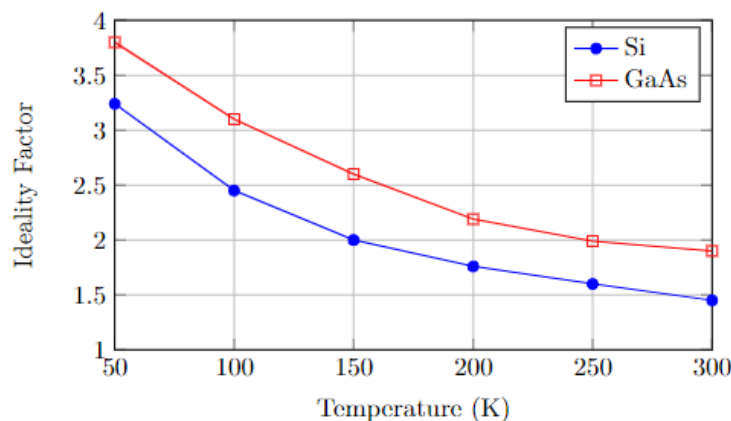
Figure 5. Illustrates the temperature dependence of the ideality factor for p-n junctions based on Si and GaAs, ranging from 50 K to 300 K with intervals of 50 K

In Figure 5, utilizing expressions (3) and (4), the following result was derived: the temperature dependence of the ideality factor for p-n junctions based on Si and GaAs, spanning temperatures from 50 K to 300 K with intervals of 50 K. The ideality factor displays a reverse dependence on temperature. This phenomenon arises because, as the temperature decreases, the dominance of the drift-diffusion mechanism diminishes, while the recombination-generation mechanism begins to take precedence. As the temperature decreases, electron diffusion in the Si crystal decreases, as well as in other crystals.

CONCLUSIONS

In this study, the ideality factor was found to depend on several factors. It was observed that the ideality factor decreases with increasing temperature. Additionally, the ideality factor dependent voltage from 0 to 1 volt for the appropriate connection voltage in silicon. Changes in the ideality factor were also observed when the thickness of the intrinsic layer varied from 10 μm to 100 μm. In all cases where the thickness of the intrinsic i-layer was less than 100 μm, distinct lines were observed at low voltages, while they converged and overlapped at high voltages. Moreover, the influence of the specific concentration of the intrinsic layer on the ideality factor was investigated as it ranged from $n_i = 10^{11}$ cm^{-3} case to $n_i = 10^{15}$ cm^{-3} case. As a result, it was determined that both external and internal factors affect the ideality factor by influencing the current transport mechanism.

ORCID
Jo'shqin Sh. Abdullayev, https://orcid.org/0000-0001-6110-6616; **Ibrokhim B. Sapaev,** https://orcid.org/0000-0003-2365-1554

REFERENCES
[1] S.M. Sze, and K.K. Ng, *Physics of Semiconductor Devices*, third edition, (John Wiley & Sons, Inc., 2007).
[2] E. Gnani, A. Gnudi, S. Reggiani, and G. Baccarani, IEEE Trans. Electron Devices, **58**(9), 2903 (2011). https://doi.org/10.1109/TED.2011.2159608
[3] Z. Arefinia, A. Asgari, Solar Energy Materials and Solar Cells, **137**, 146 (2015). https://doi.org/10.1016/j.solmat.2015.01.032
[4] O.V. Pylypova, A.A. Evtukh, P.V. Parfenyuk, I.I. Ivanov, I.M. Korobchuk, O.O. Havryliuk, and O.Yu. Semchuk, Opto-Electronics Review, **27**(2), 143 (2019). https://doi.org/10.1016/j.opelre.2019.05.003
[5] R. Ragi, R.V.T. da Nobrega, U.R. Duarte, and M.A. Romero, IEEE Trans. Nanotechnol. **15**(4), 627 (2016). https://doi.org/10.1109/TNANO.2016.2567323
[6] R.D. Trevisoli, R.T. Doria, M. de Souza, S. Das, I. Ferain, and M.A. Pavanello, IEEE Trans. Electron Devices, **59**(12), 3510 (2012). https://doi.org/10.1109/TED.2012.2219055
[7] N.D. Akhavan, I. Ferain, P. Razavi, R. Yu, and J.-P. Colinge, Appl. Phys. Lett. **98**(10), 103510 (2011). https://doi.org/10.1063/1.3559625
[8] A.V. Babichev, H. Zhang, P. Lavenus, F.H. Julien, A.Y. Egorov, Y.T. Lin, and M. Tchernycheva, Applied Physics Letters, **103**(20), 201103 (2013). https://doi.org/10.1063/1.4829756
[9] D.H.K. Murthy, T. Xu, W.H. Chen, A.J. Houtepen, T.J. Savenije, L.D.A. Siebbeles, *et al.*, Nanotechnology, **22**(31), 315710 (2011). https://doi.org/10.1088/0957-4484/22/31/315710

[10] B. Pal, K.J. Sarkar, and P. Banerji, Solar Energy Materials and Solar Cells, **204**, 110217 (2020). https://doi.org/10.1016/j.solmat.2019.110217
[11] J.Sh. Abdullayev, I.B. Sapaev, Eurasian Physical Technical Journal, **21**(3), 21–28 (2024). https://doi.org/10.31489/2024No3/21-28
[12] P. Dubey, B. Kaushik, and E. Simoen, IET Circuits, IET Circuits, Devices & Systems, (2019). https://doi.org/10.1049/iet-cds.2018.5169
[13] M.-D. Ko, T. Rim, K. Kim, M. Meyyappan, and C.-K. Baek, Scientific Reports, **5**(1), 11646 (2015). https://doi.org/10.1038/srep11646
[14] A.M. de Souza, D.R. Celino, R. Ragi, and M.A. Romero, Microelectronics J. **119**, 105324 (2021). https://doi.org/10.1016/j.mejo.2021.105324
[15] M.C. Putnam, S.W. Boettcher, M.D. Kelzenberg, D.B. Turner-Evans, J.M. Spurgeon, E.L. Warren, *et al*., Energy & Environmental Science, **3**(8), 1037 (2010). https://doi.org/10.1039/C0EE00014K
[16] Abdullayev, J. S., & Sapaev, I. B. (2024). *East European Journal of Physics*, (3), 344-349. https://doi.org/10.26565/2312-4334-2024-3-39R
[17] Elbersen, R.M. Tiggelaar, A. Milbrat, G. Mul, H. Gardeniers, and J. Huskens, Advanced Energy Materials, **5**(6), 1401745 (2014). https://doi.org/10.1002/aenm.201401745

ФАКТОРИ, ЩО ВПЛИВАЮТЬ НА КОЕФІЦІЄНТ ІДЕАЛЬНОСТІ НАПІВПРОВІДНИКОВИХ p-n ТА p-i-n ПЕРЕХІДНИХ СТРУКТУР ПРИ КРІОГЕННИХ ТЕМПЕРАТУРАХ

Джошкін Ш. Абдуллаєв[a], Іброхім Б. Сапаєв[a,b]
[a]Національний дослідницький університет ТІІАМЕ, фізико-хімічний факультет, Ташкент, Узбекистан
[b]Західно-Каспійський університет, Баку, Азербайджан

У цій статті висвітлюється залежність ідеальності фактора як від внутрішніх функціональних параметрів, так і від зовнішніх факторів у напівпровідниках при низьких температурах. Ми дослідили вплив зовнішніх факторів, таких як температура та напруга зовнішнього джерела. За допомогою чисельного моделювання та теоретичного аналізу ми детально вивчили залежності внутрішніх функціональних параметрів напівпровідникових матеріалів, включаючи концентрацію домішок, ширину забороненої зони напівпровідників, тривалість життя носіїв заряду та геометричні розміри в діапазоні від мікрометрів до нанометрів, на ідеальність фактора в структурах p-n і p-i-n переходів. Наш аналіз охоплює кріогенні температури від 50 К до 300 К з інтервалом 50 К. Для проведення цього дослідження ми зосередилися на структурах p-n і p-i-n переходів, виготовлених з Si та GaAs. Обрана модель має геометричні розміри a=10 мкм, b=8 мкм і c=6 мкм. Товщина i-шару варіювалася від 10 мкм до 100 мкм з кроком 10 мкм. Збільшення товщини i-шару призводить до відповідного збільшення ідеальності фактора.

Ключові слова: *p-n перехід; p-i-n перехід; рекомбінація за механізмом Шоклі-Ріда-Холла (SRH); внутрішні функціональні параметри; зовнішні фактори; фактор ідеальністі; кріогенні температури*

SCALE MODELING OF THE INFLUENCE OF MULTIPLE LOCALIZED DEFECTS OF METAL SURFACE ON OPTICAL ELLIPSOMETRY RESULTS

Oleksii Haluza[a,b,*], Ivan Kolenov[c,d], Iryna Gruzdo[b]

aNational Technical University "Kharkiv Polytechnic Institute", 2 Kyrpychova St., Kharkiv, 61002, Ukraine
bKharkiv National University of Radio Electronics, 14 Nauky Ave., Kharkiv, 61166, Ukraine
cInstitute of Electrophysics and Radiation Technologies of NAS of Ukraine, P.B. 8812, 28 Chernyshevsky St., Kharkiv, 61002, Ukraine
dO.Ya. Usikov Institute for Radiophysics and Electronics of NAS of Ukraine, 12, Ac. Proskura St., Kharkiv, 61085, Ukraine
Corresponding Author e-mail: oleksii.haluza@khpi.edu.ua

The work is devoted to the problem of ellipsometric studies of real surfaces and considers the case when surface inhomogeneities are individual localized defects or conglomerates with a size comparable to the wavelength of the probing radiation. Such inhomogeneities lead to angular dependences of ellipsometric parameters that have a non-classical form and cannot be described using conventional well-known models of homogeneous planar layers. This work focuses on the influence of conglomerates of localized defects on the angular dependences of ellipsometric parameters and serves as a continuation of earlier studies in which single localized defects were considered. The dependence of the degree of influence of the distance between defects on the ellipsometric parameters is examined. The parameter "critical distance" between defects is introduced, beyond which they can be considered as localized, and estimates of this parameter for the considered configurations are provided.

Keywords: *Ellipsometry, Terahertz waves, Scale modeling, Surface defects, Localized defects*
PACS: 68.35.Ct, 42.25.Ja, 78.68.+m

1.INTRODUCTION

Ellipsometry is a non-contact, precise, non-destructive method for studying the properties of surfaces and interfaces. It is based on measuring changes in the polarization state of radiation after it is reflected from the surface of a sample or passes through a transparent sample [1-3].

In most cases, a pair of parameters, Ψ and Δ (the so-called ellipsometric parameters), is the result of an ellipsometric experiment. The first parameter characterizes the relative change in amplitude ratios, and the second one represents the change in the phase difference of the orthogonal components (*p*- and *s*-components) of the electromagnetic wave during their interaction with the system under study. The simplest configuration of an ellipsometric experiment (a scheme with a rotating analyzer, RAE) is shown in Fig. 1. Electromagnetic radiation from the source S passes through a polarizer P with a known azimuth and is reflected from the sample, leading to a change in the polarization state. Next, the radiation passes through another polarizer (the Analyzer), and detector D measures the radiation amplitude. In the RAE scheme, the ellipsometric parameters Ψ and Δ are found from the dependence $I(A)$ of the intensity of the recorded signal on the azimuth of the analyzer A [2, 3].
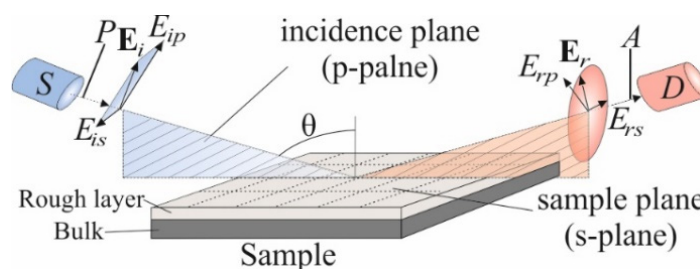
Figure 1. Schematic of the ellipsometric experiment

Ellipsometric parameters are related to the physical characteristics of the structure under study and are related to those measured by the basic equation of ellipsometry:

$$\rho = tg\Psi \cdot e^{i\Delta} = \frac{R_p}{R_s},\qquad(1)$$

where $R_{p(s)}$ are the complex Fresnel coefficients of the sample.

The advantages of ellipsometry include high accuracy and reproducibility of results, as well as the absence of a need for a reference measuring channel or reference sample. These benefits have led to its widespread application in many areas [2, 5-9]. However, ellipsometry is an indirect technique, meaning that to calculate the material characteristics, it is

necessary to solve equation (1) for the desired parameters, which are typically the optical constants of the sample material and/or the optical constants and thickness of film coatings. The exact form of the right-hand side of equation (1) is determined by the physical model chosen to describe the structure under study [1-3, 10, 11]. For analyzing ellipsometric experiments, researchers often use planar surface models, including those of clean surfaces or multilayer systems with distinct boundaries between layers. These models are usually just approximations of real structures, so the development of more accurate models for the structures under study remains one of the main challenges in ellipsometry. A specific problem arises when analyzing ellipsometric data for surfaces with deviations from planarity [12-15], such as roughness (medium and highly rough surfaces), island films, regular reliefs [16, 17], grains in polycrystals, inclusions of secondary phases, blistering, and more [18, 19]. The last three types of structures can be classified as localized defects [20]. Localized defects disrupt the statistical homogeneity of surface properties and are therefore poorly described by effective medium models (which are represented by homogeneous films with averaged optical constants [2, 21]) or random fields with homogeneous statistical properties [22-24]. Since localized defects often appear on real surfaces due to various processes, such as sputtering with high-energy particle beams or chemical etching, analyzing the results of optical studies (e.g., ellipsometry, reflectometry) is highly relevant [18, 19]. It is important to note that there is currently a lack of general understanding regarding how these surface defects impact ellipsometry results [20].

This work is a continuation of [20], which addressed the problem of creating and testing a physical ellipsometric model of localized defects using a sub-terahertz null ellipsometer with an operating wavelength of 2.14 mm. In [20], quasi-optical scale modeling of the influence of a single localized defect (a series of samples with defects of various sizes on a millimeter scale) located at the center of the sample was conducted and analyzed. It was demonstrated that if the size of a localized defect is slightly smaller than the wavelength, ellipsometry does not "see" it, while reflectometry shows a decrease in the reflection coefficient compared to a clean surface. However, conglomerates of defects are much more common in real samples. They can simultaneously affect the change in the polarization state of the probing radiation upon reflection. Therefore, a logical next step in the development of quasi-optical scale modeling is to study the simultaneous influence of multiple defects of various sizes, spaced apart at specified distances. This study focuses on experimentally examining how a group of parallelepiped defects affects radiation scattering, polarization, and the measured ellipsometric parameters. The study also examined the "localization" of defects, i.e., determining the minimum distance at which they begin to independently influence the result of the experiment.

2. EXPERIMENTAL PROCEDURE AND SAMPLES

Since optical ellipsometry operates with wavelengths on the order of half a micrometer, the size of defects that are relevant cannot exceed 1 micrometer and most often have a significantly smaller size. It is clear that artificially and controllably creating such defects with given shapes, sizes, and relative positions on a defect-free surface is currently a technically complex, time-consuming, and expensive task. Therefore, it was decided to take advantage of the property that the features of the interaction of EM radiation with objects are determined not by the absolute values of the radiation wavelength (λ) and the characteristic sizes of objects (d), but by their ratio. In our case, we are interested in ratios in the range $d/\lambda = 0.1$ to 2. To be able to create the desired defects, their size must be about 1 mm. Accordingly, to maintain the specified d/λ ratio, the wavelength must be on the order of several mm (in our case, $\lambda = 2.14$ mm). This allows for the relatively easy creation of surfaces with a preassigned defect geometry and the performance of ellipsometric (and other) measurements, the results of which can be transferred to optical-range ellipsometry. This approach is commonly called "scale modeling" and is often used in radiophysics. However, in radiophysics, reduced models are typically constructed, leading to the use of proportionally smaller wavelengths. This enables the study of the scattering of long-wavelength waves from large objects under laboratory conditions. In our case, we propose to use enlarged models and wavelengths.

To carry out large-scale modeling, in this study, a quasi-optical terahertz ellipsometer (QOTE) operating at a probing radiation wavelength of 2.14 mm (0.14 THz) was used. QOTE is built based on the PCSA (Polarizer – Compensator – Sample – Analyzer) scheme and implements a rotating-analyzer measurement scheme (Rotating Analyzer Ellipsometry, RAE) in an automated mode using specially developed hardware and software. The advantages of this scheme include the relative simplicity of design and measurements, as well as the ability to study both absorbing and transparent materials (due to the presence of a compensator). The measurement error for the ellipsometric parameters Ψ and Δ provided by QOTE is 0.05° and 0.1°, respectively.

QOTE is based on a quasi-optical transmission line - a hollow dielectric beam guide and quasi-optical devices and components for the frequency range 0.1...1 THz, developed at the O. Ya. Usikov Institute of Radiophysics and Electronics NAS of Ukraine [25, 26]. Fig. 2 shows the quasi-optical design of QOTE. The generator (G) signal is output through a standard waveguide and transmitted to the quasi-optical beamguide transmission line via a waveguide-beamguide junction (1). The signal is modulated by a mechanical amplitude modulator (2). The attenuator (3) serves as a linear polarizer in the circuit, allowing adjustment of the probing signal amplitude. The polarization plane rotator (4) rotates the polarization plane by an arbitrary angle P. Thus, in this circuit, the function of a polarizer with a variable azimuth is performed by a pair of elements: the linear polarizer itself (as part of the attenuator) and the polarization plane rotator. Next, compensator (5) converts the radiation into elliptically polarized radiation, adding a controlled phase shift between orthogonally polarized components. The measuring cell, which includes a goniometer with a sample holder, provides the required angle of incidence of radiation θ on the study object S mounted on it. The analyzer function is performed by a

pair of elements: a polarization plane rotator (6), which determines the azimuth of analyzer A, and the fixed angle analyzer itself (7). This design of the analyzer is due to the polarization sensitivity of the detector (D). The signal from the (D) goes to the input of the synchronous detector. After the synchronous detection procedure, the signal is measured using the ADC interface unit, and the result is transmitted to the PC. All rotating elements are equipped with stepper motors and controlled by a PC via a special interface. Measuring the intensity dependence on an azimuth of the analyzer is performed automatically. QOTE is described in more detail in [27].
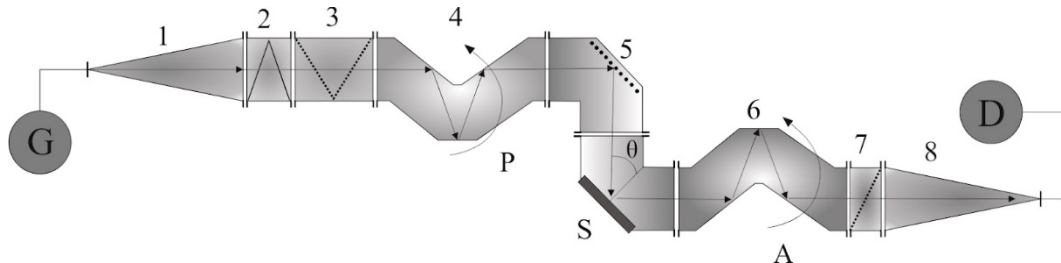
Figure 2. Quasi-optical terahertz ellipsometer scheme

The sample material for this study was Epcos No. 87 ferrite. The choice of material was based on its optical properties ($n{\sim}6.7$, $k{\sim}4.0$) [18, 19], which are similar to those of metals in the optical range.

The samples used in this study were ferrite plates with a size of $50{\times}22{\times}6$ mm. Probe beam diameter is 20 mm (Fig. 3(a)). Several identical defects, each in the form of a parallelepiped with dimensions a, b, and c, made of the same material were placed in the center of the plate and beam (Fig. 3(b)). The position of the defects is specified by a single parameter - the distance d from the sample center to the defect.
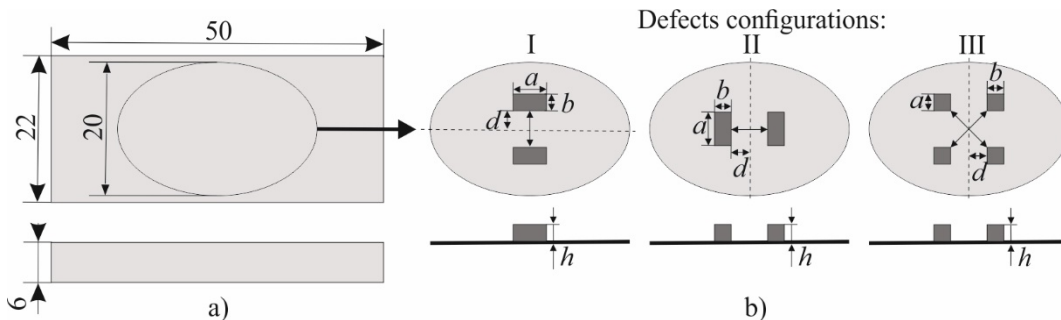

Figure 3. Schematic representation of the sample, the distribution of the beam spot, and the arrangement of defects on the sample surface

For quasi-optical scale modeling of the influence of several defects on ellipsometric parameters, three defect configurations were considered: a) two parallelepipeds with a long side parallel to the plane of incidence, located symmetrically relative to the plane of incidence at a distance of $2d$ from each other (Fig. 3b), configuration I; b) two parallelepipeds oriented with their long sides perpendicular to the plane of incidence, located symmetrically relative to the center of the sample and spaced at a distance of $2d$ (Fig. 3b), configuration II; c) four defects, square in plan ($a = b$), with sides parallel to the sides of the sample, located symmetrically at a distance d from its center (Fig. 3b), configuration III. It should be noted that the total defect area is the same in all three configurations.

The ellipsometric parameters Ψ and Δ were measured for surfaces with defects of varying sizes (parameters a, b, and h) and relative positions (parameter d). In configurations I and II, defects with plan dimensions $a = 5$ mm and $b = 2.5$ mm, and heights $h = 2.5$ mm and 1.5 mm were considered. In configuration III, the defects had dimensions $a = b = 2.5$ mm in plan and three heights $h = 2.5$ mm, 1.5 mm, and 0.5 mm. The parameter d in all configurations varied from 0 to 12 mm. All options for defect parameters and configurations are summarized in Table 1.

**Table 1.** Parameters of defects (a, b, h) and their relative position (d) for all configurations.

	a, mm	**b, mm**	**h, mm**	**d, mm**
Configuration I	5.0	2.5	1.5; 2.5	0, 1, 2, 3, 5, 7, 9, 12
Configuration II	5.0	2.5	1.5; 2.5	
Configuration III	2.5	2.5	0.5; 1.5; 2.5	0, 1, 2, 3, 5, 7, 12

The choice of defect parameters and configurations is determined by the results obtained in [20]. As mentioned above, [20] shows that a single defect, with a characteristic size less than the wavelength λ, becomes "invisible" for ellipsometry. If the defect size significantly exceeds λ, then the angular dependences of the ellipsometric parameters become non-trivial. Thus, for the study of multiple defects, defects and their configurations with dimensions comparable

to the wavelength of the probing radiation (in our case, $\lambda = 2.14$ mm) are of greatest interest. In addition, it is precisely this range of ratios of defect size to wavelength that is most interesting from the point of view of large-scale modeling of the effect of defects on the results of optical ellipsometry. The goal of the experiment was to clarify the conditions under which defects can be considered localized from the point of view of ellipsometry, i.e., when multiple defects can be considered as individual defects, as a single defect, or as a group of defects influencing each other (i.e., not localized defects). Next, we present the results of the experiment.

3. EXPERIMENTAL RESULTS

Fig. 4 shows the experimental angular dependences of Ψ and Δ for the initial (bare) ferrite surface without defects (dots). From these data, the optical constants of the substrate were determined in the bare surface model [2] ($n = 6.74$, $k = 4.02$). The lines in Fig. 4 represent the angular dependences of Ψ and Δ corresponding to these values of optical constants. One can see that the experimental data are described by the model of a bare isotropic surface with an error not exceeding the experimental error. With these optical constants, the probing radiation does not penetrate this material beyond 10 μm. Accordingly, the samples under study can be considered as bulk (without coatings), and the results of further experiments related to the presence of defects on the surface can be interpreted without taking into account interference effects in the defect and/or substrate.
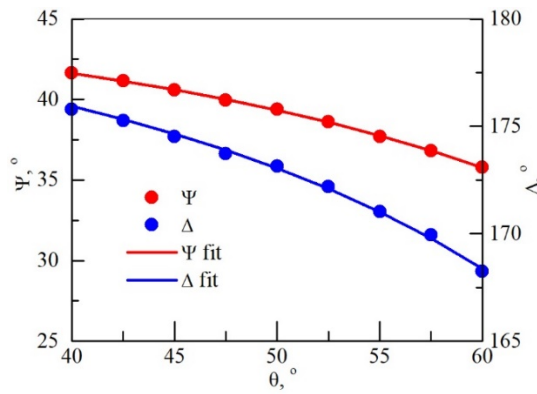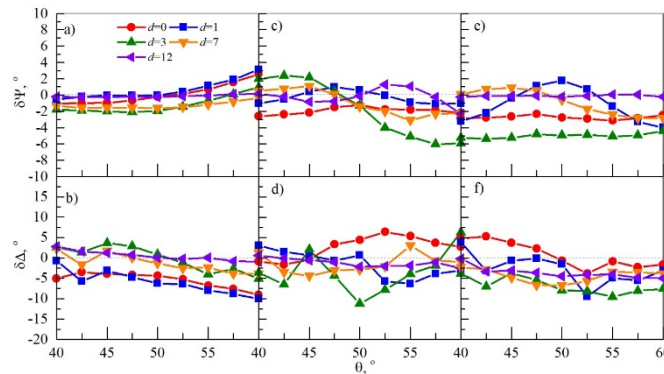

Figure 4. Angular dependencies of the experimental data (dots) and fitted model (lines) for the ellipsometric parameters Ψ and Δ of the defect-free substrate.

Next, we consider part of the experimental results that reflect the general trends in the influence of changes in defect configurations on the ellipsometric parameters Ψ and Δ. Fig. 5 shows the experimental results for defect configurations I ($h = 1.5$ mm), II ($h = 2.5$ mm), and III ($h = 2.5$ mm) as listed in Table. 1. For the convenience of analysis, the figures show the following dependencies of ellipsometric parameters differences:

$$\delta\Psi(\theta) = (\Psi(\theta) - \Psi_0(\theta)), \quad \delta\Delta(\theta) = (\Delta(\theta) - \Delta_0(\theta)), \tag{2}$$

where $\Psi_0(\theta)$ and $\Delta_0(\theta)$ are the ellipsometric parameters of the defect-free surface (see Fig. 4). Thus, the effect of a defect on the ellipsometric parameters relative to a bare surface is illustrated.

Figure 5. Experimental angular difference dependencies of ellipsometric parameters Ψ (a) and Δ (b)
for configurations I (a), b), $h = 1.5$ mm, II (c), d), $h = 2.5$ mm, III (e), f), $h = 2.5$ mm).

Fig. 5 shows that the nature of the dependencies for different configurations is similar. For all configurations with $h = 2.5$ mm, oscillations of the angular dependencies of the ellipsometric parameters are observed. At $h = 1.5$ mm, the oscillations have less amplitude. However, despite the different local nature of the dependencies for all configurations, they have similar integral properties. A single large defect ($d = 0$ mm) causes a significant deviation of the angular

dependencies $\Psi(\theta)$ and $\Delta(\theta)$ from the clean surface. As the distance d between defects increases in all three configurations, both $\Psi(\theta)$ and $\Delta(\theta)$ initially deviate further from the clean surface, but with a further increase in distance, they start to approach the clean surface values. Thus, individual defects in all configurations become "invisible" to ellipsometry as the distance between them increases.

4. ANALYSIS OF RESULTS

From the above graphs, it is difficult to quantitatively estimate the degree of deviation of the $\Psi(\theta)$ and $\Delta(\theta)$ dependencies from the "bare surface" for various defect configurations. Therefore, to characterize the degree of deviation of the angular dependencies for surfaces with and without defects, we will use the arithmetic mean of the root-mean-square differences:

$$\sigma = \frac{1}{2}\left(\sqrt{\frac{1}{n}\sum_{i=0}^{n}(\Psi_{\theta_i}^{bare} - \Psi_{\theta_i}^{def})^2} + \sqrt{\frac{1}{n}\sum_{i=0}^{n}(\Delta_{\theta_i}^{bare} - \Delta_{\theta_i}^{def})^2} \right), \tag{3}$$

where $\Psi_{\theta_i}^{bare}$ and $\Delta_{\theta_i}^{bare}$ are the ellipsometric parameters of a defect-free sample at an angle of incidence θ_i, $\Psi_{\theta_i}^{def}$ and $\Delta_{\theta_i}^{def}$ are the parameters for a sample with defects, and n is the number of measurements at different angles of incidence θ. Next, we consider the dependences $\sigma(d)$ for various configurations and defect height h (Fig. 6).
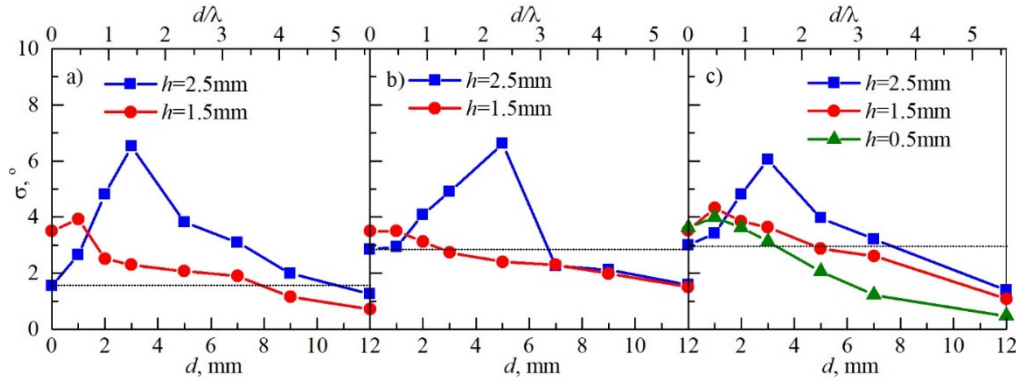
Figure 6. Dependences of σ(d) in configurations I (a), II (b), and III (c) for different defect heights.

Fig. 6 shows that in all 3 configurations, the dependences $\sigma(d)$ at h = 2.5mm ($h/\lambda \sim 1$) are qualitatively the same and quantitatively close. Namely, $\sigma(d)$ increases monotonically and reaches a maximum at $d/\lambda \sim 1.5$ (configurations I and II) and $d/\lambda \sim 2$ (configuration II). Further, σ monotonically tends to 0. At $h=1.5$mm and 0.5mm ($h/\lambda \sim \frac{3}{4}$, $h/\lambda \sim \frac{1}{4}$), the dependencies are qualitatively similar, but the maxima are less by value and shifted to the $d \sim 1$ region.

From the above results, it is clear that the influence of the considered localized defects on the ellipsometric parameters Ψ and Δ is significant and non-trivial. Thus, the presence of various configurations defects leads to a qualitative change like the angular dependencies $\Psi(\theta)$ and $\Delta(\theta)$ compared to a "bare surface". From the experimental data, it is clear that the main influence of defects appears in oscillations of ellipsometric parameters around the clean surface (Fig. 5). This effect is associated with the interference of waves reflected from different areas of the defective surface [15]. It is worth noting that for high defects ($h=2.5$mm, $h/\lambda \sim 1$) the oscillations are greater in amplitude and frequency. As the height of the defects decreases, the oscillations decrease, and for defects with a height of 0.5 mm, they are practically absent.

The results in Fig. 6 can be divided according to the h parameter (2.5, 1.5, and 0.5 mm) because the trends in the $\sigma(d)$ dependencies are similar for different defect configurations. One can see that the $\sigma(d)$ dependencies at $h=2.5$mm ($\sim 1\lambda$) have explicit maxima for all defect configurations at $d=3$-5 mm (which corresponds to ~ 1-2λ). So, at a given distance d between defects, the maximum influence of interference effects on the ellipsometric parameters occurs. With a further increase in d, the σ values monotonically decrease, which indicates a decrease in the interaction between defects. Wherein, σ(0)=σ(3.5-4.5λ), i.e. starting from a critical distance $d_{cr} = 4.5\lambda$ between defects, the defects stop interacting and can be considered as localized.

In the case of defects with a smaller height ($h=1.5$mm = $\sim 3/4\lambda$ and $h=0.5$mm = $\sim 1/4\lambda$) $\sigma(d)$ is smaller in value, which indicates less interference interaction between defects. At the same time, the dependencies $\sigma(d)$ begin to decrease monotonically starting from σ(0.5λ), which indicates the maximum interaction of defects at a distance of fractions of a wavelength. It is also worth noting that for cases $d=$(0.5 and 1.5 mm) σ(0)~σ(<1λ) we can conclude that the distance d_{cr} at which defects become localized depends on their dimensions and, firstly, turn from their height. A similar dependence is observed in the case of configuration III at $h = 0.5$ mm.

We previously observed similar non-classical behavior of ellipsometric parameters in measurements in the optical range (λ = 633 nm) [18] and in large-scale simulations with a single localized defect [20]. In [18], samples of a precipitation-hardened copper alloy were studied and subjected to radiation sputtering, which led to the appearance of a

significant number of localized defects (Fig. 7), specifically harder particles of secondary phases. In this work, the angular dependences $\Psi(\theta)$ and $\Delta(\theta)$ were obtained for the first time, with their profiles being radically different from the classical ones. Additionally, a hypothesis was formulated that explained this behavior as being due to the presence of localized defects, and predicted that if the size of such a defect is several times smaller than the wavelength, ellipsometry would cease to be sensitive to these defects.
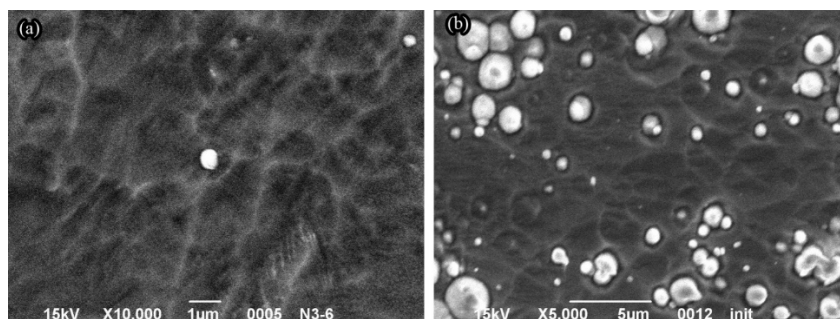
Figure 7. Examples of localized surface defects in a sputtered precipitation-hardened CuCrZr alloy:
(a) single defect and (b) multiple defects

The results of this work confirm this hypothesis. Specifically, it is shown that the behavior of the angular dependences $\Psi(\theta)$ and $\Delta(\theta)$ is linked to the presence of localized defects whose size is several times larger than the wavelength of the probing radiation. As the size of the localized defects decreases and the degree of localization increases (i.e., the distance between defects in the case of grouped defects) to sizes slightly smaller than the wavelength of the probing radiation, the defects become "invisible" to ellipsometry but continue to significantly influence specular reflection.

5. CONCLUSIONS

Thus, the work demonstrates that deviations from the classical behavior of the angular dependences of the ellipsometric parameters are grounds to assume the presence of localized defects or their conglomerates. In this case, statistically homogeneous defect layers (such as roughness, transition layers, etc.) never lead to qualitative deviations from the classical behavior of angular dependencies.

It is also shown that for all defect configurations studied, with small distances between defects, they have a joint effect on the ellipsometry results. At a certain distance, defects begin to influence ellipsometry results independently. Accordingly, a critical distance for defect localization can be introduced, beyond which they do not jointly affect the ellipsometric parameters. So, for $h/\lambda \sim 1$, d_{cr} is equal to $3.5\text{-}4.5\lambda$; for $h/\lambda \sim \frac{3}{4}$ and $\frac{1}{4}$ - less than λ. Thus, d_{cr} decreases with decreasing h/λ ratio. The detailed form of the $d_{cr}(h/\lambda)$ dependence will be investigated in a separate study.

As mentioned above, defects of relatively large sizes ($\sim\lambda$) can lead to oscillations in the angular dependences of ellipsometric parameters, which can be used to determine the characteristics of roughness. As the defect height h decreases, the oscillation period increases; therefore, to more thoroughly study the influence of defects with $h < 0.7\lambda$, measurements in a larger range of incidence angles are required.

ORCID
Oleksii Haluza, https://orcid.org/0000-0003-3809-149X; **Ivan Kolenov,** https://orcid.org/0000-0002-1741-5195
Iryna Gruzdo, https://orcid.org/0000-0002-4399-2367

REFERENCES
[1]   R.M.A. Azzam, and N.M. Bashara, *Ellipsometry and polarized light* (North Holland, Amsterdam, 1999).
[2]   H. Fujiwara, *Spectroscopic Ellipsometry: Principles and Applications* (Wiley, Chichester, 2007).
[3]   H.G. Tompkins, and W.A. McGahan, *Spectroscopic Ellipsometry and Reflectometry: A User's Guide* (Wiley, Chichester, 1999).
[4]   S. Zollner, F. Abadizaman, C. Emminger, and N. Samarasingha, Adv. Opt. Technol., **11**, 117 (2022), https://doi.org/10.1515/aot-2022-0016
[5]   B. Hajduk, H. Bednarski, and B. Trzebicka, J. Phys. Chem. B, **124**(16), 3229 (2020). https://doi.org/10.1021/acs.jpcb.9b11863
[6]   S. Bairagi, C.-L. Hsiao, R. Magnusson, J. Birch, J.P. Chu, F.-G. Tarntair, R.-H. Horng, K. Järrendahl, Opt. Mater. Express, **12**, 3284 (2022), https://doi.org/10.1364/OME.462668
[7]   M.S. Gangwar, P. Agarwal, Phys. Scr. **98**, 105944 (2023). https://doi.org/10.1088/1402-4896/acf796
[8]   W. Leigh, S. Mandal, J.A. Cuenca, D. Wallis, A.M. Hinz, R.A. Oliver, E.L.H. Thomas, and O. Williams, ACS Omega, **8**, 30442 (2023). https://doi.org/10.1021/acsomega.3c03609
[9]   K. Ungeheuer, K.W. Marszalek, M. Mitura-Nowak, *et al*., Sci Rep. **13**, 22116 (2023). https://doi.org/10.1038/s41598-023-49133-x
[10] A. Lemire, K. Grossklaus, T.E. Vandervelde, IEEE Dataport, (2024). https://dx.doi.org/10.21227/xhrd-ny57

[11] D. Schmidt, E. Schubert, and M. Schubert, in: *Ellipsometry at the Nanoscale*, edited by M. Losurdo and K. Hingerl (Springer Berlin Heidelberg, 2013), pp. 341-410.

[12] S. Bian, and O. Arteaga, Opt. Express, **31**(12), 19632-19645 (2023). https://doi.org/10.1364/oe.490197

[13] W. Yu, C. Cui, H. Li, S. Bian, and X. Chen, Photonics **9**(9), 621 (2022), https://doi.org/10.3390/photonics9090621

[14] N.C. Bruce, O.G. Rodríguez-Herrera, C.N. Ramírez, and M. Rosete-Aguilar, Appl. Opt. **60**(5), 1182 (2021). https://doi.org/10.1364/AO.410003

[15] T. V. Vorburger, and K. C. Ludema, Appl. Opt. **19**(4), 561 (1980). https://doi.org/10.1364/AO.19.000561

[16] M.G. Tchéré, S. Robert, J. Dutems, H. Bruhier, B. Bayard, Y. Jourlin, and D. Jamon, Appl. Opt. **63**(14), 3876 (2024). https://doi.org/10.1364/AO.520109

[17] G.G. Politano, and C. Versace, Spectrosc. J. **1**(3), 163 (2023). https://doi.org/10.3390/spectroscj1030014

[18] A.I. Belyaeva, A.A. Galuza, P.A. Khaimovich, *et al.*, Phys. Metals Metallogr. **117**, 1170 (2016). https://doi.org/10.1134/S0031918X16090027

[19] A.I. Belyaeva, V.Kh. Alimov, A.A. Galuza, K. Isobe, V.G. Konovalov, I.V. Ryzhkov, A.A. Savchenko, *et al.*, J. Nucl. Mater. **413**(1), 5 (2011), https://doi.org/10.1016/j.jnucmat.2011.03.026

[20] A.I. Belyaeva, A.A. Galuza, V.K. Kiseliov, I.V. Kolenov, A.A. Savchenko, Ye.M. Kuleshov, and S.Yu. Serebriansky, Telecommunications and Radio Engineering **74**(2), 171 (2015). https://doi.org/10.1615/TelecomRadEng.v74.i2.60

[21] N.L. Dmitruk, A.V. Goncharenko, and E.F. Venger, *Optics of Small Particles and Composite Medi*a, (Naukova Dumka, Kyiv, 2009).

[22] O.V. Angelsky, and P.P. Maksimyak, Optical Engineering, **34**(4), 973 (1995). https://doi.org/10.1117/12.197181

[23] X. Liu, Q. Chen, J. Zeng, Y.J. Cai, and C.H. Liang, Opto-Electron Sci. **2**, 220024 (2023). https://doi.org/10.29026/oes.2023.220024

[24] M. W. Hyde, J. Opt. Soc. Am. A, **39**(12), 2383 (2022). https://doi.org/10.1364/JOSAA.465457

[25] S. Mizrakhy, in: *IEEE First Ukraine Conference on Electrical and Computer Engineering* (UKRCON, Kyiv, Ukraine, 2017), pp. 198-201, https://doi.org/10.1109/UKRCON.2017.8100473

[26] I.A. Tishchenko, and A.I. Nosich, IEEE Microw. Mag. **4**(4), 32 (2003), https://doi.org/10.1109/MMW.2003.1266065

[27] A.A. Galuza, V.K. Kiseliov, I.V. Kolenov, A.I. Belyaeva, and Y.M. Kuleshov, IEEE Trans. THz Sci. Technol. **6**(2), 183 (2016), https://doi.org/10.1109/TTHZ.2016.2525732

МАСШТАБНЕ МОДЕЛЮВАННЯ ВПЛИВУ МНОЖИННИХ ЛОКАЛІЗОВАНИХ ДЕФЕКТІВ ПОВЕРХНІ МЕТАЛУ НА РЕЗУЛЬТАТИ ОПТИЧНОЇ ЕЛІПСОМЕТРІЇ

Олексій Галуза[a,b], Іван Коленов[c,d], Ірина Груздо[b]

[a]Національний технічний універсистет «Харківський політехнічний інститут», вул. Кирпичова, 2, м. Харків, 61002, Україна
[b]Харківський національний університет радіоелектроніки, пр. Науки, 14, м. Харків, 61166, Україна
[c]Інститут електрофізики і радіаційних технологій НАН України, вул. Чернишевського, 28, м. Харків, 61002, Україна
[d]Інститут радіофізики та електроніки ім. О.Я. Усикова НАН України, вул. Ак. Проскури, 12, 61085, м. Харків, Україна

Робота присвячена проблемі еліпсометричних досліджень реальних поверхонь і розглядає випадок, коли поверхневі неоднорідності являють собою окремі локалізовані дефекти або їх конгломерати розміром, порівняним з довжиною хвилі зондуючого випромінювання. Такі неоднорідності призводять до кутових залежностей еліпсометричних параметрів, які мають некласичний вигляд і не можуть бути описані за допомогою звичайних відомих моделей однорідних плоских шарів. Ця робота присвячена вивченню впливу конгломератів локалізованих дефектів на кутові залежності еліпсометричних параметрів і є продовженням попередніх досліджень, у яких розглядалися поодинокі локалізовані дефекти. Досліджено залежність ступеня впливу відстані між дефектами на еліпсометричні параметри. Введено параметр «критична відстань» між дефектами, за межами якого їх можна вважати локалізованими, та наведено оцінки цього параметра для розглянутих конфігурацій.

Ключові слова: *еліпсометрія; терагерцеві хвилі; масштабне моделювання; поверхневі дефекти; локалізовані дефекти*

MAGNETO-OPTICS FEATURES OF RADIATION TRANSITIONS OF NON-KRAMERS Tm^{3+} ION IN YTTRIUM-ALUMINUM GARNET CRYSTALS

Furkat K. Turotov, Mariya E. Malysheva, Ramil R. Vildanov*

National university of Uzbekistan, named after Mirzo Ulugbek, Tashkent, 100174, Uzbekistan
Corresponding Author e-mail: ramvild@gmail.com

The spectra of luminescence and magnetic circular polarization of a single crystal of thulium-yttrium garnet-aluminate Tm^{3+}:YAG have been studied within the visible spectral range at a temperature of 90 and 300 K in a magnetic field of 10 kOe. Based on the analysis of optical and magneto-optical data, the presence of "quasi-degenerate" states of excited multiplets $^1D_2$, $^3F_4$,$^3G_4$ and the ground multiplet $^3H_6$ of the Tm^{3+} RE ion in garnet-aluminate YAG at the radiative transitions $^1G_4 \rightarrow {}^3H_6$, $^1D_2 \rightarrow {}^3F_4$ and $^1D_2 \rightarrow {}^3F_3$ has been determined. The effect of quantum mechanical "mixing" plays a significant role in the occurrence of magneto-optical effects on luminescence bands caused by "forbidden" 4f→4f transitions in the non-Kramers Tm^{3+} ion having a "quasi-doublet" structure in the energy spectra.

Keywords: *Thulium-yttrium garnet; Rare-earth ions; Magneto-optical properties; Luminescence; Energy levels; Magnetic circular polarization*
PACS: 71.70.Ej; 78.20.Ls

INTRODUCTION

Yttrium aluminum garnet $Y_3Al_5O_{12}$ (YAG) doped with trivalent rare-earth (RE) ions R^{3+} is well known as a material used for creation of solid-state lasers [1-3]. This circumstance has contributed to the intensive study of the optical and magneto-optical properties and energy levels of a number of rare-earth ions R^{3+} in the garnet crystalline cell, replacing the yttrium ions Y^{3+} located in the dodecahedral positions of the garnet structure [4]. But among all these garnets with RE ions as impurities, the similar properties (in particular, magneto-optical ones) of Tm^{3+}:YAG garnet have been studied comparatively insufficiently. Therefore, at present, the magneto-optical properties of Tm^{3+} RE ions in garnet crystals are studied systematically [5-6], and this circumstance has become one of the motivating factors for this study to be conducted.

On the other hand, the presence of a large number of emission transitions observed within the wide spectral range from near infrared (IR) to ultraviolet (UV) shows that Tm^{3+}:YAG is a good material for lasers operating within the near IR range [7-9]. An effective process in the same region is emission due to the up-conversion pumping [10]; in this case also promising matrices are garnet-structure crystals for further activation by trivalent thulium ions. Another new possible application of the Tm^{3+}:YAG RE compound is its use in information display systems operating within the spectral range from 460 nm to 470 nm because of proximity of the $^1D_2 \rightarrow {}^3F_4$ emission transition to optimal operating wavelengths of video-displays in this spectral range. Therefore, the study of this transition is still of great interest, since an in-detail consideration of the spectroscopic properties of this transition to be aimed at obtaining information on mechanisms of excitation of the radiative states of Tm^{3+} ions and hence obtaining efficient generation is currently of paramount importance.

The crystalline electrostatic field (CF) created by the low-symmetry environment of the RE ion in the garnet lattice leads to a partial or almost complete "removal" of the quantum degeneracy from the Stark sublevels in the multiplets belonging to the ground $4f^{(n)}$ configuration of the ion. Further removal of degeneracy from the Stark sublevels of the RE ion with the help of the Zeeman splitting of their states by an outer magnetic field H leads to emerging induced circular anisotropy of the optical absorption and luminescence bands, which manifests itself both in magnetic circular dichroism (MCD) observed during light absorption [11] and in magnetic circular polarization of luminescence (MCPL) recorded during light radiation emission [12]. The study of the MCD and MCPL phenomena (being differential in essence) in non-Kramers RE ions (i.e. with an even number of electrons in the unfilled $4f^{(n)}$ shell) provides a fundamental opportunity to determine a symmetry of the wave functions of the Stark sublevels (including the so-called "quasi-degenerate" sublevels that cannot be resolved directly in optical experiments), from which (or to which) the optical 4f→4f transitions occur (forbidden in the electrodipole (ED) approximation) [13].

At the same time, it is well known that the main source of MCPL (or MCD) phenomena in non-Kramers RE ions is the Van Vleck "mixing" (by an outer magnetic field) of the wave functions of neighboring non-degenerate Stark sublevels combining in the optical transition. This circumstance makes it possible to reliably position the "quasi-degenerate" states in the energy spectrum of the non-Kramers RE ion. According to the results of experimental and theoretical studies of YAG (or YGaG) garnets activated by Ho^{3+} [14] and Tb^{3+} [15] RE ions, in the low-symmetry CP of the garnet a set of the "quasi-doublet" states are formed in the energy spectra of the ground and excited multiplets of non-Kramers ions [16], while no "quasi-doublets" were detected in the multiplets of Tm^{3+} ions in the similar garnets. The absorption and
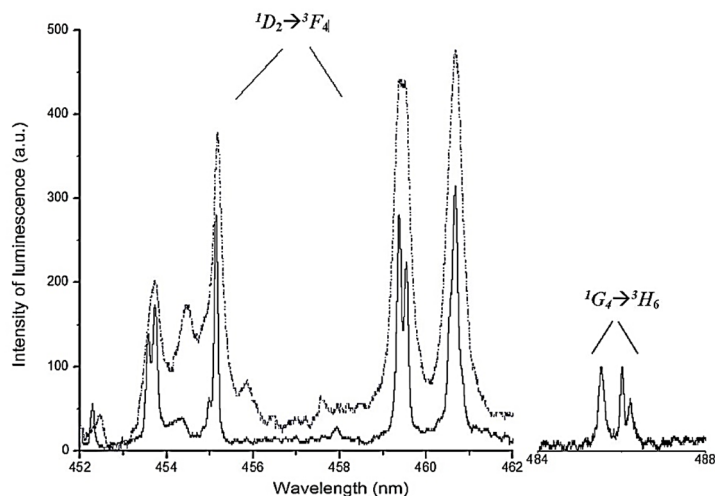
luminescence spectra of Tm³⁺:YAG have been studied in detail within the visible and near infrared ranges at various temperatures (including low ones) by J.B.Gruber et al. [17]. For the emission spectra of the transitions from the ¹D₂ state to the ³H₆, ³F₄, ³F₃ and ³F₂ multiplets to be studied, laser excitation of the optical transitions was used. Although these data provided information confirming the crystal-field splitting of the most multiplets (i.e. the *J,L,S*-states) belonging to the ground 4f⁽ⁿ⁾-configuration of the Tm³⁺ ion in the garnet structure, as well as information on the symmetry of the Stark sublevels of these multiplets, we believe that the previously obtained energy spectra of the Tm³⁺ ion in the garnet-aluminate structure should be supplemented by the corresponding "quasi-doublet" states that in turn can be detected and identified by magnetic circular polarization of luminescence methods in a wide range of wavelengths and temperatures [18]. Therefore, new studies of the emission spectra of Tm³⁺:YAG by the differential magneto-optical methods would be very useful, since their application can help in positioning and determining a symmetry of the nearby (i.e. "quasi-degenerate") Stark sublevels in non-Kramers Tm³⁺ ions. On the other hand, the similar studies of the magneto-optical activity of emission transitions in thulium-yttrium garnets seems relevant due to a certain smallness of the Faraday rotation detected in these garnets within the visible spectral range as compared to the similar spectra observed in other rare-earth garnets [19], and their analysis led to contradictory results associated with the possible absence of "quasi-degenerate" ground states in non-Kramers Tm³⁺ ions in the garnet structure. The above-mentioned contradictions discovered during the study and interpretation of magneto-optical and magnetic properties of thulium garnet Tm:YAG were the motivating factors for this work to be carried out.

MATERIALS AND METHODS

A single crystal of thulium-yttrium garnet-aluminate Tm³⁺:YAG grown by a spontaneous crystallization method from the "solution-melt" was provided by Prof. J. Heber (Physics Institute of the Technical University, Darmstadt, Germany). A sample under study containing ~1% Tm³⁺ ions was X-ray oriented and cut in the crystallographic planes of the (110) and (001); after that the sample surface was ground and polished with diamond pastes with a slowly thinning grain (down to ~1 μm). The luminescence spectra of Tm³⁺:YAG were measured at temperatures T = 90K and 300K for the radiative 4f→4f transitions ¹D₂→³F₄ and ¹G₄→³H₆ within the spectral ranges of 452-462 nm and 484-488 nm with a resolution of ~ 1.5-2.0 cm⁻¹. The differential magneto-optical spectrum of Tm³⁺:YAG, i.e. a spectrum of the MCPL degree $P = \frac{I_+ - I_-}{I_+ + I_-}$ (where $I_\pm$ is the intensity of orthogonal circularly polarized components of the luminescence line), was studied at a temperature of $T = 300$ K within the spectral range of 453-462 nm and 484-488 nm with a resolution of ~10 cm⁻¹ and orientation of the outer magnetic field $H = 10$ kOe along the [110] axis of the garnet crystal. The MCPL degree spectra was recorded by a method of light radiation polarization modulation at a frequency of ~36 kHz with a photoelastic modulator with positive optical feedback [13]. The relative errors of the measured values (intensities of luminescence and degrees of circular light polarization) in all experiments did not exceed ~3-5%.

RESULTS AND DISCUSSION

The luminescence and MCPL spectra in single crystals of thulium-yttrium garnet-aluminate were studied for the radiative transitions ¹G₄→³H₆ and ¹D₂→³F₄ within the wavelength range of 453-484 nm. The luminescence observed for the radiative transitions of the type: ¹G₄→³H₆, ¹D₂→³F₄, ¹D₂→³F₃, turns out to be the most intensive in the emission band caused by the radiative transition ¹D₂→³F₄ (Fig. 1).

Figure 1. The luminescence spectrum of Tm³⁺:YAG recorded in the emission band ¹D₂→³F₄ and ¹G₄→³H₆ at *T*=300K (blue dotted line) and at *T*=90K (black solid line)

The spectra of blue luminescence bands recorded at *T*=300K and 90K are characterized by a large number of well-resolved emission lines associated with the radiative 4f→4f transitions between the sublevels of the ¹D₂ and ³F₄ multiplets

in the Tm^{3+} ion. A decrease in the sample temperature from 300 to 90K is accompanied by a decrease in the luminescence brightness, with the intensities of the strongest emission lines at wavelengths of 455, 459, 460 nm, determined by the areas under the corresponding lines, decreasing to the same extent by approximately 1.5 times as compared to a more significant decrease in the intensity of the remaining emission lines. The redistribution of the luminescence line intensity is due to a sharp decrease in the populations of the excited Stark singlets of the $^3F_4$ and $^1D_2$ multiplet when the temperature drops. When the temperature is lowered to 90 K, it is clearly seen that the emission lines at wavelengths of 453.6 and 457 nm are doublet lines insufficiently resolved at T=78 K. The most intensive luminescence lines in the $^1D_2 \rightarrow ^3F_4$ luminescence band originate from the ground quasi-doublet state of the excited $^1D_2$ multiplet of the ground $4f^{(12)}$ configuration of the Tm^{3+} ion in YAG garnet-aluminate. The remaining emission lines are apparently due to radiative transitions from excited singlet sublevels of the $^1D_2$ multiplet to Stark sublevels of the $^3F_4$ multiplet.

Comparison of experimentally observed energies of the ground $4f^{(12)}$ configuration of Tm^{3+} ions in the crystal field (CF) of D_2 symmetry with theoretical values makes it possible to carry out symmetry identification of the radiative $4f \rightarrow 4f$ transitions in the luminescence band of $^1D_2 \rightarrow ^3F_4$ and $^1G_4 \rightarrow ^3H_6$. Symmetry identification of the radiative transitions observed in the luminescence band $^1D_2 \rightarrow ^3F_4$ and $^1G_4 \rightarrow ^3H_6$ was performed based on the data of [17] and according to the notation of [4]. Classification (in symmetry) of the Stark sublevels of the multiplets $^3F_4$, $^1G_4$, $^1D_2$ and $^3H_6$ was carried out using irreducible representations Γ_i (where i = 1,2,3,4) of the D_2 symmetry group; and the directions and notations of the axes of the local coordinate system corresponding to one of the crystallographically nonequivalent positions (the so-called c-sites) of the RE ion Tm^{3+} in the garnet structure coincide with those adopted in [4].

The spectra of the MCPL degree measured in a single crystal of thulium-yttrium garnet-aluminate on the luminescence line $^1D_2 \rightarrow ^3F_4$ (Fig. 2, Fig. 3) and on the luminescence line $^1G_4 \rightarrow ^3H_6$ (Fig. 4) at T=300 K and T=90 K in the outer magnetic field H = 10 kOe are presented in Fig. 2, Fig. 3 and Fig. 4.
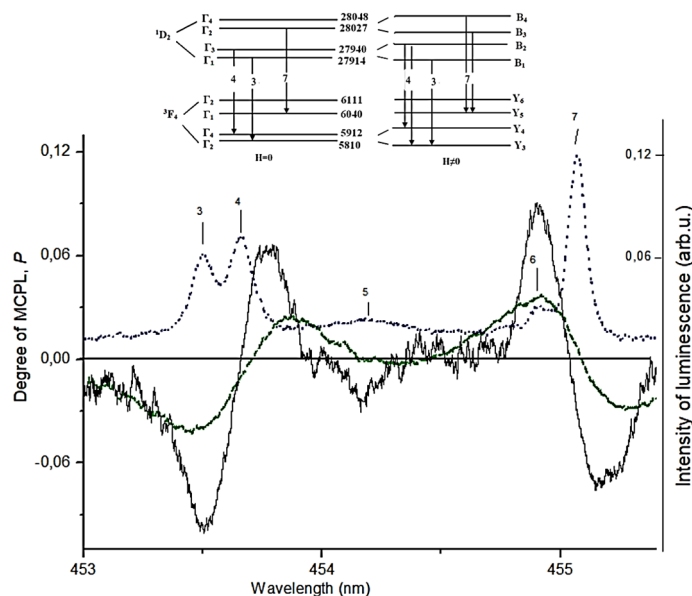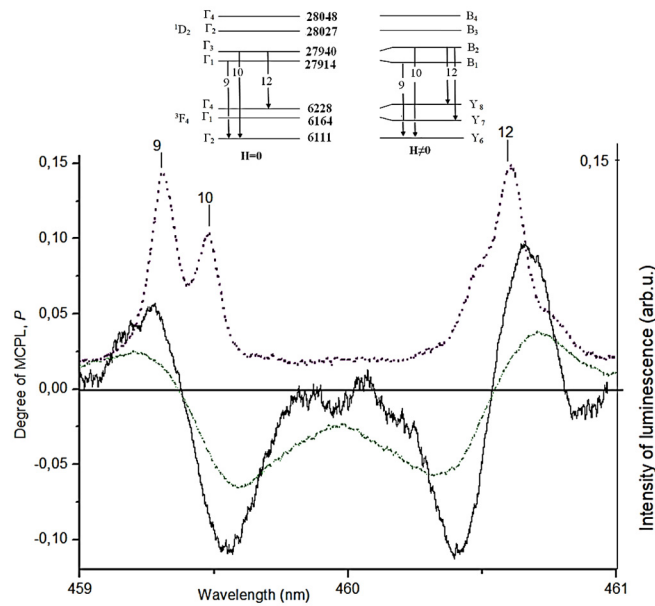

Figure 2. The spectra of the MCPL degree measured for the radiative transitions $^1D_2 \rightarrow ^3F_4$ within the wavelength range 453-456 nm at T=90 K (black) and 300 K (green). The luminescence spectra (dots) were measured at 90 K. The inset shows a diagram of optical transitions between sublevels of the multiplets $^1D_2$ and $^3F_4$ of the Tm^{3+} in Tm^{3+}:YAG with no outer magnetic field and that of H=10 kOe

A comparison of the spectra of the MCPL degree P and luminescence (fluorescence) indicates the obvious fact that despite the relatively complicated structure of the observed spectrum P, for some emission lines the dispersion of the MCPL degree spectrum can be explained in a fairly simple way. For example, on lines 4, 7 (Fig. 2), 12 (Fig. 3) and 14 (Fig. 4), within the luminescence line the spectral dependence of the MCPL degree can be approximated by inclined linear dependences for which an effect magnitude is symmetrical (or asymmetrical) relative to zero (when the effect sign changes in the "centers of gravity" of the corresponding line). Moreover, from the schemes of radiative transitions shown in Fig. 2 and Fig. 3 it follows that the lines 4 and 12 are associated with allowed (in symmetry in the D_2 group) forced optical transitions occurring from the $B_2(\Gamma_3)$ sublevel of the $^1D_2$ multiplet to the nearby Stark sublevels $Y_4(\Gamma_4)$, $Y_3(\Gamma_2)$ for the line 4 and to the $Y_8(\Gamma_4)$, $Y_7(\Gamma_1)$ sublevels for the line 12 of the $^3F_4$ multiplet. At the same time, the line 7 in Fig. 2 is caused by permitted (in symmetry) optical transitions occurring from the B_2 Stark sublevel of the $^1D_2$ multiplet with Γ_3 symmetry to the nearby $Y_8(\Gamma_4)$ and $Y_7(\Gamma_1)$ Stark sublevels of the $^3F_4$ multiplet. Besides, the special feature of the spectral dependence of the MCPL degree on the line 7 (Fig. 2) is caused by the permitted (in symmetry) optical transitions occurring from the nearby Stark sublevels $B_4(\Gamma_4)$ and $B_3(\Gamma_2)$ of the $^1D_2$ multiplet to the $Y_5(\Gamma_1)$ sublevel of the $^3F_4$ multiplet.

The scheme of optical transitions between sublevels of multiplets $^1D_2$ and $^3F_4$ of the Tm^{3+} ion in Tm^{3+}:YAG is shown in the insets to Fig. 2 and Fig. 3. On the emission line 12, the spectral dependence $P(\nu)$ is an inclined linear dependence

within the luminescence line with a change in the sign of the effect in its center. According to the general theory (see [18]), a value of the spectrum slope - P (A is the term of the MCPL degree) is due to the Zeeman splitting of the sublevels of the final and initial states combining in the optical transition; in this case, to the Zeeman splitting of the quasi-doublet state of the $^5D_1$ multiplet in the magneto-optically active transition "singlet → quasi-doublet". In the outer magnetic field, the wave functions of nearby singlets and singlets from multiplets combining in radiative transitions begin to "mix" with each other; and magnetic dipole and electric dipole transitions begin to occur between them. Using the available selection rules (in symmetry) for the matrix elements of the components of the electric and magnetic dipole moments of the RE ion from the expression for the A term of the MCPL degree, it is easy to establish the symmetry of one of the combining states in the magneto-optical transition if the symmetry of the other is known [12].

Figure 3. The spectra of the MCPL degree measured for the radiative transitions $^1D_2 \rightarrow {}^3F_4$ within the wavelength range 459-461 nm at T=90 K (black) and 300 K (green). The luminescence spectra (dots) were measured at 90 K. The inset shows a diagram of optical transitions between sublevels of the multiplets $^1D_2$ and $^3F_4$ of the Tm^{3+} ion in Tm^{3+}:YAG with no outer magnetic field and that of H=10 kOe.
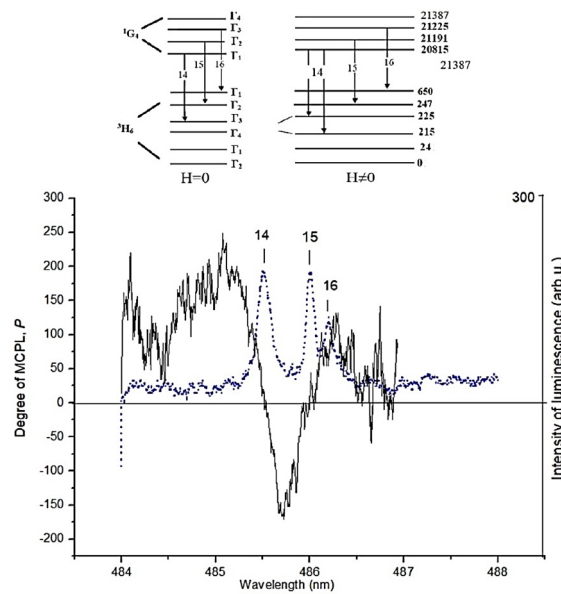
Figure 4. The MCPL degree spectra measured on radiative transitions $^1G_4 \rightarrow {}^3H_6$ within the wavelength range 483-488 nm at T=90 K (black) and 300 K (green). The luminescence spectra (dots) were measured at 90 K. The inset shows a diagram of optical transitions between sublevels of the $^1D_2$ and $^3F_4$ multiplets of the Tm^{3+} ion in Tm^{3+}:YAG in the absence of an external magnetic field and at H=10 kOe

Indeed, in accordance with the formula for the ratio of the paramagnetic term C' of the magneto-optical activity (MOA) and the diamagnetic A' term of the MOA to the dipole strength of the D transition:

$$\frac{C'}{D_1} = \frac{2\,Im\{\langle a|\hat{\mu}_z|b\rangle \cdot (\langle a|\hat{P}_x|j\rangle \cdot \langle j|\hat{P}_y|b\rangle - \langle a|\hat{P}_y|j\rangle \cdot \langle j|\hat{P}_x|b\rangle)\}}{\left[\left|\langle a|\hat{P}_x|j\rangle\right|^2 + \left|\langle j|\hat{P}_y|b\rangle\right|^2\right]}$$

$$\frac{A'}{D_2} = \frac{2\,Im\{\langle j|\hat{\mu}_z|k\rangle \cdot (\langle a|\hat{P}_x|j\rangle \cdot \langle j|\hat{P}_y|b\rangle - \langle a|\hat{P}_y|j\rangle \cdot \langle j|\hat{P}_x|b\rangle)\}}{\left[\left|\langle a|\hat{P}_x|j\rangle\right|^2 + \left|\langle k|\hat{P}_y|a\rangle\right|^2\right]}$$

(1)

where $\hat{\mu}_z$ is the z-projection operator of the ion magnetic moment (in units of μ_B); $|a\rangle$ and $|b\rangle$ are the wave functions of two closely located Stark singlets of the ion ground state; $|j\rangle, |k\rangle$ are the wave functions of two closely located Stark singlets of the excited state; $\hat{P}_{x,y}$ are the components of the ion dipole moment operator; D_1 and D_2 are the dipole "transition strengths" for the "quasi-doublet–isolated singlet" and "isolated singlet–quasi-doublet" transitions, we obtain a unique opportunity to unambiguously determine a symmetry of the Stark sublevels of the ground and excited multiplets of the non-Kramers RE ion in the garnet structure according to the selection rules in symmetry. It is easy to see that if the symmetry of the quasi-doublet states is described by the irreducible representations Γ_2 and Γ_4, then for a "diamagnetic" contribution to the MCPL to exist, it is necessary that the possible symmetry of the singlet $|a\rangle$ be described by the irreducible representation Γ_1 (or Γ_3). If this condition is met the transitions from the level $|a\rangle$ to the levels $|j\rangle$ and $|k\rangle$ will be permitted (see formula (1)). Similarly, for the existence of a "paramagnetic" contribution to the MCPL at the "quasi-doublet–singlet" transition, the singlet symmetry is to be described by irreducible representations Γ_1 (or Γ_3), in accordance with the selection rules (see (1)).

In accordance with formula (1) and the data of crystal-field calculations in Table 1, the symmetry of the Stark sublevels of the Γ_4, Γ_1 quasidoublet of the $^3F_4$ multiplet is directly dictated by the symmetry of the Γ_3 Stark sublevel of the $^1D_2$ multiplet combining in the "singlet → quasidoublet" transition.

Table 1. Theoretically calculated energies and wave functions of the Stark sublevels of the $^3H_6$, $^3F_4$ and $^1G_4$ multiplets of the Tm^{3+} ion in Tm^{3+}:YAG

№	$^{2S+1}L_J$	Energy (cm^{-1})	Major components of the Stark sublevels wavefunctions of Tm^{3+} ion ground $^3H_6$, $^3F_4$ and $^1G_4$ multiplets in the CF of D$_2$ symmetry
1		9.09	$/\Psi_1(\Gamma_2)>= -0.661(/\,^3H_6,+1> -/\,^3H_6,-1>) - 0.2379(/\,^3H_6,+5> -/\,^3H_6,-5>)$
2		17.47	$/\Psi_2(\Gamma_1)>= 0.8338/\,^3H_6,0> -0.3649(/\,^3H_6,+2> +/\,^3H_6,-2>)$
3		211.84	$/\Psi_3(\Gamma_4)>= -0.3088(/\,^3H_6,+1> +/\,^3H_6,-1>) - 0.3176(/\,^3H_6,+3> +/\,^3H_6,-3>)$ $-0.5461(/\,^3H_6,+5> +/\,^3H_6,-5>)$
4		233.24	$/\Psi_4(\Gamma_3)>= -0.4534(/\,^3H_6,+2> -/\,^3H_6,-2>) + 0.4407(/\,^3H_6,+4> -/\,^3H_6,-4>)$ $+0.3062(/\,^3H_6,+6> -/\,^3H_6,-6>)$
5		260.23	$/\Psi_5(\Gamma_1)>= -0.2555/\,^3H_6,0> -0.3676(/\,^3H_6,+2> +/\,^3H_6,-2>)$ $-0.4787(/\,^3H_6,+4> +/\,^3H_6,-4>) - 0.3104(/\,^3H_6,+6> +/\,^3H_6,-6>)$
6		265.93	$/\Psi_6(\Gamma_2)>= 0.1542(/\,^3H_6,+1> -/\,^3H_6,-1>) - 0.4671(/\,^3H_6,+3> -/\,^3H_6,-3>)$ $-0.5031(/\,^3H_6,+5> -/\,^3H_6,-5>)$
7	$^3H_6$	500.4	$/\Psi_7(\Gamma_4)>= 0.621(/\,^3H_6,+1> +/\,^3H_6,-1>) - 0.2599(/\,^3H_6,+3> +/\,^3H_6,-3>)$ $-0.2013(/\,^3H_6,+5> +/\,^3H_6,-5>)$
8		614.83	$/\Psi_8(\Gamma_3)>= -0.5257(/\,^3H_6,+2> -/\,^3H_6,-2>) + 0.448(/\,^3H_6,+4> -/\,^3H_6,-4>)$ $+0.1337(/\,^3H_6,+6> -/\,^3H_6,-6>)$
9		638.91	$/\Psi_9(\Gamma_1)>= 0.4645/\,^3H_6,0> +0.4692(/\,^3H_6,+2> +/\,^3H_6,-2>)$ $-0.3585(/\,^3H_6,+4> +/\,^3H_6,-4>) - 0.1936(/\,^3H_6,+6> +/\,^3H_6,-6>)$
10		691.13	$/\Psi_{10}(\Gamma_2)>= 0.1542(/\,^3H_6,+1> -/\,^3H_6,-1>) - 0.4671(/\,^3H_6,+3> -/\,^3H_6,-3>)$ $-0.5031(/\,^3H_6,+5> -/\,^3H_6,-5>)$
11		696.5	$/\Psi_{11}(\Gamma_4)>= 0.1106(/\,^3H_6,+1> +/\,^3H_6,-1>) - 0.5717(/\,^3H_6,+3> +/\,^3H_6,-3>)$ $-0.3945(/\,^3H_6,+5> +/\,^3H_6,-5>)$
12		772.68	$/\Psi_{12}(\Gamma_3)>= -0.1119(/\,^3H_6,+2> -\,^3H_6,-2>) - 0.3151(/\,^3H_6,+4> -/\,^3H_6,-4>)$ $+0.6186(/\,^3H_6,+6> -/\,^3H_6,-6>)$
13		784.29	$/\Psi_{13}(\Gamma_1)>= 0.1961/\,^3H_6,0> -0.355(/\,^3H_6,+4> +/\,^3H_6,-4>)$ $+0.597(/\,^3H_6,+6> +/\,^3H_6,-6>)$
14		5817.13	$/\Psi_{16}(\Gamma_1)>= 0.1402(/\,^3F_4,3> -/\,^3F_4,-3>) + 0.5330(/\,^3F_4,-1> -/\,^3F_4,1>) +$ $+0.3708(/\,^1G_4,+1> -/\,^1G_4,+1>) + 0.1975(/\,^3H_2,+1> -/\,^3H_2,-1>)$
15	$^3F_4$	5918.01	$/\Psi_{17}(\Gamma_1)>= 0.4344(/\,^3F_4,3> +/\,^3F_4,-3>) - 0.1502(/\,^3H_4,3> +/\,^3H_4,-3>) -$ $-0.1267(/\,^3H_4,1> +/\,^3H_4,-1>) + 0.3496(/\,^3F_4,1> +/\,^3F_4,-1>) + 0.2920(/\,^1G_4,-3> +$ $+/\,^1G_4,+3>) + 0.2404(/\,^1G_4,1> +/\,^1G_4,-4>)$
16		6043.83	$/\Psi_{18}(\Gamma_1)>= 0.1238(/\,^3H_4,4> +/\,^3H_4,-4>) - 0.3741(/\,^3F_4,4> +/\,^3F_4,-4>) -$ $-0.2459(/\,^3G_4,4> + +/\,^3G_4,-4>) + 0.1402(/\,^3F_4,2> +/\,^3F_4,-2>) -$ $-0.5637/\,^3F_4,0> -0.3782/\,^1G_4,0> +0.1957/H_4,0>$

№	$^{2S+1}L_J$	Energy (cm^{-1})	Major components of the Stark sublevels wavefunctions of Tm^{3+} ion ground $^3H_6$, $^3F_4$ and $^1G_4$ multiplets in the CF of D_2 symmetry
17		6116.24	$/\Psi_{19}(\Gamma_2) >= -0.1454(/\,^3F_4, +1 > -/\,^3F_4, -1 >) - 0.3596(/\,^1G_4, +3 > -/\,^1G_4, -3 >)$ $+0.1801(/\,^3H_4, +3 > -/\,^3H_4, -3 >) - 0.5504(/\,^3F_4, +3 > -\,^3F_4, -3 >)$
18		6162.15	$/\Psi_{20}(\Gamma_1) >= -0.1841/\,^3H_4, 0 > +0.5384/\,^3F_4, 0 > +0.3591/\,^1G_4, 0 >$ $+0.2914(/\,^3F_4, +2 > +/\,^3F_4, -2 >) + 0.1955(/\,^1G_4, +4 > +/\,^1G_4, -4 >)$ $-0.2989(/\,^3F_4, +4 > +/\,^3F_4, -4 >)$
19		6227.68	$/\Psi_{18}(\Gamma_4) >=> 0.4546(/\,^3F_4, 2 > -/\,^3F_4, -2 >) + 0.3414(/\,^3F_4, -4 > +/\,^3F_4, 4 >) +$ $+0.3010(/\,^1G_4, 2 > -/\,^3G_4, -2 >) + 0.1518(/\,^3H_4, -2 > -/\,^3F_4, 2 >) +$ $+0.4546(/\,^3F_4, 2 > -/\,^3F_4, -2 >) + 0.3010(/\,^1G_4, 2 > -/\,^1G_4, -2 >)$
20	$^1D_2$	27876.89	$/\Psi_{64}(\Gamma_1) >= 0.1152/\,^3P_2, 0 > +/0.455(/\,^3P_2, +2 > + \,^3P, -2 >) + 0.295(/\,^3F_2, +2 > +/\,^3F_2, -2 >)$ $+0.4382(/\,^1D_2, +2 > +/\,^1D_2, -2 >)$
21		27913.63	$/\Psi_{65}(\Gamma_3) >= 0.4437(/\,^3P_2, +2 > -/\,^3P_2, -2 >) - 0.3209(/\,^3F_2, +2 > -/\,^3F_2, -2 >)$ $+0.4459(/\,^1D_2, +2 > -/\,^1D_2, -2 >)$
22		28043.75	$/\Psi_{66}(\Gamma_2) >= 0.4624(/\,^3P_2, 1 > -/\,^3P_2, -1 >) + 0.4455(/\,^1D_2, 1 > +/\,^1D_2, -1 >) +$ $+0.2944 (/\,^3F_2, 1 > -/\,^3F_2, -1 >)$
23		28043.75	$/\Psi_{67}(\Gamma_1) >= 0.3604(/\,^3H_4, +2 > +/\,^3H_4, -2 >) + 0.4464(/\,^1G_4, -2 > +/\,^1G_4, +2 >) +$ $+ + 0.2429(/\,^3G_4, -4 > +/\,^1G_4, -4 >) + 0.1984(//\,^3H_4, -4 > +/\,^3H_4, +4 >) -$ $-0.1840(\,^3F_4, 2 > +/\,^3F_4, -2 >$
24	$^1G_4$	21191.68	$/\Psi_{56}(\Gamma_2) >= 0.3932(/\,^3H_4, -1 > -/\,^3H_4, +1 >) + 0.5208(/\,^1G_4, -1 > -/\,^1G_4, +1 >) +$ $+0.2180(/\,^3F_4, 1 > -/\,^3F_4, -1 >) + 0.1192(/\,^1G_4, +3 > -/\,^1G_4, -3 >)$
		21225.58	$/\Psi_{57}(\Gamma_3) >= 0.3969(/\,^1G_4, -4 > -/\,^1G_4, +4 >) + 0.3518(/\,^1G_4, -2 > -/\,^1G_4, +2 >) +$ $+0.3102(/\,^3H_4, -4 > -/\,^3H_4, +4 >) + 0.2713(/\,^3H_4, -2 > -/\,^3H_4, +2 >) +$ $+0.1626(/\,^3F_4, +4 > -/\,^3F_4, -4 >) + 0.1458(/\,^3F_4, +2 > -/\,^3F_4, -2 >)$

The peculiarity of the MCPL degree spectrum on line 4 in Fig. 2 is caused by the permitted (in symmetry) optical transitions occurring from the $B_2(\Gamma_3)$ sublevel of the $^1D_2$ multiplet to the nearby $Y_4(\Gamma_4)$ and $Y_3(\Gamma_2)$ Stark sublevels of the $^3F_4$ multiplet. The C-term of the MCPL degree on line 4 is due to the transition from the singlet sublevel to the quasi-doublet state. A similar analysis of the MCPL degree spectrum in Fig. 4 showed that on the luminescence line 14 in a magnetic field there is a magneto-optical transition caused by the transition between the sublevel Γ_1 (20815 cm^{-1}) of the $^1G_4$ multiplet to the nearby Stark sublevels Γ_3 (225 cm^{-1}), Γ_4 (215 cm^{-1}).

The inclined linear dependence within the luminescence line (with a change in the sign of the effect in its center) indicates the manifestation of the A - term of the MCPL degree on the line 14. In the approximation of the Gaussian contour of the luminescence band, the expression for the MCPL degree P of a non-Kramers ion:

$$P = \frac{1}{2}\mu_B H \left[\frac{(\nu - \nu_0)}{\Gamma^2} \cdot \left\{ \frac{A'}{D_2} + \frac{C'}{D_1} \right\} + \frac{1}{kT} \cdot \frac{C'}{D_1} \right] \tag{2}$$

is an inclined linear dependence shifted relative to zero, the center of the radiation line, by a value of the temperature-dependent "addition" (proportional to the amplitude of the C'- term of the MCPL degree). The first and second terms in (2) determine the contributions of the "diamagnetic" (A'-term) and temperature-dependent "paramagnetic" (C'- term) mechanisms of the MCPL of a non-Kramers RE ion, respectively; ν is the wave number (in cm^{-1}).

Considering that the magnetic moments μ_g of the corresponding quasidoublets combining in radiative transitions are determined by the values of the ratios C'/D_1 and A'/D_2 (in units μ_B), then from the experimental data (Fig. 2, Fig. 3, Fig. 4), it is easy to find the "effective" Zeeman splittings $\Delta E_{zeem}^{ef} = \mu_g H$ of the quasidoublet states combining in magneto-optically active radiative transitions. In this case, the "effective" Zeeman splittings of the corresponding quasi-doublet states $\Delta E_{zeem}^{ef} = \frac{A'}{D_2}\mu_B H$ in the $^3F_4$ multiplet can be easily found from the doubled products of the slopes of the MCPL degree spectra $\Delta P / \Delta \nu$ on the lines 4 and 12 and the squares of their half-widths Γ^2 (Fig. 1). The Zeeman splittings responsible for the emergence of the A'- terms of the MCPL degree turn out to be relatively small and equal to $\Delta E_{zeem}^{ef} = 0.16$ cm^{-1} and $\Delta E_{zeem}^{ef} = 1.01$ cm^{-1} for the emission lines 4 and 12, respectively, and $\Delta E_{zeem}^{ef} = 0.23$ cm^{-1} for the line 14 for the quasi-doublet states of the $^3H_6$ multiplet in the outer field $H = 9.5$ kOe. In this case, the value of the "effective" splitting $\Delta E_{zeem}^{ef} = \frac{C'}{D_1}\mu_B H$ of the quasi-doublet state of the $^1D_2$ multiplet for the radiative transitions "quasi-doublet–isolated singlet" on the emission line 7 can be determined similarly to how this was done above for the lines 4 and 2 . From what was found in this way (for the line 7, it is equal to $\Delta E_{zeem}^{ef} = 0.6$ cm^{-1}), it follows that the features of the MCPL degree spectra on them are apparently associated with radiative transitions occurring from the same quasi-doublet state located in the lower part of the $^1D_2$ multiplet. However, the asymmetry of

the MCPL degree spectrum observed on these lines cannot be explained only by a contribution of the MCPL C'-term caused by the above-found value of the "effective" Zeeman splitting of the quasidoublet in the $^1D_2$ multiplet (see also formula (1)) because of the smallness of the splitting itself. Therefore, the features in the behavior of the spectral dependence of magnetically polarized luminescence on the emission lines 4 and 8 are formed mainly by a mechanism of Van Vleck "mixing" of this quasi-doublet state with the states of nearby Stark singlets in the $^1D_2$ multiplet.

CONCLUSIONS

Based on the analysis of the spectral dependences of magneto-optical (MCPL) and optical (luminescence) effects in a single crystal of thulium-yttrium garnet-aluminate Tm^{3+}:YAG, it has been established that there are "quasi-degenerate" states of excited multiplets $^1D_2$, $^3F_4$,$^3G_4$ and the ground multiplet $^3H_6$ of the RE ion Tm^{3+} in the garnet-aluminate YAG in the luminescence band $^1G_4{\rightarrow}^3H_6$, $^1D_2{\rightarrow}^3F_4$ and $^1D_2{\rightarrow}^3F_3$.

Analysis of optical and magneto-optical studies show that the quantum-mechanical "mixing" plays a significant role in the mechanism of occurrence of magneto-optical effects on luminescence bands caused by "forbidden" 4f→4f transitions in the non-Kramers Tm^{3+} ion that has a "quasi-doublet" structure in the energy spectra. The results of symmetry identification of the found 4f→4f transitions are confirmed by the data of the magneto-optical studies.

ORCID

⊙**Furkat K. Turotov**, https://orcid.org/0000-0001-9008-4815; ⊙**Mariya E. Malysheva**, https://orcid.org/0000-0002-4626-7398
⊙**Ramil R. Vildanov**, https://orcid.org/0000-0001-5334-9909

REFERENCES

[1] J-X. Zhang, G. Wang, Y-F. Li, Y. Yu, Y. Wang, and Z. Lv, "Research status of rare-earth-ion-doped infrared laser," Front. Phys. **12**, 1388567 (2024). https://doi.org/10.3389/fphy.2024.1388567

[2] Ch. Zhang, Ch. Yun, Ch. Zhang, X. Zhang, and Sh. Lai, "Broadband 2.9 μm mid-infrared fluorescence behavior of Dy^{3+}/Tm^{3+} co-doped zirconium fluoride glasses," Infrared Phys. Technol. **126**, 104330 (2022). https://doi.org/10.1016/j.infrared.2022.104330

[3] G. Liu, Z. Bai, F. Yuan, Y. Huang, L. Zhang, and Z. Lin, Growth and spectroscopic characterization of Tm^{3+}:Ca$_{10}$Li(VO$_4$)$_7$ crystal-a potential crystalline medium for 2 μm lasers," J. Cryst. Growth. **520**, 62-67 (2019). https://doi.org/10.1016/j.jcrysgro.2019.05.025

[4] A.K. Zvezdin, V.M. Matveev, A.A. Mukhin, and A.I. Popov, *Rare-earth ions in magnetically ordered crystals,* (Mir, Moscow, 1985) 294 p. (in Russian)

[5] J. Kratochvíl, P. Boháček, J. Šulc, M. Němec, H. Jelínková, M. Fibrich, B. Trunda, *et al*., "Tm:GGAG disordered garnet crystal for 2 μm diode-pumped solid-state laser," Laser Phys. Lett. **18**(11), 115802 (2021). https://iopscience.iop.org/article/10.1088/1612-202X/ac2519

[6] Z. Pan, Y. Wang, Y. Zhao, H. Yuan, X. Dai, H. Cai, J. Bae, *et al*., "Generation of 84-fs pulses from a mode-locked Tm:CNNGG disordered garnet crystal laser," Photon. Res. **6**, 800-804 (2018). https://doi.org/10.1364/PRJ.6.000800

[7] L. Sun, Q. Xu, J. Lu, Sh. Su, Y. Zou, R. Liu, Z. Lei, *et al*., "Preparation and spectroscopic characteristics of Tm:YPO$_4$ crystal," J. Lumin. **257,** 119763 (2023). https://doi.org/10.1016/j.jlumin.2023.119763

[8] P. Li, F. Zhang, K. Li, Ch. Cao, Y. Li, J. Zhang, B. Yan, *et al*., "Research progress of high-frequency and high-energy solid-state lasers at 1.6 μm," Infrared and Laser Eng. **52**(8), 20230403 (2023). https://www.researching.cn/articles/OJ51f7d0919c541a12

[9] J.M. Cano-Torres, M. Rico, X. Han, M.D. Serrano, C. Cascales, C. Zaldo, V. Petrov, *et al*., "Comparative study of crystallographic, spectroscopic, and laser properties of Tm^{3+} in NaT(WO$_4$)$_2$ (T=La, Gd, Y, and Lu) disordered single crystals," Phys. Rev. B, **84**, 174207 (2011). https://doi.org/10.1103/PhysRevB.84.174207

[10] R.M. El-Agmy, W. Luthy, T. Graf, and H.I. Weber, "Excitation of Tm+3 at a wavelength of 1064 nm," Appl. Phys. B, **76**, 23-26 (2003). https://doi.org/10.1007/s00340-002-1066-6

[11] U.V. Valiev, J.B. Gruber, D. Fu, V.O. Pelenovich, G.W. Burdick, and M.E. Malysheva, "Specific features of Eu^{3+} and Tb^{3+} magnetooptics in gadolinium - gallium garnet (Gd$_3$Ga$_5$O$_{12}$)," J. Rare Earths. **29**(8), 776-782 (2011). https://doi.org/10.1016/S1002-0721(10)60541-8

[12] R.R. Rakhimov, U.V. Valiev, G.W. Burdick, R.R. Vildanov, and D. Fu, "Investigation of j – j "mixing" mechanism influence on the optical and magnetooptical properties of praseodymium yttrium-aluminum garnet PrYAG," Jour. of Lumin. **207**, 339-345 (2019). https://doi.org/10.1016/j.jlumin.2018.10.099

[13] C. Görller-Walrand, and L. Fluyt, *Handbook on the Physics and Chemistry of Rare-Earths* (North-Holland, Amsterdam, 2010). 40(244), p.107.

[14] U.V. Valiev, Sh.A. Rakhimov, N.I. Juraeva, RA. Rupp, L. Zhao, Zh. Wang, Zh. Zhai, *et al*., "Optical and magnetooptical properties of Ho^{3+}:YGG," Phys. Stat. Sol. B, **247**(1), 163-169 (2010). https://doi.org/10.1002/pssb.200945318

[15] U.V. Valiev, D.N. Karimov, M.G. Brik, C.G. Ma, R.R. Vildanov, F.K. Turotov, and V.O. Pelenovich, "Zeeman splitting features of electronic states of rare earth ions in TbF$_3$ crystal," Opt. Mater. **117**(7), 111141 (2021). https://doi.org/10.1016/j.optmat.2021.111141

[16] T.Sh. Alimov, U.V. Valiev, M.E. Malysheva, T.N. Khasanov, and V.O. Pelenovich, "The features of Pr^{3+} rare-earth ion magneto-optics in the disordered crystalline surroundings," Opt. Mater. **104**, 109848 (2020). https://doi.org/10.1016/j.optmat.2020.109848

[17] J.B. Gruber, M.E. Hills, R.M. Macfarlane, G.A. Turner, C.A. Morrison, G.A. Quarles, G. Kintz, and L. Esterowitz, "Spectra and energy levels of Tm^{3+}:Y$_3$Al$_5$O$_{12}$," Phys. Rev. B, **40**(14), 9464 (1989). https://doi.org/10.1103/PhysRevB.40.9464

[18] J.P. Riehl, and F.S. Richardson, "General theory of circularly polarized emission and magnetic circularly polarized emission from molecular systems," J. Chem. Phys. **65**, 1011–1021 (1976). https://doi.org/10.1063/1.433177

[19] D. Vojna, O. Slezak, A. Lucianetti, and T. Mocek, "Verdet Constant of Magneto-Active Materials Developed for High-Power Faraday Devices," Appl. Sci. **9**, 3160 (2019). https://doi.org/10.3390/app9153160

МАГНІТООПТИЧНІ ОСОБЛИВОСТІ РАДІАЦІЙНИХ ПЕРЕХОДІВ НЕКРАМЕРСЬКОГО ІОНУ Tm³⁺ В КРИСТАЛАХ ІТРІЄВО-АЛЮМІНІЄВОГО ГРАНАТУ

Фуркат К. Туротов, Марія Є. Малишева, Раміль Р. Вільданов

Національний університет Узбекистану імені Мірзо Улугбека, Ташкент, 100174, Узбекистан

Досліджено спектри люмінесценції та магнітної кругової поляризації монокристалу тулій-ітрієвого гранат-алюмінату Tm^{3+}:YAG у видимій області спектру за температури 90 та 300 K у магнітному полі 10 кЕ. На основі аналізу оптичних та магнітооптичних даних встановлено наявність «квазівироджених» станів збуджених мультиплетів $^1D_2$, $^3F_4$, $^3G_4$ та основного мультиплета $^3H_6$ іона Tm^{3+} RE в гранат-алюмінатному YAG на випромінювальних переходах $^1G_4 \rightarrow ^3H_6$, $^1D_2 \rightarrow ^3F_4$ та $^1D_2 \rightarrow ^3F_3$. Ефект квантово-механічного "перемішування" відіграє значну роль у виникненні магнітооптичних ефектів на смугах люмінесценції, зумовлених "забороненими" переходами $4f \rightarrow 4f$ в некрамерсовському іоні Tm^{3+}, що має "квазідублетну" структуру енергії спектри.

Ключові слова: *тулій-ітрієвий гранат; рідкоземельні іони; магнітооптичні властивості; люмінесценція; рівні енергії; магнітна кругова поляризація*

UNVEILING THE POTENTIAL OF DOUBLE PEROVSKITE HALIDES Rb$_2$CuSbH$_6$ (H = Cl, Br, I) FOR FLEXIBLE ELECTRONICS: AN INTEGRATED STUDY OF STRUCTURAL, MECHANICAL, ELECTRICAL AND OPTICAL PROPERTIES

Krishna Kumar Mishra^a*, Sonia Chahar^a, Rajnish Sharma^b

^{a}*Chitkara University Institute of Engineering and Technology, Chitkara University, Rajpura, Punjab-140401, India*
^{b}*School of Engineering and Technology, Chitkara University, Solan, Himachal Pradesh-174103, India*
*Corresponding Author e-mail: krishna.mishra@chitkara.edu.in
Received July 10, 2024; revised October 4, 2024; accepted October 29, 2024

The structural, mechanical, electrical and optical properties of double perovskite halides like Rb$_2$CuSbH$_6$ (where H = Cl, Br, and I) for flexible electronic devices are fascinating and complex. Extensive literature survey clearly establishes that there has been limited research on analyzing the potential uses of these materials for the highly sought-after sector of flexible electronic devices. In this paper, focused studies have been carried out on investigating the characteristics of these materials using QuantumATK NanoLab Software Tool. All double perovskite halides Rb$_2$CuSbH$_6$ (H = Cl, Br, I) show positive values for the elastic constants C$_{11}$, C$_{12}$, and C$_{44}$, and obey the stability trend C$_{11}$>C$_{12}$>C$_{44}$. Mechanical stability was established using Born-Huang criteria. Optimized values of Young's modulus, bulk modulus, shear modulus and Poisson ratios established that materials are stable and ductile in nature. While carrying out analysis of electronic properties, all three materials Rb$_2$CuSbCl$_6$, Rb$_2$CuSbBr$_6$, and Rb$_2$CuSbI$_6$ were found to be possessing indirect energy bandgap of 0.924 eV, 0.560 eV, and 0.157 eV, respectively. Moreover, the Complex Bandstructure (CB) naturality indicates that most evanescent wave may exist when layer separation is lowest in Rb$_2$CuSbCl$_6$ (6.0 Å), Rb$_2$CuSbBr$_6$ (6.33 Å), and highest in Rb$_2$CuSbI$_6$ (6.8 Å). Absorption bands for Rb$_2$CuSbCl$_6$, Rb$_2$CuSbBr$_6$ and Rb$_2$CuSbI$_6$ lie in the visible range with 344 nm to 574 nm, 348 nm to 688 nm and 369 nm to 608 nm respectively. The reflectivity (r) reported under this study is 0.105, 0.139 and 0.185 respectively for Rb$_2$CuSbCl$_6$, Rb$_2$CuSbBr$_6$ and Rb$_2$CuSbI$_6$. Overall, all the obtained results implicate toward need to explore the Rb$_2$CuSbH$_6$ materials in more depth for variety of electronic device applications.
Keywords: *Perovskite; QuantumATK; DFT; Optical Properties; Electronic structure; Mechanical properties*
PACS: 71.20.−b, 77.22.−d, 78.20.Ci

1. INTRODUCTION

Flexible electronic devices market is expected to grow at a Compound Annual Growth Rate (CAGR) of more than 15 % by year 2027 [1]. Advances in materials research, production, and design are continually changing flexible electronic device development. With its maturity, the technology is projected to alter healthcare and consumer electronics, enabling new smart, integrated, and highly flexible gadgets. Wearable technology, such as fitness trackers and smartwatches, has become increasingly popular, contributing significantly to the growth of the flexible electronics sector [2].

The materials used for flexible electronic devices are crucial for their functionality, durability, and flexibility [3,4]. A combination of variety of materials ultimately helps in creating a good flexible electronic device. Materials like Polyimide (PI), Polyethylene Terephthalate (PET), Polyethylene Naphthalate (PEN) are typically being used for flexible substrates. Indium Tin Oxide (ITO), Silver Nanowires, Graphene and Carbon nanotubes are used as conductive materials in the process of overall fabrication of the device. Many other materials like a-Si, indium gallium zinc oxide (IGZO), Barium Strontium Titanate (BST), polymethyl methacrylate etc. are used as conducting or dielectric materials [5]. Teflon and other specialized polymers have been used to protect devices from moisture and other environmental factors. Among all these materials, perovskites have been making their place owing to their ease of fabrication and display of high efficiency especially for solar cell devices [6-8]. The halide-based double perovskites have been explored in a number of different fields of application, including topological insulating materials [9], solar energy systems [10-14], and as superconductors [15]. Various studies have shown that Pb-halide perovskites can display an efficiency of more than 20% [16]. Efforts are being made to bring this conversion efficiency in the range of 45-50% [17].

Methylammonium lead iodide (CH$_3$NH$_3$PbI$_3$) has been investigated as a possible material for use in solar cell technology [18]. However, the material exhibited poor thermodynamic strength, showing a tendency to decompose into various phases, ultimately rendering it highly unstable [19, 20]. Perovskites have been successfully improved by using an ion exchange technique coupled with an ion exchange matrix to enhance their crystal structure in some cases [21, 22].

The double lead (Pb) halide perovskites have superior performance and technical superiority, as well as being highly efficient and cost-effective [23]. However, there remains a significant concern in the context of its instability and toxicity [24]. Pb-based perovskites are restricted from being used in photovoltaics because of this particular property. To overcome these difficulties, researchers are working on developing a perovskite-like material that does not contain lead but must have more manufacturing efficiency [25] and be capable of mixing cations [26], so as to achieve the capabilities of creating a perovskite. A good example of this is the use of organic halides in perovskites. It may be possible to reduce lead while maintaining bandgap by using DFT based computational method [27].

In recent years, researchers have developed and characterized Cs-based double halides with exceptional light-absorbing properties [28, 29]. Despite this, Cs-based materials continue to be the subject of discussion and investigation because Cs is a scarce metal that presents a financial disadvantage in large-scale commercial production. The halides Rb_2ScAgX_6 and Rb_2ScCuX_6 (X = Cl, Br, I) have been studied extensively in the past one decade. A major reason for their potential use in thermoelectric and solar cell applications consists of their cost-effectiveness [30, 31]. The use of low-cost materials to customize Sc and Ag can have a significant impact on material science and the production of solar cells.

The Rb_2CuSbH_6 series offers an opportunity for the development of customized designs and improvements in functionality due to its adaptable composition that allows for the incorporation of different halogen substitutions such as Cl, Br, and I. It is likely that the inclusion of Cl, Br, and I substitutions in Rb_2CuSbH_6 will enhance application ranges and improve performance in several technical domains by taking into account small differences in its structure.

In this study, we investigate and understand the various characteristics of these halide perovskites. It describes their fundamental behaviours and identifies their possible applications for solar cells, optoelectronic devices and other flexible electronic devices.
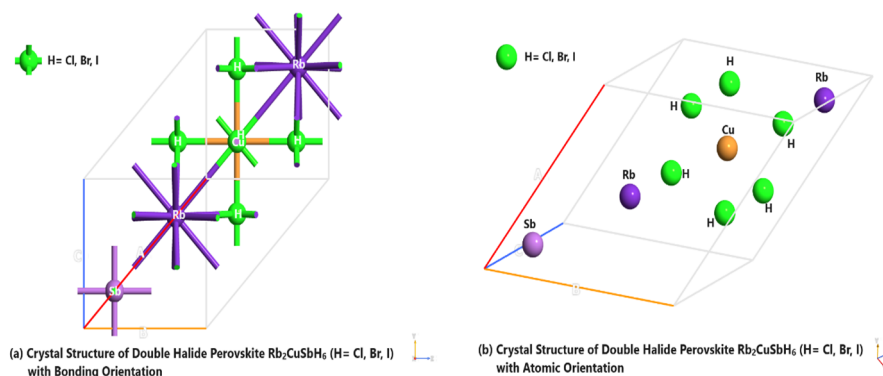
2. COMPUTATIONS AND METHODOLOGY

In this study, the structural and electronic properties of double perovskite halides, Rb_2CuSbH_6 (H = Cl, Br, I), were systematically studied employing density functional theory (DFT) simulations. The computational work was carried out utilizing the QuantumATK software, employing its latest version (V-2023.09 SP1) [32]. The crystallographic data for Rb_2CuSbH_6, which crystallizes in the orthorhombic space group (Fm-3m), was sourced from the database of Materials Project. The DFT calculations employed the Generalized Gradient Approximation (GGA) method, utilizing the Perdew-Burke-Ernzerhof (PBE) functional for exchange-correlation interactions [33-34]. The linear combination of atomic orbitals (LCAO) approach was applied to represent the wave functions, with the numerical accuracy parameters adjusted to ensure precise results. Specifically, the density mesh cutoff was fixed at 105 Hartree, and the k-point grid was sampled using a (4×4×4) Monkhorst-Pack mesh. Fermi-Dirac smearing was used with a broadening of 1000 K and a convergence tolerance of 0.0001. The structural optimization and passivation processes were conducted in an iterative manner to ensure the stability and reliability of the crystal structures. For the pseudopotentials [35], PseudoDojo projector-augmented wave (PAW) potentials were utilized, assigning suitable potentials for each constituent element: Rubidium (Z=9), Copper (Z=19), Antimony (Z=23), Chlorine (Z=7), Bromine (Z=7), and Iodine (Z=7). To accurately solve the electronic structure and determine the energy levels, the diagonalization solver was employed to address the eigenvalue problems, ensuring precise electronic property calculations.

3. RESULTS AND DISCUSSION
A. STRUCTURAL AND MECHANICAL PROPERTIES

The computational analysis in this study was conducted using the QuantumATK software, version V-2023.09 SP1 [32]. To model the exchange-correlation interactions, the Generalized Gradient Approximation (GGA) was applied, specifically utilizing the Perdew-Burke-Ernzerhof (PBE) functional. The Linear Combination of Atomic Orbitals (LCAO) method was employed for calculating electronic properties. For enhanced precision, a density mesh cutoff of 105 Hartree was used, and the k-point grid was sampled with a (4×4×4) Monkhorst-Pack mesh. Fermi-Dirac statistics were applied with a broadening of 1000 K and a convergence tolerance of 0.0001. Pseudopotentials from the PseudoDojo library were employed for the respective elements in the crystal structure, including Rubidium (Z=9), Copper (Z=19), Antimony (Z=23), Chlorine (Z=7), Bromine (Z=7), and Iodine (Z=7). The structural bonding and atomic arrangements of the double perovskite halide Rb_2CuSbH_6 (where H = Cl, Br, I) are illustrated in Figures 1(a) and 1(b) as part of Figure 1, providing a detailed depiction of the material's crystal structure.

(a) Crystal Structure of Double Halide Perovskite Rb_2CuSbH_6 (H= Cl, Br, I) with Bonding Orientation

(b) Crystal Structure of Double Halide Perovskite Rb_2CuSbH_6 (H= Cl, Br, I) with Atomic Orientation

Figure 1. Crystal Structure of double halide Rb_2CuSbH_6 (H= Cl, Br, I)

There are twelve equivalent RbH_{12} cuboctahedra, six equivalent RbH_{12} cuboctahedra, four equivalent CuH_6 octahedra, and four equivalent SbH_6 octahedra formed when Rb^{1+} bonds to 12 H^{1-} atoms. The Rb–H bond lengths for $Rb_2CuSbCl_6$, $Rb_2CuSbBr_6$ and Rb_2CuSbI_6 are respectively 3.68 Å, 3.88 Å, and 4.17 Å. For $Rb_2CuSbCl_6$, $Rb_2CuSbBr_6$

and Rb$_2$CuSbI$_6$, the lengths of the Cu–H bonds for each of these compounds are 2.52 Å, 2.65 Å, and 2.85 Å respectively. All Sb–H bond lengths are 2.68 Å, 3.86 Å and 4.17 Å for Rb$_2$CuSbCl$_6$, Rb$_2$CuSbBr$_6$ and Rb$_2$CuSbI$_6$ respectively. Rb$_2$CuSbCl$_6$, Rb$_2$CuSbBr$_6$ and Rb$_2$CuSbI$_6$ have Cl-Cl, Br-Br and I-I bond lengths of 3.57 Å, 3.75 Å, and 4.03 Å respectively. Four Rb^{1+} atoms, one Cu^{1+} atom, and one Sb^{3+} atoms are bonded to H^{1-} in a distorted linear geometry.

The equilibrium lattice contacts (a_0) and elastic constants (C_{ij}) for double perovskite halides Rb$_2$CuSbH$_6$ (H = Cl, Br, I) are shown in Table 1. According to results, the lattice constant, unit cell volume and density increase from Rb$_2$CuSbCl$_6$ to Rb$_2$CuSbBr$_6$ to Rb$_2$CuSbI$_6$. The reported values of lattice constant are 10.41 Å, 10.97 Å and 11.79 Å for Rb$_2$CuSbCl$_6$, Rb$_2$CuSbBr$_6$ and Rb$_2$CuSbI$_6$ respectively. Our results are consistent with other studies [36, 37] as mentioned in table 1. It is evident that this increasing variation in lattice constant (a_0), volume and density of unit cell are consistent with the change as the ion radius increases. There is a benefit to using alkali atoms, which are lighter, as they can minimize the density of the material, which is used as a perovskite, which can reduce the weight of a device. The reliability of our geometry optimization was confirmed through a thorough comparison with previous published results [36, 37].

Table 1. Computed equilibrium lattice (a_0) and elastic (C_{ij}) constants for Rb$_2$CuSbH$_6$ (H= Cl, Br, I)

Materials		a_0(Å)	Unit Cell Volume (Å^3)	Density (g/cm^3)	Space Group	C$_{11}$ (GPa)	C$_{12}$ (GPa)	C$_{44}$ (GPa)
Rb$_2$CuSbCl$_6$	**Present Study**	10.41	282.4	3.346		44.69	23.95	12.20
	Other Study (Exp. & Theo.)	10.23 [36] 10.19 [37]	-		3.57 [37]	52.26 [36]	27.90 [36]	12.34 [36]
Rb$_2$CuSbBr$_6$	**Present Study**	10.97	330.5	4.199		33.98	28.26	9.73
	Other Study (Exp. & Theo.)	11.00 [36]	-	-		-	-	-
Rb$_2$CuSbI$_6$	**Present Study**	11.79	409.6	4.531		8.98	30.33	7.23
	Other Study (Exp. & Theo.)	11.81 [36]	-	-		-	-	-

The elastic properties of the cubic crystal structures are determined by three independent elastic constants shown in Table 01. All double perovskite halides Rb$_2$CuSbH$_6$ (H = Cl, Br, I) show positive values for the elastic constants C$_{11}$, C$_{12}$, and C$_{44}$, and obey the stability trend C$_{11}$>C$_{12}$>C$_{44}$. Born-Huang stability criterion was used to assess mechanical stability of these materials [38, 39]: (a) C$_{11}$>0 (b) C$_{11}$-C$_{12}$>0 (c) C$_{11}$+2C$_{12}$>0 (d) C$_{44}$>0. Mechanical stability criteria are met by these materials, making them stable. The computed positive value of Cauchy's pressures C$_{12}$-C$_{44}$ concludes that all double perovskite halides (DPHs) Rb$_2$CuSbH$_6$ (H = Cl, Br, I) are ionic in nature. Below table 2 showcased the material properties from the elastic constants (GPa) for Rb$_2$CuSbH$_6$ (H= Cl, Br, I).

Table 2. Computed material properties from the elastic constants (GPa) for Rb$_2$CuSbH$_6$ (H= Cl, Br, I)

| Materials		Bulk modulus (GPa)	Shear modulus (GPa)	Young's modulus (GPa)	Poisson ratios
Rb$_2$CuSbCl$_6$	**Present Study**	30.86	11.39	27.97	0.34
	Other Study (Exp. & Theo.)	37.38 [36] 36.02 [37]	12.28 [37]		0.347 [37]
Rb$_2$CuSbBr$_6$	**Present Study**	30.17	4.96	8.32	0.45
	Other Study (Exp. & Theo.)	27.60 [36]			
Rb$_2$CuSbI$_6$	**Present Study**	23.21	21.99	37.82	0.77
	Other Study (Exp. & Theo.)	21.28 [36]			

B. ELECTRONIC PROPERTIES

Solar cells and light-emitting diodes are both efficient due to the influence of band structure on carrier transitions and movement, optical absorption coefficients, as well as electrical conductivity. In order to design optoelectronic devices, it's important to understand the band structure thoroughly. Energy Bandstructure of DPHs Rb$_2$CuSbH$_6$ (H= Cl, Br, I) are depicted in Figure 2(a)-(c) for Rb$_2$CuSbCl$_6$, Rb$_2$CuSbBr$_6$ and Rb$_2$CuSbI$_6$ respectively.

Interestingly, all three double perovskite halides have indirect bandgaps. For all compounds, the valence and conduction bands are at X and L symmetry. The indirect band gaps of Rb$_2$CuSbCl$_6$, Rb$_2$CuSbBr$_6$, and Rb$_2$CuSbI$_6$ are 0.924 eV, 0.560 eV, and 0.157 eV, respectively. Effective curvature represents the effective mass (m*) of carriers in these bands. Effective charge carriers in the valence band with a flat or dense state have a high effective mass, but with a high curvature in the conduction band states, electrons have a smaller effective mass, which makes optoelectronic devices more efficient. All the three double perovskite halides Rb$_2$CuSbH$_6$ (H= Cl, Br, I) are having a narrow band-gap semiconducting property. The study results revealed that the double perovskite halides Rb$_2$CuSbH$_6$ (H = Cl, Br, I) can be combined with wide-gap materials to improve the record of conversion efficiency in tandem solar cells.

The Complex Bandstructure (CB) consists of propagating and decaying modes, characterized by k_c. We analyzed a 2D CB to assess the materials for optical device and other photovoltaic applications [40-42]. Figure 3 illustrates the Complex Bandstructure of the double halides (a) Rb$_2$CuSbCl$_6$, (b) Rb$_2$CuSbBr$_6$, and (c) Rb$_2$CuSbI$_6$.

The variable k_c can be complex on surfaces in the c-direction. Real kc values represent traditional Bloch states (right diagram), while complex k_c values indicate surface states. The left graph shows the imaginary part, representing decay magnitude, with color codes indicating the real component of k_c.
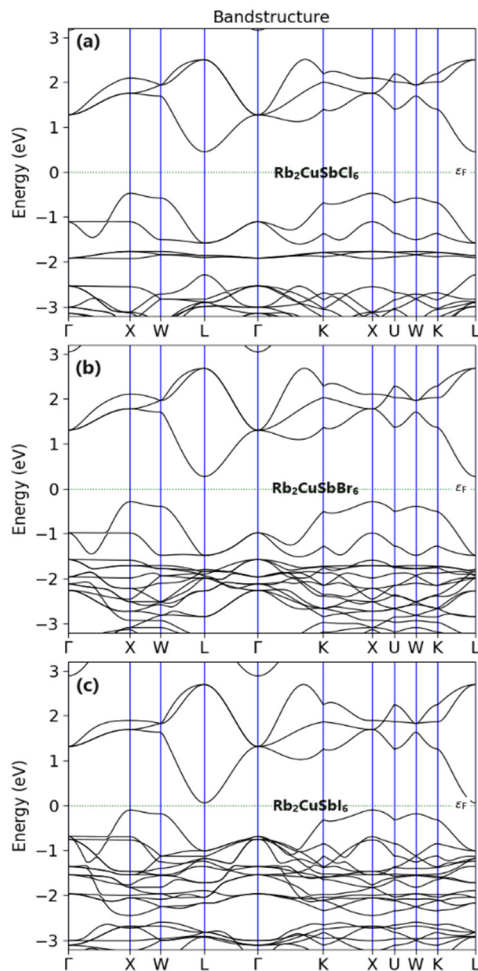

Figure 2. Energy Band structure of double perovskite halides Rb_2CuSbH_6 (H= Cl, Br, I) (a) $Rb_2CuSbCl_6$ (Eg=0.924 eV); (b)$Rb_2CuSbBr_6$ (Eg=0.560 eV); (c) Rb_2CuSbI_6 (Eg= 0.157 eV)
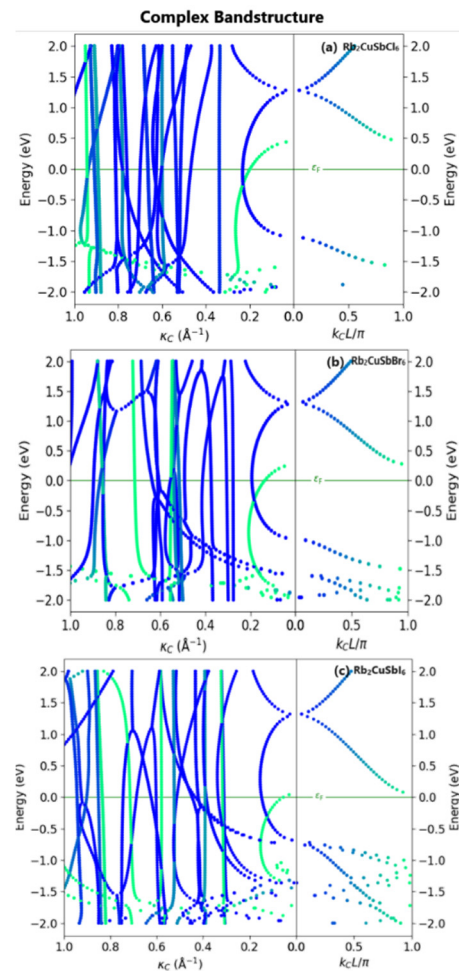
Figure 3. Complex Bandstructure of double perovskite halides Rb_2CuSbH_6 (a) $Rb_2CuSbCl_6$; (b) $Rb_2CuSbBr_6$; (c) Rb_2CuSbI_6

The analysis of the Complex Bandstructure (CB) reveals that only a few decaying modes are present in the right section, indicating the existence of evanescent waves on the material's surface. Our study indicates that double perovskite halides Rb_2CuSbH_6 materials are extremely appropriate for optoelectronic device fabrications. The nature of the CB shows that evanescent waves are favored due to the minimal layer separation, which is lowest in $Rb_2CuSbCl_6$ (6.01 Å), followed by $Rb_2CuSbBr_6$ (6.33 Å), and highest in Rb_2CuSbI_6 (6.8 Å). Thus, double perovskite halides Rb_2CuSbH_6 (H = Cl, Br, I) are promising candidates for optoelectronic and thermoelectric devices.
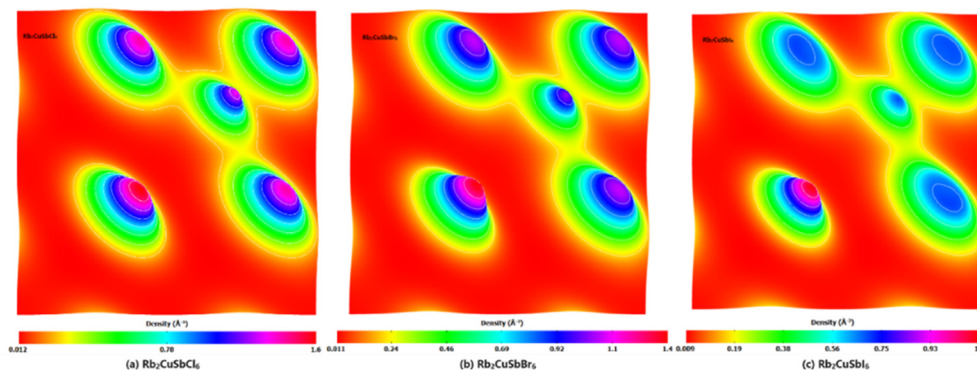
Figure 4. Electron density of double halide Rb_2CuSbH_6 (a) $Rb_2CuSbCl_6$; (b) $Rb_2CuSbBr_6$; (c) Rb_2CuSbI_6

We further investigated the electron density of these compounds to augment the results on the energy band and complex band. The electron density of double halide Rb$_2$CuSbCl$_6$, Rb$_2$CuSbBr$_6$ and Rb$_2$CuSbI$_6$ respectively are plotted in Figure 4 (a)-(c). As shown in Figure 4(a)-(c), electron density plots provide an insightful depiction of bonding nature. Rb$_2$CuSbCl$_6$ exhibits covalent bonding between Cu, Cl, and Sb atoms, while Rb atoms exhibit ionic characteristics. Simultaneously, the same covalent character is observed in Rb$_2$CuSbBr$_6$ and Rb$_2$CuSbI$_6$.

Further, Rb$_2$CuSbCl$_6$ has highest electron density 1.6 Å^{-3} and Rb$_2$CuSbI$_6$ has the lowest 1.1 Å^{-3}. The major contribution is due to halides radii. The electron density reported decreasing with increase of atomic radii of the halides. Based on Figure 5(a)-(c) and Figure 6(a)-(c), an analysis of each element's contributions to valence and conduction bands can be done in more detail. The band structure near Fermi level is used to determine VBM and CBM contributions. Alkali metal Rb plays a small role in VBM and CBM; its primary role is to stabilize the perovskite structure by serving as a charge donor.
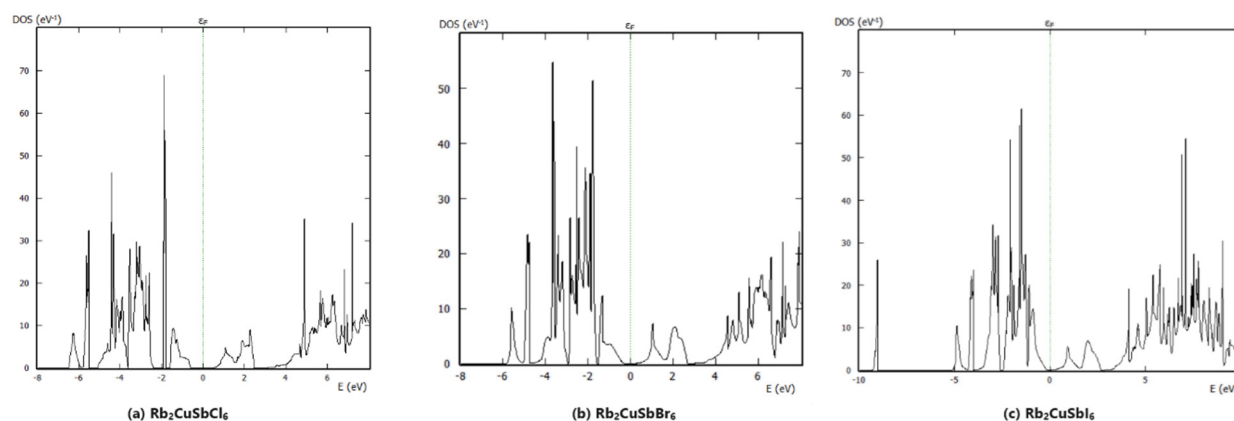
Figure 5. Density of States of double halide Rb$_2$CuSbH$_6$ (a) Rb$_2$CuSbCl$_6$; (b) Rb$_2$CuSbBr$_6$; (c) Rb$_2$CuSbI$_6$
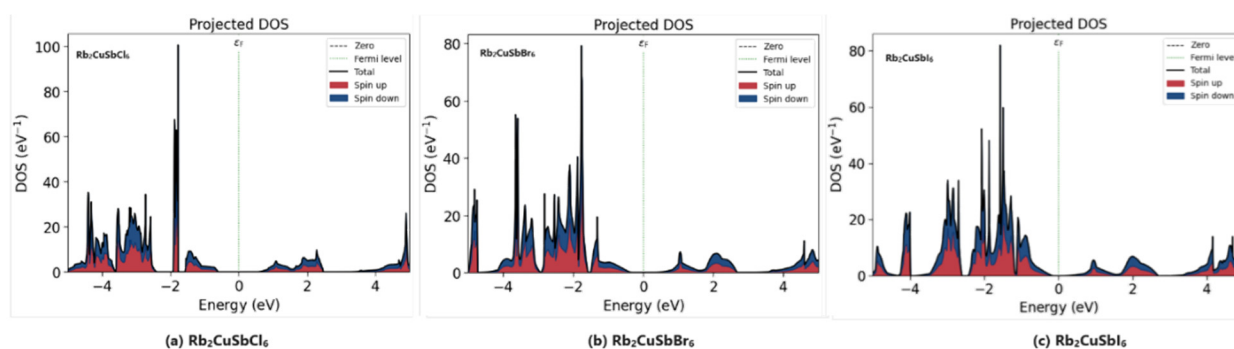
Figure 6. Projected Density of States of double halide Rb$_2$CuSbH$_6$ (a) Rb$_2$CuSbCl$_6$; (b) Rb$_2$CuSbBr$_6$; (c) Rb$_2$CuSbI$_6$

A main contribution to the VBM is the H-p orbital, and a major contribution to the CBM is the Sb-p orbital, with partial contributions from Cu-s and H-p orbitals. VBM and CBM electronic transition is primarily dominated by p and d orbitals which is evident from Figure 5(a)-(c) and 6(a)-(c).
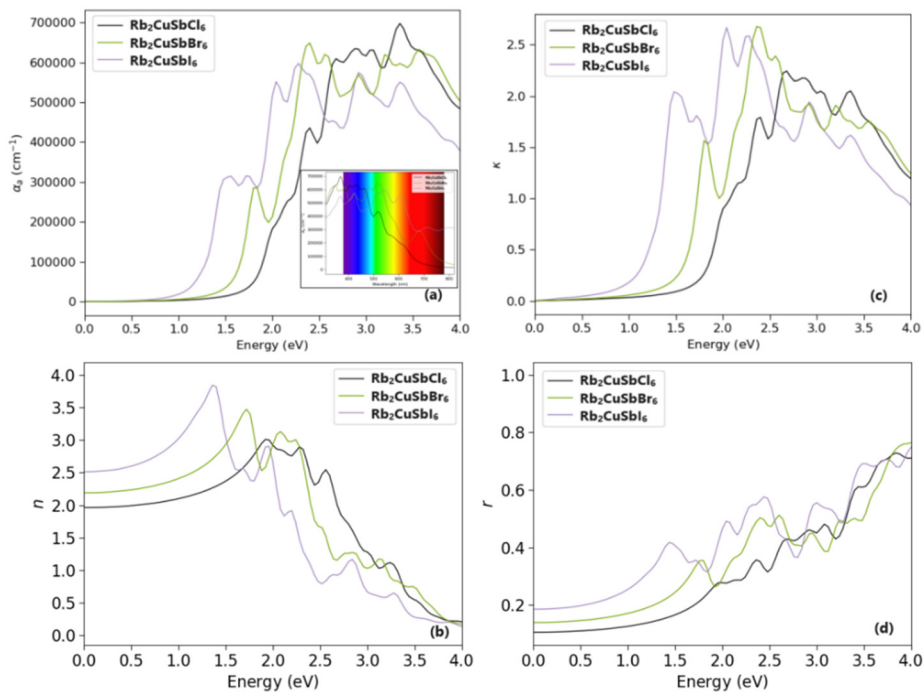
C. OPTICAL PROPERTIES

The optical properties of optoelectronic solid materials are incredibly important, including absorption, refractive index, reflectivity, and extinction loss [43]. To understand interaction between light and matter, we evaluated the optical characteristics of these double perovskite halides Rb$_2$CuSbH$_6$ (H= Cl, Br, I). The optical properties in this study are presented in two sets: (i) Real and (ii) Complex Optical Properties and are tabulated in Table 3 along with other studies done so far [36, 37].

Figure 7 (a)-(d) show the comparative study of Real Optical properties (a) absorption coefficients (α_a), (b) Refractive Index (n), (c) Extinction Coefficient (k) and (d) Reflectivity (r), of double halide Rb$_2$CuSbH$_6$ (H=Cl, Br, I) respectively. Figure 7(a) indicates the absorption bands of double halide Rb$_2$CuSbH$_6$ (H=Cl, Br, I) and reported a highest pick at 3.36 eV (697589 cm^{-1}) 2.4 eV (648741 cm^{-1}) and 2.8 eV (597548 cm^{-1}) for Rb$_2$CuSbCl$_6$, Rb$_2$CuSbBr$_6$ and Rb$_2$CuSbI$_6$ respectively. Further, we have also calculated plotted the absorption coefficients with respect to wavelength (inset plot with x-axes as wavelength) and found that all the absorption bands lie in the visible range with 344 nm to 574 nm, 348 nm to 688 nm and 369 nm to 608 nm for Rb$_2$CuSbCl$_6$, Rb$_2$CuSbBr$_6$ and Rb$_2$CuSbI$_6$ respectively and align closely with earlier published results [37]. This justifies that these double halide Rb$_2$CuSbH$_6$ (H=Cl, Br, I) possess utmost important property for its solar applications.

Table 3. Computed optical properties for double perovskite halides Rb_2CuSbH_6 (H= Cl, Br, I)

Computed Optical Properties		Units	Materials					
			Rb₂CuSbCl₆		*Rb₂CuSbBr₆*		*Rb₂CuSbI₆*	
			Present Study	*Other Study (Exp. & Theo.)*	*Present Study*	*Other Study (Exp. & Theo.)*	*Present Study*	*Other Study (Exp. & Theo.)*
Real Optical Properties	*Absorption Coefficients (αₐ)*	cm^{-1}	697589 (3.36 eV)	6.12×10^4 [37]	648741 (2.4 eV)		597548 (2.8 eV)	
	Refractive Index (n)	-	1.96		2.19		2.51	
	Extinction Coefficient (k)	-	8.0×10^{-5}		5.3×10^{-5}		6.20×10^{-5}	
	Reflectivity (r)	-	0.105		0.139		0.185	
Complex Optical Properties	*Dielectric constant (ε)*	-	3.85	4.23 [37]	4.79		6.30	
	Susceptibility (χ)	-	2.85		3.79		5.30	
	Polarizability (α)	$C.m^2V^{-1}$	0.71×10^{-38}		1.11×10^{-38}		1.9×10^{-38}	
	Optical Conductivity (σ)	$A.V^{-1}cm^{-1}$	3.53×10^3	1.9×10^4 [36]	4.23×10^3	7.8×10^4 [36]	3.6×10^3	8.2×10^4 [36]

Figure 7. Real Optical properties (Absorption, Refractive Index, Extinction Coefficients and Reflectivity) of double halide Rb_2CuSbH_6 (H=Cl, Br, I) (a) Absorption, (b) Refractive Index, (c) Extinction Coefficients and (d) Reflectivity

The refractive index is a key factor in optics, as it provides information about how light interacts with a material. It changes depending on the speed at which light travels through different media [44]. Figure 7(b) illustrates the correlation between refractive index and energy, offering valuable insights into the optical behavior of the material across different energy ranges. The Computed value of refractive index (at 0 eV) from the plot are 1.96, 2.19 and 2.51 respectively for $Rb_2CuSbCl_6$, $Rb_2CuSbBr_6$ and Rb_2CuSbI_6. Whereas the observed peak values of refractive index are 3.01 at 1.92eV for $Rb_2CuSbCl_6$; 3.47 at 1.725 eV for $Rb_2CuSbBr_6$ and 3.89 at 1.36 eV for Rb_2CuSbI_6 respectively. For the high energy spectrum, specially above the 2.08 eV, 2.4 eV and 2.72 eV respectively for $Rb_2CuSbCl_6$, $Rb_2CuSbBr_6$ and Rb_2CuSbI_6, the value of refractive index (n) values decreases below 2.0 which makes these materials best fit for solar technology (refractive index (n) benchmark for solar cell technology, n = 1.0-2.0).

The absorption capability of a material at a specific frequency can be evaluated through its extinction coefficient, which defines how electromagnetic waves propagate within the material [45]. As shown in Figure 7(c), the extinction coefficient (*k*) follows a similar trend to the Kramer-Kronig relationship with energy. The observed values of extinction coefficient are 8.0×10^{-5}, 5.3×10^{-5} and 6.20×10^{-5} for $Rb_2CuSbCl_6$, $Rb_2CuSbBr_6$ and Rb_2CuSbI_6. The minimal variation in *k* suggests these compounds are excellent candidates for solar and optoelectronic devices, particularly in the higher energy regions above 2.08 eV, 2.4 eV, and 2.72 eV, respectively, for each material (in the order of $Rb_2CuSbCl_6$, $Rb_2CuSbBr_6$ and Rb_2CuSbI_6).

Figure 7(d) illustrates the reflectivity (*r*) of the materials, which provides essential insights into how they interact with light at the surface. The reported values of reflectivity (*r*) under this study for $Rb_2CuSbCl_6$, $Rb_2CuSbBr_6$ and

Rb$_2$CuSbI$_6$ are 0.105, 0.139 and 0.185 respectively. The reflectivity (r) possesses the similar trend as refractive index has i.e. the value of r increases with heavier atom substitution.

Additionally, the complex optical properties of these double perovskite halides Rb$_2$CuSbH$_6$ (H= Cl, Br, I) were analyzed to better understand their optical properties. Both the real (Re[ε]) and imaginary (Im[ε]) parts of the dielectric function are closely linked to the energy-dependent electronic transitions within the band structure. The complex dielectric function is defined as ε=Re[ε]+Im[ε] [46]. The spectra in Figure 8(a)-(c) are compared for the double halide Rb$_2$CuSbH$_6$ (H=Cl, Br, I) in energy ranges of 0-4 eV. The value of real dielectric function Re[ε] for Rb$_2$CuSbCl$_6$, Rb$_2$CuSbBr$_6$ and Rb$_2$CuSbI$_6$ are 3.85, 4.79 and 6.30 respectively. The values of basic real dielectric function Re[ε] increases with increase of the atomic radii moving from Cl→I. Also, the values of imaginary dielectric function Im[ε] is in parity with refractive index (n). The results of this study and characteristics are in good agreement with other studies [37] as well.
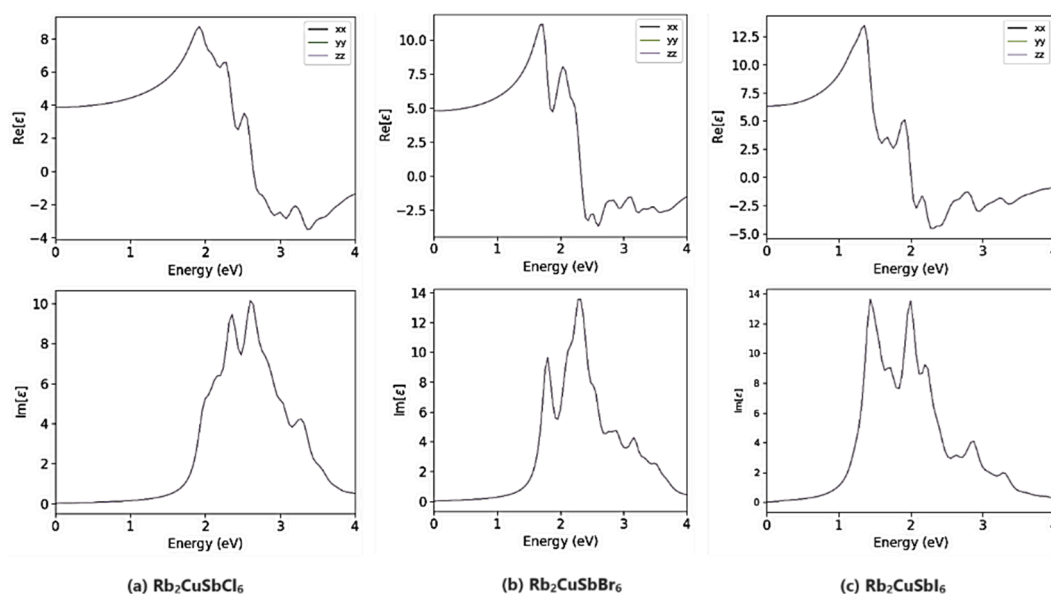
Figure 8. Dielectric Constant of double halide Rb$_2$CuSbH$_6$ (a) Rb$_2$CuSbCl$_6$; (b) Rb$_2$CuSbBr$_6$; (c) Rb$_2$CuSbI$_6$
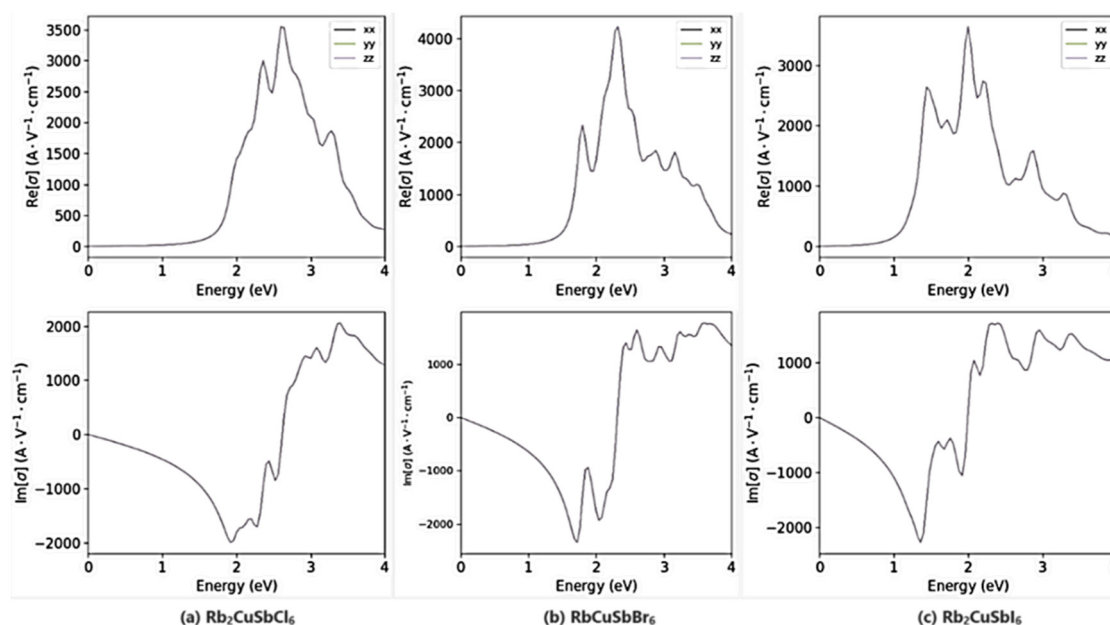
Figure 9. Optical Conductivity of double halide Rb$_2$CuSbH$_6$ (a) Rb$_2$CuSbCl$_6$; (b) Rb$_2$CuSbBr$_6$; (c) Rb$_2$CuSbI$_6$

Material optical conductivity is related to the magnitude of induced electric fields. The optical conductivity has been found to be 3.53×10^3 AV^{-1}cm^{-1}, 4.23×10^3 AV^{-1}cm^{-1} and 3.6×10^3 AV^{-1}cm^{-1} respectively for Rb$_2$CuSbCl$_6$, Rb$_2$CuSbBr$_6$ and Rb$_2$CuSbI$_6$ as shown in Figure 9(a)-(c). The results are in excellent agreement with other results [36] and suggest that these materials are excellent choice of material for optoelectronic devices. The polarizability of double halide Rb$_2$CuSbH$_6$ (H=Cl, Br, I) is also computed and represented in Figure 10(a)-(c). The polarizability is found to increasing with heavy halogen moving from Rb$_2$CuSbCl$_6$ → Rb$_2$CuSbBr$_6$ → Rb$_2$CuSbI$_6$ with the values 0.71×10^{-38} C·m^{2}V^{-1}, 1.11×10^{-38} C·m^{2}V^{-1}

and 1.9×10^{-38} C·m²V⁻¹ respectively. We have also calculated the Susceptibility of these double halide Rb_2CuSbH_6 (H=Cl, Br, I) as shown in Figure 11(a)-(c) and found an increasing trend from $Rb_2CuSbCl_6 \rightarrow Rb_2CuSbBr_6 \rightarrow Rb_2CuSbI_6$ with the values 2.85, 3.79 and 5.30 respectively which makes these material appealing for storage devices.
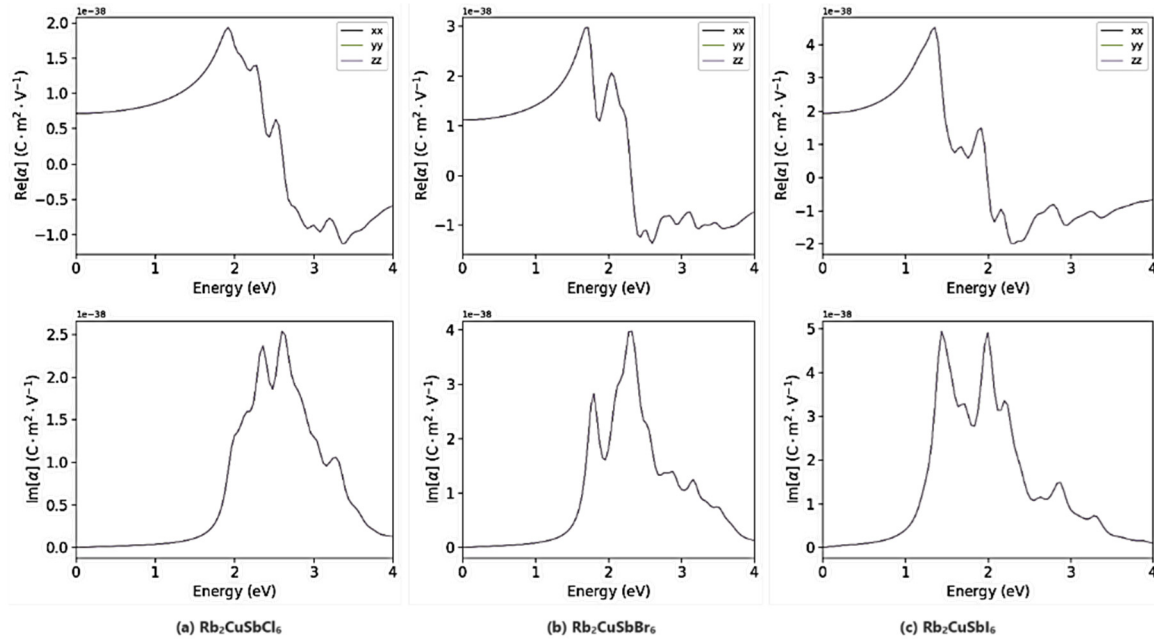
Figure 10. Polarizability of double halide Rb_2CuSbH_6 (a) $Rb_2CuSbCl_6$; (b) $Rb_2CuSbBr_6$; (c) Rb_2CuSbI_6
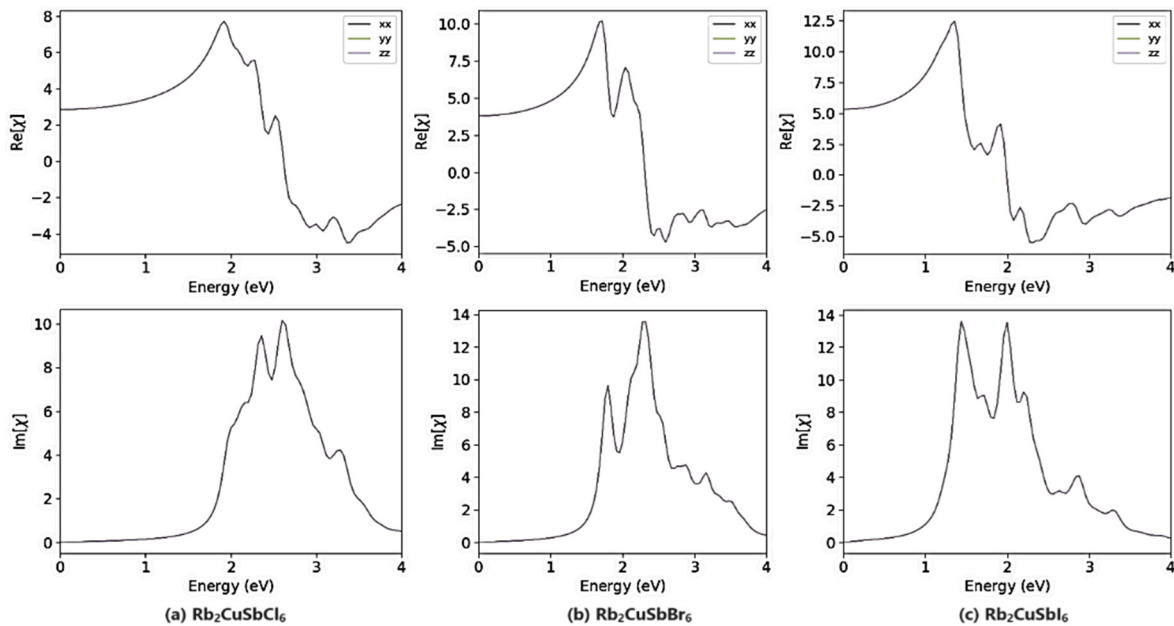
Figure 11. Susceptibility of double halide Rb_2CuSbH_6 (a) $Rb_2CuSbCl_6$; (b) $Rb_2CuSbBr_6$; (c) Rb_2CuSbI_6

4. CONCLUSIONS

The research on Rb_2CuSbH_6 (where H = Cl, Br, I) was carried out using DFT with the QuantumATK software, programmed in Python. The structural characteristics of these double perovskite halides were determined using DFT calculations based on the GGA and PBE functionals, employing the LCAO method. The key findings from this study are as follows:

1. The lattice constant (a_0), volume, and density of the unit cell for Rb_2CuSbH_6 increase progressively from $Rb_2CuSbCl_6$ to $Rb_2CuSbBr_6$ to Rb_2CuSbI_6. This trend is consistent with the increasing ionic radius of the halide ions. Additionally, incorporating alkali atoms can further reduce the material's overall density.

2. All double perovskite halides Rb_2CuSbH_6 (H = Cl, Br, I) show positive values for the elastic constants C_{11}, C_{12}, and C_{44}, and obey the stability trend $C_{11} > C_{12} > C_{44}$. The Born-Huang stability criterion was used to assess mechanical stability of these materials.

3.   All three double perovskite halides have indirect bandgaps and have a narrow band-gap semiconducting property. Pairing the double perovskite halides Rb$_2$CuSbH$_6$ (H = Cl, Br, I) with high-bandgap compounds could improve the energy conversion efficiency of tandem solar cells.

4.   Double perovskite halides Rb$_2$CuSbH$_6$ (H= Cl, Br, I) exhibit significant potential for applications in optoelectronic and thermoelectronic devices. The characteristics of the Complex Bandstructure (CB) indicate a conducive environment for the formation of evanescent waves on the surface of these materials.

5.   We evaluated the optical properties of double perovskite halides Rb$_2$CuSbH$_6$ (H=Cl, Br, I) and found that the absorption bands of these materials lie in the visible range with 344 nm to 574 nm, 348 nm to 688 nm and 369 nm to 608 nm respectively.

6.   The refractive index of Rb$_2$CuSbCl$_6$, Rb$_2$CuSbBr$_6$, and Rb$_2$CuSbI$_6$ drops below 2.0 in the high-energy spectrum. Their extinction coefficient, which helps determine absorption at specific frequencies, follows a similar energy-dependent trend as the Kramers-Kronig relations. Reflectivity increases with heavier atom substitution, with values of 0.105, 0.139, and 0.185 for Rb$_2$CuSbCl$_6$, Rb$_2$CuSbBr$_6$, and Rb$_2$CuSbI$_6$, respectively.

7.   The optical properties of Rb$_2$CuSbH$_6$ (H = Cl, Br, I) were analyzed, showing that the real dielectric function (Re[ε]) values are 3.85, 4.79, and 6.30 for Rb$_2$CuSbCl$_6$, Rb$_2$CuSbBr$_6$, and Rb$_2$CuSbI$_6$, respectively. These are linked to frequency-dependent electronic transitions within the material.

8.   We have calculated the polarizability and susceptibility of double halide Rb$_2$CuSbH$_6$ (H=Cl, Br, I) and found an increasing trend from Rb$_2$CuSbCl$_6$ Rb$_2$CuSbBr$_6$ Rb$_2$CuSbI$_6$ respectively.

The findings from this research are anticipated to provide valuable insights into potential uses for photovoltaic systems, electronic devices with optical components, and flexible electronics. This could pave the way for more cost-effective and efficient methods of utilizing solar power. Additionally, it may contribute to the creation of more adaptable and wearable technologies. The outcomes could also support the innovation of novel materials tailored for solar energy systems and various electronic applications.

ORCID

Krishna Kumar Mishra, https://orcid.org/0000-0001-6888-7654; **Sonia Chahar,** https://orcid.org/0000-0001-5250-5228
Rajnish Sharma, https://orcid.org/0000-0001-8644-016X

REFERENCES

[1]   Flexible Electronics Global Market Report (2023). https://www.globenewswire.com/news-release/2023/03/14/2626974/0/en/Flexible-Electronics-Global-Market-Report-2023.html

[2]   M.A. Amin, *et al*., "Study of double perovskites X$_2$InSbO$_6$ (X= Sr, Ba) for renewable energy; alternative of organic-inorganic perovskites," Journal of Materials Research and Technology, **18**, 4403-4412 (2022). https://doi.org/10.1016/j.jmrt.2022.04.114

[3]   Q. Mahmood, M. Younas, M.G.B. Ashiq, S.M. Ramay, A. Mahmood, and H.M. Ghaithan, "First principle study of lead-free double perovskites halides Rb$_2$Pd(Cl/Br)$_6$ for solar cells and renewable energy devices: a quantum DFT," International Journal of Energy Research, **45**(10), 14995-15004 (2021). https://doi.org/10.1002/er.6778

[4]   C. Zhang, *et al*., "Design of a novel and highly stable lead-free Cs$_2$NaBiI$_6$ double perovskite for photovoltaic application," Sustainable energy & fuels, **2**(11), 2419-2428 (2018). https://doi.org/10.1039/C8SE00154E

[5]   A. Moskvin, L. Makhnev, N. Nomerovannaya, Loshkareva, and A. Balbashov, "Interplay of p-d and d-d charge transfer transitions in rare-earth perovskite manganites," Physical Review B, **82**(3), 035106 (2010). https://doi.org/10.1103/PhysRevB.82.035106

[6]   C. Weeks, and M. Franz, "Topological insulators on the Lieb and perovskite lattices," Physical Review B, 82(8), 085310 (2010). https://doi.org/10.1103/PhysRevB.82.085310

[7]   T. Yamada, *et al*., "Self-assembled perovskite-fluorite oblique nanostructures for adaptive (tunable) electronics," Advanced Materials, **21**(13), 1363-1367 (2009). https://doi.org/10.1002/adma.200800253

[8]   J. Lettieri, M. Zurbuchen, Y. Jia, D. Schlom, S. Streiffer, and M. Hawley, "Epitaxial growth of non-c-oriented SrBi$_2$Nb$_2$O$_9$ on (111) SrTiO$_3$," Applied Physics Letters, **76**(20), 2937-2939 (2000). https://doi.org/10.1063/1.126522

[9]   H. Jin, J. Im, and A. J. Freeman, "Topological insulator phase in halide perovskite structures," Physical Review B, **86**(12), 121102 (2012). https://doi.org/10.1103/PhysRevB.86.121102

[10]   Chung, B. Lee, J. He, R. P. Chang, and M. G. Kanatzidis, "All-solid-state dye-sensitized solar cells with high efficiency," Nature, **485**(7399), 486-489 (2012). https://doi.org/10.1038/nature11067

[11]   M.M. Lee, J. Teuscher, T. Miyasaka, T.N. Murakami, and H.J. Snaith, "Efficient hybrid solar cells based on meso-superstructured organometal halide perovskites," Science, **338**(6107), 643-647 (2012). https://doi.org/10.1126/science.1228604

[12]   J. Burschka, N. Pellet, S.-J. Moon, R. Humphry-Baker, P. Gao, M.K. Nazeeruddin, and M. Grätzel, "Sequential deposition as a route to high-performance perovskite-sensitized solar cells," Nature, **499**(7458), 316-319 (2013). https://doi.org/10.1038/nature12340

[13]   S. Kashyap, R. Pandey, J. Madan, and M.K.A. Mohammed, "Reliability Test of 21% Efficient Flexible Perovskite Solar Cell Under Concave, Convex and Sinusoidal Bending," in: *IEEE Transactions on Device and Materials Reliability*, **23**(3), 380-385 (2023). https://doi.org/10.1109/TDMR.2023.3282641

[14]   S. Kashyap, *et al*., "Simulated bending test analysis of 23% efficient lead-free flexible perovskite solar cell with different bending states," Phys. Scr. 98, 114001 (2023). https://doi.org/10.1088/1402-4896/acff28

[15]   Y. Takahashi, R. Obara, Z.-Z. Lin, Y. Takahashi, T. Naito, T. Inabe, S. Ishibashi, and K. Terakura, "Charge-transport in tin-iodide perovskite CH3NH3SnI3: origin of high conductivity," Dalton Transactions, **40**(20), 5563-5568 (2011). https://doi.org/10.1039/C0DT01601B

[16] X. Zhu, B. Lv, X. Shang, J. Wang, M. Li, and X. Yu, "The immobilization effects on Pb, Cd and Cu by the inoculation of organic phosphorus-degrading bacteria (OPDB) with rapeseed dregs in acidic soil," Geoderma, **350**, 1-10 (2019). https://doi.org/10.1016/j.geoderma.2019.04.015

[17] F. Geisz, M.A. Steiner, N. Jain, K.L. Schulte, R.M. France, W.E. McMahon, E.E. Perl, *et al.*, "Building a six-junction inverted metamorphic concentrator solar cell," IEEE Journal of Photovoltaics, **8**(2), 626-632 (2017). https://doi.org/10.1109/JPHOTOV.2017.2778567

[18] J. Haruyama, K. Sodeyama, L. Han, and Y. Tateyama, "First-principles study of ion diffusion in perovskite solar cell sensitizers," Journal of the American Chemical Society, **137**(32), 10048-10051 (2015). https://doi.org/10.1021/jacs.5b03615

[19] Z. Li, Q. Xu, Q. Sun, Z. Hou, and W.J. Yin, "Thermodynamic stability landscape of halide double perovskites via high-throughput computing and machine learning," Advanced Functional Materials, **29**(9), 1807280 (2019). https://doi.org/10.1002/adfm.201807280

[20] Y. Zhang, *et al.*, "Intrinsic instability of the hybrid halide perovskite semiconductor $CH_3NH_3PbI_3$," Chinese Physics Letters, **35**(3), 036104 (2018). https://doi.org/10.1088/0256-307X/35/3/036104

[21] Wu, J.-j. Shi, M. Zhang, Y.-l. Cen, W.-h. Guo, and Y.-h. Zhu, "Promising photovoltaic and solid-state-lighting materials: two-dimensional Ruddlesden–Popper type lead-free halide double perovskites $Cs_{n+1}In_n/2Sb_n/2I3_{n+1}$ (n=3) and $Cs_{n+1}In_n/2Sb_n/2Cl3_{n+1}/Cs_{m+1}Cu_m/2B_m/2Cl3_{m+1}$(n=3, m=1)," Journal of Materials Chemistry C, **6**(43), 11575-11586 (2018). https://doi.org/10.1039/c8tc03926g

[22] J. Jiang, C.K. Onwudinanti, R.A. Hatton, P.A. Bobbert, and S. Tao, "Stabilizing lead-free all-inorganic tin halide perovskites by ion exchange," The Journal of Physical Chemistry C, **122**(31), 17660-17667 (2018). https://doi.org/10.1021/acs.jpcc.8b04013

[23] Z. Shi, *et al.*, "Symmetrization of the crystal lattice of $MAPbI3$ boosts the performance and stability of metal–perovskite photodiodes," Advanced Materials, **29**(30), 1701656 (2017). https://doi.org/10.1002/adma.201701656

[24] M.-G. Ju, *et al.*, "Toward eco-friendly and stable perovskite materials for photovoltaics," Joule, **2**(7), 1231-1241 (2018). https://doi.org/10.1016/j.joule.2018.04.026

[25] C.C. Stoumpos, *et al.*, "Ruddlesden–Popper hybrid lead iodide perovskite 2D homologous semiconductors," Chemistry of Materials, **28**(8), 2852-2867 (2016). https://doi.org/10.1021/acs.chemmater.6b00847

[26] H. Chen, S. Xiang, W. Li, H. Liu, L. Zhu, and S. Yang, "Inorganic perovskite solar cells: a rapidly growing field," Solar Rrl, **2**(2), 1700188 (2018). https://doi.org/10.1002/solr.201700188

[27] Z. Deng, F. Wei, S. Sun, G. Kieslich, A. K. Cheetham, and P. D. Bristowe, "Exploring the properties of lead-free hybrid double perovskites using a combined computational-experimental approach," Journal of Materials Chemistry A, 4(31), 12025-12029 (2016). https://doi.org/10.1039/C6TA05817E

[28] W. Zhou, *et al.*, "Lead-free small-bandgap $Cs_2CuSbCl_6$ double perovskite nanocrystals," The Journal of Physical Chemistry Letters, **11**(15), 6463-6467 (2020). https://doi.org/10.1021/acs.jpclett.0c01968

[29] G. Yu, *et al.*, "How the Copper Dopant Alters the Geometric and Photoelectronic Properties of the Lead-Free $Cs_2AgSbCl_6$ Double Perovskite," Advanced Theory and Simulations, **4**(8), 2100142 (2021). https://doi.org/10.1002/adts.202100142

[30] M.Z. Asghar, M.A. Khan, S. Niaz, N. Noor, and A. Dahshan, "Tuning of the bandgap of Rb2ScAgX6 (X= Cl, Br, I) double perovskites through halide ion replacement for solar cell applications," Materials Science in Semiconductor Processing, **148**, 106819 (2022). https://doi.org/10.1016/j.mssp.2022.106819

[31] A. Ayyaz, G. Murtaza, A. Usman, M. Umer, M.Q. Shah, and H.S. Ali, "First principles insight on mechanical stability, optical and thermoelectric response of novel lead-free $Rb_2ScCuBr_6$ and $Cs_2ScCuBr_6$ double perovskites," Materials Science in Semiconductor Processing, **169**, 107910 (2024). https://doi.org/10.1016/j.mssp.2023.107910

[32] QuantumATK version U-2023.09, Synopsys QuantumATK (https://www.synopsys.com/silicon/quantumatk.html).

[33] J.P. Perdew, *et al.*, "Atoms, molecules, solids, and surfaces: Applications of the generalized gradient approximation for exchange and correlation," Physical review B, **46**(11), 6671 (1992). https://doi.org/10.1103/PhysRevB.46.6671

[34] J.P. Perdew, K. Burke, and M. Ernzerhof, "Generalized gradient approximation made simple," Physical review letters, **77**(18), 3865 (1996). https://doi.org/10.1103/physrevlett.77.3865

[35] J. van Setten, *et al.*, "The PseudoDojo: Training and grading a 85 element optimized norm-conserving pseudopotential table," Computer Physics Communications, **226**, 39-54 (2018). https://doi.org/10.1016/j.cpc.2018.01.012

[36] Q. Mahmood, *et al.*, "Tunning of band gap of double perovskites halides Rb2CuSbX6 (X= Cl, Br, I) for solar cells and energy harvesting," Materials Science and Engineering: B, **286**, 116088 (2022). https://doi.org/10.1016/j.mseb.2022.116088

[37] T.-Y. Tang, and Y.-L. Tang, "Physical and optoelectronic properties of double halide perovskites A2CuSbX6 (A=Cs, Rb, K; X=Cl, Br, I) based on first principles calculations," Chemical Physics, **570**, 111897 (2023). https://doi.org/10.1016/j.chemphys.2023.111897

[38] M. Born, and K. Huang, *Dynamical theory of crystal lattices*, (Oxford university press, 1996).

[39] K. Bougherara, S. Al-Qaisi, A. Laref, T.V. Vu, and D. Rai, "Ab initio Insight of the Electronic, Structural, Mechanical and Optical Properties of X3P2 (X= Mg, Ca) from GGA and Hybrid Functional (HSE06)," Journal of Superconductivity and Novel Magnetism, **35**(1), 79-86 (2022). https://doi.org/10.1007/s10948-021-06009-3

[40] K.K. Mishra, "Study on structural, mechanical, electronic, vibrational, optical and thermo-dynamical behaviour of ZB Structured BeZ (Z= S, Se and Te) using ATK-DFT," Metallurgical and Materials Engineering, **26**(3), 253-278 (2020). https://doi.org/10.1016/j.physleta.2024.129817

[41] S. Chahar, K.K. Mishra, and R. Sharma, "Analysing the suitability of CaTiO3/Ca1–xSrxTiO3/SrTiO3 perovskite for fabrication of optoelectronic devices using QuantumATK tool: a study for electronic and optical properties," Physica Scripta, **99**(3), 035963 (2024). https://doi.org/10.1088/1402-4896/ad29cd

[42] K.K. Mishra, S. Chahar, and R. Sharma, "An extensive investigation of structural, electronic, and optical properties of inorganic perovskite Ca_3AsCl_3 for photovoltaic and optoelectronic applications: A first-principles approach using Quantum ATK Tool," Solid State Communications, **390**, 115623 (2024). https://doi.org/10.1016/j.ssc.2024.115623

[43] S. Chahar, K.K. Mishra, and R. Sharma, "Investigation of Structural, Electronic, and Optical Characteristics of a Novel Perovskite Halide, Mg_3AsCl_3, for Electronic Applications," Physica status solidi (b), 2400171 (2024). https://doi.org/10.1002/pssb.202400171

359

Unveiling the Potential of Double Perovskite Halides Rb$_2$CuSbH$_6$ (H = Cl, Br, I)...

EEJP. 4 (2024)

[44] S. Chahar, C. Malan, K.K. Mishra, and R. Sharma, "Optimizing novel perovskite Mg$_3$AsBr$_3$ through uniaxial stress: A comprehensive study of its potential in solar and optoelectronic applications," Physica Scripta, **99**, 095994 (2024): https://doi.org/10.1088/1402-4896/ad6bd1

[45] D. Schwartz, et al., "Air Stable, High-Efficiency, Pt-Based Halide Perovskite Solar Cells with Long Carrier Lifetimes," Physica status solidi (RRL)–Rapid Research Letters, **14**(8), 2000182 (2020). https://doi.org/10.1002/pssr.202000182

[46] L.K. Gautam, H. Haneef, M. Junda, D.S. John, and N. Podraza, "Approach for extracting complex dielectric function spectra in weakly-absorbing regions," Thin Solid Films, **571**, 548-553 (2014). https://doi.org/10.1016/j.tsf.2014.03.020

ПОТЕНЦІАЛ ПОДВІЙНИХ ГАЛОГЕНІДІВ ПЕРОВСКІТУ Rb$_2$CuSbH$_6$ (H = Cl, Br, I) ДЛЯ ГНУЧКОЇ ЕЛЕКТРОНІКИ: КОМПЛЕКСНЕ ДОСЛІДЖЕННЯ СТРУКТУРНИХ, МЕХАНІЧНИХ, ЕЛЕКТРИЧНИХ ТА ОПТИЧНИХ ВЛАСТИВОСТЕЙ

Крішна Кумар Мішра[a], Соня Чахар[a], Раджніш Шарма[b]

[a]Інститут інженерії та технологій Університету Чіткара, Університет Чіткара, Раджпура, Пенджаб-140401, Індія
[b]Школа інженерії та технологій, Університет Чіткара, Солан, Гімачал-Прадеш-174103, Індія

Структурні, механічні, електричні та оптичні властивості подвійних галогенідів перовскіту, таких як Rb$_2$CuSbH$_6$ (де H = Cl, Br та I) для гнучких електронних пристроїв, захоплюючі та складні. Дослідження літератури чітко встановлює, що дослідження щодо аналізу потенційного використання цих матеріалів у дуже затребуваному секторі гнучких електронних пристроїв були обмежені. У цій статті були проведені цілеспрямовані дослідження щодо вивчення характеристик цих матеріалів за допомогою програмного засобу QuantumATK NanoLab. Усі галогеніди подвійного перовскіту Rb$_2$CuSbH$_6$ (H = Cl, Br, I) демонструють позитивні значення пружних констант C11, C12 та C44 і підкоряються тенденції стабільності C11>C12>C44. Механічну стабільність встановлювали за критеріями Борна-Хуанга. Оптимізовані значення модуля Юнга, модуля об'ємної пружності, модуля зсуву та коефіцієнтів Пуассона встановили, що матеріали є стабільними та пластичними за своєю природою. Під час проведення аналізу електронних властивостей було виявлено, що всі три матеріали Rb$_2$CuSbCl$_6$, Rb$_2$CuSbBr$_6$ і Rb2CuSbI$_6$ мають непряму заборонену зону 0,924 eB, 0,560 eB і 0,157 eB відповідно. Більше того, природність комплексної смугової структури (CB) вказує на те, що найбільша кількість хвиль, що завмирають, може існувати, коли поділ шарів найменший у Rb$_2$CuSbCl$_6$ (6,0 Å), Rb$_2$CuSbBr$_6$ (6,33 Å) і найвищий у Rb$_2$CuSbI$_6$ (6,8 Å). Смуги поглинання для Rb2CuSbCl6, Rb2CuSbBr6 і Rb2CuSbI6 лежать у видимому діапазоні від 344 нм до 574 нм, від 348 нм до 688 нм і від 369 нм до 608 нм відповідно. Коефіцієнт відбиття (r), зазначений у цьому дослідженні, становить 0,105, 0,139 і 0,185 відповідно для Rb$_2$CuSbCl$_6$, Rb$_2$CuSbBr$_6$ і Rb$_2$CuSbI$_6$. Загалом, усі отримані результати вказують на необхідність більш глибокого вивчення матеріалів Rb$_2$CuSbH$_6$ для різних застосувань електронних пристроїв.

Ключові слова: *перовскіт; QuantumATK; DFT; оптичні властивості; електронна структура; механічні властивості*

OBTAINED AND STUDIED STRUCTURAL ASPECTS OF THE $Ge_{0.9}Er_{0.1}S$ COMPOUND WITH Ge → Er SUBSTITUTIONS

R.Z. Ibaeva[a]*, G.B. Ibragimov[a], A.S. Alekperov[b,c], ●R.E. Huseynov[a]

[a]Institute of Physics, Ministry of Science and Education Republic of Azerbaijan, Baku, AZ-1143, Azerbaijan
[b]Azerbaijan State Pedagogical University, Baku, AZ-1000, Azerbaijan
[c]Baku Engineering University, Khirdalan, AZ-0101, Azerbaijan
*Corresponding Author e-mail: raidaibayeva1@gmail.com

In this work, $Ge_{0.9}Er_{0.1}S$ was synthesised by partially replacing Ge atoms with Er atoms. The crystal structure of the resulting compound was studied by X-ray diffraction. The research found that Er atoms can completely replace Ge atoms in the crystal structure. Therefore, the compound can crystallize into one phase. It was established that the structure of this compound corresponds to orthorhombic symmetry and space group Pnma. The crystallographic parameters of the $Ge_{0.9}Er_{0.1}S$ compound were determined by analyzing the X-ray diffraction spectrum using the Rietveld method. Based on the obtained structure on different atomic planes, an explanation of the crystal structure of the $Ge_{0.9}Er_{0.1}S$ semiconductor is given. It is established that one of the main elements in the formation of the crystal structure are the ionic radii of the elements Ge, Er and S.

Keywords: *$Ge_{0.9}Er_{0.1}S$; Crystal structure; X-ray diffraction; Lattice parameters*
PACS: 61.05.cp; 61.82.Fk

1. INTRODUCTION

Materials with semiconductor properties are materials with wide application potential in modern electronics and spintronics. Recently, theoretical and experimental research has been carried out in the direction of studying the optical, magnetic, thermal and electrical properties of functional materials [1-5]. It is known that the physical properties of semiconductors depend on their electronic and crystal structure. Therefore, the structural properties of these materials are studied using modern research methods. One such material is GeS crystal. This crystal is a crystal with a layered structure. X-ray diffraction studies showed that the crystal structure of this compound corresponds to orthorhombic symmetry. In this compound, interesting optical properties are observed in compounds obtained by partial replacement of germanium atoms with rare earth elements. Therefore, $Ge_{1-x}Ln_xS$ crystals have been synthesized for a long time and various optical properties have been studied.

The photoconductivity of GeS and $Ge_{1-x}Nd_xS$ compounds ($x = 0.005$ and 0.01) was studied at low temperatures ($T = 80$-300 K). An analysis of the obtained spectra revealed that significant changes in photoconductivity are observed when Ge atoms are partially replaced by Nd atoms. Elementary excitation of the exciton type was observed in $Ge_{1-x}Nd_xS$ compounds in the temperature range 200 K $< T < 350$ K [6]. When Ge atoms were replaced by rare earth elements, optically active processes were also observed in the $Ge_{1-x}Sm_xS$ and $Ge_{1-x}Gd_xS$ compounds [7,8]. Previous studies have established that substitution with rare earth elements causes significant changes in the optical properties of semiconductors. But in many cases, rare earth elements cannot replace cations in a crystal. In this case, the crystal structure of the material is complex. Thus, a two-phase, three-phase system is formed [9]. With a complex crystal structure, it is difficult to study the structural aspects of the physical properties of substances. In the course of structural studies of $Ge_{1-x}Ln_xS$ crystals, it was established that Ln atoms can completely replace Ge atoms. Therefore, it is possible to study these systems. Data obtained from studying such systems can be used as a model when studying compounds with similar physical properties and structures.

It is known that changes in interatomic distances occur due to differences in ionic radii during cation-cation substitutions. These changes can affect the crystal structure. As the concentration increases during the substitutions, changes in the crystal structure also increase. Therefore, the structure of new materials obtained by cation-cation and anion-anion substitution requires careful study. Although the structure of many compounds included in the GeS and $Ge_{1-x}Ln_xS$ system has been studied, the structure of compounds obtained by replacing Ge atoms with Er atoms has not been sufficiently studied. It is known that Er atoms have a smaller ionic radius compared to the elements Nd, Sm and Gd [10]. Consequently, in compounds included in the $Ge_{1-x}Er_xS$ system, a crystal structure with higher symmetry is possible. In this work, the compound $Ge_{0.9}Er_{0.1}S$ was synthesized and its crystal structure was studied by X-ray diffraction. Crystallographic parameters: space group, syngony, lattice parameters, atomic coordinates, interatomic distances and angles between bonds were determined by analyzing the spectrum obtained at room temperature.

361

Obtained and Studied Structural Aspects of the $Ge_{0.9}Er_{0.1}S$ Compound...

EEJP. 4 (2024)

2. EXPERIMENTAL PART
2.1. Synthesis of samples.

The process of synthesis of the $Ge_{0.9}Er_{0.1}S$ compound was carried out according to standard methods under vacuum conditions at high temperatures according to the synthesis of the chalcogenide semiconductor GeS. The synthesis used germanium with a resistivity of ρ = 50 Ohm·cm. The stoichiometric amounts of each of the elements Ge, S and Er were calculated, weighed on a high-precision electronic balance, taken in appropriate quantities and mixed. The resulting mixture was placed in a vacuum (10^{-3} mm Hg) in a quartz tube with a length of l = 15 cm and a diameter of d = 2 cm. To prevent the explosion of the ampoule, the germanium element was ground into powder and m = 10 g was taken. Once the material is ready, the synthesis process begins. This process was carried out in two stages. In the first stage, the ampoule was placed in an oven and heated to a temperature T = 300 ºC at a rate of 5ºC/min. The synthesis was carried out at this temperature for 12 hours. Then the temperature was increased to the melting temperature of germanium (T = 930 ºC) at a rate of 3 ºC/min. The synthesis was carried out at this temperature for 12 hours. The temperature of the upper part of the furnace is 50ºC higher than the melting point of germanium, and the temperature of the lower part is lowered by 50ºC. Then the ampoule was lowered from above at a speed of 3 mm/h. Upon completion of this process, a $Ge_{0.9}Er_{0.1}S$ single crystal with geometric dimensions of $10\times8\times6$ mm^3 was obtained. Because this compound has a layered crystal structure, it can be easily separated in parallel planes. Therefore, samples for research were prepared by grinding them into small particles.

2.2. Structural analysis

The crystal structure of the $Ge_{0.9}Er_{0.1}S$ compound was studied by X-ray diffraction. This method allows one to determine phase analysis, crystal structure, and structural phase transitions in chalcogenide semiconductors with fairly high accuracy [11,12]. The samples were first ground in a mortar and then analyzed on a CuKα 40 kV, 40 mA, λ = 1.5406 Å X-ray diffractometer (D8 Advance, Bruker, Germany). The studies were carried out at room temperature and under normal conditions. The resulting spectra were analyzed by the Rietveld method in the Mag2Pol program.

3. RESULTS AND DISCUSSIONS

The crystal structure of the $Ge_{0.9}Er_{0.1}S$ compound was studied by X-ray diffraction in the diffraction angle range $5° \leq 2\theta \leq 50°$. The spectrum obtained at room temperature and under normal conditions is shown in Figure 1.
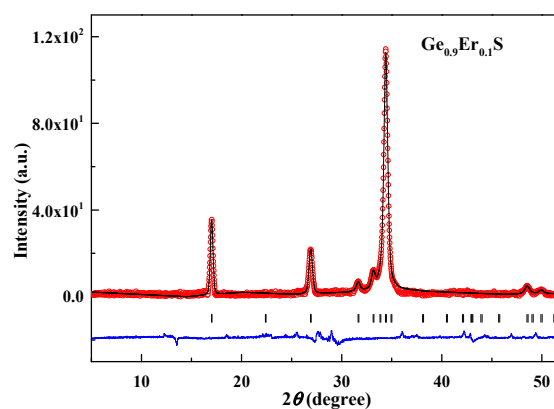
Figure 1. X-ray structural spectrum of the compound $Ge_{0.9}Er_{0.1}S$.

Shown are the experimentally obtained spectrum points (red dots), the curve calculated in the Mag2Pol program (black line), atomic planes corresponding to the Miller indices (vertical lines), and the difference between theory and experiment (blue line). As can be seen from the spectrum, three main diffraction maxima are observed in the resulting spectrum over a wide range. These maxima correspond to the diffraction angles 2θ = 17°, 27° and 34°. During the analysis in the Mag2Pol program, it was found that this spectrum corresponds to orthorhombic symmetry with the space group Pnma, and the central diffraction maxima correspond to (2 0 0), (2 0 1) and (4 0 0). aircraft. During the calculation, it was determined that the lattice parameters of the $Ge_{0.9}Er_{0.1}S$ crystal are: a = 4.318(3) Å, b = 3.649(6) Å, c = 10.491(2) Å and V = 165.43 $Å^3$ (Rp = 6.23, Rwp = 5.02 and χ^2 = 1.32%). The $Ge_{0.9}Er_{0.1}S$ compound was synthesized in a single-phase case. This is because Er atoms can completely replace Ge atoms in the crystal structure. It is known that Ge atoms when forming the GeS compound are in a divalent state and form covalent bonds with divalent S atoms. Lanthanides form compounds in both divalent and trivalent states. When Er atoms replace Ge atoms, they become divalent. Another reason why Er atoms can replace Ge atoms in a crystal structure is that the difference in the ionic radii of these atoms is small. Thus, in the divalent case, the ionic radius of germanium atoms is R_{Ge2+} = 0.72 Å, the ionic radius of erbium atoms is R_{Er2+} = 1.09 Å, and the difference between them is ΔR_{Er-Ge} = 0.37 Å [10]. As you can see, this value is not so large compared to interatomic distances. Therefore, replacements were possible. Obtaining a single-phase system by substitution is very important for explaining the structural features of the physicochemical processes occurring in these compositions.

To obtain more accurate information about the crystal structure, it is important to determine the coordinates of the atoms. The coordinates of Ge, Er and S atoms were determined by analyzing the X-ray diffraction spectrum of the $Ge_{0.9}Er_{0.1}S$ compound (Fig. 1) using the Rietveld method. It has been established that Ge and Er atoms upon substitution are located in the same crystallographic position. The coordinates of their atoms correspond to: $x/a = 0.622$, $y/b = 0.25$, $z/c = 0.372$, and the coordinates of the S atoms: $x/a = 0.848$, $y/b = 0.25$, $z/c = 0.501$.

The $Ge_{0.9}Er_{0.1}S$ compound has a very simple crystal structure. So, since the Ge(Er) and S atoms have the same concentration, then the number of their atoms in the elementary lattice is the same. To visualize the crystal structure, the crystal structure of the $Ge_{0.9}Er_{0.1}S$ compound was determined on the $\vec{a}\vec{b}$, $\vec{a}\vec{c}$ and $\vec{b}\vec{c}$ planes in the Diamond 3.2 program. The resulting structure at different levels is presented in Figure 2 and the $\vec{b}\vec{c}$ plane, as can be seen from the given structure, there are 4 germanium (erbium) atoms and 4 sulfur atoms in the elementary lattice, therefore $Z = 4$. The elementary lattice consists of two different layers. if the bonds were located inside the layer and formed a high symmetry parallel to the $\vec{a}$, $\vec{b}$ and $\vec{c}$ axes, then an elementary lattice with cubic systems would be obtained. However, as can be seen, the $Ge_{0.9}Er_{0.1}S$ compound crystallizes in orthorhombic systems with slightly lower symmetry. This structural effect can also be observed in the angle values of the interconnects. Thus, the Ge-S-Ge bond takes on 4 different values depending on its distance in the elementary lattice: 132º, 90º, 56º, 37º. It is known that the ideal crystal structure with high symmetry for binary b-compounds is the NaCl model. If the $Ge_{0.9}Er_{0.1}S$ compound crystallized according to this model, then the intervalence angles would be 90° and 45°. The difference in contact angle values is explained by the difference in the symmetry of the crystal structure.
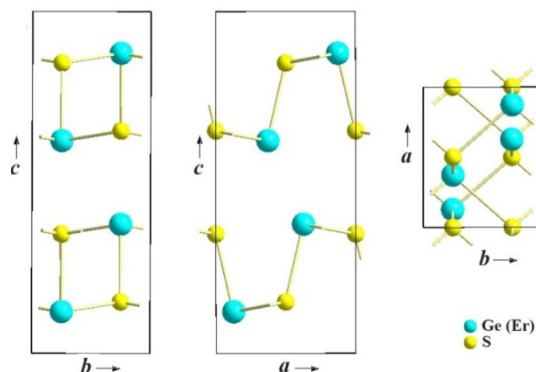
Figure 2. Crystal structure of the $Ge_{0.9}Er_{0.1}S$ compound along the $\vec{a}\vec{b}$, $\vec{a}\vec{c}$ and $\vec{b}\vec{c}$ planes

A layered crystal structure is also observed in interatomic distances. Thus, it was determined that the distance between the Ge(Er) and S atoms inside the layer is $l_{Ge(Er)-S} = 2.44$ Å, and the interatomic distances between the layers are $l_{Ge(Er)-S} = 3.27$ Å. Thus, the layered $Ge_{0.9}Er_{0.1}S$ crystal is located parallel to the planes and has a shape that can be easily separated from each other mechanically.

Many interesting physical properties are observed in semiconductor compounds with a layered crystal structure. Thus, during some physical processes, the interlayer distances and other crystallographic parameters change. During these changes, not only the mechanical properties change but also the physical properties of the material as a whole. During the structural studies of the $TlGaSe_2$ crystal at high pressures, it was found that the structural phase transition occurs at a pressure of $P = 0.5$ GPa. However, during the analysis, it was found that the symmetry of the crystal was monoclinic C2/c both before and after the phase transition [13]. It was determined that the main reason for the phase transition is a sharp decrease in the value of the distance between the layers under the action of pressure. As you can see, the distance between the layers also plays an important role in layered semiconductors. Therefore, it is important to understand the structural elements when studying these crystals. For this reason, the results obtained in the study of the crystal structure of the $Ge_{0.9}Er_{0.1}S$ semiconductor are very important. These results are very important both from the point of view of studying the structure of the crystal and from the point of view of explaining the structural aspects of its physical properties. Thanks to the simple crystal structure, it is possible to explain the physicochemical processes occurring in the $Ge_{0.9}Er_{0.1}S$ compound.

4. CONCLUSIONS

The compound $Ge_{0.9}Er_{0.1}S$ with a layered crystal structure was synthesized and its crystal structure was studied by X-ray diffraction. In the course of studies carried out by the Rietveld method, it was found that Er atoms can completely replace Ge atoms in the crystal structure. The X-ray diffraction spectrum obtained at room temperature was analyzed in the Mag2Pol program and the crystallographic parameters were determined. The structural features of the $Ge_{0.9}Er_{0.1}S$ compound are shown based on the values of interatomic distances and intervalence angles, and the crystal symmetry and layered structure are explained. The role of the values of ionic radii and valence of the atoms included in the composition in the formation of bonds is shown. It is known that oxidation is constantly occurring on the surface of materials. This process is observed even in some oxide materials of complex composition [14]. It is observed more in non-oxide materials. There are a number of methods to prevent this process and minimize oxidation. The main method is to ensure the saturation of all bonds in the synthesized sample. In this case, metal atoms cannot form bonds with oxygen atoms. In this

regard, the $Ge_{0.9}Er_{0.1}S$ compound can be considered stable. Therefore, elements made from this combination can work stably for a long time.

R.E. Huseynov, https://orcid.org/0000-0003-0636-3948

REFERENCES

[1] G.B. Ibragimov, and R.Z. Ibaeva, "Light absorption by free charge carriers with scattering mechanisms in a semiconductor superlattice," Journal of Surface Investigation: X-ray, Synchrotron and Neutron Techniques, **18**, 116-120 (2024). https://doi.org/10.1134/S1027451024010099

[2] G.B. Ibragimov, and R.Z. Ibayeva, "Theory of intraband absorption of electromagnetic radiation in cylindrical quantum wires," Journal of Non-Oxide Glasses, **12**, 31-34 (2020). https://chalcogen.ro/31_IbragimovGB.pdf

[3] T.K. Nurubeyli, "The effect of plasma density on the degree of suppression of analyte signals in ICP-MS," Technical Physics, **65**, 1963-1968 (2020). https://doi.org/10.1134/S1063784220120166

[4] G.B. Ibragimov, R.Z. Ibaeva, A.S. Alekperov, and B.G. Ibragimov, "Light absorption by free charge carriers in the presence of phonons in an anisotropic quantum wire," Advanced Physical Research, **6**, 56-62 (2024). https://doi.org/10.62476/apr61.62

[5] T.K. Nurubeyli, "Coefficient of relative sensitivity in mass spectrometers with inductively coupled plasma," Inorganic Materials: Applied Research, **11**, 552-557 (2020). https://doi.org/10.1134/S2075113320030351

[6] A.S. Alekperov, A.O. Dashdemirov, A.E. Shumskaya, and S.H. Jabarov, "High-temperature exciton photoconductivity of $Ge_{1-x}Nd_xS$ crystals," Crystallography Reports, **66**, 1322-1327 (2021). https://doi.org/10.1134/S1063774521070026

[7] A.O. Dashdemirov, S.G. Asadullayeva, A.S. Alekperov, N.A. Ismayilova, and S.H. Jabarov, "Electronic and optical properties of GeS and GeS:Gd," International Journal of Modern Physics B, **35**, 2150305 (2021). https://doi.org/10.1142/S0217979221503057

[8] A.S. Alakbarov, A.O. Dashdemirov, R.B. Bayramli, and K.S. Imanova, "Effect of the gamma ırradıatıon on the structure and excıton photoconductıvıty of layered GeS:Sm sıngle crystal," Advanced Physical Research, **3**, 39-45 (2021). http://jomardpublishing.com/UploadFiles/Files/journals/APR/V3N1/5Alakparov.pdf

[9] B.G. Tagiyev, O.B. Tagiyev, A.I. Mammadov, V.X. Quang, T.G. Naghiyev, S.H. Jabarov, M.S. Leonenya, *et al.*, "Structural and luminescence properties of $Ca_xBa_{1-x}Ga_2S_4$: Eu^{2+} chalcogenide semiconductor solid solutions," Physica B: Condensed Matter, **478**, 58-62 (2015). https://doi.org/10.1016/j.physb.2015.08.061

[10] L.T. Bugaenko, S.M. Ryabykh, and A.L. Bugaenko, "A nearly complete system of average crystallographic ionic radii and its use for determining ionization potentials," Moscow University Chemistry Bulletin, **63**, 303-317 (2008). https://doi.org/10.3103/S0027131408060011

[11] M.N. Mirzayev, S.H. Jabarov, E.B. Asgerov, R.N. Mehdiyeva, T.T. Thabethe, S. Biira, and N.V. Tiep, "X-ray diffraction and thermodynamics kinetics of SiB_6 under gamma irradiation dose," Silicon, **11**, 2499-2504 (2019). https://doi.org/10.1007/s12633-018-0039-2

[12] Y.I. Aliyev, Y.G. Asadov, A.O. Dashdemirov, R.D. Aliyeva, T.G. Naghiyev, and S.H. Jabarov, "Polymorphic transformations and thermal expansion of some modifications in $Ag_{1.5}Cu_{0.5}Se$ and $Ag_{0.4}Cu_{1.6}Se$,", International Journal of Modern Physics B, **33**, 1950271 (2019). https://doi.org/10.1142/S0217979219502710

[13] S.H. Jabarov, T.G. Mammadov, A.I. Mammadov, S.E. Kichanov, V.B. Aliyeva, and E.V. Lukin, "Structural phase transition in $TlGaSe_2$ under high pressure," Journal of Surface Investigation. X-ray, Synchrotron and Neutron Techniques, **9**, 35-40 (2015). https://doi.org/10.1134/S102745101501005X

[14] F.G. Agayev, S.H. Jabarov, G.Sh. Ayyubova, M.N. Mirzayev, S.V. Trukhanov, E.L. Trukhanova, M.A. Darwish, *et al.*, "Structure and thermal properties of $BaFe_{11.1}In_{0.9}O_{19}$ hexaferrite," Physica B: Condensed Matter, **580**, 411772 (2020). https://doi.org/10.1016/j.physb.2019.411772

ОТРИМАНО ТА ДОСЛІДЖЕНО СТРУКТУРНІ АСПЕКТИ СПОЛУКИ $Ge_{0.9}Er_{0.1}S$ ІЗ ЗАМІНОЮ $Ge \rightarrow Er$
Р.З. Ібаєва[a], Г.Б. Ібрагімов[a], А.С. Алекперов[b,c], Р.Е. Гусейнов[a]

[a]Інститут фізики Міністерства науки і освіти Азербайджанської Республіки, Баку, AZ-1143, Азербайджан
[b]Азербайджанський державний педагогічний університет, Баку, AZ-1000, Азербайджан
[c]Бакинський інженерний університет, Хирдалан, AZ-0101, Азербайджан

У цій роботі шляхом часткової заміни атомів Ge на атоми Er було синтезовано сполуку $Ge_{0.9}Er_{0.1}S$. Кристалічна структура отриманої сполуки досліджена методом рентгенівської дифракції. Дослідження показало, що атоми Er можуть повністю замінити атоми Ge в кристалічній структурі. Тому сполука може кристалізуватися в одну фазу. Встановлено, що структура цієї сполуки відповідає орторомбічній симетрії та просторовій групі Pnma. Кристалографічні параметри сполуки $Ge_{0.9}Er_{0.1}S$ визначали шляхом аналізу рентгенівського спектру за методом Рітвельда. На основі отриманої структури на різних атомних площинах дано пояснення кристалічної структури напівпровідника $Ge_{0.9}Er_{0.1}S$. Встановлено, що одними з основних елементів у формуванні кристалічної структури є іонні радіуси елементів Ge, Er і S.
Ключові слова: *$Ge_{0.9}Er_{0.1}S$; кристалічна структура; рентгенівська дифракція; параметри гратки*

STUDIES OF THE IMPACT OF UV ON CMC PVA/ZnO NANOCOMPOSITE FILMS PREPARED WITH A SIMPLE SOLUTION CASTING METHOD

Sarah A. Ibrahim[a], Abderrazek Oueslati[b], Abdelhedi Aydi[b]*

aLaboratory of Multifunctional Materials and Applications (LaMMA), LR16ES18, Faculty of Sciences of Sfax, University of Sfax, BP 1171, 3000 Sfax, Tunisia
bLaboratory of spectroscopic characterization and optical materials, Faculty of Sciences, University of Sfax, B.P. 1171, 3000 Sfax, Tunisia
*Corresponding Author e-mail: aydi_abdelhedi@yahoo.fr
Received July 27, 2024; revised September 24, 2024; accepted September 24, 2024

The synthesis of nanocomposite films comprising carboxymethyl cellulose/ polyvinyl alcohol (CMC PVA) mixed with zinc oxide nanoparticles (ZnO NPs) through a simple solution casting method is examined. Furthermore, the impact of ZnO NPs and UV-irradiation exposure for varying durations (20,45,75h) on the morphology (FE-SEM) is investigated. The X-ray diffraction (XRD), Fourier-transform infrared (FTIR) spectroscopy, and ultraviolet-visible (UV-Vis) spectroscopy are utilized to analyze the as-prepared films. Furthermore, the field-emission scanning electron microscopy (FE-SEM) images reveal a noticeable change in the morphology of CMC PVA/ZnO nanocomposite films attributed to the significant impact of ZnO nanoparticles and UV exposure. The XRD spectra demonstrate a modification in the amorphous phase of the samples as a result of UV exposure The FTIR analysis reveals that the exposure to UV radiation positively influenced the polymer's structure, as evidenced by notable changes in the infrared peaks. Additionally, the UV-Vis spectroscopy results indicate that longer UV exposure times (75 hours) and the addition of ZnO nanoparticles resulted in improved absorption characteristics within the produced films. The nanocomposite films displayed an adjustable energy gap (Eg) that varied between (4.52 eV and 4.55 eV) as the duration of UV irradiation increased from (20 hours) (75 hours) led to a reduction in the energy gap (Eg) value to (4.50 eV). This phenomenon is believed to be caused by the substantial influence of UV radiation on the development of structural defects. Ultimately, the Energy gap Eg of the nanocomposite films was influenced by the duration of UV. The results demonstrate that there is significant potential for the utilization of CMC/PVA/ZnO nanocomposite films in various crucial optoelectronic applications.

Keywords: *CMC/PVA/ZnO; Nanocomposites Properties; ZnO Nanoparticles; Energy Gap; UV irradiation; X-ray*

1. INTRODUCTION

Over the past few years, there has been a notable surge in the study of polymers with varied optical properties, largely attributed to their extensive range of uses such as sensors and light-emitting diodes. The optical attributes of these substances can be readily modified by managing the levels of fillers. Despite the extensive research conducted on these materials, there is still much to explore and understand [1] Polyvinyl alcohol (PVA) is a polymer with a semi-crystalline structure that is soluble in water. It possesses remarkable film-forming and adhesive characteristics, rendering it highly valuable in various technological, pharmaceutical, and biomedical fields due to its intriguing physical properties. [2] Polyvinyl alcohol (PVA) is a polar polymer with hydroxyl groups linked to methane carbons via a carbon chain backbone. The incorporation of OH groups enable the creation of PVA composites through hydrogen bonding interactions. PVA showcases advantageous traits including a notable charge storage capability, robust dielectric strength, and optical and electrical properties that are modulated by the filler material employed. By incorporating chalcogenide semiconductors and metal oxide semiconductors into PVA, optical properties of the host matrix can be significantly enhanced. Consequently, PVA has emerged as a promising candidate in the fields of electronics and optoelectronics [3]. One of the derivatives commonly used in various industries is carboxymethyl cellulose (CMC). This compound undergoes treatment with chloroacetic acid (ClCH$_2$CO$_2$H). CMC is utilized in various industries such as cosmetics, paints, pharmaceuticals, mineral processing, food, textiles, ceramic foam, biodegradable films, and paper. It functions as a thickening agent, binding agent, stabilizer for suspensions, and agent for retaining water in these industries [4]. The frequently utilized natural polysaccharide polymer possesses outstanding biodegradability, biocompatibility, and film-forming characteristics. Due to its safety and lack of toxicity, it finds extensive application in the pharmaceutical, food, and packaging sectors [5] The frequently utilized natural polysaccharide polymer possesses outstanding biodegradability, biocompatibility, and film-forming characteristics. Due to its safety and lack of toxicity, it finds extensive application in the pharmaceutical, food, and packaging sectors [6]. Moreover, zinc oxide nanoparticles (ZnO NPs) exhibit versatile properties as a metal oxide, showcasing remarkable electrochemical and physicochemical attributes. These include elevated chemical stability and a wide-ranging absorption spectrum [7]. The wide energy range and stable thermal properties of this material make it exhibit semiconductor characteristics, indicating promising prospects for its utilization in electronic and optoelectronic technologies like solar cells and storage devices. [8,9] Sunlight is made up of a continuous spectrum of electromagnetic energy separated into three major wavelength bands: ultraviolet (5%), visible and infrared

(45%), and 50%. The UV light region is found between (100-400) nm. International UV radiation is classified as follows by the Commission on Illumination: There are three types of wavelengths: long tidal wave UVA (315-400 nm), UVB (280-315 nm), and UVC (short wave) (100–280 nm) [10]. The impact of UV exposure on the electrical and optical characteristics of solution-processed transparent ZnO films has been a subject of study by Hwai-En Lin and colleagues. Researchers have shown considerable interest in exploring the chemical and physical attributes of CMC/PVA blend materials, including the analysis of CMC/PVA samples, as demonstrated by Al-Muntaser and others. [12]. The Co/ZnO-CMC nanocomposite was thoroughly investigated to analyze its structural, optical, thermal, and electrical characteristics, with a specific focus on its potential utilization in solid-state battery applications. Channa et al. [13]. The hybrid nanocomposite films of PVA/PVP/CMC-ZnO were fabricated through the solution casting technique. [14] The solution casting technique was effectively utilized to fabricate lightweight and elastic polymer nanocomposites of CMC/PVA/ZnO-NPs in a recent study, resulting in enhanced optical properties. ZnO nanoparticles were incorporated as conducting fillers, while a CMC/PVA blend was utilized as the polymer matrix. Various techniques and protocols were examined to systematically analyze the optical and structural characteristics of this composite system. The significance of this study in academia lies in the comprehension of the fundamental nanoscale mechanisms that improve the functional characteristics of composite materials. This research seeks to improve the structural and optical features of CMC/PVA/ZnO nanocomposite-based films through photo-irradiation (UV light) exposure of the as-prepared samples.

2. THEORETICAL PART

The proportion of the incident light beam that is not reflected upon striking a material surface is either absorbed or transmitted through the substance. The amount of beam that is absorbed is influenced by the thickness of the materials and the interaction of photons with them, as stated by the Beer-Lambert Law. Equation (1) establishes the connection between the brightness of the incident light and the light that is transmitted [15].

$$I = I_o e^{-\alpha t} \tag{1}$$

The incident and transmitted light intensities are denoted by (Io) and (I), respectively, the symbol (α) is used to denote the optical absorption coefficient, while (t) is used to represent the thickness of the film. The optical absorption coefficient (α) can be determined from the optical absorption spectrum Equation (2) by using the absorbance relation A = log (Io/I) .[16,17]

$$\alpha = 2.303 \frac{A}{t} \tag{2}$$

The energy band gap can be calculated using the following equation, where λ represents the wavelength of the incident light. [18,19]

$$\alpha h \upsilon = B(h\upsilon - E_g)^r \tag{3}$$

Where: E_g: optical energy gap for indirect transition in (eV), B: constant depended on type of material, r: The refractive index is unchanging and can vary between 1/2, 3/2, 2, or 3, contingent upon the specific material and the nature of the optical transition.

Scherer's equation is utilized to estimate the average crystallite size (D). Subsequently, various calculations can be performed based on this estimation. [20,21].

$$D = \frac{\kappa \lambda}{\beta \cos\theta}. \tag{4}$$

The lattice parameter (a) was determined through calculations based on X-ray diffraction findings, utilizing specific mathematical relationships [22]

$$\frac{1}{d_{hkl}^2} = \frac{(h^2 + k^2)}{a^2} + \frac{l^2}{c^2}. \tag{5}$$

Where d_{hkl}: is the inter planer distance for a given plane with Miller indices (hkl).

3. EXPERIMENTAL PART

The powdered carboxymethyl cellulose (CMC) was obtained from AVONCHEM, a UK-based company, with an average molecular weight of 67.000 g/mole. The powdered PVA was acquired from Thomas Baker, with an average molecular weight of 14.000 g/mole, and was manufactured in India. Zinc oxide (ZnO) nanoparticles with an average particle size of 22.15 nm were utilized in the fabrication of a CMC/ PVA/ZnO nanocomposite film, which was manufactured in the United States by Sky Spring Nanomaterials, Inc. The combination of CMC and PVA was prepared by dissolving 0.25 g of each polymer in 17 ml of distilled water through the solution casting technique. Subsequently, ZnO NPs powder was added in varying amounts of (0.008) g, along with 8 ml of distilled water, and mixed with the precursor solution of CMC/PVA blend. In order to achieve full dissolution, the precursor solution underwent magnetic stirring for a duration of 24 hours at ambient temperature. The CMC/ PVA/ZnO nanocomposite was then formed by carefully pouring the solution onto glass plates measuring (5) cm in diameter, and subsequently allowing it to gradually evaporate over a period of (5-9) days at room temperature. The outcome of this procedure led to the creation of a consistent

layer. The nanocomposite film composed of as-synthesized CMC /PVA/ZnO exhibited a measured thickness of (0.044) μm. Moreover, the as-prepared films were exposed to UV sterlizer (UV -209b) (8) watt (220-275) nm made in China. The sample was exposed to the lamp for durations of 20, 45, and 75 hours, with the distance between the sample and the lamp kept constant for each irradiation time. The T70/T80 Series UV/Vis Spectrometer, a UV-Visible spectrophotometer, was employed to examine the absorption and transmission spectra across the wavelength range of 200-900 nm. The composite characteristics of each film were assessed through FTIR spectroscopy (Bruker-Tensor 27 with ATR unit). The samples' thicknesses were measured utilizing a Japanese-made digital micrometre model (Tasha), which has a measurement accuracy of (0.001) mm and a measurement range of (0-150) mm. Fourier transform infrared spectroscopy (FTIR) was performed on all films utilizing an FTIR spectrometer (Bruker-Tensor 27 type with ATR unit). A completely computerized X-ray diffractometer 106 Materials Science and Modern Manufacturing (XRD; Aeris – Malvern Panalytical's company-made in Holland, the investigation focused on analysing the composition of CMC, PVA polymer, and CMC/PVA/ZnO and ZnO nanocomposite films at Al Khora Company. High-resolution scanning electron microscopy FESEM (Inspect F50-EFI company-made in Holland, the surface composition and the presence of cracks were analysed in pure CMC and CMC/ZnO nanocomposite films by Al Khora Company.

3. RESULTS AND DISCUSSION
XRD, Field Emission Scanning Electron Microscope (FESEM), FTIR, Uv- Visible Spectroscopy and UV irradiation, were performed to examine the structure and morphology of the samples

3.1. X-ray diffraction analysis (XRD)
Display Figure 1 (A) the ZnO nanoparticles' X-ray diffraction pattern. It was evident from the study of the ZnO nanoparticles' X-ray diffraction patterns that they were single-phase in nature [21].
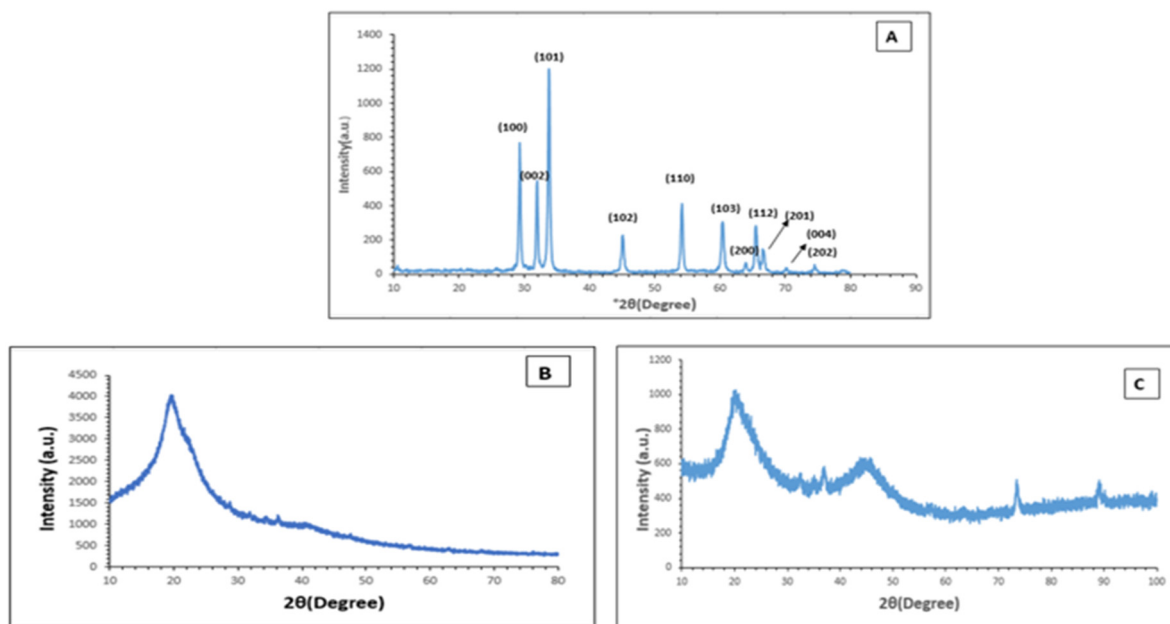
Figure 1. Display the X-ray diffraction patterns of (A) ZnO NPs, (B)CMC/PVA/Zno Nanocomposite Film and (C) CMC/PVA/ZnO Nanocomposite Film after UV-irradiation for 75h

When the peaks for ZnO occur at an angle of 2Θ = 29.385, 32.0275, 33.8567, 45.1378, 53.8266, 54.2048, 60.4452, 63.9796, 65.5435, 66.6788, and 74.5686 degrees, the crystalline nature results. With crystal planes (100), (002), (101), (102), (110), (103), (200), (112), (201), (004) and (202), ZnO has a hexagonal crystal structure. The values are in agreement with the data on the International Center of Diffraction Data (ICDD) card No. (36-1451). that agree with research [23,24] The estimated average size of ZnO nanoparticles (NPs) average 25.5203 nm, as determined using equation (4) and presented in Table (1).

In addition, a solitary peak at 2θ = 19.6314° was observed in the X-ray diffraction (XRD) analysis of the PVA/CMC/ZnO nanocomposite film prior to exposure to UV radiation, as illustrated in Figure 1-B, that implies the amorphous structure of the CMC/PVA/ZnO nanocomposite film. The XRD spectrum of the CMC/PVA/ZnO nanocomposite film, as shown in Figure (1-C), demonstrates several peaks at 2θ = 20.79, 32.47, 36.89, 45.66,73.47, 49.02, with lower intensity compared to Figure (1-B) after being exposed to UV-irradiation for 75 hours. he results suggest that UV-irradiation has influenced the film by increasing the amorphous phase and reducing its crystallinity. The prolonged UV-irradiation time of 75 hours has led to an increase in disorder and defects in the structure, ultimately causing a

reduction in the degree of crystallinity of the film. The two polymers utilized in the present study exhibited characteristics of semi-crystalline materials due to the presence of both crystalline and amorphous regions. Additionally, the broad peak observed in the CMC/PVA/ZnO film may be attributed to the crystalline cellulose structure of CMC [25,26].

Table 1. XRD Parameters for ZnO

	2θ (deg)	FWHM (deg)	Intensity (I/Io)	d ($A°$)	D (nm)	(hkl)
1	29.385	0.3337	57	3.03709	25.27	(100)
2	32.0275	0.3252	42	2.79228	25.93	002)
3	33.8567	0.3449	100	2.64548	24.45	(101)
4	45.1378	0.4079	19	2.00707	20.67	(102)
5	53.8266	0.1734	4	1.70179	48.64	(110)
6	54.2048	0.365	36	1.6908	23.10	(103)
7	60.4452	0.4134	27	1.53031	20.40	(200)
8	63.9796	0.3933	4	1.45403	21.44	(112)
9	65.5435	0.3686	26	1.42307	22.88	(201)
10	66.6788	0.4067	12	1.40157	20.73	(004)
11	74.5686	0.3107	4	1.2716	27.14	(202)

3.2. Field Emission Scanning Electron Microscope (FESEM)

The technique employed serves to characterize the surface morphology of ZnO nanoparticles, as well as PVA/CMC/ZnOnanocomposite films, both prior to and following 75 hours of UV irradiation, as illustrated in Figures 2(A-B and C) . The FESEM image in Figure (2-A) confirms the formation of ZnO nanoparticles depict dense clusters of particles, indicating their spherical and granular morphology. A higher resolution FESEM image reveals an aggregation of particles with uniform size, suggesting a multidimensional structure. These findings are consistent with previous research conducted by other scholars [27,28] Fig. (2-B) The CMC–PVA/ZnO nanocomposite film displayed small white particles unevenly distributed across the surface of the biopolymer matrix, indicating the presence of ZnO nanoparticles and that the pores were tighter before UV-irradiation. The FESEM image depicted in Fig. (2-C) illustrates a surface that appears rougher due to the significant impact of UV-irradiation on the CMC/PVA/ZnO nanocomposite film. The shape of the film underwent a transformation, resembling a mixture of large and small non-uniform prominent particles.
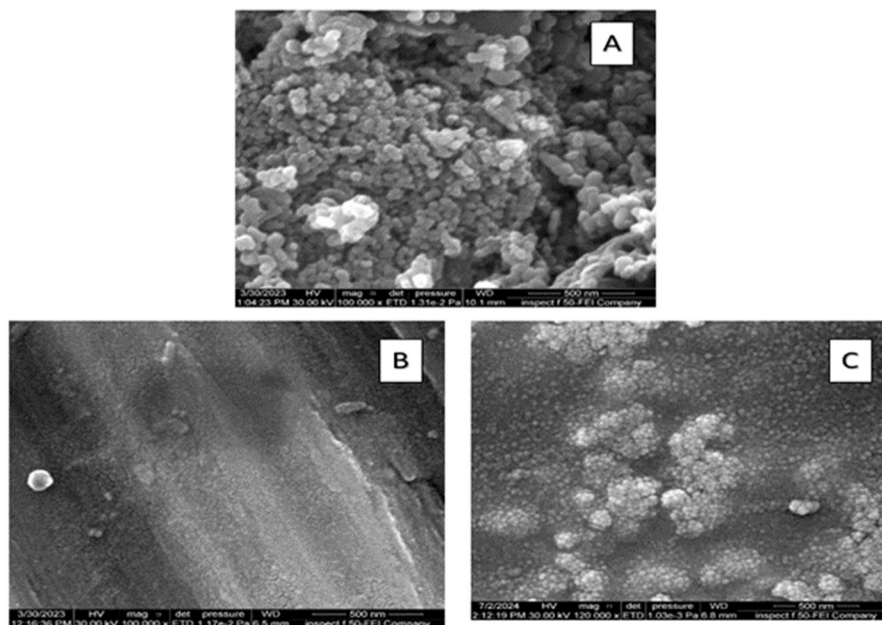
Figure 2. FESEM images for (A) ZnO NPs, (B) CMC/PVA/ZnONanocomposite Film Before UV-Irradiation, and (C) CMC/PVA/ZnO Nanocomposite Film after UV-Irradiation for 75 h

The FTIR spectra illustrating the ZnO thin films that were prepared are displayed in Figure 3.The measurements were conducted at ambient temperature within the spectrum of 500–4000 cm^{-1}. The spectrum of pure ZnO-NPs powder depicted in the analysis of Fig (3-A) involved the use of infrared tests in order to determine the characteristics and quality of the metal NPs. The absorption bands in metals in the fingerprint region, particularly those below 1000 cm^{-1}, were a result of inter-atomic vibrations. Furthermore, the peaks at (708.69 and 1505.58) cm^{-1} indicate the stretching and deformation vibrations of Zn-O, respectively. The recorded metal-oxygen vibrations of the individual metal oxides align with the frequencies reported in existing literature [29]. Moreover, an analysis of the FTIR spectrum of the

PVA/CMC/ZnO nanocomposite film prior to UV irradiation was conducted, as illustrated in Figure (3-B) and Table (2). The CMC and PVA polymers exhibited O-H and C-H stretching modes, respectively, with infrared peaks at (3200-3550) cm^{-1} and (2920) cm^{-1}. Moreover, the composite films displayed a distinct O=C=O stretching mode at (1340-1360) cm^{-1}.
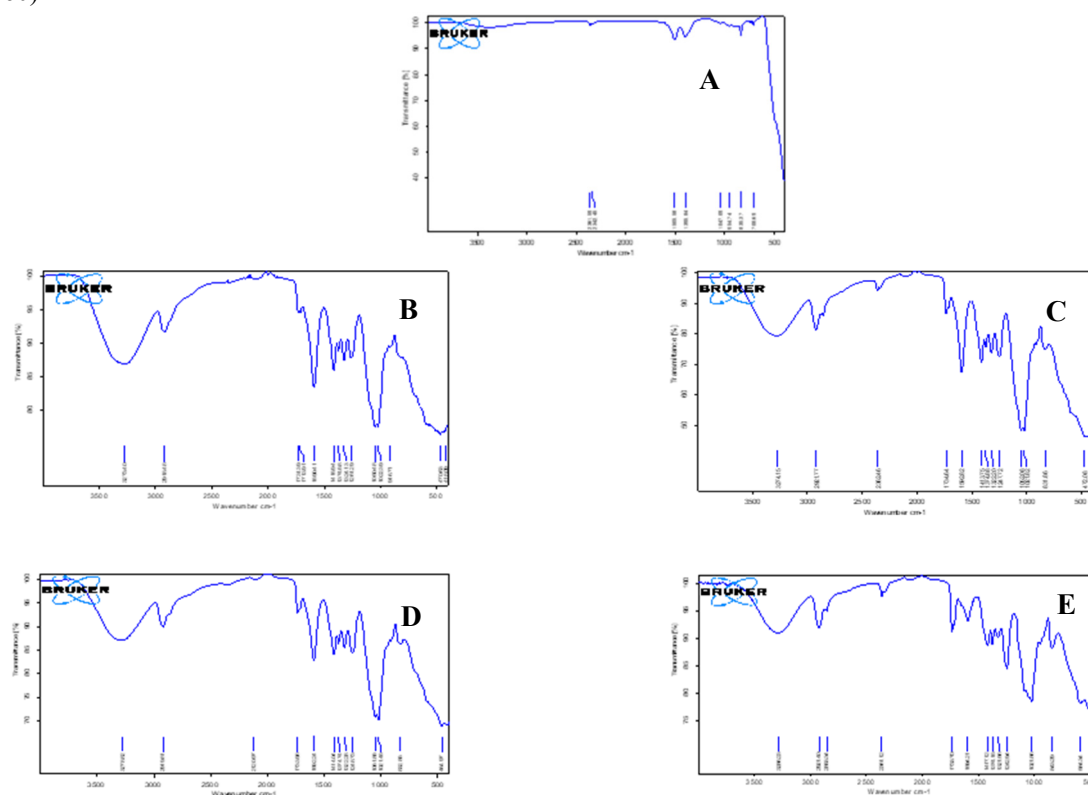
Figure 3. A-F.- The FTIR spectra of (A) ZnO NPs, (B) CMC/PVA/ZnO nanocomposite films before UV-irradiation and (C-E) after UV-irradiation at different times; 20 h, 45 h, and 75 h.

Furthermore, the CMC polymer exhibited an asymmetrical stretching vibration of COO- at (1591.00) cm^{-1}. The blend films contained the C=O carbonyl stretch bond (1733.55cm^{-1}) from vinyl alcohol, along with acetate groups (PVA polymer). The IR absorption bands at (1414.61 cm^{-1}), (1300-1461 cm^{-1}), and (1050-1300) cm^{-1} were designated for the C-H scissoring and C-H bending, as well as C-O stretch of PVA polymer, respectively [5, 30,31]. Based on the findings of the FTIR analysis, it was confirmed through the FTIR spectra that a nanocomposite film of CMC/PVA/ZNO was formed, showing a minor shift in the IR peaks. The polymers and ZNO NPs were effectively mixed together physically without any chemical bonding taking place. It was observed that the presence of ZNO NPs did not alter the IR spectral features of the polymer matrix. These results provide further validation to the conclusions drawn in a previous study [32,33,34]. The influence of UV exposure on the composition properties of PVA/CMC/ZnO nanocomposite films is illustrated in Figs. (3 C-E). The IR absorption bands corresponding to different irradiation times (20 45, 75) are specified in Table (2).

Table 2. FTIR-Characteristic of CMC/PVA/ZnO Nanocomposite Film

Assignments	Wavenumber (cm^{-1})		
	After 20h	After 45h	After 75h
O-H Stretching	3274.15	3278.82	3286.23
C-H stretching	2921.77	2919.81	2921.40 2853.34
C-H, CH2 bending	2362.46	2120.97	2361.12
COO- stretching Carbonyl group	1734.64 1592.82	1733.98 1592.24	1733.70 1594.21
C-H scissoring	1413.75 1322.20	1414.04 1374.74 1322.28	1417.12 1373.15 1321.56
C-O stretch	1247.72 1052.08 1021.82	1248.73 1051.85 1021.45	1242.94 1021.86
1,4--β Glycoside of Cellulos	831.86	832.85	834.29

Figs. 3 C-E show that the IR peaks of OH stretching mode (3200-3550) cm^{-1} were observed for all irradiation times. Vibrational transitions ranging from 4000 to 3275 cm-1 were observed during the time intervals of 20, 45 and 75 hours. The stretching of C-H bonds at 2920 cm-1 was noted in both PVA and CMC polymers, with some variations in wavenumber. Additionally, the absorption related to the single bond character of C=O carbonyl stretching at 1733.61 cm^{-1} was observed in vinyl alcohol and acetate groups (PVA polymer), while the C-O stretch bond (1050-1300 cm^{-1}) was present throughout all irradiation times. New IR peaks were observed at different times of irradiation, including 1592.82 cm^{-1} for 20 h 1592.24 cm^{-1} at 45 h, 1594.21 cm^{-1} at 75h. Additionally, asymmetrical COO-stretching (1591.67 cm^{-1}) and CH scissoring (1300-1461 cm-1) of a carbonyl group were consistently observed throughout the irradiation process. The origin of the IR absorption bands observed can be attributed to the exposure of the samples to UV radiation. Furthermore, after 26 hours of irradiation, A recent IR band at 1417.12 cm^{-1} associated with C-H bending was identified the CC rocking mode was observed at 20, 45, and 75 hours of irradiation. The infrared (IR) findings of PVA/CMC/ZnO nanocomposite films exposed to UV-irradiation for varying durations indicate that the consistent intensities of the aforementioned IR peaks (2919, 1417, 1374, 1322, and 1052 cm^{-1}) changed as the UV exposure time increased. These results can be attributed to the structure of PVA, which consists of parallel chains connected by hydrogen bonds. The impact of UV irradiation on the PVA/CMC/ZnO nanocomposite film is significant, affecting both hydrogen bonding and chain order. The decrease in intensity of these bands under UV radiation suggests that there was no change in the chemical structure, only in the value transmission, and no bond appeared or disappeared. Furthermore, the FTIR spectrum for all samples indicates that there were no chemical interactions between the nanoparticles and polymers, suggesting that only physical reactions occurred.

3.4. Ultraviolet-visible (UV-vis) spectroscopy

The UV-Visible absorption spectra were analyzed for a blend film of CMC/ PVA and a nanocomposite film of PVA-CMC/ZnO, as illustrated in Figure 4 .The UV absorption edge for the CMC/PVA film was observed to be approximately 245 nm, indicating a possible $\pi \rightarrow \pi^*$ electronic transition. This finding is in agreement with prior studies (25-29), thereby affirming the results. The UV absorption edge of the PVA/CMC/ZnO nanocomposite film was measured at 255 nm. There is a significant enhancement in the light absorption intensity of this film in both the UV and visible regions compared to the CMC/PVA blend film spectrum. The incorporation of ZnO NPs into the polymer matrix is believed to be the cause of these results. This conclusion is consistent with findings from prior research [35,5,36].
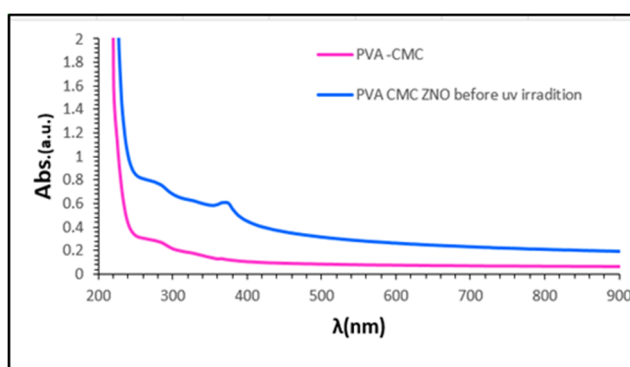
Figure 4. UV- Vis Absorption spectrum for CMC/PVA/ZnO Nanocomposite Films at Different UV-irradiation Times
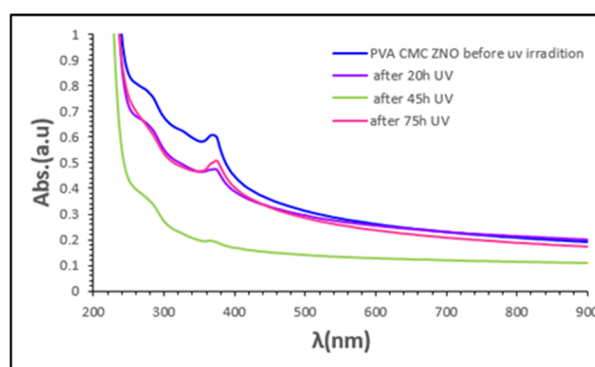
Figure 5. UV- Vis Absorption spectrum for CMC/PVA/ZnO Nanocomposite Films at Different UV-irradiation Times
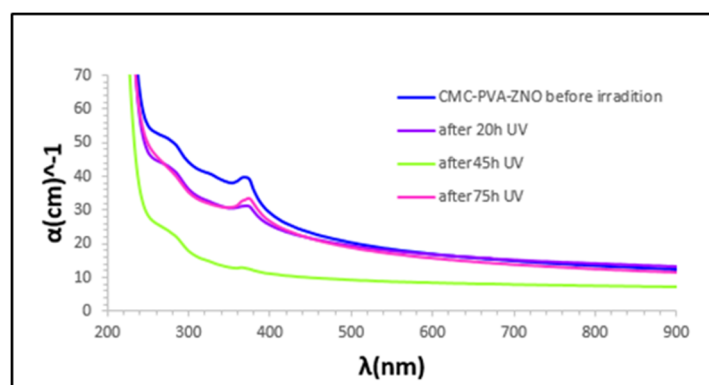
Figure 6. UV-Vis Absorption Coefficient for CMC/PVA/ZnO Nanocomposite Films at Different UV-irradiation Times

Figure 5 illustrates the absorption spectra of CMC/PVA/ZnO nanocomposite films before and after UV irradiation for different durations (20, 45, and 75 hours). The figure shows that the absorption intensity increased with UV-irradiation time compared to the unirradiated sample. This increase was attributed to the higher energy of atoms, resulting in more

collisions between incident atoms, leading to decreased transmittance and increased absorbance [35,36] Additionally, A notable shift towards longer wavelengths (from 260 nm to 280 nm) in the absorption edge was detected, accompanied by increased intensity as a result of extended UV-irradiation exposure. The results demonstrate that the UV-irradiation impact led to a reduction in the optical energy band-gap of the synthesized film, as it generated defect levels, consequently enhancing the influence of the defects Moreover, the absorption coefficient (α) for each sample was determined utilizing Equation (2) illustrated in Figure 6.This parameter characterizes the ability of a substance to absorb light of a particular wavelength over a given distance. In cases where the absorption coefficient value was below ($\alpha < 104$ cm^{-1}), it indicated the presence of an indirect electronic transition [37].

Figure 7 illustrates the variation in the optical energy band gap (Eg) of CMC/PVA/ZnO nanocomposite films before and after exposure to UV radiation. The findings suggest that increasing the UV exposure time from 20 to 75 hours resulted in an increase in the Eg values of the films from 4.43 to 4.55 eV, as outlined in Table 3. Moreover, extending the UV exposure time to 75 hours led to a decrease in the Eg of the film. This phenomenon can be attributed to the rise in disorder within the film due to the emergence of new defect levels in the band-gap of the nanocomposite film, ultimately leading to a narrowing of the Eg [35.37,38]
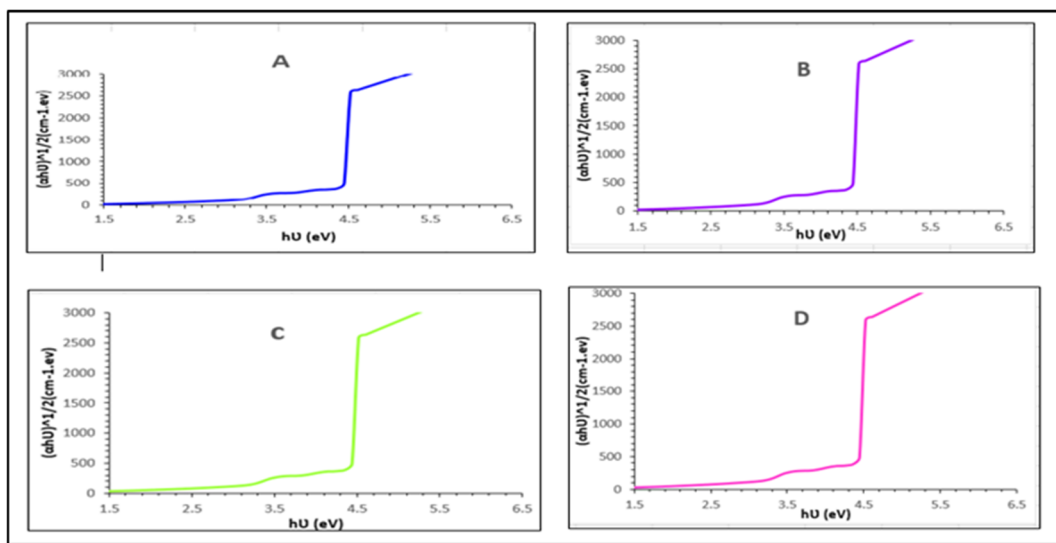
Figure 7. UV-Vis Optical energy gap for CMC/PVA/ZnO(A) CMC/PVA/ZnO Nanocomposite Film Before UV-Irradiation(B) CMC/PVA/ZnO Nanocomposite Film after UV-Irradiation for 20h(c) CMC/PVA/ZnO Nanocomposite Film after UV-Irradiation for 45h(D) CMC/PVA/ZnO Nanocomposite Film after UV-Irradiation for 75h

Table 3. Energy band gap value of CMC/PVA/ZnO Nanocomposite Films

Eg (eV)	UV-irradiation times (h)
4.43	0
4.52	20
4.55	45
4.50	75

CONCLUSIONS

The investigation focused on the synthesized CMC/PVA/ZnO nanocomposite film prepared through a simple solution casting method and the impact of UV-irradiation duration on the resulting films. Analysis of XRD data indicated that the structure quality of the samples was altered by the UV-irradiation time, leading to an increase in their amorphous characteristics. The FESEM images displayed a notable change in the morphology of the nanocomposite films based on the duration of UV exposure. Furthermore, the FTIR spectrum illustrated that ZnO and UV exposure played a beneficial role in the polymer structure by establishing covalent bonds between PVA and CMC. Lastly, The UV-Vis analysis demonstrated an increase in the absorption strength of the nanocomposite films as a result of the notable impact of ZnO NPs and UV exposure. The change in the optical band gap of the films, linked to the length of UV exposure, indicates their potential use in optoelectronic applications.

Conflicts of Interest.
The authors declare no conflict of interest.
Data availability statement.
The data that support the findings of this study are available from the corresponding author upon reasonable request.

ORCID

🆔**Sarah A. Ibrahim,** https://orcid.org/0009-0008-6462-3414; 🆔**Abdelhedi Aydi,** https://orcid.org/0000-0001-9656-9688

REFRENCES

[1] V.S. Sangawar, and M.C. Golchha, "Evolution of the optical properties of Polystyrene thin films filled with Zinc Oxide nanoparticles," Int. J. Sci. Eng. Res. **4**(6), 2700 (2013). https://www.ijser.org/onlineResearchPaperViewer.aspx?Evolution-of-the-optical-properties-of-Polystyrene-thin-films-filled-with-Zinc-Oxide-nanoparticles.pdf

[2] H.G. Basavaraj, C.G. Renuka, C.A. Harihar, Y. Sangappax, B.L. Rao, and R. Madhukumar, "Physicochemical mechanical and optical properties of polymer inorganic composite thin films: Applications," AIP Conference Proceedings, **2244**, 110009 (2020). https://doi.org/10.1063/5.0009947

[3] E.M. Abdelrazek, A.M. Abdelghany, A.E. Tarabiah, and H.M. Zidan, "AC conductivity and dielectric characteristics of PVA/PVP nanocomposite filled with MWCNTs," Journal of Materials Science: Materials in Electronics, **30**, 15521–15533 (2019). https://doi.org/10.1007/s10854-019-01929-2

[4] A.Y. Yassin, A.M. Abdelghany, and R.S. Salama, and A.E. Tarabiah, "Structural, Optical and Antibacterial Activity Studies on CMC/PVA Blend Filled with Three Different Types of Green Synthesized ZnO Nanoparticles," Journal of Inorganic and Organometallic Polymers and Materials, **33**, 1855–1867 (2023). http://dx.doi.org/10.1007/s10904-023-02622-y

[5] Y.M. Jawad, M.F.H. Al-Kadhemy, and J.A.S. Salman, "Synthesis structural and optical properties of CMC/MgO nanocomposites," Mater. Sci. Forum, **1039**, MSF, 104–114 (2021). https://doi.org/10.4028/www.scientific.net/MSF.1039

[6] H.E. Ali, A. Atta, and M.M. Senna, "Physico-Chemical Properties of Carboxymethyl Cellulose (CMC)/Nanosized Titanium Oxide (TiO2) Gamma Irradiated Composite," Arab J. Nucl. Sci. Appl. **48**(4), 44–52 (2015).

[7] A.E. Tarabiah, H.A. Alhadlaq, Z.M. Alaizeri, A.A.A. Ahmed, G.M. Asnag, and M. Ahamed, "Enhanced structural, "optical, electrical properties and antibacterial activity of PEO/CMC doped ZnO nanorods for energy storage and food packaging applications,". J. Polym. Res. **29**(5), 1-16 (2022). https://doi.org/10.1007/s10965-022-03011-8

[8] A. Wibowo, M.A. Marsudi, M.I. Amal, *et al.*, "ZnO nanostructured materials for emerging solar cell applications". RSC Adv. **10**(70), 42838-42859 (2020). https://doi.org/10.1039/D0RA07689A

[9] Y. Sun, D. Wen, and X. Bai, "Nonvolatile ternary resistive switching memory devices based on the polymer composites containing zinc oxide nanoparticles". Phys Chem Chem Phys. **20**(8), 5771-5779 (2018). https://doi.org/10.1039/C7CP07887K

[10] A. Svobodova, D. Walterova, and J. Vostalova, "Ultraviolet light induced alteration to the skin.," Biomed. Pap. Med. Fac. Univ. Palacky. Olomouc. Czech. Repub. **150**(1), 25–38 (2006). https://doi.org/10.5507/bp.2006.003

[11] H. Lin, J. Hong, R. Nitta, Y. Kubota, Y. Katanayagi, H. Wagata, T. Kishi, *et al.*, "Effects of UV irradiation on the electrical and optical properties of solutionprocessed transparent ZnO films," Appl. Surf. Sci. **289**, 135–141 (2019). https://doi.org/10.1016/j.mssp.2020.105266

[12] A.A. Al-Muntaser, R.A. Pashameah, K. Sharma, E. Alzahrani, M.O. Farea, and M.A. Morsi. "α-MoO3 nanobelts/CMC-PVA nanocomposites: hybrid materials for optoelectronic and dielectric applications," J. Polym. Res. **29**(7), 1-11 (2022). https://doi.org/10.1007/s10965-022-03134-y

[13] M.M. Abutalib, and A. Rajeh, "Structural, thermal, optical and conductivity studies of Co/ZnO nanoparticles doped CMC polymer for solid state battery applications," Polymer Testing, **91**, 106803 (2020). https://doi.org/10.1016/j.polymertesting.2020.106803

[14] A.A. AlMuntaser, E. Alzahrani, H.M. Abo-Dief, A. Saeed, E.M. Alshammari, A.M. Al-Harthi, and A.E. Tarabiah, "Tuning the structural, optical, electrical, and dielectric properties of PVA/PVP/CMC ternary polymer blend using ZnO nanoparticles for nanodielectric and optoelectronic devices," Optical Materials, **140**, 13901 (2023). https://doi.org/10.1016/j.optmat.2023.113901

[15] K.H.H. Al-Attiyah, A. Hashim, and S.F. Obaid, "Fabrication of novel (carboxy methyl cellulose–polyvinylpyrrolidone–polyvinyl alcohol)/lead oxide nanoparticles: structural and optical properties for gamma rays shielding applications," Int. J. Plast. Technol. **23**(1), 39–45 (2019). https://doi.org/10.1007/s12588-019-09228-5

[16] A. Hashim, and A. Hadi, "Novel lead oxide polymer nanocomposites for nuclear radiation shielding applications," Ukrainian Journal of Physics, **62**(11), 978–983 (2017). https://doi.org/10.15407/ujpe62.11.0978

[17] T.A. Jasim, A.A. Saeed, F.J. Kadhum, and M.F.H. Al-Kadhemy, "Effect of Gamma Irradiation on The Optical Properties of PVA/Ag Nano-composite," GJSR Journal, **8**(2), (2020). http://dx.doi.org/10.1088/1757-899X/928/7/072137

[18] J.D. Patterson, and B.C. Bailey, *Solid-state physics: introduction to the theory*, (Springer Science & Business Media, 2007).

[19] N.A. Darweesh, A.A. Saeed, and M.F. Al-Kadhemy, "Influence of Weathering on Physical Properties and Sun Light Transmitted through PMMA/ Safranin Films for Greenhouse Applications," Mustansiriyah Journal of Pure and Applied Sciences, MJPAS **1**(1), 40-53 (2023).

[20] F.M. Nada, S.A. Hussain, S.K. Muhammad, and A.H.O. Alkhayatt, "Hydrothermally growth of TiO2 Nanorods, characterization and annealing temperature effect," Kuwait Journal of Science, **48**(3), 1-10 (2021). https://doi.org/10.48129/kjs.v48i3.10417

[21] P.S. Sundaram, T. Sangeetha, S. Rajakarthihan, R. Vijayalaksmi, A. Elangovan, and G. Arivazhagan, "XRD structural studies on cobalt doped zinc oxide nanoparticles synthesized by coprecipitation method: Williamson-Hall and size-strain plot approaches," Physica B: Condensed Matter, **595**, 412342 (2020). https://doi.org/10.1016/j.physb.2020.412342

[22] C. Hammond, *The basics of crystallography and diffraction*, (Oxford, 2001).

[23] T. Ji, R. Zhang, X. Dong, D.E. Sameen, S. Ahmed, S. Li, and Y. Liu, "Effects of Ultrasonication Time on the Properties of Polyvinyl Alcohol/Sodium Carboxymethyl Cellulose/Nano-ZnO/Multilayer Graphene Nanoplatelet Composite Films," Nanomaterials, **10**(9), 1797 (2020). https://doi.org/10.3390/nano10091797

[24] S.L. Perumal, P. Hemalatha, M. Alagara, and K. N. Pandiyaraj, "Investigation of structural, optical and photocatalytic properties of Sr doped ZnO nanoparticles," Int. J. Phys. Sci. **4**, 1-13 (2015). https://doi.org/10.23851/mjs.v34i1.1226

[25] Y. Zahedi, B. Fathi-Achachlouei, and A.R. Yousefi, "Physical and mechanical properties of hybrid montmorillonite/zinc oxide reinforced carboxymethyl cellulose nanocomposites," International Journal of Biological Macromolecules, **108**, 863–873 (2018). https://doi.org/10.1016/j.ijbiomac.2017.10.185

[26] G.A.H.A. Jabbar, A.A. Saeed, and M.F. Hadi AL-Kadhemy, "Optical characteristics and bacterial-resistance ability of PVA/ZnO nanocomposites," Kuwait Journal of Science, **50**(3), 209-215 (2023). https://doi.org/10.1016/j.kjs.2023.03.004

[27] Q.M. Al-Bataineh, A.A. Ahmad, A.M. Alsaad, and A.D. Telfah, "Optical characterizations of PMMA/metal oxide nanoparticles thin films: bandgap engineering using a novel derived model," Heliyon, **7**(1), e05952 (2021). https://doi.org/10.1016/j.heliyon.2021.e05952

[28] M. Anandalli, T.M. Kanakaraj, V. Hebbar, J. Naik, and R.F. Bhajantri, "Physico-chemical properties of PMMA/ZnO nanocomposite capped with 1 chloro-9, 10-bis (phenyl ethynyl) anthracene," in AIP Conference Proceedings, **1953**(1), 30189 (2018). https://doi.org/10.1063/1.5032524

[29] S. Maensiri, P. Laokul, and V. Promarak, "Synthesis and optical properties of nanocrystalline ZnO powders by a simple method using zinc acetate dihydrate and polyvinyl pyrrolidone," J. Cryst. Growth, **289**(1), 102-106 (2006). https://doi.org/10.1016/j.jcrysgro.2005.10.145

[30] S. Hashem, M. Fadhil, and K. Naji, "Study Physical Characteristics of Polyvinyl Alcohol/Carboxymethyl cellulose Blend Films," **55**(393), 298–305 (2022). https://doi.org/10.48129/kjs.20553

[31] H. Helmiyati, Z.S.Z. Hidayat, I.F.R. Sitanggang, and D. Liftyawati, "Antimicrobial packaging of ZnO–Nps infused into CMC–PVA nanocomposite films effectively enhances the physicochemical properties," Polymer Testing, **104**, 107412 (2021). https://doi.org/10.1016/j.polymertesting.2021.107412

[32] V.S. Sangawar, and M.C. Golchha, "Evolution of the optical properties of Polystyrene thin films filled with Zinc Oxide nanoparticles," Int. J. Sci. Eng. Res. **4**(6), 2700-2705 (2013). https://www.ijser.org/researchpaper/Evolution-of-the-optical-properties-of-Polystyrene-thin-films-filled-with-Zinc-Oxide-nanoparticles.pdf

[33] I. Kim, K. Viswanathan, G. Kasi, K. Sadeghi, S. Thanakkasaranee, and J. Seo, "Poly (Lactic Acid)/ZnO Bionanocomposite Films with Positively Charged ZnO as Potential Antimicrobial Food Packaging Materials," Polymers, **11**(9), 1427 (2019). https://doi.org/10.3390/polym11091427

[34] Y. Yao, Z. Sun, X. Li, Z. Tang, X. Li, J.J. Morrell, Y. Liu, *et al.*, "Effects of Raw Material Source on the Properties of CMC Composite Films," Polymers, **14**(1), 1–15 (2022). https://doi.org/10.3390/polym14010032

[35] N.T.T. Thuy, *et al.*, "Green synthesis of silver nanoparticles using plectranthus amboinicus leaf extract for preparation of CMC/PVA nanocomposite film," J. Renewable Mater. **9**(8), 1393–1411 (2021). https://doi.org/10.32604/jrm.2021.015772

[36] A.M. Youssef, *et al.*, "Development and Characterization of CMC/PVA Films Loaded with ZnO-Nanoparticles for Antimicrobial Packaging Application," Der Pharma Chemica, **9**(9), 157–163 (2017).

[37] T.S. Soliman, A.M. Rashad, I.A. Ali, S.I. Khater, and S.I. Elkalashy, "Investigation of Linear Optical Parameters and Dielectric Properties of Polyvinyl Alcohol/ZnO Nanocomposite Films," Phys. Status Solidi Appl. Mater. Sci. **217**(19), 1-8 (2020). https://doi.org/10.1002/pssa.202000321

[38] S. Villarruel, *et al.*, "Changes induced by UV radiation in the presence of sodium benzoate in films formulated with polyvinyl alcohol and carboxymethyl cellulose," Mater. Sci. Eng. C, **56**, 545–554 (2015). https://doi.org/10.1016/j.msec.2015.07.003

ДОСЛІДЖЕННЯ ВПЛИВУ УФ-ВИПРОМІНЮВАННЯ НА НАНОКОМПОЗИТНІ ПЛІВКИ PVA/ZnO, ВИГОТОВЛЕНІ МЕТОДОМ ЛИТТЯ З РОЗЧИНУ

Сара А. Ібрагім[a], Абдерразек Уеслаті[b], Абдельхеді Айді[b]
[a]Лабораторія багатофункціональних матеріалів і застосувань, Факультет наук Сфакса, Університет Сфакса, Сфакс, Туніс
[b]Лабораторія спектроскопічної характеристики та оптичних матеріалів, факультет природничих наук, Університет Сфакса, Сфакс, Туніс

Розглянуто синтез нанокомпозитних плівок, що містять карбоксиметилцелюлозу/полівініловий спирт (СМС PVA), змішаний з наночастинками оксиду цинку (ZnO NPs) простим методом лиття з розчину. Крім того, досліджено вплив наночастинок ZnO та УФ-опромінення протягом різної тривалості (20, 45, 75 годин) на морфологію (FE-SEM). Для аналізу підготовлених плівок використовуються рентгенівська дифракція (XRD), інфрачервона (FTIR) спектроскопія з перетворенням Фур'є та ультрафіолетова видима (UV-Vis) спектроскопія. Крім того, зображення скануючої електронної мікроскопії з польовою емісією (FE-SEM) показують помітну зміну в морфології нанокомпозитних плівок CMC PVA/ZnO, пов'язану зі значним впливом наночастинок ZnO та ультрафіолетового випромінювання. XRD-спектри демонструють модифікацію аморфної фази зразків у результаті УФ-опромінення. Аналіз FTIR показує, що вплив УФ-випромінювання позитивно вплинуло на структуру полімеру, про що свідчать помітні зміни в інфрачервоних піках. Крім того, результати УФ-видимої спектроскопії вказують на те, що довший час УФ-опромінення (75 годин) і додавання наночастинок ZnO призвели до покращення характеристик поглинання у створених плівках. Нанокомпозитні плівки демонстрували регульований енергетичний зазор (Eg), який змінювався між (4,52 еВ і 4,55 еВ), коли тривалість УФ-опромінення збільшувалася з (20 годин) (75 годин), що призвело до зменшення значення енергетичного зазору (Eg) до (4,50 еВ). Вважається, що це явище спричинене значним впливом УФ-випромінювання на розвиток структурних дефектів. Зрештою, на енергетичний розрив Eg нанокомпозитних плівок впливала тривалість ультрафіолетового випромінювання. Результати демонструють, що існує значний потенціал для використання нанокомпозитних плівок CMC/PVA/ZnO у різних важливих оптоелектронних застосуваннях.
Ключові слова: *CMC/PVA/ZnO; властивості нанокомпозитів; наночастинки ZnO; енергетична щілина; УФ-опромінення; ультрафіолет*

THERMOLUMINESCENCE BEHAVIOR AND KINETIC ANALYSIS OF QUARTZ UNDER GAMMA IRRADIATION

Aqshin Abishov, Sahib Mammadov, Muslim Gurbanov, Ahmad Ahadov, Aybeniz Ahadova

Institute of Radiation Problems, Ministry of Science and Education, Azerbaijan
Corresponding Author e-mail: a.abishov@irp.science.az
Received July 8, 2024; revised September 19, 2024; accepted September 30, 2024

This study investigates the luminescence characteristics of quartz samples irradiated with a 60Co gamma source across a dose range of 57 to 570 Gy. Prior to irradiation, the samples were annealed at 650°C for two hours. The thermoluminescence (TL) spectra were measured at a heating rate of 5°C/sec, revealing two primary peaks at approximately 200°C and 320°C. The intermediate peak displayed a shoulder around 150°C. It was observed that the peak temperature maximum (Tm) at 206±2°C remained constant regardless of the irradiation dose. The intensity of the intermediate peak decreased significantly over time, with a lifetime estimated at 8±2 days for most doses and 19±2 days for the highest dose (570 Gy). Dose-response studies showed a linear relationship between the TL intensity and the irradiation dose up to 600 Gy. Comparisons with natural quartz samples indicated significant differences in glow curve shapes and sensitivities. Computerized glow curve deconvolution (CGCD) methods confirmed that the annealed quartz glow curve could be described as a superposition of four first-order kinetic peaks. These findings provide important insights into the stability and behavior of TL signals in quartz, which are crucial for applications in radiation dosimetry and archaeological dating.
Keywords: *Quartz; Isothermal decay, Lifetime; Radiation dosimetry; GlowFit*
PACS: 78.60.Kn

INTRODUCTION

Quartz is widely used in dating and dose reconstruction applications and it requires precise determination of the trap parameters for the intermediate glow peaks in this mineral [1,2]. Investigation of the lifetimes of these peaks is essential for determining the appropriate time frame for conducting retrospective measurements. These intermediate energy level peaks appear in the glow curve within the temperature range of 150–250°C. The intermediate temperature peaks of quartz can be used for dose determination because, due to their relatively short lifetimes, the geological TL signal, i.e., peaks in the higher temperature region, is expected to be weak compared to that produced by artificial radiation. Burnt bricks or roof slabs, which form a significant and integral part of building structures, are widely used in retrospective and emergency dosimetry. As trapped electrons are released by heating, the electrons accumulated over time are released and the TL intensity is canceled by their production.

This research explored the thermoluminescence (TL) properties of quartz [3] identified ten trapping centers with activation energies between 0.62 and 2.96 eV through kinetic analysis of the glow curve. Each glow curve component was tested for linearity. Further analysis using Tm-Tstop and various heating rates (VHR) provided the kinetic parameters, including activation energy (E, eV). The quartz samples' minimum detectable dose (MDD) was determined, and the dosimeter demonstrated good reproducibility. The fading signal was also evaluated over different storage durations.

The TL characteristics and the structural changes in the irradiated quartz were analyzed by examining the crystallinity index through infrared bands of the SiO_4 tetrahedron in the mid-infrared region [4]. Colorless quartz, containing aluminum impurities, turns dark smoky upon exposure to ionizing radiation. The TL glow curve analysis identified four trapping sites with TL peaks at 169, 212, 279, and 370°C. Kinetic parameters, including the order of kinetics, activation energy, and frequency factor, were determined using Chen's peak shape method and the initial rise method. The study discussed the role of $[AlSiO_4/h+]0$ centers (formed when Si^{4+} is replaced by Al^{3+} and charge compensated by a hole) in color development and luminescence, correlating FTIR and TL results. A range of studies have explored the influence of pre-treatment on the thermoluminescent properties of quartz. The glow curves of various quartzes showed glow peaks around 150-170, 190-220 and 290-320°C, which have been reported by several researchers [5,6]. Kitis [7] found that the sensitivity of quartz to heat and irradiation treatments varied, with a significant change in sensitivity occurring at around 10 Gy. Those changes were significant when predose treatment was combined with the heat treatment. This was further explored by [8], who observed that the intensity of glow peaks in synthetic quartz increased between room temperature and 200°C after heat treatments, with good stability above 250°C. The glow-curve of a quartz annealed at 900ºC irradiated to 10 Gy shows three peaks; the main peak at 71 °C and two other peaks at 125°C and 177°C [9]. The center responsible for peak at 177°C is stable at ambient temperature and estimated values for the activation energy and frequency factor of the peak were as ~1.24 eV and ~10^{12} s^{-1} respectively. The intensity of the peak at 177°C shows sublinear dose dependency in the range 1–300 Gy. Based on the impact of irradiation dose on the peak position authors suggested that the peak follows non-first-order kinetics. The involvement

of specific defects in the production of thermoluminescence in quartz was highlighted by [10], who identified the $(AlO_4)0$ center and suggested the involvement of H^+ ions. These studies suggest that pre-treatment can significantly impact the thermoluminescent properties of quartz, with specific defects playing a key role in this process.

TL peaks around 150 and 200°C were reported also in [11], while glassy quartz exhibited the second peak at 300°C. TL intensity as a function of heating rate showed a decrease in TL intensity and a shift of TL peaks to higher temperatures due to thermal quenching. Using a computerized glow curve deconvolution program, the glow curve of quartz was resolved into five distinct peaks.

The thermoluminescence (TL) peaks in the intermediate temperature range (350-550 K) of the quartz glow curve are crucial for dose evaluation in both dating and retrospective dosimetry. Despite numerous studies on the TL properties of quartz in this temperature range, there is no consensus on the published values of the trap parameters (thermal activation energy and frequency factor). There is also inconsistency in measurements across different types of quartz and a lack of a consistent progression of trap depth with glow curve temperature.

MATERIALS AND METHODS

Retrospective and emergency dosimetry considers fired bricks and other ceramic products that contain quartz as potential dosimeters. Quartz can be present in the composition of these materials as natural impurities in the raw materials or as fillers to improve the quality of the fired products. In this work we used quartz extracted from fired bricks. The extraction procedure for quartz from intact brick samples involves soaking the sample in dilute hydrofluoric or hydrochloric acid in an ultrasonic bath at room temperature for several hours to loosen the clay matrix. Once softened, the sample is rinsed in distilled water and gently crushed. The crushed sample is then dried, sieved, magnetically separated, and rinsed in acetone. Etched crystals are treated with aluminum chloride, washed, and re-sieved before TL analysis. The quartz fraction with a size of 100-200 μm was used for the experiments. Part of the samples were heated to 650°C for two hours before irradiation. Irradiation was carried out in a gamma irradiator with a dose rate of 0.095 Gy/sec. The dose rate was determined by the electron paramagnetic resonance method using alanine dosimetry using the Magnettech Miniscope MS400 EPR Spectrometer [12]. TL measurements were performed in a Harshaw TLD3500 Manual Reader in a N_2 atmosphere using a Chance Pilkington HA-3 heat- absorbing filter with 80% transmittance response in visible regions (400–700 nm). The methodology of TL measurement is described in previous papers [13,14].

RESULTS AND DISCUSSIONS

Luminescence curves of quartz samples irradiated with a ^{60}Co gamma source in the range of 57 to 570 Gy are shown in Figure 1. Prior to irradiation, the quartz samples were heated at 650°C for two hours. TL spectra were measured at a heating rate of 5°C/sec. Since the TL spectra were taken one day after irradiation, a lower temperature peak in the region of 110°C is not observed. This peak is known to have a short half-life even at room temperature. The spectra clearly show two main peaks, the first at about 200°C and the second at 320°C. The first peak in turn has a shoulder on the left side somewhere around 150°C. The inset in Figure 1 also illustrates the dose dependence of the position of the peak temperature maximum (Tm). The value of Tm is 206±2 °C and is independent of the irradiation dose. As shown below, the intensity of the intermediate peak decreases with time during storage, even at room temperature. It was found that the peak positions remain stable during long-term storage, although the intensity decreases by more than half.
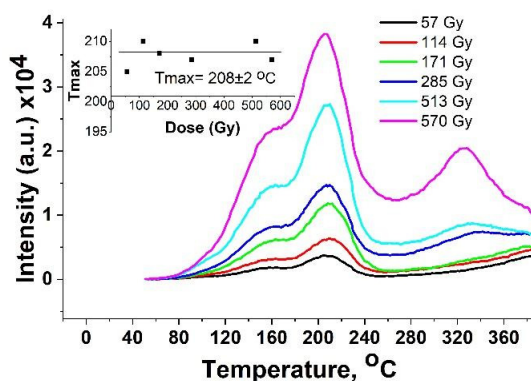
Figure 1. Glow curves of samples heated at 650°C for two hours and irradiated at different doses. The dose dependence of the position of peak maximum temperature (Tm) is given in the inset

The dependence of the temperature at peak maximum ($Tmax$) of a thermoluminescence (TL) glow peak on the radiation dose is a well-known feature in the TL literature. This shift in $Tmax$ with accumulated dose makes it a dynamic experimental parameter. The OTOR model predicts this effect, though it is more commonly explained using the empirical general order kinetics equation. In this framework, the dependence of $Tmax$ on radiation dose is stronger for second-order kinetics and diminishes for first-order kinetics. However, experimental verification of this shift is not

consistent, despite extensive TL literature on dose response studies. The OTOR model also forms the basis for the single unit TL peak model, which helps in evaluating kinetic parameters and deconvoluting complex TL glow curves but is not used to explain broader TL effects like dose response and sensitivity variations.

Figure 1 clearly shows that the temperature at peak maximum ($Tmax$) of any TL peak for all studied materials remains constant across different doses, indicating no dependence of $Tmax$ on dose. Regardless of the events during trap filling (irradiation), a certain number of traps are filled with n_0 electrons by the end of irradiation, making the unbleached TL integral correspond to N traps, where $n_0 = N$. After thermal or optical bleaching, some trapped electrons (n_{01}) escape, leaving a portion (N_1) of traps empty. During subsequent TL readout, the number of empty traps is $N - N_1$. Increasing the duration of thermal or optical bleaching increases the number of empty traps ($N - N_1$), thus enhancing the probability of re-trapping, which contributes to the shift in $Tmax$ and an increase in kinetic order.
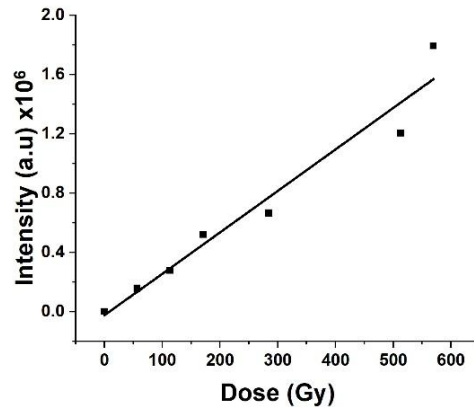
Figure 2. Dose dependence of intermediate temperature TL peaks of quartz heated at 650°C.

The predictions concerning the shift of $Tmax$ as a function of radiation dose has been assessed by [15] using TL peaks derived according to the OTOR phenomenological model, as well as using synthetic TL peaks derived from analytical expressions. It is shown that in the case of non-first-order kinetics, the shift of $Tmax$ as a function of trap emptying is confirmed by experimental results.

Dose dependence of annealed quartz presented in Figure 2. The TL intensity of this glow peak was calculated from the area under the glow curve in the temperature range 180-240°C. Figure 2 shows that the intensity of the glow peak at 206oC shows a linear dependence on the irradiation dose within the dose range up to 600 Gy.
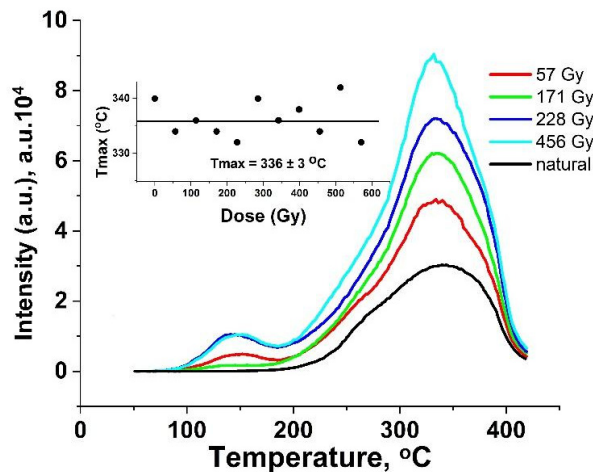

Figure 3. Glow curves of unheated samples irradiated at different doses. The dose dependence of the position of peak maximum temperature (Tm) is given in the inset

For the composition with the annealed quartz, the glow curves of the natural quartz are shown in Fig. 3. Changes in the shape of the glow curve are obvious: firstly, the natural quartz that has not been irradiated shows no peaks in the temperature region up to 250°C and only one broad peak above the 300°C temperature region. Secondly, the sensitivity of the peaks in the intermediate temperature range is several times lower than that of the annealed samples. At the same time, the peak at around 336°C shows no significant shift with increasing irradiation dose, again indicating that this peak or its components most likely follow first order kinetics (see inset in Fig. 3).

Computerized glow curve deconvolution (CGCD) methods were used to determine the number of peaks and kinetic parameters (kinetic orders b, activation energy E and frequency factor s) associated with the

thermoluminescence (TL) glow peaks in annealed quartz irradiated at 570 Gy (Fig.4). The results of the CGCD method analysis indicate that the glow curve of quartz annealed at 650ºC can best be described as a superposition of four glow peaks, all of which have first order kinetics. Estimated parameters of four peaks are listed in Table 1.
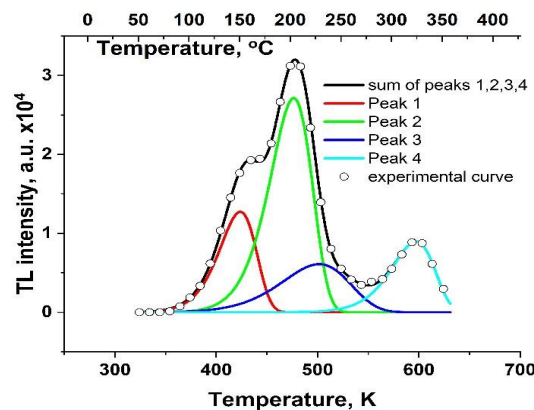
Figure 4. The TL spectrum of quartz deconvoluted into four first-order peaks. The quartz was heated to 650ºC and irradiated with a dose of 570 Gy

Table 1. Kinetic parameters of the four deconvoluted peaks

Peak ID	Tm, K	E, eV	S, s^{-1}
Peak 1	424	0.82	2,70E+9
Peak 2	476	0.91	1.73E+9
Peak 3	502	0.61	0.33E+6
Peal 4	597	1.41	3.69E+11

Figure 5. Changes in the TL intensity of intermediate peaks with time at room temperature. Quartz samples were irradiated at different doses

Fading process, which are very important in radiation dosimetry and archaeological dating, of individual TL peaks of this material were also investigated. Each of samples irradiated at 57, 114, 171, 285, 513 and 570 Gy were read after 5, 12 and 43 days. The dose responses of all the glow curves show a similar pattern, with peak temperatures remaining in the same positions. Figure 5 shows the decay of the intermediate peak i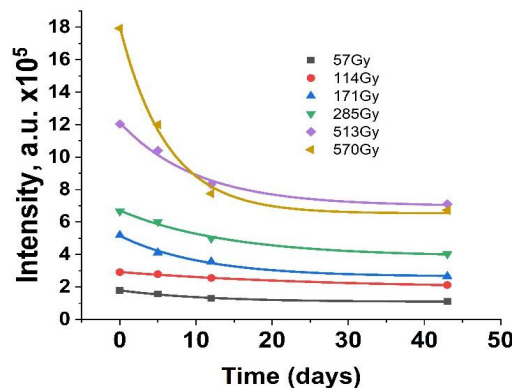ntensity at room temperature. The experimental data were fitted using the exponential decay function, which allows the lifetime of the responsible center to be estimated at room temperature. For all samples it was estimated to be 8±2 days, except for the sample irradiated at 570 Gy. For these samples the estimated lifetime was 19±2 days.

Quartz luminescence is typically explained phenomenologically, such as through thermoluminescence (TL), where a trapped electron is thermally excited to the conduction band and recombines with a nearby hole in the valence band. However, this explanation does not fully account for the large difference between the band gap energy and the emitted photon energy, often attributed to increased lattice vibrational energy.

Itoh et al. [10] proposed a different, physically-based defect pair model. They explained both optically stimulated luminescence (OSL) and two prominent TL bands (110 °C and 325 °C) through reactions involving defect species created during ionizing irradiation. This model builds on the alkali halide model for luminescence. In quartz, various defect species, especially the aluminum ion (Al^{3+}), play crucial roles. Al^{3+} replaces Si^{4+} in the crystal structure, and charge balance is maintained by interstitial protons or alkali ions like Li^+ and Na+.

When quartz undergoes β or γ ionizing radiation, electron/hole pairs are generated, and interstitial charge-balancing ions are released. For example, as $AlO_4M^+ = AlO_4 + M^+$, where M^+ moves and is captured by defects,

forming complexes such as $XO_4 + M+ = XO_4/M^+$. According to [6], the positively charged $[XO_4/M^+]$ complex can absorb an electron to form a neutral $[XO_4/M^+]0$, suggested as the source of the 110 °C TL band. Further, the $[XO_4/M^+]0$ complex may exist in different states, each responsible for different TL bands, such as those at 160 °C and 220 °C.

CONCLUSIONS

This research analyzed the luminescence behavior of quartz samples subjected to gamma irradiation within the range of 57 to 570 Gy. The study revealed that the peak temperature maximum (Tm) of the thermoluminescence (TL) peaks was consistently observed at 206±2°C, regardless of the irradiation dose. Additionally, the intermediate peak intensity exhibited significant decay over time, with lifetimes estimated at 8±2 days for most doses, except for the 570 Gy dose, which showed a longer lifetime of 19±2 days.

The dose-response analysis indicated a linear relationship between the TL intensity of the glow peak at 206°C and the irradiation doses up to 600 Gy. Comparisons with natural quartz samples demonstrated significant differences: natural quartz showed no peaks up to 250°C and only a broad peak above 300°C. The sensitivity of intermediate temperature range peaks in natural quartz was markedly lower than in annealed samples, suggesting distinct kinetic behaviors.

Furthermore, computerized glow curve deconvolution (CGCD) revealed that the glow curve of annealed quartz could be best described as a superposition of four first-order kinetic peaks. These findings underscore the stability and reliability of the 206°C peak in TL studies and highlight the notable differences between natural and annealed quartz. This provides valuable information for applications in radiation dosimetry and archaeological dating.

ORCID

Aqshin Abishov, https://orcid.org/0000-0003-2467-4344; **Sahib Mammadov,** https://orcid.org/0000-0002-4547-4491
Muslim Gurbanov, https://orcid.org/0000-0003-3321-1026; **Ahmad Ahadov,** https://orcid.org/0000-0002-6039-8714;
Aybeniz Ahadova, https://orcid.org/0000-0001-9173-9537

REFERENCES

[1] I. Veronese, A. Giussani, and M.C. Cantone, *The Thermoluminescence Peaks of Quartz at Intermediate Temperatures and Their Use in Dating and Dose Reconstruction*, 2005.
[2] I. Veronese, A. Giussani, H.Y. Goksu, and M. Martini, Radiat. Environ. Biophys. **43**, 51 (2004). https://doi.org/10.1007/s00411-004-0228-9
[3] N. El-Faramawy, A. Gad, H.A. Alazab, and S. Farouk, J. Mater. Res. **37**, 3784 (2022). https://doi.org/10.1557/s43578-022-00751-7
[4] A.K. Sandhu, O.P. Pandey, J. Mater. Sci. Mater. Electron. **32**, 20767 (2021). https://doi.org/10.1007/s10854-021-06590-2
[5] F.O. Ogundare, F.A. Balogun, J.A. Olowofela, C.E. Mokobia, and O.O. Fasunwon, Nucl. Instruments Methods Phys. Res. Sect. B Beam Interact. with Mater. Atoms, **243**, 156 (2006). https://doi.org/10.1016/j.nimb.2005.07.191
[6] O.M. Williams, N.A. Spooner, Radiat. Meas. **108**, 41 (2018). https://doi.org/10.1016/j.radmeas.2017.11.005
[7] G. Kitis, V. Pagonis, R. Chen, and G. Polymeris, Radiat. Prot. Dosimetry, **119**, 438 (2006). https://doi.org/10.1093/rpd/nci548
[8] A.N. Yazici, and H. Toktamiş, Radiat. Eff. Defects Solids, **162**, 439 (2007). https://doi.org/10.1080/10420150701195327
[9] S. Thomas, M.L. Chithambo, and J. Lumin, **197**, 406–411 (2018). https://doi.org/10.1016/j.jlumin.2018.02.003
[10] N. Itoh, D. Stoneham, and A.M. Stoneham, J. Appl. Phys. **92**, 5036 (2002). https://doi.org/10.1063/1.1510951
[11] A. Monti, *Point Defects in Quartz: Role in Trapping and Luminescence*, (University Milano-Bicocca, 2020).
[12] S. Mammadov, East Eur. J. Phys. (1), 442 (2024). https://doi.org/10.26565/2312-4334-2024-1-48
[13] S. Mammadov, M. Gurbanov, L. Ahmadzade, and A. Abishov, Radiat. Phys. Chem. **219**, 111650 (2024). https://doi.org/10.1016/j.radphyschem.2024.111650
[14] Mammadov, M. Gurbanov, and A. Ahadov, Eur. J. Chem. **15**, 149 (2024). https://doi.org/10.5155/eurjchem.15.2.149
[15] G. Kitis, E. Mouza, and G.S. Polymeris, Phys. B: Condens. Matter, **577**, 411754 (2020). https://doi.org/10.1016/j.physb.2019.411754

ТЕРМОЛЮМІНЕСЦЕНЦІЙНА ПОВЕДІНКА ТА КІНЕТИЧНИЙ АНАЛІЗ КВАРЦУ ПІД ГАММА-ОПРОМІНЕННЯМ
Акшин Абішов, Сахіб Мамедов, Муслім Гурбанов, Ахмад Ахадов, Айбеніз Ахадова
Інститут радіаційних проблем Міністерства науки і освіти Азербайджану

Це дослідження досліджує характеристики люмінесценції зразків кварцу, опромінених гамма-джерелом 60Co в діапазоні доз від 57 до 570 Гр. Перед опроміненням зразки відпалювали при 650°C протягом двох годин. Спектри термолюмінесценції (TL) вимірювали при швидкості нагріву 5°C/с, виявляючи два первинних піки приблизно при 200°C і 320°C. Проміжний пік показав плече близько 150°C. Було помічено, що пік максимуму температури (Tm) при 206±2°C залишався постійним незалежно від дози опромінення. Інтенсивність проміжного піку значно зменшувалася з часом, причому тривалість життя оцінювалася в 8±2 дні для більшості доз і 19±2 дні для найвищої дози (570 Гр). Дослідження залежності доза-відповідь показали лінійну залежність між інтенсивністю TL і дозою опромінення до 600 Гр. Порівняння із зразками природного кварцу показало значні відмінності у формах кривих світіння та чутливості. Методи комп'ютеризованої деконволюції кривої світіння (CGCD) підтвердили, що криву світіння відпаленого кварцу можна описати як суперпозицію чотирьох кінетичних піків першого порядку. Ці знахідки дають важливу інформацію про стабільність і поведінку сигналів TL у кварці, які мають вирішальне значення для застосування в радіаційній дозиметрії та археологічному датуванні.
Ключові слова: *кварц; ізотермічний розпад, час згасання; радіаційна дозиметрія; GlowFit*

PHYSICAL MECHANISMS OF CLEAR AIR TURBULENCE

V.O. Lykhatskyi[a]*, V.I. Tkachenko[a,b], L.S. Bozbiei[b]

[a]Kharkiv National University named after V.N. Karazin, Ukraine
[b]National Science Center "Kharkiv Institute of Physics and Technology," National Academy of Sciences of Ukraine
*Corresponding Author e-mail: tkachenko@kipt.kharkov.ua

Clear air turbulence (CAT) is a significant type of atmospheric turbulence that poses risks to aviation. Unlike other forms of turbulence, it occurs without substantial cloudiness, often under clear skies or with minimal cloud cover at the observation site. CAT can arise under various meteorological conditions, such as high atmospheric pressure, sunny weather, or in the presence of mountain ranges. Forecasting CAT is crucial for aviation safety, although its prediction is challenging due to its variability, sharp localization in the air flow, and variability in size and duration. Indirect signs can help predict CAT zones; however, direct observation is difficult, making it essential to develop forecasting methods and conduct research to ensure flight safety.
Keywords: *Turbulence; Clear air; Aviation; Instability parameter; Bénard cells*
PACS: 629.7.015:551.557.3

INTRODUCTION

Clear air turbulence (CAT) is a relatively recent innovation in the aviation industry with potential applications in free atmosphere and wind tunnels [1]. Identifying the locations of CAT occurrence is crucial because it allows aircraft to fly without the need for reconnaissance planes and provides data on the presence of turbulence and its potential impact on aviation infrastructure [2]. Moreover, the phenomenon of CAT is used for modeling turbulence levels in wind tunnels to understand the complexity of periodic turbulence [3]. This technology is utilized by airlines to obtain information about turbulence and to facilitate the accessibility of innovations and customer choices [4]. Through this technology, airlines can establish shared code-sharing agreements, allowing them to make reciprocal flights on certain routes. This reduces operating costs, increases flight frequency, and even introduces new routes, which may enhance accessibility for passengers. Such an approach can also foster innovation and customer choice by improving service and expanding routes. Passengers gain more flight options and the convenience of moving around, which can increase their satisfaction and loyalty to airlines. Additionally, payload sensors for measuring turbulent flows are being developed for flights on Hybrid Quadrotor (HQ) drones [5]. However, these sensors failed to directly measure turbulence intensity near the nozzle and the corresponding far field [6].

CAT technology opens many potential scenarios for the aviation industry, some of which are being explored under the Horizon 2020 research and innovation program. It is known that various factors influence CAT occurrence, such as thermal stratification, infrared radiative cooling, horizontal gradients, and large-scale vertical movements [7]. Additionally, temperature rise and changes in wind patterns are potential factors that can increase CAT parameters. To assess such changes in CAT frequency and severity, studies were conducted in the pan-Arctic region, introducing the use of four turbulence indices [8].

Thanks to rapid improvements in onboard instruments and atmospheric observation systems, in most cases, aircraft can avoid regions of adverse weather associated with developed CAT. However, they still encounter unexpected turbulent conditions in regions far from storms and clouds. This phenomenon poses a problem for understanding and predicting CAT. While most CAT incidents lead to mild discomfort, some can be critical, resulting in serious injuries to passengers and damage to the aircraft.

Researchers of CAT have attempted to explain the physical mechanisms and instabilities underlying dynamic processes in the atmosphere. The main instabilities [9, 10] proposed include:

- The impact of the ratio of vertical inhomogeneity of temperature and air velocity, measured by the Richardson number (instability parameter) [1];
- Kelvin-Helmholtz (KH) instability in shear layers [2];
- Bénard cells and related Langmuir circulations [11];
- Rayleigh-Taylor instability [12, 13];
- Waves generated by mountain flows [14], which occur when atmospheric flow crosses mountainous terrain. As a result, gravity waves are formed, which can become unstable and turn into turbulence. Such waves are often observed in mountainous regions and can impact flight safety;
- Inertial-gravity waves from clouds and other sources [15] can be generated from cloud structures and other atmospheric irregularities. They propagate through the atmosphere and can cause turbulence under certain conditions. These waves play a crucial role in the transport of energy and momentum in the atmosphere;

- Spontaneous imbalance theory [16] explains the occurrence of turbulence due to spontaneous imbalance in strong anticyclones. In such conditions, instabilities may arise, leading to turbulence. This is important for understanding turbulence in areas with strong anticyclones;
- Horizontal vortex tubes [17] are specific turbulence structures that form in clear skies. They result from complex dynamic processes in the atmosphere and can significantly affect aircraft flights. These structures are difficult to predict and can appear suddenly.

The issue of CAT has been widely studied as aircraft flying at altitudes above 5 km have encountered it. Since it is a phenomenon that occurs outside of convective activity, detecting and measuring it has been challenging. Observational studies have shown that CAT is associated with mesoscale phenomena such as jet streams, troughs, ridges, and fronts. Flow conditions such as high vertical speeds, wind shear, and low Richardson numbers have correlated with CAT regions. On the theoretical front, in the 1960s and 70s, KH instability in stably stratified fluid was considered an explanation for CAT formation. Hence, the Richardson number has been used as a CAT index. In subsequent decades, focus shifted to operational forecasting methods, with a range of indices using combinations of the Richardson number, vertical wind shear, horizontal convergence, deformation, etc. Recent years have seen a resurgence of interest in theoretical aspects, with some proposed as sources of intense CAT. Among theories based on inertial-gravity waves, the connection with the actual location where CAT is encountered often remains unclear. Among "local" theories (KH instability, frontogenesis, and spontaneous imbalance), detecting the trigger or critical disturbance remains complex.

While various forecasting methods are employed, key questions remain. The presence of a large number of different indices (about 10) in the GTG procedure indicates the lack of a satisfactory theory. The difficulties in confirming various theories lie in the scarcity of PIREPs, which so far remain the only source of observation. In the future, satellite data may offer global coverage, simplifying the verification of theories. As seen in previous sections, there is a wide range of mechanisms proposed for CAT. Given the different ways of CAT formation, it is likely that a different mechanism operates in each category. In our view, if we look at the two ends of the spectrum, possible mechanisms are: moderate turbulence - inertial and gravity waves; and strong turbulence - horizontal vortex tubes. Rather than trying to find a universal mechanism and prediction method for all forms of CAT, it may be beneficial to focus on the severe form, which is potentially more harmful, although rarer. There is evidence that the formation and existence of horizontal vortex tubes of appropriate scale may be the source of intense clear-air turbulence. Extensive research has been conducted on main shear flows. It would be fruitful to explore the role of secondary structures in shear flows and their connections with atmospheric flows. Studies of the way CAT is sustained/decayed may be a promising area of research. A more holistic approach to the problem, including modeling weather systems, processes on land and sea, air traffic corridors, and urban effects, could be another area of investigation.

Currently, there is no single and universal model that would best define CAT and be easily predicted.

Different theories, such as Kelvin-Helmholtz instability, thermal convection, interaction of air masses, aerodynamic processes and others, choose different explanations for the occurrence of CAT in the atmosphere. Leather with these models has its advantages and limitations.

Therefore, the optimal model of the occurrence of CAT is difficult to complicate, since it is still complex in nature and the phenomenon depends on a large number of factors. Its understanding requires a comprehensive approach, taking into account various theories and factors affecting atmospheric processes. Prediction of CAT requires further research and consideration of various aspects of interaction in complex atmospheric conditions.

The existence of such a large number of mechanisms for the occurrence of CAT does not provide an answer to the question: under what conditions can CAT occur?

The purpose of the work is a critical review of the proposed mechanisms for the occurrence of CAT and the identification of the most likely for CAT prediction.

The article did not mention the specific technologies used to detect CAT. In fact, technologies such as LIDAR (Laser Atmospheric Scanning System), radar systems, satellite surveillance and special sensors on aircraft are used for this purpose. These instruments make it possible to detect turbulence even where it is not accompanied by clouds or other obvious signs.

In practice, mathematical models that take into account the difference in wind speed at different heights (in particular, the analysis of the Richardson number), forecasting based on meteorological data and specialized programs for analyzing weather conditions are used to detect CAT. These techniques help predict where turbulence may occur, which is important for flight safety.

To make sure that we are talking about the turbulence of clean air, several indicators are used. The most important of them is the Richardson number, which allows you to determine how likely turbulence is. Sudden changes in wind speed, temperature differences at different altitudes and data from on-board instruments that record pressure changes and other characteristics of air flows are also taken into account.

THE RICHARDSON NUMBER (INSTABILITY PARAMETER)

For analyzing the conditions of turbulence formation in a temperature-inhomogeneous atmosphere, a dimensionless parameter called the Richardson number (R_i) is often used [12]:

$$R_i = \frac{g(\gamma_a - \gamma)}{T \beta^2}, \tag{1}$$

where:
- g is the acceleration due to gravity,
- T is the mean temperature of the layer,
- γ_a is the adiabatic lapse rate,
- γ is the actual vertical temperature gradient,
- β is the vertical gradient of the mean wind speed.

In cases where $R_i < R_{i\,\text{кр}}$ for the layer under consideration, the conditions are favorable for the formation and development of turbulence. The widespread use of the Richardson number is due to its theoretical basis in hydrodynamic stability theory, making it a fundamental dimensionless criterion for clear air turbulence (CAT). To determine Richardson numbers for meteorological support of aviation, layers of thickness 500 m or less should be used. Unfortunately, the lack of such data from network stations makes it difficult to calculate this parameter accurately. According to studies by S.M. Shmeter [19-21], errors in calculating Richardson numbers based on temperature-wind sounding data can reach up to 400 %.

Thus, the Richardson number can only be applied to forecast atmospheric turbulence if sufficient data on vertical profiles of wind and temperature are available. Research by I.G. Bdzhilko [22, 23] has shown that the presence of intense turbulence in the atmosphere should not be noted in layers with small Richardson numbers but rather at those levels where large changes in Ri values with altitude are observed. In addition to the Richardson number, several other empirical functions (indices) are used to assess the potential development of turbulence in the upper troposphere, including the indices of Reshetov [24], Matveev [25], and Buldovsky [26].

The existence of numerous criteria for the turbulent state of the atmosphere using the Richardson number suggests that the problem of predicting atmospheric turbulence that causes aircraft turbulence is being studied by many researchers. This problem has not yet been fully resolved. Both synoptic and physical-statistical methods are practically used for CAT forecasting. Both approaches are characterized by the tendency to comprehensively consider a number of factors associated with CAT development conditions [1].

The method of calculating the Richardson number is used to enhance the accuracy of numerical calculations by interpolating results obtained at different levels of discretization.

Advantages:

1. Increased Accuracy: Allows for more precise results by combining data from various levels of discretization or increasing the calculation step.

2. Efficiency: Can significantly reduce the volume of calculations, as it typically uses existing information from different discretization levels instead of additional calculations.

3. Universality: Applicable to various types of numerical methods, improving their accuracy.

Disadvantages:

1. Sensitivity to Errors: Sensitive to errors in initial data, which can lead to incorrect or insufficiently accurate extrapolation.

2. Increased Computational Complexity: In some cases, achieving additional accuracy may require more computational operations or additional levels of discretization, increasing computational complexity.

3. Limitations in Accuracy: Significant accuracy improvements are not always achievable, especially if the initial data are already of high accuracy or have limited or low precision.

The Richardson number calculation method is a powerful and useful tool for enhancing the accuracy of numerical calculations, but it has its limitations that need to be considered during its application.

Therefore, the Richardson number is a parameter that determines the degree of instability or the conditions for the transition from laminar to turbulent flow in fluid dynamics. This indicator is used to assess the flow regime of a fluid or gas, considering characteristics such as speed and density. The value of the Richardson number indicates which transfer forces (e.g., convection or diffusion) dominate the mass or heat transfer processes in the flow. A condition where the Richardson number is close to a critical value can cause a transition from one flow regime to another, from laminar to turbulent.

Research on the Richardson number is crucial for understanding and predicting turbulent processes in various environments, including the atmosphere, oceans, and technical systems. Determining this parameter helps manage and analyze flows in different media, enhancing technologies and strategies to improve the efficiency and control of these processes.

KELVIN-HELMHOLTZ INSTABILITY IN SHEAR LAYERS

Most theoretical analyses conducted in the 1960s and 1970s suggested that clear air turbulence (CAT) results from Kelvin-Helmholtz (KH) instability due to shear layers in the atmosphere. Kelvin-Helmholtz instability arises when there is a velocity shear across the interface between two fluid layers. The formation of a two-dimensional vortex ring caused by KH-type instability can be explained as shown in Figure 1. Low-speed (bottom) and high-speed (top) regions create a shear layer, as shown in Figure 1A–B. Then, the instability of the shear layer (KH instability) forms a ring-shaped vortex through the transfer of shear into a pair of rotations, as seen in Figure 1C–D. In other words, this process involves converting non-rotational vorticity or shear into rotational vorticity, or converting shear into Liutex. Afterward, the pair

of rotations merges into a single vortex but still contains a pair of cores within the rotation, as shown in Figure 1E–H. Therefore, vortex pairing is a prominent feature of KH instability. Note that although KH instability relates to inviscid flow, it can still be used to describe "shear layer instability" for viscous flow as an approximation [3]. The formation, growth, and decay of KH waves similar to those observed in laboratory shear flows near regions associated with turbulence have been observed [2].
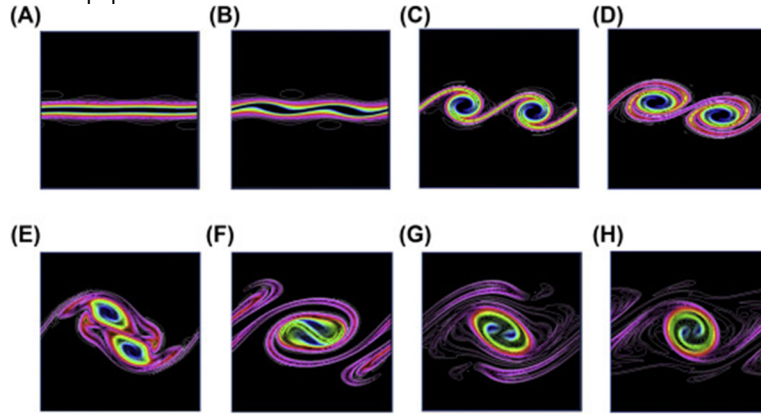
Figure 1. Numerical simulation in 2-D of KH instability (starting from (A) to (H) respectively) [3]

KH instability is a linear instability of the interface between two flows. For two fluid flows with different densities (ρ_1, ρ_2) and velocities (U_1, U_2) separated by a horizontal interface under the assumptions of inviscid conditions and no surface tension at the interface, the speed of wave-like disturbances is given by:

$$c = \frac{\rho_1 U_1 + \rho_2 U_2}{(\rho_1 + \rho_2)} \pm \sqrt{-\frac{\rho_1 \rho_2 (U_1 - U_2)^2}{(\rho_1 + \rho_2)^2} - \frac{\rho_2 - \rho_1}{(\rho_1 + \rho_2)} \frac{g}{k}}, \tag{2}$$

where:
- g is the acceleration due to gravity,
- k is the wave number [4].

If there is no velocity difference, the configuration is unstable for $\rho_2 > \rho_1$, meaning that the heavier fluid is on top [4]. This situation corresponds to Rayleigh-Taylor instability [9]. If there is a velocity difference, the flow becomes unstable for large wave numbers:

$$k > \frac{\rho_1^2 - \rho_2^2}{\rho_1 \rho_2 (U_1 - U_2)^2} g. \tag{3}$$

Other effects, such as surface tension, viscosity, and rotation, have been studied [5-8]. Viscosity and rotation have a stabilizing effect and impose a limiting wave number, but higher wave numbers remain unstable. Surface tension suppresses instability if:

$$(U_1 - U_2)^2 < \frac{2(\rho_1 + \rho_2)}{\rho_1 \rho_2} \sqrt{Tg(\rho_1 - \rho_2)}. \tag{4}$$

Surface tension is significant for high curvature or high wave numbers and is relevant for the air-sea interface but not for atmospheric fronts [8]. The latest data on the effect of surface tension on KH instability can be found in [12]. If there is continuous stratification and velocity changes as a function, the Howard-Miles criterion for instability is given as:

$$R_i < \frac{1}{4}. \tag{5}$$

based on the Richardson number ($R_i = N^2 / (U')^2$, where $N^2 = -(g/\bar{\rho}) d\bar{\rho}/dz$, $N -$ Brent$-$Weissal frequency and $U' = dU/dz$) [13]. This criterion was initially used as a CAT predictor. However, large regions with low RiRiRi values can exist without triggering CAT, and it is now considered only a necessary condition for CAT [13].

It is essential to note that the Howard-Miles criterion (5) coincides with the criterion for the onset of KH instability in equal-density environments, which can be represented by the stability parameter $w^2 > 2$ [12]:

$$w^{-2} = R_i < \frac{1}{4}. \tag{5a}$$

Hence, the KH instability criterion serves as a supplementary criterion to the Richardson number and addresses all shortcomings mentioned in Section 2 of this study.

The KH instability calculation method for shear layers is used to analyze instability phenomena in hydrodynamics, particularly during the interaction of two media with different densities and velocities.

Advantages:

1. Explanation of Turbulence Formation: It allows a better understanding of the conditions and mechanisms for the emergence of turbulent flows during the interaction of different media.

2. Risk Prediction: Helps predict instability and the risks of vortex formation or inhomogeneities in moving media.

3. Practical Applications: Has significant importance in studying hydrodynamic phenomena in nature and engineering systems, such as oceanography, aerodynamics, and hydroelectric power.

Disadvantages:

1. Complexity of Calculations: Calculations can be complex and require significant computational power, especially when analyzing complex systems or large scales.

2. Model Limitations: Only considers certain aspects of instability, which may limit accuracy in predicting turbulent phenomena under specific conditions.

3. Non-homogeneous Conditions: In real-world conditions, KH instability can be influenced by various factors altering its characteristics, complicating precise prediction.

The KH instability calculation method is valuable for understanding turbulent processes, but it requires cautious application and consideration of its limitations when analyzing complex hydrodynamic systems.

Thus, KH instability is a significant phenomenon in hydrodynamics and aerodynamics because it influences turbulence development and flow pattern formation in fluid or gaseous environments. This process occurs when two media with different densities or velocities meet, leading to the formation of shear layers. Research into KH instability is crucial for understanding mixing processes, mass, and energy transfer, and for developing turbulence management strategies in natural and technical systems. This opens up opportunities for improving prediction and control of such processes in various fields where KH instability significantly impacts.

The alignment of KH instability and Howard-Miles criteria based on the Richardson number makes KH instability in shear layers the most likely candidate for describing the emergence of CAT.

BENARD CELLS

A separate series of experimental studies was dedicated to the formation of ordered convective cells in a two-layer medium, with both layers initially at rest. The lower layer consisted of Bénard cells made from an oil-aluminum suspension. The upper layer was composed of air above the surface of the suspension, confined by a thin transparent glass plate. The results of experimental and theoretical investigations are provided in [12].

Experimental studies have shown that in a two-layer medium at rest in the horizontal plane (with the lower layer being oil and the upper layer being air) heated from below, convective cells form in each layer. The cells in the liquid and air layers, which are in contact with each other, are arranged in pairs, one above the other, and have approximately the same geometric dimensions. Convective motion occurs in opposite directions inside and on the periphery of the cells: in the air layer, the air moves upward inside the cell, and in the oil, it moves downward. The coincidence of the sizes of Bénard cells in oil and air indicates their similarity, so it can be assumed, as noted in [27], that the Rayleigh and Prandtl numbers for these media are the same.

The theoretical study was conducted using cylindrical geometry, unlike the classical Rayleigh theory, which uses a Cartesian coordinate system. Cylindrical geometry is more natural because the thermal columns arising at the lower boundary of the layer have a cylindrical geometry. This approach made it possible to describe internal convective flows, formulate the energetic principle of forming cells of a specific diameter, and confirm these findings experimentally.

In concluding this section, it should be noted that observational data on solar granulation evidently suggest that the system of equations used in cylindrical geometry correctly describes the convective mass transfer of solar material when neglecting the Sun's rotation and magnetic field generation.

From the obtained results regarding the emergence of Bénard cells, it follows that vertical air movement occurs in the studied air layer: upwards in the center of the cells and downwards at their periphery. For an external observer moving horizontally through an ordered structure of such cells, there is a periodic action of lifting and lowering forces. Such almost periodic action of forces depends on the direction of movement in the horizontal plane and can be observed as a consequence of the emergence of CAT.

Thus, this section presents data on the experimental and theoretical foundations of studying Bénard cells in air that contacts Bénard cells made from oil below. It has been shown that Bénard cells in the air can create mutually opposing air movements that may be perceived by a horizontally moving object as manifestations of CAT.

The method of Bénard cells calculation [12] can be used to analyze and predict the characteristics of fluid or gas flows, particularly their instabilities and the formation of periodic structures.

Advantages:

1. Understanding Flows: Allows better understanding of the structure and movement within a fluid or gas, which is useful in hydrodynamics and aerodynamics.

2. Nature Studies: Helps analyze and understand natural phenomena, such as currents in rivers, oceans, atmospheric processes, and the movement of solar material on the Sun.

3. Practical Applications: Used to improve technologies and engineering solutions, particularly in transportation, energy, and aerospace industries.

Disadvantages:

1. Complexity of Calculations: Calculations involving Bénard cells can be quite complex due to the need to consider many factors and parameters.

2. Model Limitations: The method is linear and may be limited in predicting the behavior of fluid or gas under complex conditions or in systems with numerous influencing factors.

3. Need for Accurate Data: Calculation results may be sensitive to initial conditions and input data, requiring high measurement accuracy.

The Bénard cell method is a valuable tool for flow analysis, but its application requires caution and consideration of its limitations when studying complex hydrodynamic and aerodynamic systems.

Thus, Bénard cells represent a unique and complex pattern of movement arising in fluid or gas flows under the influence of instability factors, such as gravity, incompressibility, viscosity, and surface tension. These cells form regular geometric structures similar to hexagonal or honeycomb patterns, which are observed in various natural conditions, such as in atmospheric phenomena or convective mass transfer on the Sun.

Research on Bénard cells helps understand and study complex physical processes occurring in fluid or gaseous environments. This is important for developing new forecasting technologies for natural phenomena and creating effective engineering solutions, especially in areas related to fluid motion, transport, aerodynamics, and geophysics.

RAYLEIGH-TAYLOR INSTABILITY

Rayleigh-Taylor instability occurs at the interface between two fluids of different densities when the denser fluid is positioned above the less dense one in a gravitational field. This leads to the development of disturbances at the interface, which gradually increase and result in the mixing of the fluids. A monograph [12] is dedicated to a comprehensive study of instability in stratified viscous media. One of the key aspects of this work is the analysis of Rayleigh-Taylor instability, which plays a significant role in various fields of science and engineering.

The main characteristics of this phenomenon include:

1. Primary disturbances at the fluid interface gradually grow if the denser fluid is on top, leading to the development of complex structures and mixing of the fluids.

2. The influence of viscosity and surface tension significantly impacts the development of instability. High surface tension can suppress the growth of disturbances, while high viscosity slows down the instability process [12].

Advantages:

1. Simplicity of the Model: The Rayleigh-Taylor instability model is based on relatively simple mathematical equations, making it easy to analyze and predict the primary aspects of the process.

2. Widespread Application: The method is used in many fields, including astrophysics, geophysics, and industrial processes, making it a versatile tool for research and practical applications.

Disadvantages:

1. Idealized Theoretical Model: The theoretical model of Rayleigh-Taylor instability is idealized and does not consider many real-world factors, such as turbulence, medium heterogeneity, and external influences, which can significantly affect the results.

2. Dependence on Initial Conditions: The method's outcomes are highly dependent on initial conditions and disturbances, which can complicate its application in real-world scenarios and require additional adjustments.

Thus, the studies presented in the monograph highlight the importance of the Rayleigh-Taylor method for understanding hydrodynamic instability. The authors emphasize that although the method is an effective tool for theoretical research, its application requires caution and consideration of all limitations and specific conditions. Further research is aimed at improving models and expanding their applications, particularly by including additional factors for a more accurate assessment of instability processes in real-world conditions.

DISCUSSION AND COMPARISON

Clear air turbulence (CAT) is a complex physical phenomenon that occurs in the atmosphere under clear skies or with minimal cloudiness. To understand this phenomenon, we will consider the main mechanisms that cause turbulence formation under such conditions:

1. Solar Radiation: Solar radiation heats the Earth's surface, which, in turn, heats the air. Hot air rises, while cooler air descends. This process creates vertical air currents, which can be a source of turbulence.

2. Mountain Ridges: When air passes over mountain ridges, changes in altitude occur. This can lead to the formation of wave-like structures that cause turbulence.

3. Thermal Instability: Differences in air temperature and humidity can create instability and promote turbulence development.

4. Horizontal Wind Speed Gradients: Variations in wind speed at different altitudes can lead to the development of horizontal turbulence.

Compared to other types of atmospheric turbulence, clear air turbulence has a less pronounced nature and can be challenging to predict. Research into this phenomenon is essential for the safety of air transportation and the development of effective forecasting methods.

Several primary instability mechanisms have been identified as playing a crucial role in CAT development:

- Richardson Number (Instability Parameter): A dimensionless parameter that determines the conditions for transition from laminar to turbulent flow in fluid dynamics. A critical value of the Richardson number indicates potential turbulence.
- Kelvin-Helmholtz Instability: Occurs in shear layers when there is a velocity difference between two fluid layers, leading to the formation of vortices and turbulence.
- Bénard Cells: Convective cells that form due to temperature differences and can create periodic structures affecting airflow stability.
- Rayleigh-Taylor Instability: Develops at the interface of two fluids with different densities, resulting in the denser fluid descending into the less dense one, which can lead to mixing and turbulence.

By comparing these mechanisms, it becomes clear that each plays a role under specific conditions, contributing to the overall complexity of CAT. Understanding and modeling these mechanisms can help improve CAT prediction and enhance aviation safety.

CONCLUSIONS AND SUMMARY

The results of the study confirmed the importance of understanding and accounting for various instability mechanisms for predicting clear air turbulence (CAT). From our perspective, the most likely mechanisms for CAT formation include:

- The Richardson Number: Used as a primary instability parameter to determine conditions under which turbulence is likely to occur.
- The Stability Parameter for Kelvin-Helmholtz Instability: This parameter helps predict turbulence resulting from velocity differences in shear layers.
- Conditions for the Stability of Bénard Cells: These cells create ordered convective patterns that can influence turbulence.
- Conditions for Rayleigh-Taylor Instability: This occurs when a denser fluid lies atop a less dense one, leading to instability and potential turbulence.

Recent studies show a correlation between the Richardson number and the inverse value of the stability parameter for Kelvin-Helmholtz instability. Therefore, the combined use of these criteria is both reasonable and promising. Utilizing the aforementioned mechanisms for CAT formation helps reduce risks for passengers and aircraft while enhancing overall comfort and efficiency of air travel.

To improve CAT forecasting, further research is needed, especially in the integration of different approaches and the development of more accurate predictive models. Comprehensive data collection from satellite observations, in-flight sensors, and other technological advancements can aid in verifying existing theories and refining CAT prediction methods. Addressing the complex interactions between various instability mechanisms and their impact on atmospheric turbulence is essential for ensuring the safety of aviation and advancing our understanding of atmospheric dynamics.

ORCID
V.I. Tkachenko, https://orcid.org/0000-0002-1108-5842; **L.S. Bozbiei,** https://orcid.org/0009-0002-2712-0099

REFERENCES
[1] S. Businger, T. Cherubini, I. Dors, J. McHugh, R.A. McLaren, J.B. Moore, J.M. Ryan, *et al.*, "Supporting the missions of the Mauna Kea Observatories with GroundWinds incoherent UV lidar measurements," in: *Proceedings Volume Adaptive Optical System Technologies II*, (Waikoloa, Hawai'i, United States, 2003) https://doi.org/10.1117/12.479588
[2] R. Kivits, M. Charles, N. Ryan, "A post-carbon aviation future: Airports and the transition to a cleaner aviation sector," https://doi.org/10.1016/j.futures.2009.11.005
[3] P.K. Kundu, I.M. Cohen, and D.R. Dowling, "Instability," in: *Fluid Mechanics*, (Sixth Edition), (Academic Press, Elsevier Inc, 2016). pp. 533-602. https://doi.org/10.1016/B978-0-12-405935-1.00011-3
[4] K. Kinder, *Friendly Skies or Turbulent Skies: an Evaluation of the US Airline Industry and Antitrust Concerns*, 91 South. Calif. Law R. 943 (2018).
[5] C. Zappa, S. Brown, and N. Laxague, "Using ship-deployed high-endurance unmanned aerial vehicles for the study of ocean surface and atmospheric boundary layer processes," Front. Mar. Sci. Sec. Ocean Observation, **6**, (2019). https://doi.org/10.3389/fmars.2019.00777
[6] R. Fontaine, G. Elliott, J. Austin, and J.B. Freund, "Very near-nozzle shear-layer turbulence and jet noise," Journal of Fluid Mechanics. **770**, 27-51 (2015). https://doi.org/10.1017/jfm.2015.119
[7] G. Sommeria, "Three-Dimensional Simulation of Turbulent Processes in an Undisturbed Trade Wind Boundary Layer," Journal of the Atmospheric Sciences, **33**(2) 216-241 (1976). https://doi.org/10.1175/1520-0469(1976)033%3C0216:TDSOTP%3E2.0.CO;2
[8] J. Atrill, L. Sushama, and B. Teufel, "Clear-air turbulence in a changing climate and its impact on polar aviation," Saf. Extreme Environ. **3**, 103–124 (2021). https://doi.org/10.1007/s42797-021-00036-y
[9] V.O. Lykhatskyi, L.S. Bozbei, and V.I. Tkachenko, "Clear Sky Turbulence Formation Mechanisms," in: *Abstracts of reports of the 20th conference on high-energy physics and nuclear physics*, (Kharkiv, 2024).
[10] *The 7th International scientific and practical conference "European congress of scientific achievements"*, (Barca Academy Publishing, Barcelona, Spain, 2024). pp. 241.

[11] L.S. Bozbiei, B.V. Borts, and V.I. Tkachenko, *Natural phenomena: Benard cells with free boundaries: educational and methodological guide for the course: "Resource-saving and environmentally friendly technologies"*, (V.N. Karazin Kharkiv National University, Kharkiv, 2015). (in Ukrainian)

[12] O.L. Andrieieva, and V.I. Tkachenko, *Hydrodynamic stoichiometry of stratified viscous media*, (V.N. Karazin Kharkiv National University, Kharkiv, 2020). (in Ukrainian)

[13] O.L. Andreeva, and V.I. Tkachenko, "Analytical Solution and Neutral Curves of the Stationary Linear Rayleigh Problem with Rigid or Mixed Boundary Conditions in Cylindrical Geometry," East Eur. J. Phys. **2**(4), 52–57 (2015). https://doi.org/10.26565/2312-4334-2015-4-04

[14] Y.H. Pao, and A. Goldburg, editors, *Clear Air Turbulence and its detection*, (Plenum Press, New York, USA, 1969).

[15] J.E. Simpson, *Gravity currents in the environment and the laboratory*, (Cambridge University Press, Cambridge, UK, 1997).

[16] J.A. Knox, "Possible mechanisms of Clear-Air Turbulence in Strongly Anticyclonic Flows," Monthly Weather Review, **125**, 1251–1259 (1997). https://doi.org/10.1175/1520-0493(1997)125%3C1251:PMOCAT%3E2.0.CO;2

[17] T.L. Clark, and L.F. Radke, "Clear Air Turbulence," ICAO journal, **56**(7), 5 (2001).

[18] P.V. Hobbs, and G.D. Chellis, "Clear-air turbulence," Aviation, space, and environmental medicine, **75**(6), 539-546 (2004).

[19] S.M. Shmeter, "Structure of meteorological parameter fields in the cumulonimbus cloud zone," Trudy TsAO, (88), 41-57 (1969). (in Russian)

[20] J.C. Wyngaard, *Turbulence in the Atmosphere*, (Cambridge University Press, 2010).

[21] J.A. Knox, "Possible mechanisms of clear-air turbulence in strongly anticyclonic flows," Monthly Weather Review, 125(6), 1251–1259, 1997.

[22] I.H. Bdzhilko, "Atmospheric turbulence: The effect of changes in the Richardson number," Meteorolohichnyi Zhurnal, (4), 45-60 (2020). (in Ukrainian)

[23] I.H. Bdzhilko, "The mechanism of turbulent processes in the atmosphere," Visnyk of the National Academy of Sciences of Ukraine, (7), 35-50 (2019). (in Ukrainian)

[24] V.H. Reshetov, "Methods of estimating turbulence in the atmosphere," Meteorolohichnyi zhurnal, (3), 25-40 (2018). (in Ukrainian)

[25] L.T. Matvieiev, "Analysis and forecasting of atmospheric turbulence," Zhurnal heofizychnykh doslidzhen, (6), 50-65 (2019). (in Ukrainian)

[26] A.M. Buldovskyi, "Turbulence index in the troposphere: theory and practice," Visnyk of the National Academy of Sciences of Ukraine, (5), 70-85 (2020). (in Ukrainian)

[27] L.D. Landau, and E.M. Lifshitz, *Fluid Mechanics, vol. 6*, 2nd edition, (Elsevier, 2008).

ФІЗИЧНІ МЕХАНІЗМИ ТУРБУЛЕНТНОСТІ ЧИСТОГО ПОВІТРЯ

В.О. Лихацький[a], В.І. Ткаченко[a,b], Л.С. Бозбей[b]
[a]Харківський національний університет імені В.Н. Каразіна, Харків, Україна
[b]Науковий центр «Харківський фізико-технічний інститут» НАН України, Харків, Україна

Турбулентність чистого повітря (CAT) – це значний тип атмосферної турбулентності, який становить ризик для авіації. На відміну від інших форм турбулентності, вона виникає без значної хмарності, часто при ясному небі або з мінімальною хмарністю в місці спостереження. CAT може виникати за різних метеорологічних умов, таких як високий атмосферний тиск, сонячна погода або при наявності гірських хребтів. Прогнозування CAT має вирішальне значення для авіаційної безпеки, хоча його прогнозування є складним через його мінливість, різку локалізацію в потоці повітря та мінливість розміру та тривалості. Непрямі ознаки можуть допомогти передбачити зони CAT; однак безпосереднє спостереження є складним, тому необхідно розробляти методи прогнозування та проводити дослідження для забезпечення безпеки польотів.
Ключові слова: *турбулентність; чисте повітря; авіація; параметр нестабільності; комірки Бенара*

INTERFEROMETRIC LOCATING THE WAIST OF A LASER BEAM

Vyacheslav A. Maslov*, Konstantin I. Muntean

V.N. Karazin Kharkiv National University,4 Svoboda Sq., Kharkiv 61022, Ukraine
*Corresponding Author e-mail: *v.a.maslov@karazin.ua*
Received September 18, 2024; revised November 11, 2024; accepted November 22, 2024

An interferometric method for determining the location of a laser beam waist has been developed, which implements the dependence of the wavefront curvature on its distance to the waist. The initial laser beam, the waist location of which must be determined, is split by a shear interferometer into reference and information beams, which form a spatially non-localized interference field in reflected light. The period of the interference fringes observed in any cross-section of the interference field carries information about the location of the waist of the initial laser beam relative to this section. The distance from the waist to the plane of recording the period of the interference fringes is calculated using the formulas of Gaussian optics. The fundamental difference of this method from currently known ones allows for increasing the accuracy of the obtained result while simultaneously reducing the laboriousness of the measurement process**.**
Keywords: *Laser; Gaussian beam; Waist location; Wavefront curvature; Shear interferometer; Two-beam interference; Period of the interference fringes*
PACS: 42.55.Lt; 42.60.Da; 42.25.Bs; 47.32.C–

INTRODUCTION

Determination of the spatial parameters of a laser beam is of fundamental importance in such practical applications as laser material processing [1], including laser welding [2] and cutting [3] in the aerospace and automotive industries, laser powder metallurgy [4], laser therapy in medicine [5], optical metrology [6], development of refractive [7], diffractive [8] and reflective [9] optics, spatial light modulators [10], acousto-optic deflectors [11], optical phased arrays [12] and other optical components [13], matching of eigenmodes of optical devices [14], efficient input of laser radiation into fiber systems [15], precision laser tracing [16], and others.

Currently, the Gaussian model of a laser beam is widely used to describe the process of radiation propagation, both in various optical systems and in free space. Although this model does not satisfy Maxwell's equations, it provides acceptable accuracy of engineering calculations for most typical optical systems and satisfactory agreement with experimental results. The simplest Gaussian model describes the spatial characteristics of a stigmatic laser beam with cylindrical symmetry. The location of the laser beam waist plays a fundamental role in the Gaussian model, since it establishes the origin of the coordinate system, which must be determined with the highest possible accuracy. From a fundamental point of view, the algorithm for determining the waist location is completely clear. First, taking into account the length of the laser resonator and the radii of curvature of its mirrors, it is necessary to calculate the spatial parameters of the radiation beam, including the location of the waist inside the resonator, following the classic article by Kogelnik and Lee [17]. Then we sequentially calculate the change in the location of the beam waist after passing through each element of the optical system, using the thin lens formula and taking into account the thickness and refractive index of both focusing and non-focusing optical elements. This theoretically clear approach is practically of little use, since it involves extensive calculations and, for a number of reasons, does not provide high accuracy of the calculation results. Therefore, laser specialists prefer to find the location of the waist experimentally.

To this time, a number of experimental methods have been developed for determining the location of the waist [18-36] for laser radiation sources with different spatial, temporal, power and spectral characteristics. The very existence of a large number of methods confirms that all of them are unsatisfactory due to either insufficient versatility or due to the relatively low accuracy of the measurement result.

The currently valid international standard ISO 11146-1/2/3:2021 [37 – 39] recommends determining the location of the waist by measuring the beam widths in at least 10 different sections located along the optical axis on both sides of the waist, with the measurement of the radiation density distribution in each section repeated at least five times. The obtained results are approximated by a hyperbolic dependence, and the vertex of the hyperbola indicates the location of the waist. However, such a method can rarely be implemented, as in practice the waist is usually inaccessible for direct measurements or does not physically exist. In this case, the standard recommends forming an artificial waist with an aberration-free focusing element, carrying out the above measurement procedure and calculating the location of the artificial waist. Then, based on the parameters of the focusing element and the distances from its main planes to the artificial and original waists, it is necessary to calculate the location of the original waist according to [17]. The ISO 11146 standard requires the use of a CCD camera to measure beam widths, which are determined by calculating the first and second moments of the radiation power density distribution using the formulas given in the standard. If a CCD camera is

unavailable or cannot be used for any reason, the standard provides for the following alternative methods for measuring beam widths: the variable aperture method, the Foucault knife-edge method, the moving slit method, which are used when the radiation beam width is large, its power is high, or when CCD cameras with a suitable spectral range are not available.

Thus, all known methods for determining the location of the waist, except diffraction methods [23, 24] and specific ionization methods [21, 32], which require direct access to the waist, implement the relationship between the width of the laser beam in any section and the distance from this section to the beam waist. The main disadvantages of the known methods are as follows:

– reduced accuracy of measurement of radiation beams with low divergence, which are of greatest practical interest. As is known, such beams have a large width, which changes little from section to section. In this case, even a small error in measuring the beam width, as shown in [40], leads to a large error in the measurement result. In addition, wide-aperture focusing elements have increased aberrations, which further worsens the accuracy of the result;

– a certain labor intensity, since in order to increase the accuracy of the measurement result, it is necessary to repeatedly measure the beam width in the maximum possible number of its sections at the maximum possible distance between the sections.

The purpose of this work is to increase the accuracy of determining the waist location of a laser beam while simultaneously reducing the laboriousness of the measurement process.

THEORETICAL RELATIONS

Based on the relationship between the curvature $R(z)$ of the wavefront at any point of the optical axis of the laser beam and the distance from this point to the beam waist, an interferometric method is proposed for determining the location of the laser beam waist [41], which does not require direct access to the waist. According to this method, the original laser beam, the location of the waist of which must be determined, is split into information and reference coherent beams that form a non-localized two-beam interference pattern in the space. This pattern is similar to the spatial interference pattern from two coherent point sources, i. e. it is a family of nested two-sheet hyperboloids of revolution with foci at the location of the imaginary waists of the laser beams. As is known, the intensity of the two-beam interference field at any point in space depends only on the wavelength of the radiation, the distance between the two sources, and the distance from the observation point to the origin. Knowing the wavelength of the radiation, the distance between two, imaginary in our case, waists and the period of the interference pattern in any registration plane, we can calculate the distance from the period registration point to the origin of coordinates, and therefore determine the location of the waists. Thus, the problem of determining the location of the original waist, which is inaccessible or does not physically exist, is reduced to determining the parameters of the interference pattern from the pair of imaginary waists we have created.

Analysis of the known methods of forming two interfering beams from one original beam shows that in our case, only a system of two parallel planes is applicable, which forms two imaginary waists, the distance between which is determined only by the parameters of the formation system itself. Any other known system (Fresnel biprism, Biye bilens, Fresnel and Lloyd mirrors, etc.) forms sources, the distance between which also depends on the unknown distance between the plane of the waist of the original laser beam and the formation system. The technical implementation of the system of two parallel planes can be a transparent plane-parallel plate or a Michelson interferometer tuned to zero order. In the case of using a plane-parallel plate, the distance 2C between the imaginary waists of the interfering beams is equal to (Figure 1):

$$2C = \frac{2d \cos \alpha}{(n^2 - \sin^2 \alpha)^{\frac{1}{2}}}, \tag{1}$$

where d is the plate thickness; n is the refractive index of the plate material; α is the angle of incidence of the laser beam on the plate.
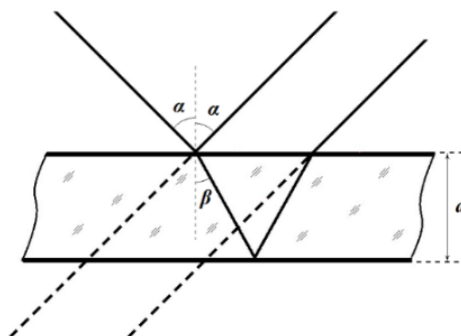

Figure 1. Ray path in a plane-parallel plate.

It follows from formula (1) that the distance between the imaginary waists of the interfering radiation beams, i.e. the position of the foci of the family of two-sheeted hyperboloids, depends on the angle of incidence of the laser beam on the

plane-parallel plate, and, therefore, the interference pattern of two Gaussian beams formed by a system of two parallel planes is not a complete analogue of the classical interference pattern from two real point sources. It follows from Figure 2 that a complete analogy of interference patterns should be observed only in the far field of the laser beam.
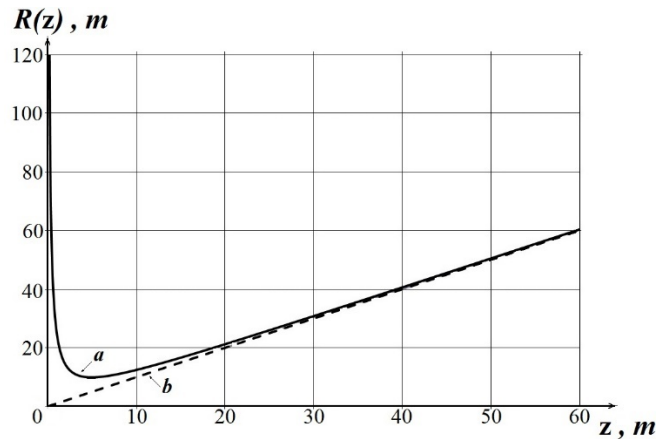

Figure 2. Dependence of the wave front curvature on the distance to the radiation center
a) Gaussian beam ($\lambda = 0.6328$ μm, $\omega_0 = 1.0$ mm), b) point source.

When observing the interference pattern in an arbitrary recording plane, the interference fringes can be calculated as the lines of intersection of this plane with the family of hyperboloids. The shape, width and direction of the fringes depend only on the selected orientation of the recording plane.

Let us consider the cases of observing an interference pattern that occur in practice. The origin of coordinates is placed in the middle between the imaginary waists, the abscissa axis is drawn through the centers of both waists (Figure 3). In all cases, the observation plane is at a distance of $l \gg 2C$ from the origin of coordinates. The following cases of the location of the photorecorder's light-sensitive area are fundamentally possible:

1) the ordinate axis passes through the center of the photorecorder's light-sensitive area normally to it. An interference pattern is observed in the form of a series of practically equidistant fringes, which can be considered straight with high accuracy;

2) the photorecorder's area is located at an angle to both coordinate axes - this is the case most often realized in practice when measuring the spatial parameters of a laser beam. The interference pattern is a family of curved nonequidistant fringes;

3) the abscissa axis passes through the center of the photorecorder's light-sensitive area normally to it. The interference pattern has the form of a family of concentric rings.
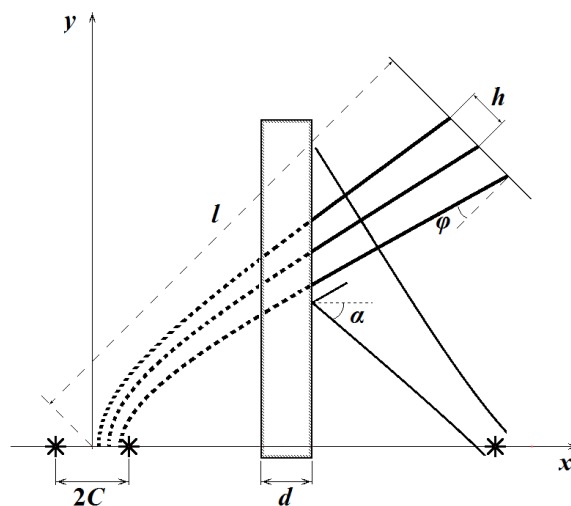
Figure 3. Scheme of formation of interfering beams

These three cases exhaust the entire set of observed interference patterns. When forming an interference pattern using a plane-parallel plate, all three positions of the recording plane can be obtained by changing the angle of incidence of the radiation beam on the plate. When forming an interference pattern using a Michelson interferometer adjusted to the zero order, the third case of observation is realized.

The period h of the interference fringes depends on the distance l between the recording plane and the origin. Solving together the equation for the optical path difference between the interfering beams and the equation for the recording

plane, we obtain, taking into account (1), a calculation formula for determining the distance from the recording plane to the origin of coordinates by the period of the interference fringes

$$l = \frac{(h\,d\,\sin 2\alpha \cos^2 \alpha\,[\cos(\alpha+\varphi)+\mathrm{tg}\,\alpha \sin(\alpha+\varphi)])^2}{\lambda(n^2-\sin^2\alpha)^{\frac{1}{2}}},$$

where λ is the radiation wavelength; φ is the angle of incidence of the radiation beam on the recording plane. If the recording plane is placed perpendicular to the interfering beams, which is almost always possible, then $\varphi = 0$ and the calculation formula is simplified

$$l = \frac{h\,d\,\sin 2\alpha}{(n^2-\sin^2\alpha)^{\frac{1}{2}}}. \tag{3}$$

When using a Michelson interferometer, it is more convenient to measure the diameters of concentric rings instead of the fringe period. In this case, the calculation formula takes the following form

$$l = \left[\frac{d\,(D_{n+1}^2 - D_n^2)}{\lambda n}\right]^{\frac{1}{2}},$$

where d is the thickness of the equivalent air plate of the Michelson interferometer; D_n and D_{n+1} are the diameters of any two adjacent interference rings.

Thus, by setting the angle of incidence of the laser beam on a plane-parallel plate and measuring the period of the interference fringes in the recording plane, we determine the distance from the recording plane to the origin using the above formula.

We will estimate the measurement error of the waist location by differentiating formula (3):

$$\frac{\delta l}{l} \approx \left[\left(\frac{\delta h}{h}\right)^2 + \left(\frac{\delta d}{d}\right)^2 + \delta\alpha^2 + \left(\frac{\delta\lambda}{\lambda}\right)^2 + \delta n^2\right]^{\frac{1}{2}}.$$

Typical values of the error components are as follows: $\delta h/h \approx 10^{-3}$; $\delta d/d \approx 10^{-4}$; $\delta\alpha \approx 10^{-4}$, $\delta\lambda/\lambda \approx 10^{-6}$; $\delta n \approx 10^{-4}$, which allows us to estimate $\delta l/l \approx 10^{-3}$.

It is worth noting the feature of the above-described interference measurement method, which distinguishes it from the known methods of measuring the spatial parameters of a laser beam and allows us to consider it promising for measuring the location of the waist of beams with small (on the order of fractions of an angular second) divergence angles. For example, in known methods, a small difference in beam widths, which is measured with a large error even for large beam divergence angles, tends to zero as the divergence angle decreases, which leads to a complete loss of the information contained in it. In the described interferometric method, the value of the informative parameter – the period of the interference pattern – increases with decreasing beam divergence angle, which allows us to advance in measuring the waist location for beams with small divergence angles beyond known methods by changing the parameters or design of the interference pattern formation system.

## VALIDATION OF THE INTERFEROMETRIC METHOD

The following equipment was used to confirm the operability and accuracy of the interferometric method: He-Ne laser LG-56 with a plane-sphere resonator and a radiation wavelength of 0.632816 μm, a plane-parallel plate from the OSK-2 optical bench kit, 20.75 mm thick, made of K8 optical glass with a relative refractive index of $n = 1.514627$ for a laser wavelength, a collimator from the OSK-2 bench with a focal length of 1600 mm, a goniometer GS-5, two 1st-category geodetic rods with a nominal length of 1 meter, an indicator bore gauge NI-50 18–50, a microdensitometer MF-2; screens, adjustment tables, sheet film.

The tests were carried out as follows. The waist of the original laser beam of the LG-56 coincides with the surface of its output flat mirror. The location of the waist of the original laser beam was measured by the section method and the above-described interferometric method. Then the divergence of the beam was reduced using a collimator and the changed location of the beam waist was again measured by both methods. Consistent application of this procedure allowed us to obtain and measure a series of beam waist position values in the divergence angle range from ~ 10' to ~ 3".

The laser beam width was measured using the section method using screens with sheet photographic film, successively installed at different distances from the waist with a step of 5 m. The maximum distance from the output flat mirror of the laser was 75 m. The distance from the output mirror of the laser was set by successively moving two geodetic rods with a nominal length of 1 m. A screen with photographic film was placed at the measured distance. After processing the film, the diameter of the radiation spot obtained on it at the half-intensity level was measured using an MF-2

microdensitometer. The waist position was determined according to ISO 11146-1 by approximating the measurement results with a hyperbolic function.

The waist position was measured using the interference method using a standard plane-parallel plate from the OSK-2 optical bench with a thickness of 20.75 mm. The plate was mounted on the goniometer's rotary table so that the front reflecting surface of the plate coincided with the axis of rotation of the table. The angle of incidence of the laser beam on the plate varied within the range 0° ÷ 45°. The initial distance from the laser output mirror to the front surface of the plane-parallel plate was 75 m and was set, as in the previous case, by the method of repositioning the geodetic rods. A screen with a sheet of photographic film was placed at a distance of 1 m in the radiation beam reflected from the plate to record the interference pattern. A typical appearance of the obtained interference patterns is shown in Figure 4. Processing and photometry of the films were carried out in the same way as in the previous case. The location of the waist relative to the plane of recording the interference pattern was determined by calculation using the above formula (3).

a   b
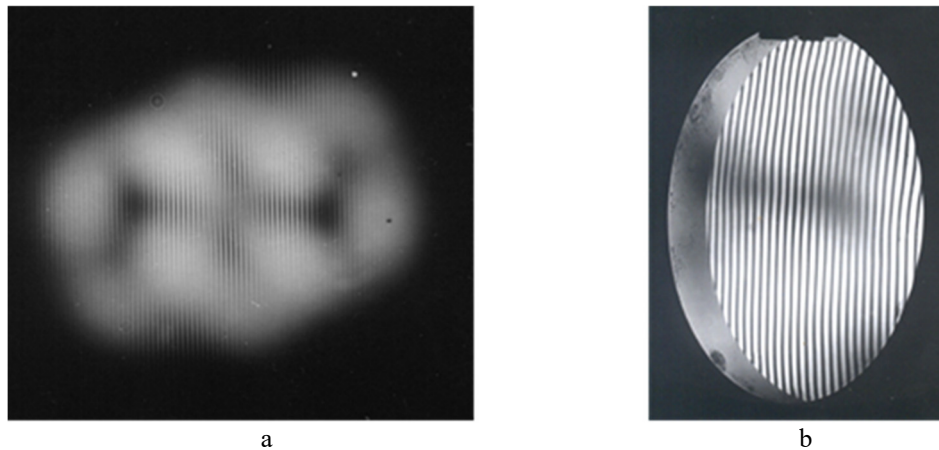
Figure 4. Interference patterns for beams with different divergence θ
a) θ = 8'15"; b) θ = 1'48" (reduced by 3 times)

DISCUSSION OF RESULTS

As a result of testing the measuring devices described above, the following was established:

— for the initial beam of radiation from the LG-56 laser with a divergence angle of ~ 10', both methods give results that coincide with each other with an accuracy of about 2 %;

— as the divergence angle decreases, i. e. when the location of the waist changes, the accuracy of the coincidence of the results decreases;

— the section method recommended by ISO 11146-1 is advisable to use to determine the location of the beam waist with a divergence angle exceeding 30", while the measurement error is about 10 %. The reason for limiting the measurement range is an increase in the measurement error in determining the location of the waist;

— the interference method is advisable to use to determine the location of beam waists with divergence angles exceeding 5', while the measurement error is no more than 5 %. The reason for limiting the measurement range is a decrease in the number of interference fringes observed in the radiation beam reflected from the plate to two. It is assumed that the measurement range can be expanded by changing the dimensions of the plane-parallel plate.

CONCLUSIONS

An interferometric method for determining the location of a laser beam waist has been developed, implementing the known relationship between the curvature of the wavefront in any cross-section of the radiation beam and the distance from this section to the beam waist. The tests conducted confirmed the operability of the interferometric method for determining the location of the laser beam waist, and the results obtained allow us to recommend this method as the most accurate of those currently known.

The laboratory testing process was carried out using fairly complex and bulky universal optical devices and precision measuring instruments. The development of a specialized device controlled by a microcontroller will significantly reduce the time of a single measurement by simplifying the operations of optical adjustments, setting the measurement angle, the process of scanning the interference pattern and processing the obtained data.

It should also be noted that, due to the significantly greater complexity of operation, the Michelson interferometer is advisable to use for unique measurements in cases where the use of wide-aperture plane-parallel plates of large thickness and weight is limited by the technological capabilities of their manufacture. The use of the Michelson interferometer is designed for future needs, while the existing level of needs can be fully satisfied by using those plane-parallel plates, the industrial production of which has been mastered at present.

ORCID

Vyacheslav A. Maslov, https://orcid.org/0000-0001-7743-7006; **Konstantin I. Muntean,** https://orcid.org/0000-0001-6479-3511

REFERENCES

[1] Mohl, S. Kaldun, C. Kunz, F. A. Muller, U. Fuchs, and S. Graf, "Tailored focal beam shaping and its application in laser material processing", J. Laser Appl. **31**, 042019 (2019). https://doi.org/10.2351/1.5123051

[2] Y. Mi, S. Mahade, F. Sikstrom, I. Choquet, S. Joshi, and A. Ancona, "Conduction mode laser welding with beam shaping using a deformable mirror", Opt. Laser Technol. **148**, 107718 (2022). https://doi.org/10.1016/j.optlastec.2021.107718

[3] N. Levichev, P. Herwig, A. Wetzig, and J.R. Duflou, "Towards robust dynamic beam shaping for laser cutting applications", Proc. CIRP, **111**, 746 (2022). https://doi.org/10.1016/j.procir.2022.08.116

[4] A.R. Bakhtari, H.K. Sezer, O.E. Canyurt, O. Eren, M. Shah, and S. Marimuthu, "A review on laser beam shaping application in laser-powder bed fusion", Adv. Eng. Mater. **26**, 2302013 (2024). https://doi.org/10.1002/adem.202302013

[5] O. Savchenko, in: *Laser technologies in orthodontic practice – Achievements and prospects, Conference proceedings of the International scientific and practical conference* (Seoul, Republic of Korea, 2019), pp. 109-114, https://doi.org/10.36074/22.12.2019.v1.35

[6] K.J. Gasvik, *Optical Metrology*, 3rd ed., (John Wiley & Sons, Ltd, 2002).

[7] H. Le, P. Penchev, A. Henrottin, D. Bruneel, V. Nasrollahi, J.A. Ramos-de-Campos, and S. Dimov, "Effects of top-hat laser beam processing and scanning strategies in laser micro-structuring", Micromachines, **11**, 221 (2020). https://doi.org/10.3390/mi11020221

[8] A. Forbes, F. Dickey, M. DeGama, and A. du Plessis, "Wavelength tunable laser beam shaping", Opt. Lett. **37**, 49 (2012). https://doi.org/10.1364/OL.37.000049

[9] M.A. Moiseev, E.V. Byzov, S.V. Kravchenko, and L. L. Doskolovich, "Design of LED refractive optics with predetermined balance of ray deflection angles between inner and outer surfaces", Optics Express, **23**, A1140 (2015), https://doi.org/10.1364/OE.23.0A1140

[10] C. Rosales-Guzmán, and A Forbes, "How to shape light with spatial light modulators," SPIE, **30**, 57 (2017).

[11] T. Häfner1, J. Strauß, C. Roider, J. Heberle, and M. Schmidt, "Tailored laser beam shaping for efficient and accurate microstructuring", Applied Physics A, **124,** 111 (2018). https://doi.org/10.1007/s00339-017-1530-0

[12] C. Halbhuber, "Heat conduction joining with the multispot focusing lens: Joining plastics and metal", PhotonicsViews, **19**, 60 (2022). https://doi.org/10.1002/phvs.202200044

[13] A.G. Nalimov, V.V. Kotlyar, S.S. Stafeev, and E.S. Kozlova, "Metalens for detection of a topological charge", Optical Memory and Neural Networks, **32**, S187 (2023). https://doi.org/10.3103/S1060992X23050144

[14] I.V. Petrusenko, and Yu.K. Sirenko, "Generalized mode-matching technique in the theory of guided wave diffraction. Part 3: wave scattering by resonant discontinuities", Telecommunications and Radio Engineering, **72**, 555 (2013). https://doi.org/10.1615/TelecomRadEng.v72.i7.10

[15] A.E. Mandel, and A.S. Perin, *Study of the efficiency of radiation input and losses at the joints of optical fiber*, (TUSUR, Tomsk, 2018). https://studfile.net/preview/16874330 (in Russian)

[16] O.B. Kovalev, I.O. Kovaleva, and V.V. Belyaev, "Ray tracing method for simulation of laser beam interaction with random packings of powders", AIP Conf. Proc., **1939**, 020028 (2018).https://doi.org/10.1063/1.5027340

[17] H. Kogelnik, and T. Li, "Laser beams and resonators", Appl. Opt. **5**, 1550 (1966). https://doi.org/10.1364/AO.5.001550

[18] J.A. Arnaud, "Gaussian laser beam-waist radius measuring apparatus", Patent United States No. 13,612,885 (10 Dec. 1969).

[19] J.A. Arnaud, "Apparatus for locating and measuring the beam waist radius of a Gaussian laser beam", Patent United States No. 3617755A (11 Febr., 1971).

[20] E.H.A. Granneman, and M.J. van der Wiel, "Laser beam waist determination by means of multiphoton ionization", Rev. Sci. Instrum. **46**, 332 (1975). https://doi.org/10.1063/1.1134202

[21] Y. Suzaki, and A. Tachibana, "Measurement of the Gaussian laser beam divergence," Appl. Opt. **16**, 1481 (1975). https://doi.org/10.1364/AO.16.001481

[22] G.N, Vinokurov, V.A. Gorbunov, V.P. Dyatlov, V.N. Sizov, and A.D. Starikov, "Method for the determination of the position of the focal plane of converging laser beams", Soviet Journal of Quantum Electronics, **6**, 364 (1976). https://doi.org/10.1070/QE1976v006n03ABEH011092

[23] E. Stijns, "Measuring the spot size of a Gaussian beam with an oscillating wire", IEEE J. Quantum Electron. **QE-16**, 1298 (1980). https://doi.org/10.1109/JQE.1980.1070431

[24] Y.C. Kiang, and R.W. Lang, "Measuring focused Gaussian beam spot sizes: a practical method", Appl. Opt., **22**, 1296 (1983). https://doi.org/10.1364/AO.22.001296

[25] J.T. Luxon, D.E. Parker, and J. Karkheck, "Waist location and Rayleigh range for higher-order mode laser beams", Appl. Opt. **23**, 2088 (1984). https://doi.org/10.1364/AO.22.001296

[26] S. Nemoto, "Determination of waist parameters of a Gaussian beam", Appl. Opt. **25**, 3859 (1986). https://doi.org/10.1364/AO.25.003859

[27] S. Nemoto, "Waist shift of a Gaussian beam by plane dielectric interfaces", Appl. Opt. **27**, 1833 (1988). https://doi.org/10.1364/AO.27.001833

[28] P.D. Gupta, and S. Bhargava, "An experiment with Gaussian laser beam", Am. J. Phys. **56**, 563 (1988). https://doi.org/10.1119/1.15555

[29] S. Nemoto, "Waist shift of a Gaussian beam by a dielectric plate", Appl. Opt. **28**, 1643 (1989). https://doi.org/10.1364/AO.28.001643

[30] P.B. Chipple, "Beam waist and M2 measurement using a finite slit", Opt. Eng. **33**, 461 (1994). https://doi.org/10.1117/12.169739

[31] C.R.C. Wang, C.C. Hsu, W.Y. Liu, W.C. Tsai, and W.B. Tzeng, "Determination of laser beam waist using photoionization time-of-flight", Rev. Sci. Instrum. **65**, 2776 (1994). https://doi.org/10.1063/1.1144615

[32] J. P. Landry, "*Optical oblique-incidence reflectivity difference microscopy: Application to label-free detection of reactions in biomolecular microarrays*, (University of California, Davis 2008).

[33] J. Wang and J. P. Barton, "Actual focal length of a symmetric biconvex microlens and its application in determining the transmitted beam waist position", Appl. Opt. **49**, 5828 (2010). https://doi.org/10.1364/AO.49.005828

[34] A.B. Ortega, M.L.A. Carrasco, J.A.D. Pintle, M.M.M. Otero, and M.D.I. Castillo, "New method to characterize Gaussian beams", Proc. SPIE, **8011**, in: *22nd Congress of the International Commission for Optics: Light for the Development of the World, 80114X* (2011). https://doi.org/10.1117/12.902192

[35] Y. You, J. Urakawa, A. Rawankar, A. Aryshev, H. Shimizu, Y. Honda, L. Yan, W. Huang, and C. Tang, "Measurement of beam waist for an optical cavity based on Gouy phase", Nuclear Instruments and Methods in Physics Research Section A, **694**, 6 (2012). https://doi.org/10.1016/j.nima.2012.07.022

[36] E.A. Bibikova, N. Al-wassiti, and N.D. Kundikova, Diffraction of a Gaussian beam near the beam waist, J. Eur. Opt. Soc.-Rapid Publ. **15**, 17 (2019). https://doi.org/10.1186/s41476-019-0113-4

[37] ISO [11146]-1:2021 "Lasers and laser-related equipment: – Test methods for laser beam widths, divergence angles and beam propagation ratios – Part 1: Stigmatic and simple astigmatic beams". https://www.iso.org/obp/ui/#iso:std:iso:11146:-1:ed-2:v1:en

[38] ISO 11146-2:2021 "Lasers and laser-related equipment: – Test methods for laser beam widths, divergence angles and beam propagation ratios – Part 2: General astigmatic beams". https://www.iso.org/obp/ui/#iso:std:iso:11146:-2:ed-2:v1:en

[39] ISO/TR 11146-3:2004 "Lasers and laser-related equipment: – Test methods for laser beam widths, divergence angles and beam propagation ratios – Part 3: Intrinsic and geometrical laser beam classification, propagation and details of test methods". https://www.iso.org/obp/ui/#iso:std:iso:tr:11146:-3:ed-1:v1:en

[40] M.F. Malikov, *Fundamentals of metrology*, (Kommerpribor Publishing House, Moscow, 1949).

[41] G.A. Zimokosov, and K.I. Muntean, "Method for determining the beam waist coordinate of an optical quantum generator", USSR Author's Certificate No. 550917 (31 Oct. 1975).

ІНТЕРФЕРОМЕТРИЧНИЙ МЕТОД ВИЗНАЧЕННЯ ПОЛОЖЕННЯ ПЕРЕТЯЖКИ ПУЧКА ЛАЗЕРНОГО ВИПРОМІНЮВАННЯ

Вячеслав О. Маслов, Костянтин І. Мунтян
Харківський національний університет імені В.Н. Каразіна, майдан Свободи, 4, Харків, Україна, 61022

Розроблено інтерферометричний метод визначення місця перетяжки пучка лазерного випромінювання, що реалізує залежність кривизни хвильового фронту від його відстані до перетяжки. Вихідний лазерний пучок, розташування перетяжки якого необхідно визначити, розщеплюється інтерферометром зсуву на опорний та інформаційний пучки, що утворюють у відбитому світлі нелокалізоване в просторі інтерференційне поле. Період інтерференційних смуг, що спостерігаються в будь-якому перерізі інтерференційного поля, несе інформацію про місцезнаходження перетяжки вихідного лазерного пучка щодо цього перерізу. Відстань від перетяжки до площини реєстрації періоду інтерференційної картини обчислюється за формулами гаусової оптики. Принципова відмінність цього метода від відомих нині дозволяє підвищити точність отриманого результату за одночасного зниження трудомісткості процесу виміру.

Ключові слова: *лазер; гауссів пучок; розташування перетяжки; кривизна хвильового фронту; інтерферометр зсуву; двопроменева інтерференція; період інтерференційної картини*

NUMERICAL STUDY ON THE EFFECTS OF THERMAL AND MASS STRATIFICATION ON CHEMICALLY REACTING UNSTEADY MHD NANOFLUID PAST AN OSCILLATING VERTICAL PLATE THROUGH A POROUS MEDIUM

 Hemant Agarwal[a], **Shyamanta Chakraborty**[b], **Rupam Shankar Nath**[a]

aDepartment of Mathematics, Gauhati University,Guwahati-781014, Assam, India
bUGC-HRDC, Gauhati University, Guwahati-781014, Assam, India
∗Corresponding Author e-mail: hemantagarwal55@gmail.com

The purpose of this study is to study the combined influence of thermal and mass stratification on unsteady magnetohydrodynamic nanofluid past a vertically oscillating plate with variable temperature. The problem's governing equations are numerically solved using the implicit Crank-Nicolson approach. Significant results from the thermal and mass stratification are contrasted with the environment where stratification is absent. The velocity decreases with both kinds of stratification, while the temperature decreases with thermal stratification and the concentration decreases with mass stratification. We use graphs to demonstrate the effects of the different parameters, including phase angle, thermal radiation, magnetic field strength, heat sources/sinks, and chemical reactions. Additionally, the Skin-Friction Coefficient, the Nusselt Number, and the Sherwood Number are computed and represented graphically. The findings highlight the critical role of stratification in improving fluid dynamics and increasing the efficiency of heat and mass transfer processes, providing essential information for engineering and environmental applications under similar circumstances.

Keywords: *Mass Stratification; Chemical Reaction; Nanofluid; Thermal Stratification; Oscillating Vertical Plate; Crank-Nicolson Method; Thermal Radiation; Porous Medium; MHD*

PACS: 44.05.+e, 44.25.+f, 44.27.+g, 44.40.+a, 47.11.-j, 44.30.+v

1. INTRODUCTION

The term "nanofluid" is used to describe a specific form of artificial fluid in which particles with sizes typically less than 100 nanometers are suspended in a base fluid. The unique thermal and mechanical features of nanofluids have attracted a lot of attention in recent years, leading to their widespread implementation. One of the most promising applications in the field of heat transfer is the use of nanofluids, which perform better than their base fluids in terms of both thermal conductivity and convective heat transfer coefficients. They are helpful in a range of heat transfer applications, such as solar collectors, heat exchangers, and the cooling of electronic devices, thanks to their capacity to dissipate heat effectively.

Choi and Eastman [1] was the first to introduce the concept of nanofluid, which indicates that floating metallic nanoparticles in standard heat transfer fluids could create a revolutionary novel kind of heat transmission fluid. In a partly heated rectangular enclosure, Oztop and Abu-Nada [2] conducted a numerical investigation on several kinds of nanoparticles and how they impact on heat transmission and fluid flow. The authors of the papers Das and Jana [3] and [4] examined the radiation-induced free convection flow of nanofluids in a vertical plate and channel, respectively. Titanium dioxide, aluminium oxide, and copper nanofluids were the subject of investigation in both reports. The study conducted by Rashidi et al. [5] investigates the utilisation of lie group theory to provide a solution for the movement of nanofluid across a chemically reactive horizontal plate, considering the generation or absorption of heat. The study conducted by Abolbashari et al. [6] applies the homotopy analysis method (HAM) to examine the entropy of the nanofluid composed of water as the fundamental fluid and member of four different kinds of nanoparticles: TiO_2, Al_2O_3, Cu, and CuO. The nanofluid past over a stretched permeable surface. Kameswaran et al. [7] studied the impact of several factors on convection heat and mass transfer in nanofluid move across a stretching sheet, including the viscous dissipation, soret effect, hydro-magnetic, chemical reaction, and viscous dissipation. For the purpose of exploring the impact of certain factors, a numerical study was carried out by Motsumi and Makinde [8] on the flow via the boundary layer of nanofluids over a movable flat plate. The study aimed to analyze the consequence of viscous dissipation, thermal diffusion, and thermal radiation. Furthermore, Sheikholeslami et al. [9] examined the flow of MHD nanofluids numerically to determine the impact of viscous loss on the flow. As it move via a upright plate, Chamkha and Aly [10] numerically evaluates an MHD nanofluid that has heat production or absorption impacts. The analytical examination on the MHD nanofluid movement for different types of water-based nanoparticles as they travelled through a continuously stretching/shrinking permeable sheet was conducted by Turkyilmazoglu [11] within the framework of velocity slip and temperature leap. A circular tube was used to perform experimental study on a diluted CuO/water nanofluid by Fotukian et al. [12]. In their research of the MHD Cu-water nanofluid subjected to Lorentz forces, Sheikholeslami et al. [13] utilised the Lattice Boltzmann method. In addition, Sandeep and Reddy [14] investigated the influences of nonlinear thermal radiation on

the flow of MHD Cu-water nanofluids across a cone and a wedge. The influences of mass and heat transfer on nanofluids travelling through a moving or stationary upright plate in the presence of a heat source were studied by Reddy et al. [15] and Mahanthesh et al. [16], respectively. Vemula et al. [17] performed an analytical study to examine the motion of magnetohydrodynamic (MHD) nanofluids flowing past a vertically oriented plate that is accelerating exponentially, while also having a temperature that changes. The united impacts of mass and heat stratification across an upright wavy truncated cone and a wavy surface were studied by Cheng [**?**] and [19], respectively. In addition, the impact of these effects on infinite vertical cylinders has been studied by Paul and Deka [20]. Krishna et al. [21] studied MHD Carreau fluid flows, emphasizing how bouyancy and exponential heat sources modify fluid behaviour. Recent efforts by Gowri and Selvaraj [22] and Selvaraj et al. [23] have focused on rotational effects and the dynamics of accelerated flows in porous media, offering deeper insights into how rotational forces affect MHD parabolic flows. The study conducted in Nath and Deka [24] examined the impact of both temperature stratification and chemical reactions on the flow around an indefinite vertical plate. Similarly, the investigation in Kalita et al. [25] focused on the influence of these factors on the flow around an accelerated upright plate and Nath et al. [26], conducted a study on how thermal stratification affects the flow of unstable parabolic motion around a upright plate that extends infinitely. Nath and Deka [27] conducted a study on how heat and mass stratification affect the movement of an unstable magnetohydrodynamic nanofluid across an upright plate. The plate's temperature varies exponentially, and the study was conducted in a porous media. In a similar vein, Nath and Deka [28] investigated numerically how temperature and mass stratification affect the flow of a magnetohydrodynamic nanofluid that is unstable as it passes across a porous medium with an exponentially accelerating upright plate. An endless upright plate with a temperature that drops exponentially and changing mass diffusion in a porous medium was studied by Nath and Deka [29] in terms of the effect on temperature and mass stratification. The MHD ternary hybrid nanofluid was the subject of a numerical study by Nath and Deka [30]. The study revolved around a cylinder that was stretched vertically within a porous medium that had heat stratification and radiation. The study conducted by Sheikholeslami et al. [31] examined the influence of the diffusion of heat and heat generation on the erratic multi-channel hydrodynamics (MHD) flow of a radiatively and electrically conducting nanofluid passing through a porous medium across an oscillating upright plate. Rammoorthi and Mohanavel [32] looked into how a magnetic field's radiation can affect the convective movement of a reactive chemically hybrid nanofluid across an upright plate.

In this work, we investigate the behavior of an unsteady MHD nanofluid in a porous media as it flows through an oscillating vertical plate with variable temperature. The unique aspects of this particular problem are as follows: It makes use of a numerical method that is both efficient and unconditionally stable, and it guarantees convergence with ease. So far, no one has tried to show how mass and temperature stratification work together to affect MHD nanofluid as it circulates across a porous medium with ramping temperature and concentration, past an oscillating vertical plate. Nanoparticles of Ag-water and Cu-water was studied for how thermal and mass stratification affected them in the occurrence of a magnetic field(M), thermal radiation(R), heat generation or absorption(Q), and chemical reaction(Kr). As far as we know, no attempt has ever been made to carry out this kind of research. Nanofluid stratification research is a promising and rapidly expanding field with potential applications in medical technology, catalysis, and energy storage.
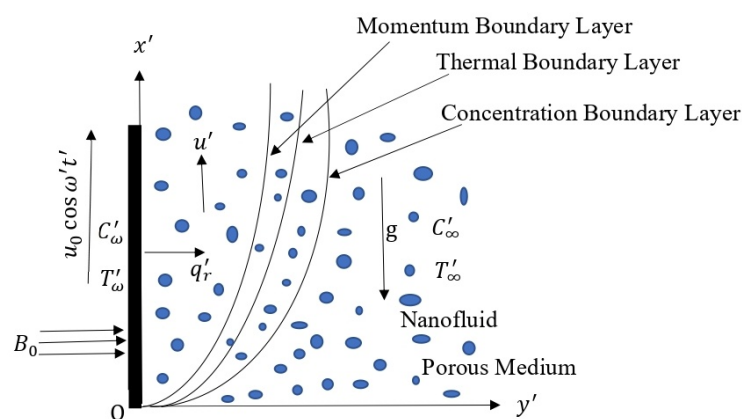

Figure 1. Physical Model and Coordinate System

2. MATHEMATICAL FORMULATION

Examine the transfer of heat and flow in nanofluids as they pass an oscillating vertical plate with changing temperature. The flow is erratic, viscous, incompressible, and exhibits free convection. The x' axis is oriented vertically and parallel to the surface of the plate, while the magnetic field is oriented perpendicular to the direction of propagation with the y' axis. The initial assumption is that the surrounding nanofluid and the plate have the same temperature and concentration,

denoted as T'_∞ and C'_∞ accordingly. At $t' > 0$, the plate starts to oscillate vertically inside its own plane at a frequency of ω'. Simultaneously, the temperature exhibits a linear increase over time, while the concentration is denoted as C'_w. The plate is assumed to be exposed to a uniform magnetic field B_0, and the heat produced by viscous and joule dissipation is not taken into account. It is crucial to analyze the radiative heat flux that is perpendicular to the direction of the plate, which is represented by the symbol q'_r. Our work will focus on the analysis of a water-based nanofluid including nanoparticles of silver (Ag) and copper (Cu). The governing equations of momentum, energy, and concentration for nanofluid given by authors in Mahanthesh et al. [16] and Vemula et al. [17] using the boundary layer approximation and Boussinesq are written as

$$\rho_{nf}\frac{\partial u'}{\partial t'} = \mu_{nf}\frac{\partial^2 u'}{\partial y'^2} + g(\rho\beta_T)_{nf}(T' - T'_\infty) + g(\rho\beta_C)_{nf}(C' - C'_\infty) - \sigma_{nf}B_0^2 u'$$
$$-\frac{\mu_{nf}}{k'_p}u' \tag{1}$$

$$\frac{\partial T'}{\partial t'} = \frac{k_{nf}}{(\rho c_p)_{nf}}\frac{\partial^2 T'}{\partial y'^2} - \frac{1}{(\rho c_p)_{nf}}\frac{\partial q'_r}{\partial y'} + \frac{Q_0}{(\rho c_p)_{nf}}(T' - T'_\infty) - \gamma u' \tag{2}$$

$$\frac{\partial C'}{\partial t'} = D_{nf}\frac{\partial^2 C'}{\partial y'^2} - k_1(C' - C'_\infty) - \xi u' \tag{3}$$

The initial and boundary conditions are as follows:

$$\begin{array}{llll} u' = 0 & T' = T'_\infty & C' = C'_\infty & \forall y', t' \le 0 \\ u' = u_0 \cos\omega't' & T' = T'_\infty + (T'_w - T'_\infty)At' & C' = C'_w & \text{at } y' = 0, t' > 0 \\ u' = 0 & T' \to T'_\infty & C' \to C'_\infty & \text{as } y' \to \infty, t' > 0 \end{array}$$

where, $(\beta_T)_{nf}, (\beta_C)_{nf}, \rho_{nf}, \mu_{nf}, \sigma_{nf}, B_0, g, k'_p, k_{nf}, (\rho c_p)_{nf}, Q_0, q'_r, D_{nf}, k_1$ denote the thermal expansion coefficient of the nanofluid, coefficient of expansion for species concentration of the nanofluid, the density of the nanofluid, dynamic viscosity of the nanofluid, electrical conductivity of the nanofluid, uniform magnetic field, acceleration due to gravity, porous medium permeability, thermal conductivity of the nanofluid, heat capacitance of the nanofluid, uniform volumetric heat source/sink, radiative heat flux, mass diffusion coefficient of the nanofluid, chemical reaction coefficient respectively. Moreover, the "thermal stratification parameter" and "mass stratification parameter" are denoted as $\gamma = \frac{dT'_\infty}{dx'} + \frac{g}{C_p}$ and $\xi = \frac{dC'_\infty}{dx'}$ respectively. The concept of "thermal stratification" encompasses the phenomenon of vertical temperature advection, denoted as $\left(\frac{dT'_\infty}{dx'}\right)$, wherein the temperature of the surrounding fluid varies with height, and work of compression, denoted as $\left(\frac{g}{C_p}\right)$, which represents the rate at which reversible work is performed on fluid particles through compression. The mathematical representations of certain physical quantities are in the following manner:

$$\mu_{nf} = \frac{\mu_f}{(1-\phi)^{2.5}}, \quad \rho_{nf} = (1-\phi)\rho_f + \phi\rho_s, \quad (\rho c_p)_{nf} = (1-\phi)(\rho c_p)_f + \phi(\rho c_p)_s$$

$$(\rho\beta_T)_{nf} = (1-\phi)(\rho\beta_T)_f + \phi(\rho\beta_T)_s, \quad (\rho\beta_C)_{nf} = (1-\phi)(\rho\beta_C)_f + \phi(\rho\beta_C)_s$$

$$\sigma = \frac{\sigma_s}{\sigma_f}, \quad \sigma_{nf} = \left[1 + \frac{3\phi(\sigma-1)}{(\sigma+2) - \phi(\sigma-1)}\right]\sigma_f, \quad k_{nf} = \left[\frac{(k_s + 2k_f) - 2\phi(k_f - k_s)}{(k_s + 2k_f) + \phi(k_f - k_s)}\right]k_f$$

where $\rho_s, \rho_f, \mu_f, \phi, (\rho c_p)_s, (\rho c_p)_f, \sigma_f, k_s, k_f$ denote the density of nanoparticles, density of base fluid, viscosity of base fluid, volume fraction of nanoparticle, heat capacitance of nanoparticles, heat capacitance of base fluid, electrical conductivity of nanoparticles, thermal conductivity of nanoparticles and thermal conductivity of base fluid respectively. The Rosseland estimate [33] is used to get a good idea of the flux of radiative heat q'_r in Eq. (2), since the nanofluid is thought to be an optically thick fluid. According to the study by Turkyilmazoglu [11], we can rewrite Eq. (2) as

$$\frac{\partial T'}{\partial t'} = \frac{1}{(\rho c_p)_{nf}}\left(k_{nf} + \frac{16\sigma^* T'^3_\infty}{3k_f k}\right)\frac{\partial^2 T'}{\partial y'^2} + \frac{Q_0}{(\rho c_p)_{nf}}(T' - T'_\infty) - \gamma u'$$

Now, we provide the subsequent non-dimensional quantities:

$$U = \frac{u'}{u_0}, \quad t = \frac{t'u_0^2}{\nu_f}, \quad y = \frac{y'u_0}{\nu_f} = \frac{y'}{L_{ref}}, \quad \theta = \frac{T' - T'_\infty}{T'_w - T'_\infty}, \quad C = \frac{C' - C'_\infty}{C'_w - C'_\infty}, \quad M = \frac{\nu_f\sigma_f B_0^2}{\rho_f u_0^2}$$

$$Gr = \frac{g\beta_{T_f}\nu_f(T'_w - T'_\infty)}{u_0^3}, \quad Gc = \frac{g\beta_{C_f}\nu_f(C'_w - C'_\infty)}{u_0^3}, \quad Pr = \frac{(\mu c_p)_f}{k_f}, \quad Sc = \frac{\nu_f}{D_{nf}}, \quad R = \frac{k_f k'}{4\sigma^* T'^3_\infty},$$

$$\omega = \frac{\omega'\nu_f}{u_0^2}, \quad Q = \frac{Q_0\nu_f}{u_0^2(\rho c_p)_f}, \quad K = \frac{u_0^2 k'_p}{\nu_f^2}, \quad Kr = \frac{\nu_f k_1}{u_0^2}, \quad S = \frac{\gamma\nu_f}{u_0(T'_w - T'_\infty)}, \quad F = \frac{\xi\nu_f}{u_0(C'_w - C'_\infty)}$$

The non-dimensional forms of the Eq. (1)-(3) are given by

$$\frac{\partial U}{\partial t} = a_1\frac{\partial^2 U}{\partial y^2} + a_2 Gr\theta + a_3 GcC - a_4 MU - a_1\frac{U}{K} \tag{4}$$

$$\frac{\partial \theta}{\partial t} = a_5\frac{\partial^2 \theta}{\partial y^2} + a_6\theta - SU \tag{5}$$

$$\frac{\partial C}{\partial t} = \frac{1}{Sc}\frac{\partial^2 C}{\partial y^2} - KrC - FU \tag{6}$$

where,

$$x_1 = (1-\phi) + \phi\left(\frac{\rho_s}{\rho_f}\right), \quad x_2 = (1-\phi) + \phi\frac{(\rho\beta_T)_s}{(\rho\beta_T)_f}, \quad x_3 = (1-\phi) + \phi\frac{(\rho\beta_C)_s}{(\rho\beta_C)_f}$$

$$x_4 = 1 + \frac{3\phi(\sigma - 1)}{(\sigma + 2) - \phi(\sigma - 1)}, \quad x_5 = (1-\phi) + \phi\frac{(\rho C_p)_s}{(\rho C_p)_f}, \quad x_6 = \frac{(k_s + 2k_f) - 2\phi(k_f - k_s)}{(k_s + 2k_f) + \phi(k_f - k_s)}$$

$$a_1 = \frac{1}{(1-\phi)^{2.5}x_1}, \quad a_2 = \frac{x_2}{x_1}, \quad a_3 = \frac{x_3}{x_1}, \quad a_4 = \frac{x_4}{x_1}, \quad a_5 = \frac{x_6 + \frac{4}{3R}}{x_5 Pr}, \quad a_6 = \frac{Q}{x_5}$$

Non-dimensional form of initial and boundary conditions are:

$U = 0$	$\theta = 0$	$C = 0$	$\forall y, t \leq 0$
$U = \cos\omega t$	$\theta = t$	$C = 1$	at $y = 0, t > 0$
$U = 0$	$\theta \to 0$	$C \to 0$	as $y \to \infty, t > 0$

$$\tag{7}$$

Table 1. Thermo-physical properties of water and nanoparticles [16]

Physical Properties	H_2O (base fluid)	Ag	Cu
ρ (kg/m^3)	997.1	10500	8933
C_p (J/kgK)	4179	235	385
k (W/mK)	0.613	429	401
$\beta_t \times 10^6$ (K^{-1})	210	18.9	16.7
$\beta_c \times 10^6$ (K^{-1})	214	56.7	50.1
σ (s/m)	5.5×10^{-6}	63×10^6	59.6×10^6

3. METHOD OF SOLUTION

It is impossible to find the exact solutions for coupled partial differential equations Eq. (4)-(6) with initial and boundary conditions (7). Therefore, to resolve them, we employ an implicit crank-Nicolson finite difference approach. The finite difference scheme of the Eq. (4) is as follows

$$\frac{U_i^{n+1} - U_i^n}{\frac{\Delta t}{2}} = a_1\left[\frac{U_{i-1}^{n+1} - 2U_i^{n+1} + U_{i+1}^{n+1}}{(\Delta y)^2}\right] + a_1\left[\frac{U_{i-1}^n - 2U_i^n + U_{i+1}^n}{(\Delta y)^2}\right] + a_2 Gr\left[\theta_i^{n+1} + \theta_i^n\right]$$

$$+ a_3 Gc\left[C_i^{n+1} + C_i^n\right] - a_4 M\left[U_i^{n+1} + U_i^n\right] - \frac{a_1}{K}\left[U_i^{n+1} + U_i^n\right]$$

$$\Rightarrow U_i^{n+1} - U_i^n = \frac{a_1\Delta t}{2(\Delta y)^2}\left[U_{i-1}^{n+1} - 2U_i^{n+1} + U_{i+1}^{n+1}\right] + \frac{a_1\Delta t}{2(\Delta y)^2}\left[U_{i-1}^n - 2U_i^n + U_{i+1}^n\right]$$

$$+\frac{a_2 Gr \Delta t}{2}\left[\theta_i^{n+1} + \theta_i^n\right] + \frac{a_3 Gc \Delta t}{2}\left[C_i^{n+1} + C_i^n\right] - \frac{a_4 M \Delta t}{2}\left[U_i^{n+1} + U_i^n\right]$$

$$-\frac{a_1 \Delta t}{2K}\left[U_i^{n+1} + U_i^n\right]$$

$$\Rightarrow U_i^{n+1} - U_i^n = b_1\left[U_{i-1}^{n+1} - 2U_i^{n+1} + U_{i+1}^{n+1}\right] + b_1\left[U_{i-1}^n - 2U_i^n + U_{i+1}^n\right] + b_2\left[\theta_i^{n+1} + \theta_i^n\right]$$

$$+b_3\left[C_i^{n+1} + C_i^n\right] - b_4\left[U_i^{n+1} + U_i^n\right] - b_5\left[U_i^{n+1} + U_i^n\right]$$

$$\Rightarrow -b_1 U_{i-1}^{n+1} + (1 + 2b_1 + b_4 + b_5)U_i^{n+1} - b_1 U_{i+1}^{n+1} = b_1 U_{i-1}^n + (1 - 2b_1 - b_4 - b_5)U_i^n + b_1 U_{i+1}^n$$

$$+b_2\left[\theta_i^{n+1} + \theta_i^n\right] + b_3\left[C_i^{n+1} + C_i^n\right] \qquad (8)$$

where, $b_1 = \frac{a_1 \Delta t}{2(\Delta y)^2}$, $\quad b_2 = \frac{a_2 Gr \Delta t}{2}$, $\quad b_3 = \frac{a_3 Gc \Delta t}{2}$, $\quad b_4 = \frac{a_4 M \Delta t}{2}$, $\quad b_5 = \frac{a_1 \Delta t}{2K}$

Likewise, the finite difference scheme of the Eq. (5) can be outlined as follows

$$\frac{\theta_i^{n+1} - \theta_i^n}{\frac{\Delta t}{2}} = a_5\left[\frac{\theta_{i-1}^{n+1} - 2\theta_i^{n+1} + \theta_{i+1}^{n+1}}{(\Delta y)^2}\right] + a_5\left[\frac{\theta_{i-1}^n - 2\theta_i^n + \theta_{i+1}^n}{(\Delta y)^2}\right] + a_6\left[\theta_i^{n+1} + \theta_i^n\right]$$

$$-S\left[U_i^{n+1} + U_i^n\right]$$

$$\Rightarrow \theta_i^{n+1} - \theta_i^n = \frac{a_5 \Delta t}{2(\Delta y)^2}\left[\theta_{i-1}^{n+1} - 2\theta_i^{n+1} + \theta_{i+1}^{n+1}\right] + \frac{a_5 \Delta t}{2(\Delta y)^2}\left[\theta_{i-1}^n - 2\theta_i^n + \theta_{i+1}^n\right]$$

$$+\frac{a_6 \Delta t}{2}\left[\theta_i^{n+1} + \theta_i^n\right] - \frac{S \Delta t}{2}\left[U_i^{n+1} + U_i^n\right]$$

$$\Rightarrow \theta_i^{n+1} - \theta_i^n = b_6\left[\theta_{i-1}^{n+1} - 2\theta_i^{n+1} + \theta_{i+1}^{n+1}\right] + b_6\left[\theta_{i-1}^n - 2\theta_i^n + \theta_{i+1}^n\right] + b_7\left[\theta_i^{n+1} + \theta_i^n\right]$$

$$-b_8\left[U_i^{n+1} + U_i^n\right]$$

$$\Rightarrow -b_6 \theta_{i-1}^{n+1} + (1 + 2b_6 - b_7)\theta_i^{n+1} - b_6 \theta_{i+1}^{n+1} = b_6 \theta_{i-1}^n + (1 - 2b_6 + b_7)\theta_i^n + b_6 \theta_{i+1}^n$$

$$-b_8\left[U_i^{n+1} + U_i^n\right] \qquad (9)$$

where, $b_6 = \frac{a_5 \Delta t}{2(\Delta y)^2}$, $\quad b_7 = \frac{a_6 \Delta t}{2}$, $\quad b_8 = \frac{S \Delta t}{2}$

Also, the finite difference scheme of the Eq. (6) can be outlined as follows

$$\frac{C_i^{n+1} - C_i^n}{\frac{\Delta t}{2}} = \frac{1}{Sc}\left[\frac{C_{i-1}^{n+1} - 2C_i^{n+1} + C_{i+1}^{n+1}}{(\Delta y)^2}\right] + \frac{1}{Sc}\left[\frac{C_{i-1}^n - 2C_i^n + C_{i+1}^n}{(\Delta y)^2}\right] - Kr\left[C_i^{n+1} + C_i^n\right]$$

$$-F\left[U_i^{n+1} + U_i^n\right]$$

$$\Rightarrow C_i^{n+1} - C_i^n = \frac{\Delta t}{2Sc(\Delta y)^2}\left[C_{i-1}^{n+1} - 2C_i^{n+1} + C_{i+1}^{n+1}\right] + \frac{\Delta t}{2Sc(\Delta y)^2}\left[C_{i-1}^n - 2C_i^n + C_{i+1}^n\right]$$

$$-\frac{Kr \Delta t}{2}\left[C_i^{n+1} + C_i^n\right] - \frac{F \Delta t}{2}\left[U_i^{n+1} + U_i^n\right]$$

$$\Rightarrow C_i^{n+1} - C_i^n = b_9\left[C_{i-1}^{n+1} - 2C_i^{n+1} + C_{i+1}^{n+1}\right] + b_9\left[C_{i-1}^n - 2C_i^n + C_{i+1}^n\right] - b_{10}\left[C_i^{n+1} + C_i^n\right]$$

$$-b_{11}\left[U_i^{n+1} + U_i^n\right]$$

$$\Rightarrow -b_9 C_{i-1}^{n+1} + (1 + 2b_9 + b_{10})C_i^{n+1} - b_9 C_{i+1}^{n+1} = b_9 C_{i-1}^n + (1 - 2b_9 - b_{10})C_i^n + b_9 C_{i+1}^n$$

$$-b_{11}\left[U_i^{n+1} + U_i^n\right] \qquad (10)$$

where, $b_9 = \frac{\Delta t}{2Sc(\Delta y)^2}$, $\quad b_{10} = \frac{Kr \Delta t}{2}$, $\quad b_{11} = \frac{F \Delta t}{2}$ To address the issue, a rectangular region is partitioned into an arrangement of lines that are parallel to the coordinate axes, with a spacing of Δy in space and Δt in time. In this context, the variable i denotes the spatial grid points, which are spaced out by Δy. On the other hand, the variable n represents the temporal grid points, which are separated by Δt. The mesh system being evaluated for computation has step sizes of $\Delta y = 0.01$ and $\Delta t = 0.001$. By considering the initial condition stated in Eq. (7), we obtain the following:

$$U_i^0 = 0, \theta_i^0 = 0, C_i^0 = 0 \quad \text{for all } i$$

Now, using the left boundary condition of Eq. (7), we get:

$$U_0^n = \cos \omega t, \theta_0^n = t, C_0^n = 1 \quad \text{for all } n$$

Similarly, using the right boundary condition of Eq. (7), we obtain:

$$U_{i_{max}}^n = 0, \theta_{i_{max}}^n = 0, C_{i_{max}}^n = 0 \quad \text{for all } n$$

The initial conditions tell us what U, θ, and C are at the 1st time level, which is on the right-hand side of equations (8)–(10). The boundary conditions tell us what U, θ, and C are at the (n+1)th time level, which is also on the right-hand side of equations (8)–(10). Using the right sides of equations (8)-(10), it is possible to derive every value from the left-hand side at the (n+1)th time level. For every unknown $(n-1)$ time level, this procedure is repeated. At each internal node point on a specific (n)th level, a tridiagonal system of equations is composed of equations (8)-(10). To solve these systems of equations, the Thomas algorithm, which was devised by Carnahan et al. [34], is employed. U, θ, and C values are thus acquired at every internal node on a unique i at the (n+1)th time level. During each time step of the calculation, the tridiagonal equations corresponding to variables U, θ, and C are resolved through iterative procedures. The procedure of iteration concludes while the estimated percentage of round-off error for two successive iterations falls within the error tolerance of 10^{-4} at all grid points. It is assumed that the outcomes for U, θ, and C have attained their steady-state value when there are no absolute differences between the values of these variables at each grid point following two consecutive time steps. The numerical technique is considered consistent due to the local truncation error, which has an order of $[(\Delta y)^2 + (\Delta t)^2]$ and approaches zero as Δy and Δt approach zero. Apart from that, Soundalgekar and Ganesan [35] proved that the implicit finite-difference approach of the Crank-Nicolson type is unconditionally stable. The convergence of the numerical scheme is guaranteed by this because of its stability and compatibility.

4. RESULT AND DISCUSSIONS

In order to acquire a comprehensive picture of the situation, we computed numerical values for many physical parameters, including velocity, temperature, concentration, skin friction, Nusselt number, and Sherwood number. These calculations were performed for varying values of the parameters $S, F, Gc, Gr, K, M, Q, R, Kr$, and the phase angle (ωt). The numerical computations were executed using MATLAB, and the results are presented in figures (3)-(17). To verify the accuracy of the numerical method used, our study is compared to one by Rajesh et al. [17], which did not account for the effects of thermal stratification and heat source. The results of the current investigation are very comparable, as illustrated in Fig. 2. Table 2 displays the findings of the Nusselt number comparison between Ag(water) and Rajesh et al. [17] for various values of ϕ and R, excluding the presence of S and Q.

In the course of the research, the following values were utilized: $S = 0.7, F = 0.7, Gr = 5, Gc = 5, M = 2, K = 5, R = 3, Q = 1, Kr = 0.3, Pr = 0.71, Sc = 0.22, \omega t = \pi/3, \phi = 0.05$ and $t = 0.7$. The combined influence of the mass stratification (F) and thermal (S) factors on the non-dimensional velocity is seen in Fig. 3. The velocity diminishes when the thermal stratification (S) and mass stratification (F) intensify. There is a decrease in the effective convective potential between the hot plate and the fluid that is surrounding it when the parameter for thermal stratification, denoted by (S), is
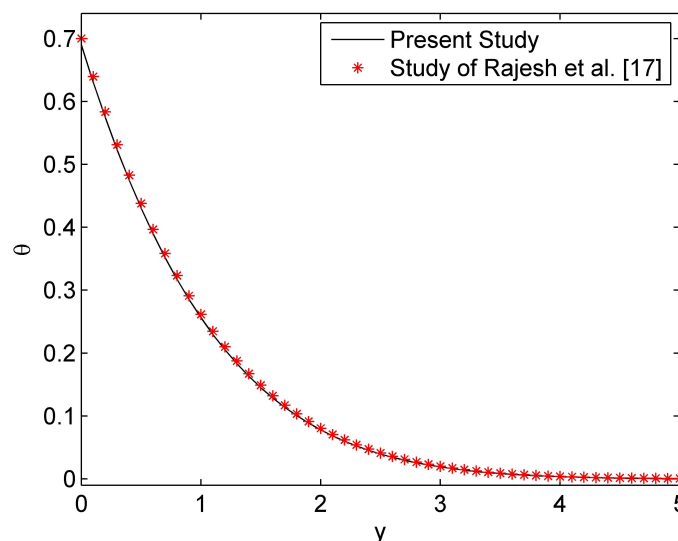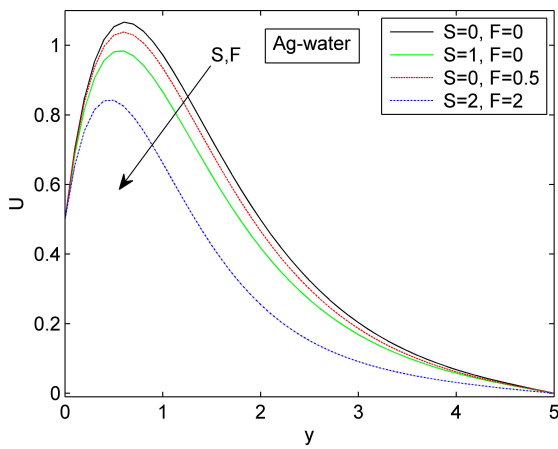

Figure 2. Comparison of the Temperature Profile without S, Q

Table 2. Comparison of Nusselt number for Ag(water) when $Pr = 6.2, t = 0.5$ and in absence of S, Q
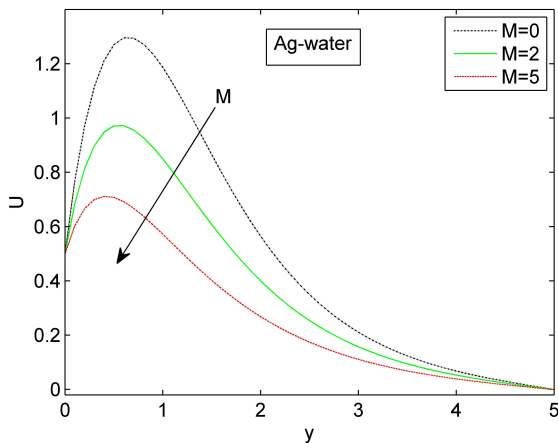
ϕ	R	Rajesh et al. [17]	Present Study
0		1.6530	1.6523
0.01		1.6820	1.6812
0.02	3	1.7109	1.7101
0.03		1.7399	1.7391
0.04		1.7689	1.7681
	1	1.4133	1.4126
	3	1.7689	1.7681
0.04	5	1.8785	1.8777
	7	1.9322	1.9313
	9	1.9641	1.9632

Figure 3. Velocity Profile for various values of S, F
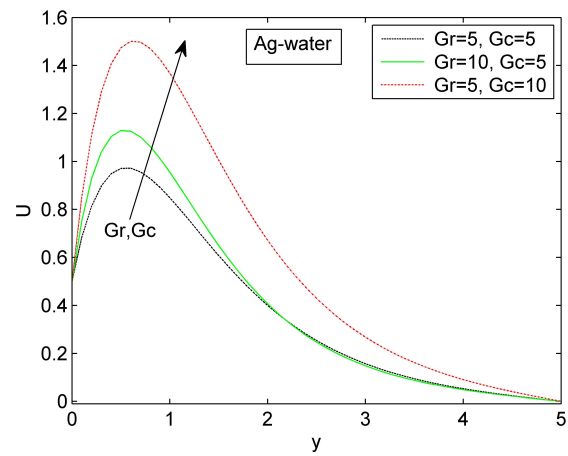
Figure 4. Velocity Profile for various values of Gr, Gc

Figure 5. Velocity Profile for various values of M
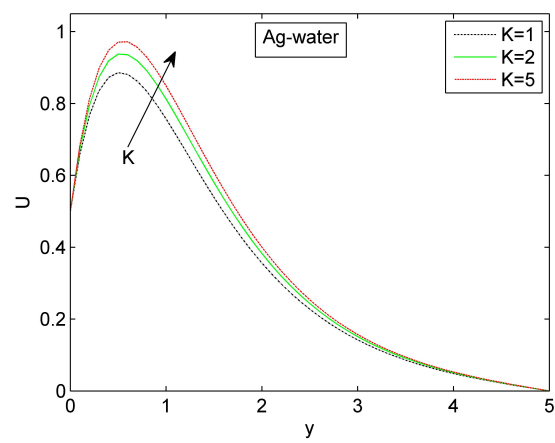
Figure 6. Velocity Profile for various values of K

increased. The buoyancy force is diminished due to this, leading to a decrease in the flow velocity. Moreover, elevating the mass stratication (F) value decreases the gradient of concentration between the surrounding environment and the surface. This leads to a decrease in the upward force exerted by the fluid, thereby causing a decrease in the velocity of the fluid flow. The velocity of the nanofluid is influenced by the combined effects of Gr and Gc, as illustrated in Fig. 4. An rise in the values of Gr and Gc leads to an increase in velocity. Increasing both Gr and Gc enhances the strength of the thermal and mass buoyancy forces. This suggests that both the thermal and mass buoyancy effects have a tendency to boost the velocity of the nanofluid. As depicted in Fig. 5, the fluid velocity diminishes with a rise in the magnetic parameter (M). It is observed that the thickness of the momentum boundary layer reduces as the magnetic parameter (M) increases. This pattern arises due to the Lorentz force generated by the transverse magnetic field, which causes a decrease

in the velocity of the nanofluid. The relationship between the porosity parameter (K) and the velocity of the nanofluid is seen in Fig. 6. The velocity is directly proportional to the value of the porosity parameter. Fig.7 demonstrates a reduction in the velocity of the nanofluid as the phase angle (ωt) increases.
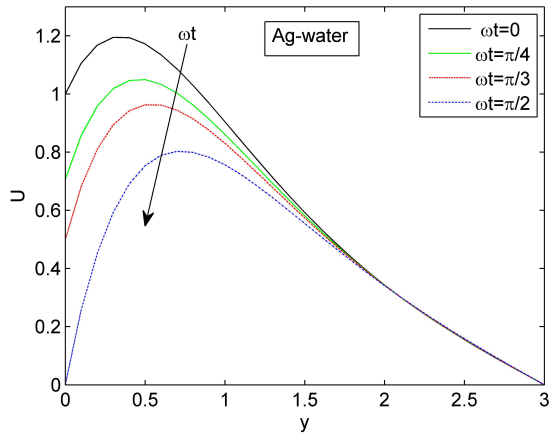

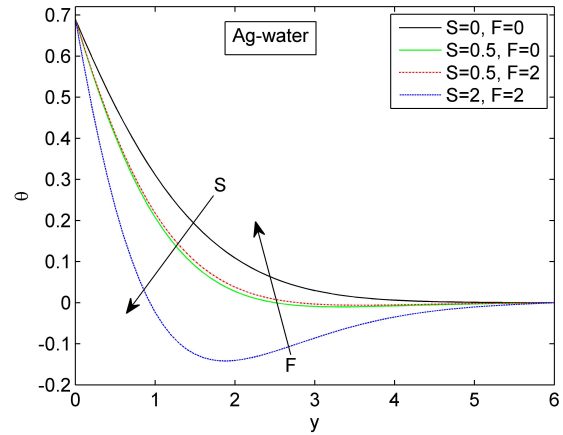**Figure 7.** Velocity Profile for various values of ωt

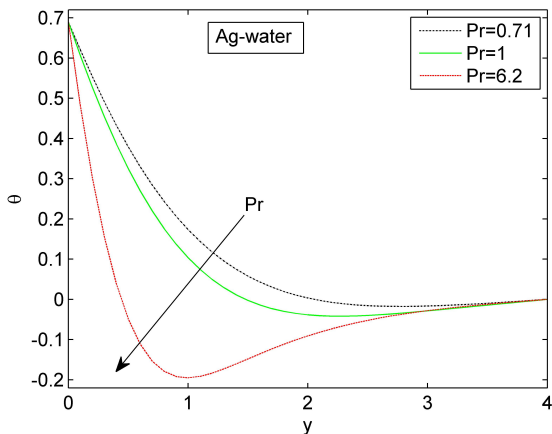**Figure 8.** Temperature Profile for various values of S, F

Figure 9. Temperature Profile for various values of Pr
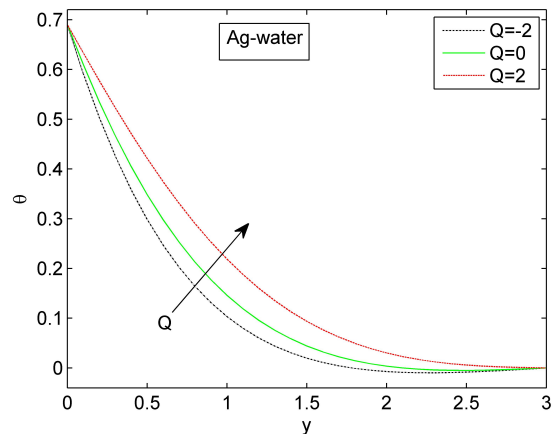
Figure 10. Temperature Profile for various values of Q

According to Fig. 8, the temperature of the nanofluid decreases with increasing thermal stratification (S) but increases with increasing mass stratification (F). The presence of thermal stratification (S) will cause a decrease in the temperature difference between the vertical plate and the surrounding fluid. As a result, the thermal boundary layer increases in thickness and the temperature decreases. It has been discovered that the boundary layer temperature will become negative for specific values of the stratification parameters (S, F). This phenomenon occurs because the fluids in close proximity to the plate may exhibit lower temperatures compared to the surrounding medium. Fig. 9 demonstrates the impact of the Prandtl number (Pr) on the temperature distribution of the nanofluid. As the Prandtl number increases, the temperature of the nanofluid decreases. A fluid with a high Prandtl number exhibits a diminished thermal conductivity. Consequently, the fluid's ability to conduct heat decreases, resulting in a decrease in the transfer rate and a reduction in the thickness of the thermal boundary layer. Therefore, the temperature of the nanofluid decreases. The influence of a heat source parameter (Q) on the temperature profile may be shown in Fig. 10. As the heat source parameter (Q) rises, the temperature of the nanofluid likewise gets higher. This characteristic corresponds to the overall physical behavior of the fluid. The temperature of the nanofluid lowers as the values of R increase in Fig. 11. This is due to the correlation between greater R values and lower thermal radiative flux, leading to lower temperatures. This can be seen as evidence of a decline in temperatures.

As seen in Fig. 12, the concentration of the nanofluid decreases as the mass stratification increases (F), while it increases when the thermal stratification occurs (S). Furthermore, Fig. 13 illustrates the impact of the Schmidt number (Sc) on the concentration profile. The concentration decreases whenever the Sc value increases. The concentration falls as the value of the chemical reaction parameter (Kr) increases, as depicted in Fig. 14. The concentration gradient is nullified due to a destructive chemical reaction, resulting in the cancellation of the buoyancy effect.
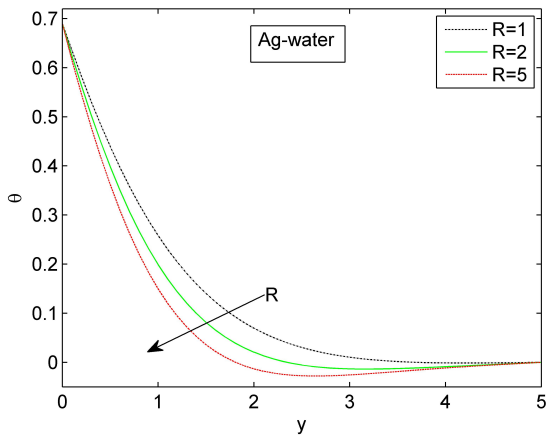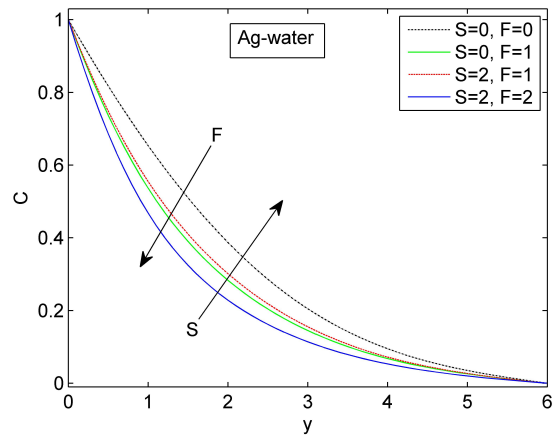
Figure 11. Temperature Profile for various values of R

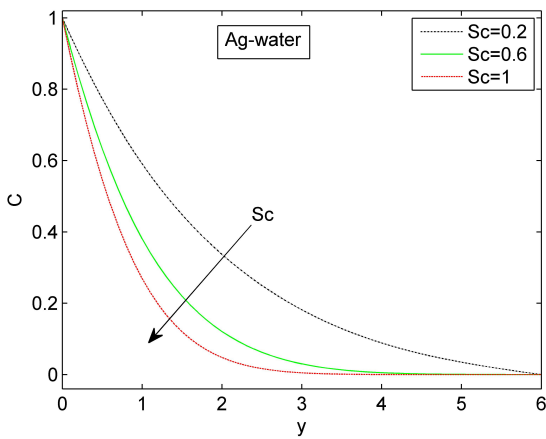**Figure 12.** Concentration Profile for various values of S, F

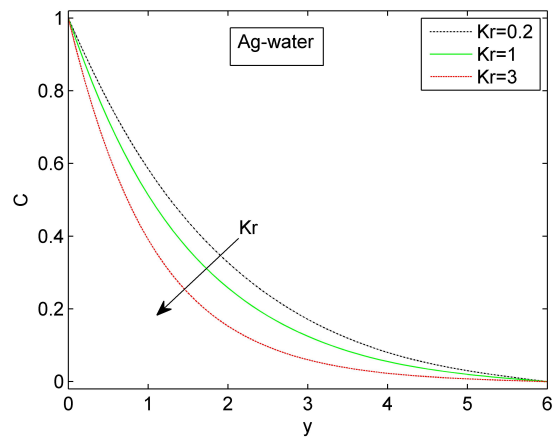**Figure 13.** Concentration Profile for various values of Sc

Figure 14. Concentration Profile for various values of Kr

4.1. Skin-Friction Coefficient, Nusselt Number and Sherwood Number

The skin-friction coefficient(C_f), the Nusselt number(Nu) and the Sherwood number(Sh) are defined, respectively as follows

$$C_f = \frac{\tau_w}{\rho_f u_0^2}, \quad Nu = \frac{q_w L_{ref}}{k_f(T_W' - T_\infty')}, \quad Sh = \frac{q_m L_{ref}}{D_{nf}(C_W' - C_\infty')}$$

where τ_w, q_w, q_m are the shear stress or skin-friction , rate of the heat flux and the rate of mass transfer from the surface of the plate correspondingly defined by

$$\tau_w = \mu_{nf}\left(\frac{\partial u'}{\partial y'}\right)_{y'=0}, \quad q_w = k_{nf}\left(\frac{\partial T'}{\partial y'}\right)_{y'=0}, \quad q_m = D_{nf}\left(\frac{\partial C'}{\partial y'}\right)_{y'=0}$$

By utilizing non-dimensional quantities, we obtain

$$C_f = \frac{1}{(1-\phi)^{2.5}}\left(\frac{\partial U}{\partial y}\right)_{y=0}, \quad Nu = -\frac{k_{nf}}{k_f}\left(\frac{\partial \theta}{\partial y}\right)_{y=0}, \quad Sh = -\left(\frac{\partial C}{\partial y}\right)_{y=0}$$

The outcomes of thermal and mass stratification parameters on the skin-friction coefficient(C_f), Nusselt number(Nu), and Sherwood number(Sh) are shown in Figures 15, 16 and 17. In both stratification, the skin-friction coefficient decreases. Without stratification, the Nusselt number would continue to decline indefinitely, but increasing mass stratification(F) and reducing thermal stratification(S) would help it to approach a stable state. Likewise, the Sherwood number obtains a stable state for greater thermal stratification(S) and lower mass stratification(F).

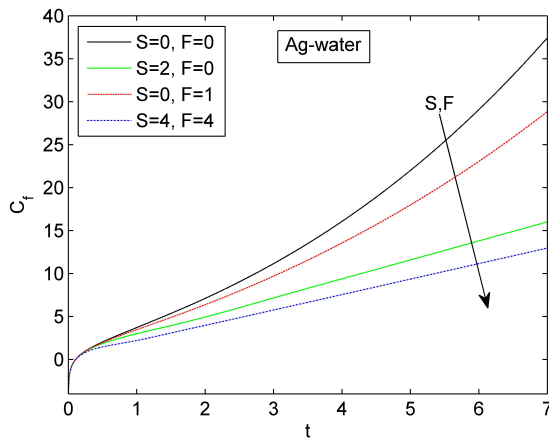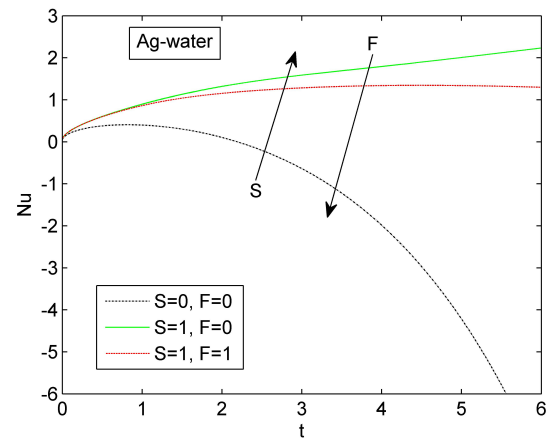**Figure 15.** Skin-friction Coefficient for various values of S, F

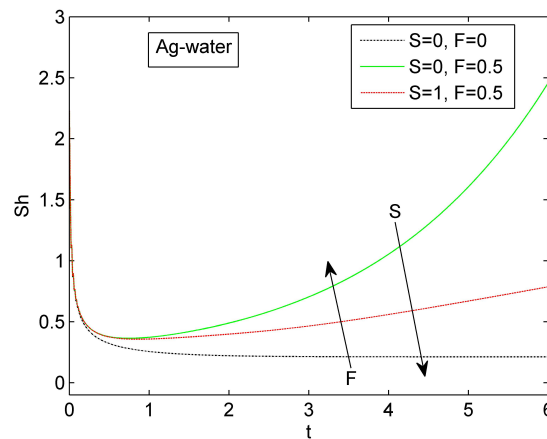**Figure 16.** Nusselt Number for various values of S, F

Figure 17. Sherwood Number for various values of S, F

5. CONCLUSIONS

This research paper explores the effects of thermal and mass stratification on unsteady MHD nanofluid for Ag-water and Cu-water as it pasts an oscillating vertical plate in a porous medium with variable temperature. The outcomes of this study reveal that when the thermal stratification parameter is increased, the velocity, temperature, and skin friction coefficient all decrease, but the concentration rises significantly. Moreover, A decrease in velocity, concentration, and the Nusselt number, together with an increase in temperature, are the outcomes of increasing the mass stratification parameter. The stratification significantly enhances the thermal conductivity of the nanofluid. The increased thermal conductivity enables more efficient heat transfer, making it applicable in several industries like power generation, cooling of electronic components, and manufacturing of vehicles. In numerous chemical reactions, Ag nanoparticles function as effective catalysts. They can increase reaction velocity and selectivity due to their huge surface area and distinctive electrical characteristics. Our research will help them be used to treat pollution, make chemicals, and make catalytic converters.

ORCID

 Hemant Agarwal, https://orcid.org/0009-0004-2115-6482; **Shyamanta Chakraborty**, https://orcid.org/0000-0001-5839-4856; **Rupam Shankar Nath**, https://orcid.org/0009-0002-2352-0538

REFERENCES

[1] S.U.S. Choi, and J.A. Eastman, Enhancing thermal conductivity of fluids with nanoparticles. Technical report, (Argonne National Lab.(ANL), Argonne, IL, United States, 1995). https://ecotert.com/pdf/196525_From_unt-edu.pdf

[2] H.F. Oztop, and E. Abu-Nada, "Numerical study of natural convection in partially heated rectangular enclosures filled with nanofluids," International journal of heat and fluid flow, **29**(5), 1326–1336 (2008). https://doi.org/10.1016/j.ijheatfluidflow.2008.04.009

[3]   S. Das, and R.N. Jana, "Natural convective magneto-nanofluid flow and radiative heat transfer past a moving vertical plate,' Alexandria Engineering Journal, **54**(1), 55–64 (2015). https://doi.org/10.1016/j.aej.2015.01.001

[4]   S. Das, R.N. Jana, and O.D. Makinde, "Transient natural convection in a vertical channel filled with nanofluids in the presence of thermal radiation," Alexandria Engineering Journal, **55**(1), 253–262 (2016). https://doi.org/10.1016/j.aej.2015.10.013

[5]   M.M. Rashidi, E. Momoniat, M. Ferdows, and A. Basiriparsa, "Lie group solution for free convective flow of a nanofluid past a chemically reacting horizontal plate in a porous media," Mathematical Problems in Engineering, 2014, (2014). https://doi.org/10.1155/2014/239082

[6]   M.H. Abolbashari, N. Freidoonimehr, F. Nazari, and M.M. Rashidi, "Entropy analysis for an unsteady mhd flow past a stretching permeable surface in nano-fluid," Powder Technology, **267**, 256–267 (2014). https://doi.org/10.1016/j.powtec.2014.07.028

[7]   P.K. Kameswaran, M. Narayana, P. Sibanda, and P.V.S.N. Murthy, "Hydromagnetic nanofluid flow due to a stretching or shrinking sheet with viscous dissipation and chemical reaction effects," International Journal of Heat and Mass Transfer, **55**(25-26), 7587–7595 (2012). https://doi.org/10.1016/j.ijheatmasstransfer.2012.07.065

[8]   T.G. Motsumi, and O.D. Makinde, "Effects of thermal radiation and viscous dissipation on boundary layer flow of nanofluids over a permeable moving flat plate,' Physica Scripta, **86**(4), 045003 (2012). https://dx.doi.org/10.1088/0031-8949/86/04/045003

[9]   M. Sheikholeslami, S. Abelman, and D.D. Ganji, "Numerical simulation of mhd nanofluid flow and heat transfer considering viscous dissipation," International Journal of Heat and Mass Transfer, **79**, 212–222 (2014). https://doi.org/10.1016/j.ijheatmasstransfer.2014.08.004

[10] A.J. Chamkha, and A.M. Aly, "MHD free convection flow of a nanofluid past a vertical plate in the presence of heat generation or absorption effects," Chemical Engineering Communications, **198**(3), 425–441 (2010). https://doi.org/10.1080/00986445.2010.520232

[11] M. Turkyilmazoglu, "Exact analytical solutions for heat and mass transfer of mhd slip flow in nanofluids," Chemical Engineering Science, **84**, 182–187 (2012). https://doi.org/10.1016/j.ces.2012.08.029

[12] S.M. Fotukian, and M.N. Esfahany, "Experimental study of turbulent convective heat transfer and pressure drop of dilute cuo/water nanofluid inside a circular tube," International communications in heat and mass transfer, **37**(2), 214–219 (2010). https://doi.org/10.1016/j.icheatmasstransfer.2009.10.003

[13] M. Sheikholeslami, M.G. Bandpy, R. Ellahi, and A. Zeeshan, "Simulation of MHD cuo–water nanofluid flow and convective heat transfer considering lorentz forces," Journal of Magnetism and Magnetic Materials, **369**, 69–80 (2014). https://doi.org/10.1016/j.jmmm.2014.06.017

[14] N. Sandeep, and M.G. Reddy, "Heat transfer of nonlinear radiative magnetohydrodynamic cu-water nanofluid flow over two different geometries," Journal of Molecular Liquids, **225**, 87–94 (2017). https://doi.org/10.1016/j.molliq.2016.11.026

[15] P.C. Reddy, M.C. Raju, and G.S.S. Rajum, "Free convective heat and mass transfer flow of heat-generating nanofluid past a vertical moving porous plate in a conducting field," Special Topics and Reviews in Porous Media: An International Journal, **7**(2), 2016. https://doi.org/10.1615/SpecialTopicsRevPorousMedia.2016016973

[16] B. Mahanthesh, B.J. Gireesha, and R.S.R. Gorla, "Heat and mass transfer effects on the mixed convective flow of chemically reacting nanofluid past a moving/stationary vertical plate," Alexandria engineering journal, **55**(1), 569–581 (2016). https://doi.org/10.1016/j.aej.2016.01.022

[17] R. Vemula, L. Debnath, and S. Chakrala, "Unsteady mhd free convection flow of nanofluid past an accelerated vertical plate with variable temperature and thermal radiation," International Journal of Applied and Computational Mathematics, **3**(2), 1271–1287 (2017). https://doi.org/10.1007/s40819-016-0176-5

[18] C.-Y. Cheng, "Double-diffusive natural convection along a vertical wavy truncated cone in non-newtonian fluid saturated porous media with thermal and mass stratification," International Communications in Heat and Mass Transfer, **35**(8), 985–990 (2008). https://doi.org/10.1016/j.icheatmasstransfer.2008.04.007

[19] C.-Y. Cheng, "Combined heat and mass transfer in natural convection flow from a vertical wavy surface in a power-law fluid saturated porous medium with thermal and mass stratification," International Communications in Heat and Mass Transfer, **36**(4), 351–356 (2009). https://doi.org/10.1016/j.icheatmasstransfer.2009.01.003

[20] A. Paul, R.K. Deka, et al., "Unsteady natural convection flow past an infinite cylinder with thermal and mass stratification," Int. J. Eng. Math. **2017**, 8410691 (2017). https://doi.org/10.1155/2017/8410691

[21] P.M. Krishna, N. Sandeep, and R.P. Sharma, "Computational analysis of plane and parabolic flow of mhd carreau fluid with buoyancy and exponential heat source effects," The European Physical Journal Plus, **132**, 202–216 (2017). https://doi.org/10.1140/epjp/i2017-11469-9

[22] T. Gowri, and A. Selvaraj, "Rotational effect of unsteady mhd-parabolic flow past a vertical plate through porous medium with uniform temperature mass diffusion," International Journal of Mechanical Engineering, **6**, 2468–2473 (2021). https://www.kalaharijournals.com/resources/DEC_337.pdf

[23] A. Selvaraj, S.D. Jose, R. Muthucumaraswamy, and S. Karthikeyan, "MHD-parabolic flow past an accelerated isothermal vertical plate with heat and mass diffusion in the presence of rotation," Materials Today: Proceedings, **46**, 3546–3549 (2021). https://doi.org/10.1016/j.matpr.2020.12.499

[24] R.S. Nath, and R.K. Deka, "The effects of thermal stratification on flow past an infinite vertical plate in presence of chemical reaction," East European Journal of Physics, (3), 223–232 (2023). https://doi.org/10.26565/2312-4334-2023-3-19

[25] N. Kalita, R.K. Deka, and R.S. Nath, "Unsteady flow past an accelerated vertical plate with variable temperature in presence of thermal stratification and chemical reaction," East European Journal of Physics, (3), 441–450 (2023). https://doi.org/10.26565/2312-4334-2023-3-49

[26] R.S. Nath, R.K. Deka, and H. Kumar, "The effect of thermal stratification on unsteady parabolic flow past an infinite vertical plate with chemical reaction," East European Journal of Physics, (4), 77–86 (2023). https://doi.org/10.26565/2312-4334-2023-4-08

[27] R.S. Nath, and R.K. Deka, "Theoretical study of thermal and mass stratification effects on mhd nanofluid past an exponentially accelerated vertical plate in a porous medium in presence of heat source, thermal radiation and chemical reaction," International Journal of Applied and Computational Mathematics, **10**(2), 92 (2024). https://doi.org/10.1007/s40819-024-01721-9

[28] R.S. Nath, and R.K. Deka, "Thermal and mass stratification effects on MHD nanofluid past an exponentially accelerated vertical plate through a porous medium with thermal radiation and heat source," International Journal of Modern Physics B, 2550045 (2024). https://doi.org/10.1142/S0217979225500456

[29] R.S. Nath, and R.K. Deka, "Thermal and mass stratification effects on unsteady parabolic flow past an infinite vertical plate with exponential decaying temperature and variable mass diffusion in porous medium," ZAMM-Journal of Applied Mathematics and Mechanics/Zeitschrift für Angewandte Mathematik und Mechanik, **104**(6), e202300475 (2024). https://doi.org/10.1002/zamm.202300475

[30] R.S. Nath, and R.K. Deka, "A numerical study on the mhd ternary hybrid nanofluid (cu-al2o3-tio2/h2o) in presence of thermal stratification and radiation across a vertically stretching cylinder in a porous medium," East European Journal of Physics, (1), 232–242 (2024). https://doi.org/10.26565/2312-4334-2024-1-19

[31] M. Sheikholeslami, H.R. Kataria, and A.S. Mittal, "Effect of thermal diffusion and heat generation on mhd nanofluid flow past an oscillating vertical plate through porous medium," Journal of Molecular Liquids, **257**, 12–25 (2018). https://doi.org/10.1016/j.molliq.2018.02.079

[32] R. Rammoorthi, and D. Mohanavel, "Influence of radiative magnetic field on a convective flow of a chemically reactive hybrid nanofluid over a vertical plate," Journal of Advanced Research in Fluid Mechanics and Thermal Sciences, **105**(1), 90–106 (2023). https://doi.org/10.37934/arfmts.105.1.90106

[33] S. Rosseland, *Astrophysik und atom-theoretische Grundlagen*, (Springer-verlag, berlin, 1931).

[34] B. Carnahan, H.A. Luther, and J.O. Wilkes, *Applied numerical methods*, (john willey and sons. Inc., New York, 1969), pp. 168–169.

[35] V.M. Soundalgekar, and P. Ganesan, "Finite-difference analysis of transient free convection with mass transfer on an isothermal vertical flat plate," International Journal of Engineering Science, **19**(6), 757–770 (1981). https://doi.org/10.1016/0020-7225(81)90109-9

ЧИСЕЛЬНЕ ДОСЛІДЖЕННЯ ВПЛИВУ ТЕРМІЧНОЇ ТА МАСОВОЇ СТРАТИФІКАЦІЇ НА ХІМІЧНО РЕАГУЮЧИЙ НЕСТАЦІОНАРНИЙ МГД-ПОТІК НАНОФЛЮЇДУ ПОВЗ ОСЦИЛЮЮЧУ ВЕРТИКАЛЬНУ ПЛАСТИНУ ЧЕРЕЗ ПОРИСТЕ СЕРЕДОВИЩЕ

Хемант Агарвал[a], **Шьяманта Чакраборті**[b], **Рупам Шанкар Нат**[a]
[a]Департамент математики, Університет Гаухаті, Гувахаті-781014, Ассам, Індія
[b]UGC-HRDC, Університет Гаухаті, Гувахаті-781014, Ассам, Індія

Метою цього дослідження є вивчення спільного впливу термічної та масової стратифікації на нестаціонарну магнітогідродинамічну нанофлюїд повз вертикально коливальну пластину зі змінною температурою. Основні рівняння задачі розв'язуються чисельно за допомогою неявного підходу Кренка-Ніколсона. Значні результати термічної та масової стратифікації контрастують із середовищем, де стратифікація відсутня. Швидкість зменшується при обох типах стратифікації, тоді як температура зменшується при термічній стратифікації, а концентрація зменшується при масовій стратифікації. Ми використовуємо графіки, щоб продемонструвати вплив різних параметрів, у тому числі фазового кута, теплового випромінювання, напруженості магнітного поля, джерел тепла/стікача та хімічних реакцій. Крім того, обчислюються та представлені графічно коефіцієнт шкірного тертя, число Нуссельта та число Шервуда. Результати підкреслюють критичну роль стратифікації в покращенні динаміки рідини та підвищенні ефективності процесів тепло- та масообміну, надаючи важливу інформацію для інженерних та екологічних застосувань за подібних обставин.

Ключові слова: *стратифікація маси; хімічна реакція; нанофлюїд; термічна стратифікація; осцилююча вертикальна пластина; метод Кренка-Ніколсона; теплове випромінювання; пористе середовище; МГД*

INFLUENCE OF ELECTROPHYSICAL PARAMETERS OF MAGNETODIELECTRIC LAYER ON A PCP ON ITS ELECTRODYNAMIC CHARACTERISTICS

Mikhail V. Nesterenko*, **Victor A. Katrich,** **Oleksandr M. Dumin,** **Natalya K. Blinova**

V.N. Karazin Kharkiv National University, 4, Svobody Sq., Kharkiv, Ukraine, 61022
*Corresponding Author: mikhail.v.nesterenko@gmail.com

Within the framework of the impedance concept, approximate analytical formulas for the distributed surface impedance of the magnetodielectric layer with the inhomogeneous permeability and permittivity located on a perfectly conducting plane (PCP) for the cases of a quadratic law of changes in electrical parameters along the layer thickness are obtained. A comparative analysis of electromagnetic waves reflection coefficient from this structure for various laws of change of the permeability and permittivity is presented.

Keywords: *Magnetodielectric layer; Impedance concept; Surface impedance; Inhomogeneous permeability; Inhomogeneous permittivity; Reflection coefficient*
PACS: 82.45Mp; 84.40.Lj

INTRODUCTION

One of the ways to expand the limits of change in the electrodynamic characteristics of antenna and waveguide devices in SHF and EHF bands is the deposition of dielectric (ε-type), magnetic (μ-type), magnetodielectric (μ,ε-type) coatings, in the general case, with variable physical properties, directly on their metal radiating devices (for example, [1]-[12] for ε-type, [10]-[14] for μ-type) and waveguide surfaces (for example, [15]-[19] for ε-type, [20]-[23] for μ-type, [24]-[31] for μ,ε-type), including metamaterial coating [30]-[34]. Modern technologies to produce thin-film coatings make it possible to obtain non-uniform in the direction perpendicular to the ideally conducting plane of the base and inhomogeneous structures [31], [35]-[41]. Note that the nonuniformity of the coating is achieved by using multilayered magnetodielectrics. To calculate the parameters of the devices by setting and solving the corresponding boundary value problem, it is desirable to use the boundary conditions of the impedance type [12], [30], [31], [42]-[48].

An approximate analytical solution of the field equations for an inhomogeneous magnetodielectric layer on a PCP with a linear law of change the permittivity is obtained in [31] by the authors. A similar solution was found in [51] also by the authors for a layer with a linear law of change in magnetic permeability.

In this paper the approximate analytical expressions for the distributed surface impedance of the magnetodielectric layer with the inhomogeneous permeability and permittivity located on a PCP for the cases of a quadratic law of changes in electrical parameters along the layer thickness are presented. If the surface impedance is found, it is not difficult to determine other electrodynamic characteristics of the structure under consideration (for example, reflection (absorption) coefficient [21]-[23] or backscattering cross section [43]). A comparative analysis of reflection characteristics for various laws of change the permeability and permittivity is also presented.

APPROXIMATE BOUNDARY CONDITIONS FOR ELECTROMAGNETIC FIELDS

The one-sided impedance boundary conditions allow to decrease the number of interfacing electrodynamic volumes which should be taken into account for the solution of a problem. Rejecting the need to determine fields inside the adjacent metal-dielectric elements at the problem formulation level is the main benefit of the impedance approach. The Shchukin-Leontovich impedance condition on the connected boundary surface S (see for example [12, 30, 31, 42-48]) can be written in following form:

$$[\mathbf{n},\mathbf{E}]\big|_S = \overline{Z}_S[\mathbf{n},[\mathbf{n},\mathbf{H}]]\big|_S , \qquad (1)$$

where $\mathbf{E}$ and $\mathbf{H}$ are the vectors the electrical and magnetic fields with harmonic time dependence (in our case, the time t dependence is $e^{i\omega t}$, $\omega = 2\pi f$ is the circular frequency, f is the frequency, measured in Hz), $\mathbf{n}$ is the normal to impedance surface, directed inside the impedance region, $\overline{Z}_S = \overline{R}_S + i\overline{X}_S = Z_S / Z_0$ is the surface impedance normalized to the resistance of free space $Z_0 = 120\pi$ Ohm.

Thus, only the tangential components of the electromagnetic fields are involved in the boundary condition (1), there are some restrictions on the form of the surface S. It is clear that the condition (1) holds if the radius of surface curvature is much greater than the length of the incident electromagnetic wave.

SURFACE IMPEDANCE OF MAGNETODIELECTRIC LAYER WITH INHOMOGENEOUS PARAMETERS ON PCP

Let us consider a plane layer of a magnetodielectric substance specified in Cartesian coordinate system (x, y, z) for $-\infty < x, y < \infty$, $-h_d \leq z \leq h_d$ with permeability μ_1 and permittivity ε_1. The layer is placed on PCP at $z = h_d$. Let the plane monochromatic electromagnetic wave with $E_x(z) = E_{0x}e^{-ikz}$ ($k = 2\pi/\lambda$, λ is the wavelength in a free space) be incident from the free half-space $z = -\infty$ on the magnetodielectric layer (Fig. 1).
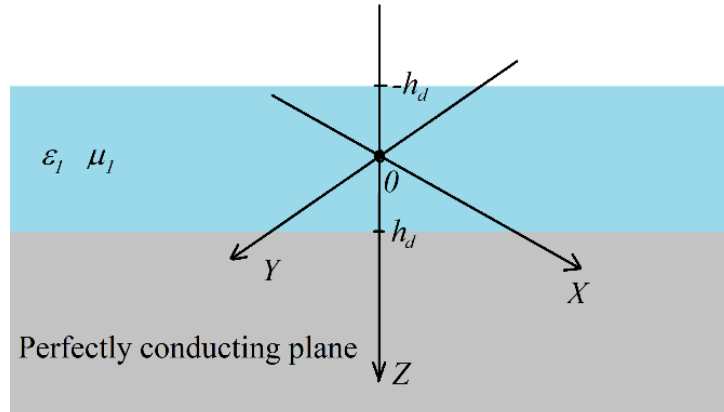
Figure 1. The dipole geometry and accepted designations

Then the distributed surface impedance for this layer determined by the expression (1) can be written as

$$\overline{Z}_S = E_{0x}(-h_d) / H_{0y}(-h_d) , \tag{2}$$

where the fields $E_{0x}(-h_d)$ and $H_{0y}(-h_d)$, i.e. $E_x(z)$ and $H_y(z)$ at the plane $z = -h_d$, inside the magnetodielectric layer with material parameters $\mu_1 = \mu_1(z)$, $\varepsilon_1 = const$ can be found as solution of the following differential equations

$$\frac{d^2 E_x(z)}{dz^2} - \frac{1}{\mu_1(z)}\frac{d\mu_1(z)}{dz}\frac{dE_x(z)}{dz} + k^2\mu_1(z)\varepsilon_1 E_x(z) = 0, \tag{3a}$$

$$H_y(z) = \frac{i}{k\mu_1(z)}\frac{dE_x(z)}{dz}, \tag{3b}$$

with the boundary conditions on the surfaces $z = \pm h_d$.

For the case $\varepsilon_1 = \varepsilon_1(z)$, $\mu_1 = const$, the field equations have the form

$$\frac{d^2 E_x(z)}{dz^2} + k^2\mu_1\varepsilon_1(z)E_x(z) = 0, \tag{4a}$$

$$H_y(z) = \frac{i}{k\mu_1}\frac{dE_x(z)}{dz}, \tag{4b}$$

also, with the boundary conditions on the surfaces $z = \pm h_d$.

The equations (3) and (4) are valid for arbitrary permeability and permittivity functions $\mu_1(z)$ and $\varepsilon_1(z)$. The relation (2) for normal incidence of plane wave on the plane magnetodielectric layer is exact. The solutions of the equations (3) and (4) are quite complex, can be obtained analytically for a limited number of the functions $\mu_1(z)$ ($\varepsilon_1(z)$), and can be expressed by special functions. If the distribution $\mu_1(z)$ or $\varepsilon_1(z)$ is a relatively slow varying function within the layer, then an approximate solution in a class of elementary functions can be obtained.

Let consider the following form of $\mu_1(z)$ and $\varepsilon_1(z)$:

$$\mu_1(z) = \mu_1(0)[1 - \mu_r f(z)], \tag{5a}$$

$$\varepsilon_1(z) = \varepsilon_1(0)[1 - \varepsilon_r f(z)], \tag{5b}$$

where the constant $\mu_r = |[\mu_1(0) - \mu_1(-h_d)]/\mu_1(0)|$ ($\varepsilon_r = |[\varepsilon_1(0) - \varepsilon_1(-h_d)]/\varepsilon_1(0)|$) is the relative value of permeability (or permittivity) change in the layer ($\mu_r \ll 1$, $\varepsilon_r \ll 1$), $f(z) = (-z/h_d)^n$, ($n = 1, 2, 3...$) is a predefined function. Then for the linear law of change of function $f(z) = (-z/h_d)$ the approximate analytical solution of the equation system (3) and (4) by the method of expanding the desired function into a series in a small parameter μ_r (ε_r) up to terms of order μ_r^2 (ε_r^2) have the form ([51], [31])

$$\bar{Z}_S^\mu = i\bar{Z}_1^\mu (1 - \mu_r) \frac{\tan(k_{1\mu} h_d)}{1 + \mu_r f_{Lin}(k_{1\mu} h_d)\tan(k_{1\mu} h_d)}, \tag{6a}$$

$$\bar{Z}_S^\varepsilon = i\bar{Z}_1^\varepsilon \frac{\tan(k_{1\varepsilon} h_d)}{1 + \varepsilon_r f_{Lin}(k_{1\varepsilon} h_d)\tan(k_{1\varepsilon} h_d)},$$
$$f_{Lin}(k_{1\mu(\varepsilon)} h_d) = \left(\frac{1}{2k_{1\mu(\varepsilon)} h_d} + \frac{i}{2} \right), \tag{6b}$$

where h_d is the total thickness of the magnetodielectric layer; $k_{1\mu}^2 = k^2 \mu_1(0)\varepsilon_1$, $\bar{Z}_1^\mu = \sqrt{\mu_1(0)/\varepsilon_1}$; $k_{1\varepsilon}^2 = k^2 \mu_1 \varepsilon_1(0)$ $\bar{Z}_1^\varepsilon = \sqrt{\mu_1/\varepsilon_1(0)}$ respectively for (6a) and (6b).

We further use the same method for solving equations (3) and (4) for the quadratic law of change permeability and permittivity $f(z) = (z/h_d)^2$. Then the result is:

$$f = 10.0 \quad \bar{Z}_S^\mu = i\bar{Z}_1^\mu (1 - \mu_r) \frac{\tan(k_{1\mu} h_d) + \mu_r f_{Sq1}(k_{1\mu} h_d)}{1 + \mu_r f_{Sq2}(k_{1\mu} h_d)\tan(k_{1\mu} h_d)}, \tag{7a}$$

$$\bar{Z}_S^\varepsilon = i\bar{Z}_1^\varepsilon \frac{\tan(k_{1\varepsilon} h_d) + \varepsilon_r f_{Sq1}(k_{1\varepsilon} h_d)}{1 + \varepsilon_r f_{Sq2}(k_{1\varepsilon} h_d)\tan(k_{1\varepsilon} h_d)},$$
$$f_{Sq1}(k_{1\mu(\varepsilon)} h_d) = \frac{1}{k_{1\mu(\varepsilon)} h_d} - \frac{\tan(k_{1\mu(\varepsilon)} h_d)}{(k_{1\mu(\varepsilon)} h_d)^2}, \quad f_{Sq2}(k_{1\mu(\varepsilon)} h_d) = \frac{k_{1\mu(\varepsilon)} h_d}{6}. \tag{7b}$$

The field reflection coefficient R from the structure under consideration, and, accordingly, the power absorption coefficient A will be determined by the following expressions:

$$R = |1 - \bar{Z}_S^{\mu(\varepsilon)}|/|1 + \bar{Z}_S^{\mu(\varepsilon)}|, \quad A = 1 - R^2. \tag{8}$$

NUMERICAL RESULTS

The material parameters of the magnetodielectric TDK IR-E110 used in these calculations at the frequency band $f = 7 \div 12$ GHz according [25] are $\varepsilon_1 = 8.84 - i0.084$ and $\mu_1 = 2.42 - 0.0825 f[GHz] - i0.994$. If the layer thickness is equal to the quarter wavelength in the magnetodielectric ($h_d \approx 1.8$ mm at GHz), as seen in the Figs. 2a-5a, the reflection coefficient R has the distinct minimum both for $\mu_1(z)$ and for $\varepsilon_1(z)$ (first resonance). Here and further in the Fig. 2: if μ_r, $\varepsilon_r > 0$, then $\mu_1(z)$, $\varepsilon_1(z)$ increasing towards the PCP, if μ_r, $\varepsilon_r < 0$, then $\mu_1(z)$, $\varepsilon_1(z)$ decreasing towards the PCP. The next resonance occurs at the layer thickness equal to three quarters of the wavelength in the magnetodielectric ($h_d \approx 5.4$ mm at $f = 10.0$ GHz). Moreover, these resonances are observed for both considered laws of distribution of material parameters in the layer.

Due to the losses in the substance, we do not have a perfect absorption for the uniform distribution, as the black curves show in all the figures. Thus, a small decrease in the refractive index of the medium at the air-medium interface makes it possible to reduce reflection compared to the case of an increase in this index (Figs. 2a,b, 4a,b – red curves), and even compared to a homogeneous medium (Figs. 4a, b – red and black curves). The latter is very important for creating new structures with strong radio wave absorption. For a relatively thick layer of a medium, see Figs. 2c, 4c, the reflection is smaller in the case of a decrease in the refractive index in the direction of an ideal conductor, since it is more difficult for a wave that has entered the medium to leave it.
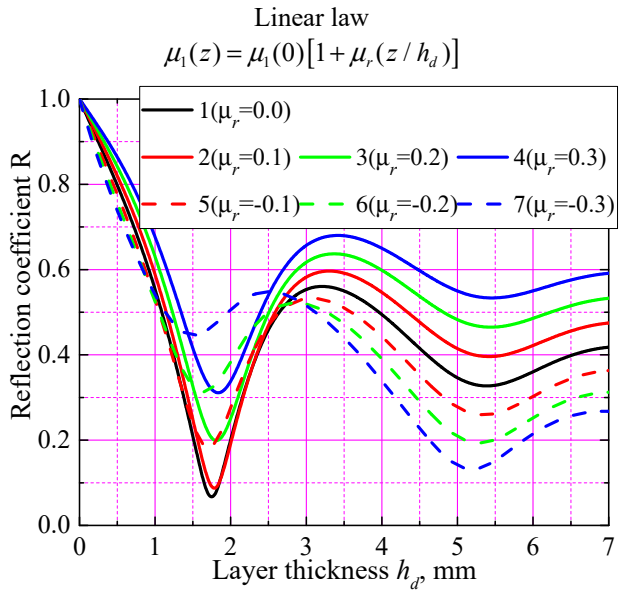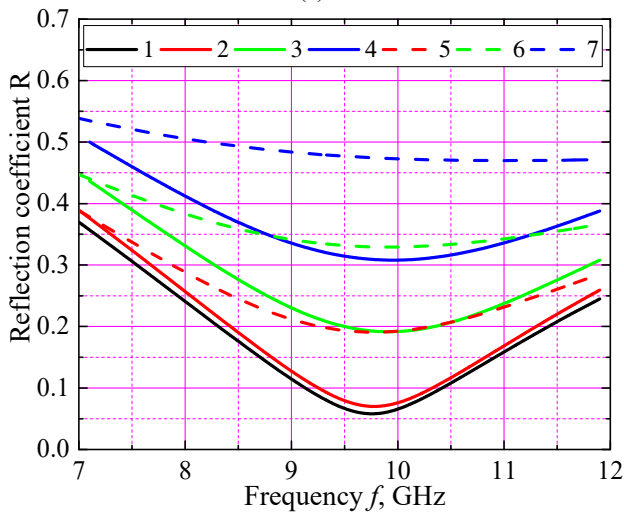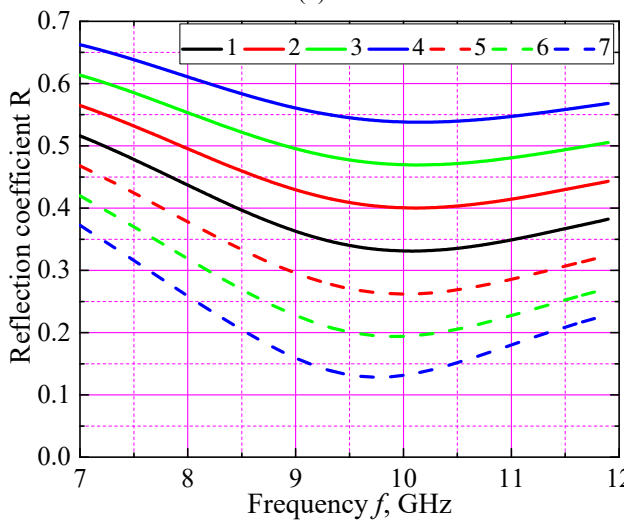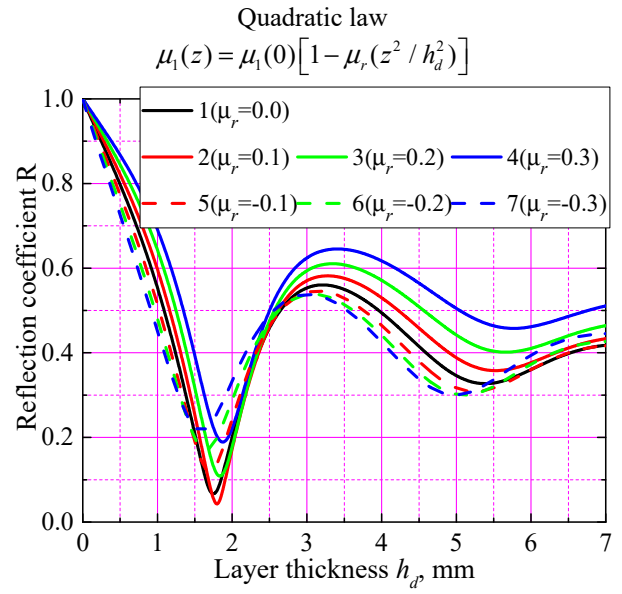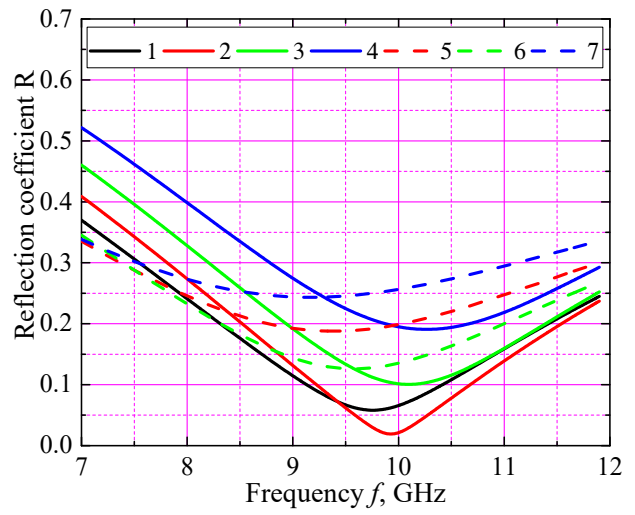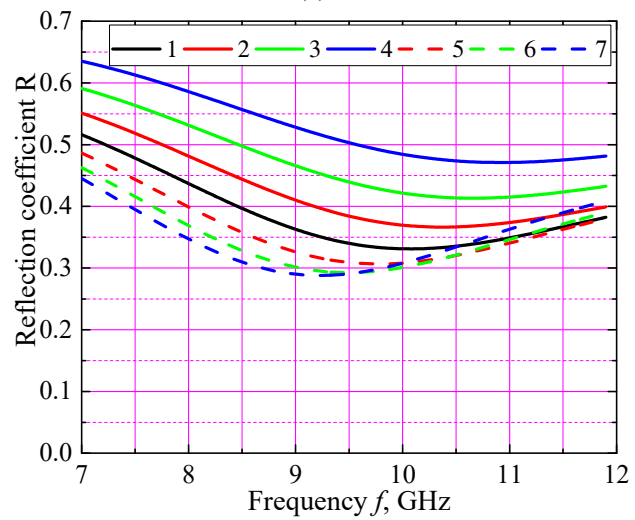
Figure 2. Reflection coefficient R versus layer thickness h_d at $f = 10$ GHz (a); and frequency (b) - $h_d = 1.8$ mm, (c) - $h_d = 5.4$ mm for linear law $\mu_1(z)$.
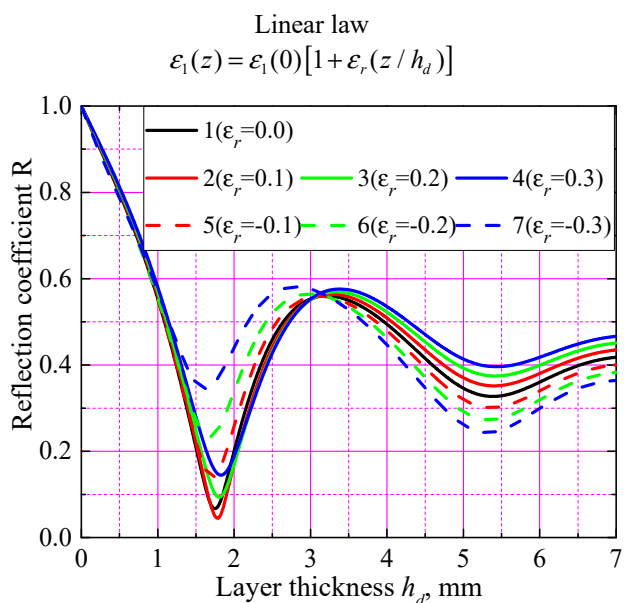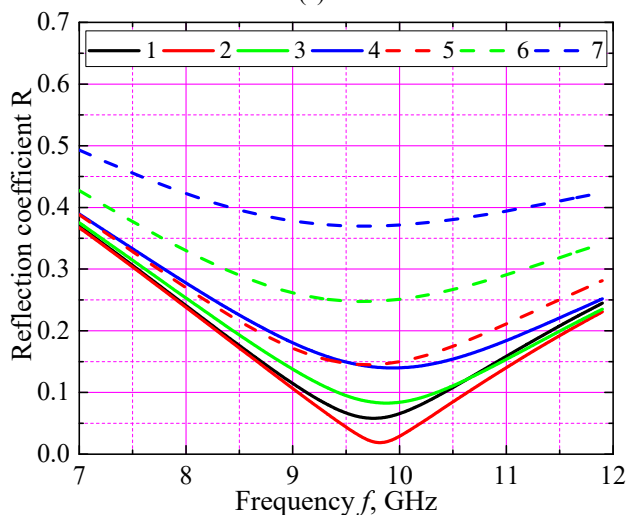
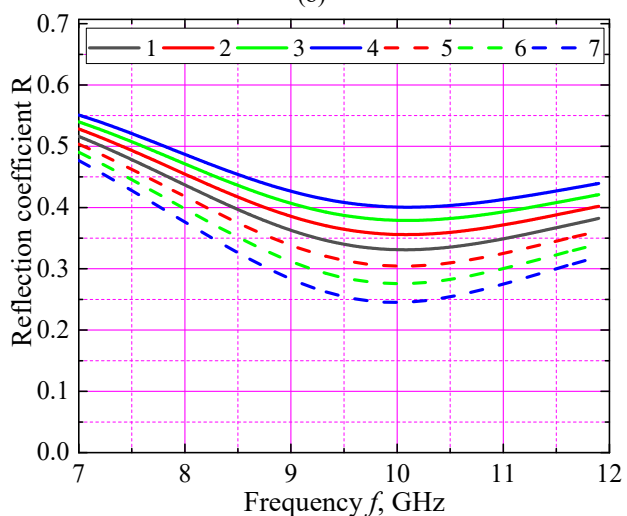**Figure 3.** Reflection coefficient R versus layer thickness h_d at $f = 10$ GHz (a); and frequency (b) - $h_d = 1.8$ mm, (c) - $h_d = 5.4$ mm for quadratic law $\mu_1(z)$.
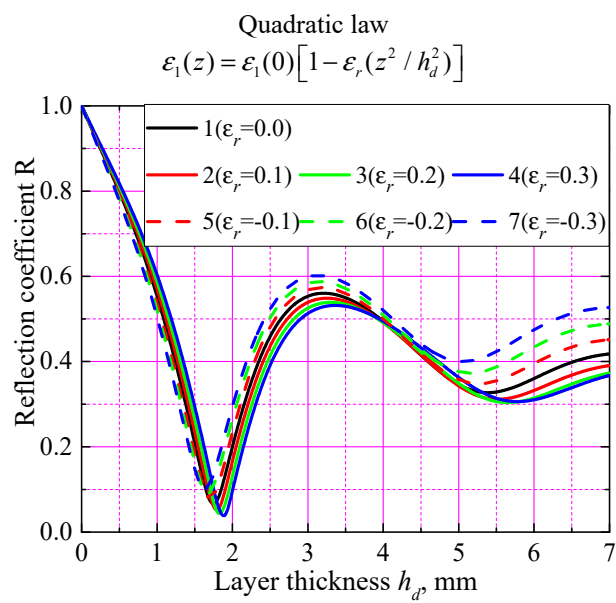
Linear law
$$\varepsilon_1(z) = \varepsilon_1(0)\left[1 + \varepsilon_r(z / h_d)\right]$$

Quadratic law
$$\varepsilon_1(z) = \varepsilon_1(0)\left[1 - \varepsilon_r(z^2 / h_d^2)\right]$$

Figure 4. Reflection coefficient R versus layer thickness h_d at $f = 10$ GHz (a); and frequency (b) - $h_d = 1.8$ mm, (c) - $h_d = 5.4$ mm for linear law $\varepsilon_1(z)$.
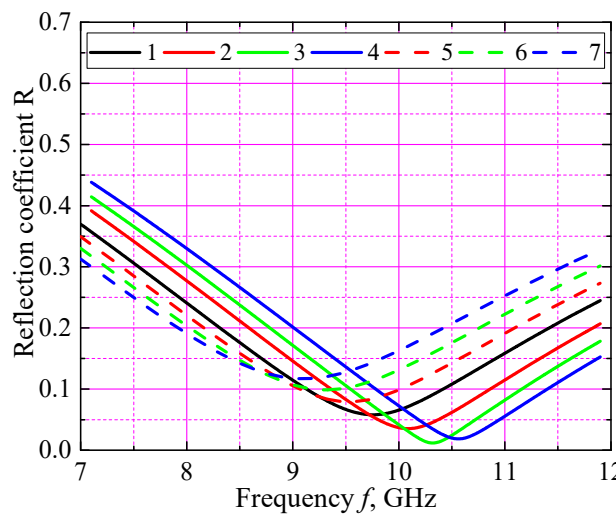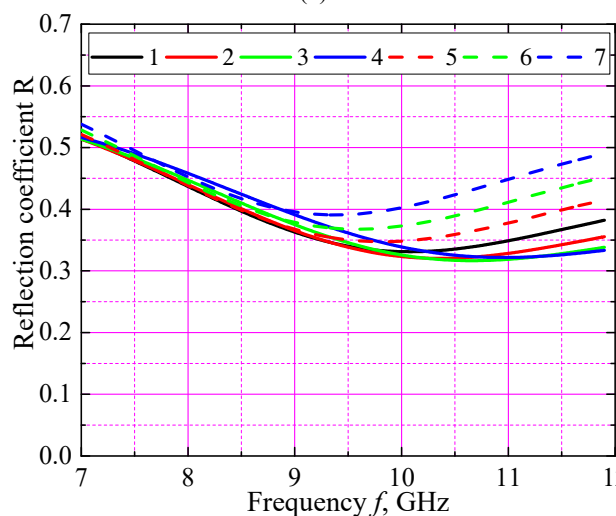
Figure 5. Reflection coefficient R versus layer thickness h_d at $f = 10$ GHz (a); and frequency (b) - $h_d = 1.8$ mm, (c) - $h_d = 5.4$ mm for quadratic law $\varepsilon_1(z)$.

CONCLUSION

The work presents an approximate analytical solution of the field equations for finding the distributed surface impedance of a magnetodielectric layer with the inhomogeneous permeability and permittivity located on PCP. In contrast to the known solutions for creating coatings with inhomogeneous parameters, when a multilayer magnetodielectric is used, the solution found is valid for the continuous change in the parameters of the magnetodielectrics inside the layer according to a certain law. The analysis shows that the influence of the magnetodielectric inhomogeneity on the surface impedance can reach tens of percent compared to the case of a uniform layer, which can be considered as additional means of controlling the electrodynamic characteristics of antenna-waveguide devices and creating new absorbing structures. Note that similar results can also be obtained for cylindrical [12] and spherical [30] structures if the corresponding field equations are solved in the cylindrical or spherical coordinate systems. Expressions for the surface impedances of metal conductors coated with the magnetodielectric layer were obtained in [12] for the case of the uniform coating and are in quite satisfactory agreement with the experimental data presented in [3], [7].

ORCID

Mikhail V. Nesterenko, https://orcid.org/0000-0002-1297-9119; **Victor A. Katrich**, https://orcid.org/0000-0001-5429-6124
Oleksandr M. Dumin, https://orcid.org/0000-0001-5067-9689; **Natalya K. Blinova,** https://orcid.org/0000-0001-9388-0008

REFERENCES

[1] K. Iizuka, "An experimental study of the insulated dipole antenna immersed in a conducting medium," IEEE Trans. Antennas Propag. **11**, 518-532 (1963). https://doi.org/10.1109/TAP.1963.1138080

[2] W. G. Swaiciuer, and L. Peters, "Radar cross sections of dielectric or plasma coated conducting spheres and circular cylinders," IEEE Trans. Antennas Propag. **11**, 558-569 (1963). https://doi.org/10.1109/TAP.1963.1138087

[3] D. Lamensdorf, "An experimental investigation of dielectric-coated antennas," IEEE Trans. Antennas Propag. **15**, 767-771 (1967). https://doi.org/10.1109/TAP.1967.1139049

[4] R.W.P. King, S.R. Mishra, K.M. Lee, and G.S. Smith, "The insulated monopole: admittance and junction effects," IEEE Trans. Antennas Propag. **23**, 172-177 (1975). https://doi.org/10.1109/TAP.1975.1141044

[5] B.P. Sinha, and S.A. Saoudy, "Rigorous analysis of finite length insulated antenna in air," IEEE Trans. Antennas Propag. **38**, 1253-1258 (1990). https://doi.org/10.1109/8.56963

[6] S.A. Saoudy, and Sinha, "Wiener-Hopf type analysis of dielectric-coated dipole antenna in relatively dense medium," IEEE Trans. Antennas Propag. **39**, 1057-1061 (1991). https://doi.org/10.1109/8.97338

[7] A.R. Bretones, A. Salinas, R.G. Martín, and I S. García, "Time-domain analysis of dielectric-coated wire antennas and scatterers," IEEE Trans. Antennas Propag. **42**, 815-819 (1994). https://doi.org/10.1109/8.301700

[8] T.W. Hertel, and G.S. Smith, "The insulated linear antenna-revisited," IEEE Trans. Antennas Propag. **48**, 914-920 (2000). https://doi.org/10.1109/8.865224

[9] X. Li, K.E K. Drissi, and F. Paladian, "Insulated vertical antennas above ground," IEEE Trans. Antennas Propag. **52**, 321-324 (2004). https://doi.org/10.1109/TAP.2003.822445

[10] M. V. Nesterenko, "Analytical methods in the theory of thin impedance vibrators," Prog. Electromagn. Res. B, **21**, 299-328 (2010). http://dx.doi.org/10.2528/PIERB10020105

[11] M. V. Nesterenko, V. A. Katrich, S. L. Berdnik, Yu. M. Penkin, and V. M. Dakhov, "Application of the generalized method of induced EMF for investigation of characteristics of thin impedance vibrators," Prog. Electromagn. Res. B, **26**, 149-178 (2010). http://dx.doi.org/10.2528/PIERB10052902

[12] M. V. Nesterenko, V. A. Katrich, Y. M. Penkin, V. M. Dakhov, and S. L. Berdnik, *Thin Impedance Vibrators. Theory and Applications*. (Springer Science+Business Media, NY, 2011).

[13] A.R. Bretones, R. G. Martín, and I. S. García, "Time-domain analysis of magnetic-coated wire antennas," IEEE Trans. Antennas Propag. **43**, 591-596 (1995). https://doi.org/10.1109/8.387174

[14] M. Nesterenko, V. Katrich, S. Berdnik, O. Dumin, and Y. Antonenko "Asymmetric impedance vibrator for multi-band communication systems," Prog. Electromagn. Res. M, **102**, 81-89 (2021). http://dx.doi.org/10.2528/PIERM21031207

[15] H.O. Schaik, "The performance of an iris-loaded planar phased-array antenna of rectangular waveguides with an external dielectric sheet," IEEE Trans. Antennas Propag. **26**, 413-419 (1978). https://doi.org/10.1109/TAP.1978.1141860

[16] R. Luebbers, and B. Munk, "Some effects of dielectric loading on periodic slot arrays," IEEE Trans. Antennas Propag. **26**, 536-542 (1978). https://doi.org/10.1109/TAP.1978.1141887

[17] A.J. Sangster, "Conversion factors for the power radiated by a small slot in loaded rectangular waveguide," Microwaves, Optics Acoustics, **3**, 104-108 (1979). https://doi.org/10.1049/ij-moa.1979.0024

[18] J.Y. Lee, T.Sh. Horng, and N G. Alexopoulos, "Analysis of cavity-backed aperture antennas with a dielectric overlay," IEEE Trans. Antennas Propag. **42**, 1556-1562 (1994). https://doi.org/10.1109/8.362779

[19] F. L. Whetten, and C. A. Balanis, "Effects of a dielectric coating on leaky-wave long-slot waveguide antennas," IEEE Trans. Antennas Propag. **44**, 1166-1171 (1996). https://doi.org/10.1109/8.511826

[20] R. A. Pucel, and D. J. Masse, "Microstrip propagation on magnetic substrates—Part I: Design theory," IEEE Trans. Microw. Theory Techn. **20**, 304–308 (1972). https://doi.org/10.1109/TMTT.1972.1127749

[21] S. Berdnik, V. Katrich, M. Nesterenko, and Yu. Penkin, "E-plane T-junction of rectangular waveguides with vibrator-slot coupling between arms," Telecommun. Radio Engineer. **74**, 1225-1240 (2015). https://doi.org/10.1615/TelecomRadEng.v74.i14.10

[22] L. Zheng, X. Yang, W. Gong, M. Qiao, and X. Li, "Ultralow thickness-bandwidth ratio magnetic absorber with printed FSS for S and C Bands," IEEE Anten. Wireless Prop. Lett. **21**, 576-580 (2022). https://doi.org/10.1109/LAWP.2021.3138634

[23] N. Prasad, P. Pardhasaradhi, B. T. P. Madhav, V. L. Raju, and P. P. Priya, "A Triband hexagonal shaped polarization insensitive absorber by tuning graphene material in Terahertz frequency domain," Prog. Electromagn. Res. M, **116**, 145-154 (2023). http://dx.doi.org/10.2528/PIERM23031508

[24] K. Yoshitomi, and H.R. Sharobim, "Radiation from a rectangular waveguide with a lossy flange," IEEE Trans. Antennas Propag. **42**, 1398-1403 (1994). https://doi.org/10.1109/8.320746

[25] K. Yoshitomi, "Radiation from a slot in an impedance surface," IEEE Trans. Antennas Propag. **49**, 1370-1376 (2001). https://doi.org/10.1109/8.954925

[26] M.V. Nesterenko, and Yu.M. Penkin, "Diffraction radiation from a slot in the impedance end of a semi-infinite rectangular waveguide," Radiophysics Quantum Electronics, **47**, 489–499 (2004). https://doi.org/10.1023/B:RAQE.0000047240.37895.ea

[27] M. V. Nesterenko, V. A. Katrich, and Yu. M. Penkin, "Diffraction of H_{10}-wave by stepped rectangular waveguide coupling with impedance slot iris," Telecommun. Radio Eng., **63**, 569-588 (2005). https://doi.org/10.1615/TelecomRadEng.v63.i7.10

[28] S. L. Berdnik, V. A. Katrich, Yu. M. Penkin, M. V. Nesterenko, and S. V. Pshenichnaya, "Energy characteristics of a slot cut in an impedance end-wall of a rectangular waveguide and radiating into the space over a perfectly conducting sphere," Prog. Electrom.. Res. M, **34**, 89-97 (2014). https://doi.org/10.2528/PIERM13112006

[29] Yu. M. Penkin, V. A. Katrich, M. V. Nesterenko, and N. K. Blinova, "Effect of surface impedance on radiation fields of spherical antennas," Prog. Electromagn. Res. L, **71**, 83-89 (2017). http://dx.doi.org/10.2528/PIERL17090102

[30] Yu. M. Penkin, V. A. Katrich, M. V. Nesterenko, S. L. Berdnik, and V. M. Dakhov, *Electromagnetic Fields Excited in Volumes with Spherical Boundaries*, (Cham, Switzerland: Springer Nature Switzerland AG, 2019).

[31] M. V. Nesterenko, V. A. Katrich, Yu. M. Penkin, S. L. Berdnik, and O. A. Dumin, *Combined Vibrator-Slot Structures: Theory and Applications*, (Cham, Swizerland: Springer Nature Swizerland AG, 2020).

[32] A.N. Lagarkov, V.N. Semenenko, A A. Basharin, and N.P. Balabukha, "Abnormal radiation pattern of metamaterial waveguide," PIERS Online, **4**, 641-644 (2008).

[33] S.L. Berdnik, V.A. Katrich, V.I. Kiyko, M.V. Nesterenko, and Yu.M. Penkin, "Power characteristics of a T-junction of rectangular waveguides with a multi-element monopole-slotted coupling structure," Telecommun. Radio Eng., **75**, 489-506 (2016). https://doi.org/10.1615/TelecomRadEng.v75.i6.20

[34] S.L. Berdnik, M.V. Nesterenko, Yu.M. Penkin, and S.N. Shulga, "Testing of thin metamaterial coatings by a waveguide-slot method," in Proc. II Intern. Conf. Inform. and Telecomm. Technol. and Radio Electronics, 287-290 (2017).

[35] R.E. Stovall, and K.K. Mei, "Application of a unimoment technique to a biconical antenna with inhomogeneous dielectric loading," IEEE Trans. Antennas Propag. **23**, 335-342 (1975). https://doi.org/10.1109/TAP.1975.1141090

[36] Z. Shen, and R. H. MacPhie, "Input admittance of a multilayer insulated monopole antenna," IEEE Trans. Antennas Propag. **46**, 1679-1686 (1998). https://doi.org/10.1109/8.736621

[37] K. Takizawa, and O. Hashimoto, "Transparent wave absorber using resistive film at V-band frequency," IEEE Trans. Microwave Theory Tech., **47**, 1137–1141 (1999). https://doi.org/10.1109/22.775450

[38] J. A. Brandao Faria, "A matrix approach for the internal impedance of multilayered cylindrical structures," Prog. Electromagn. Res. B, **28**, 351-367 (2011). http://dx.doi.org/10.2528/PIERB1102150

[39] L. Chen, M. B. Özakin, S. Ahmed, and H. Bagci, "A memory-efficient implementation of perfectly matched layer with smoothly varying coefficients in discontinuous Galerkin time-domain method," IEEE Trans. Antennas Propag. **69**, 3605-3610 (2021). https://doi.org/10.1109/TAP.2020.3037651

[40] Z. Wang, L. Tang, L. Zhou, Z. Jiang, Z. Liu, and Y. Lin, "Methodology to design variable-thickness streamlined radomes with graded dielectric multilayered wall," IEEE Trans. Antennas Propag. **69**, 8015-8020 (2021). https://doi.org/10.1109/TAP.2021.3083799

[41] M. I. Hossain, N. Nguyen, and A. M. Abbosh, "Broadband magnetic absorber based on double-layer frequency-selective surface," IEEE Trans. Antennas Propag. **70**, 410-419 (2022). https://doi.org/10.1109/TAP.2021.3096199

[42] S. V. Yuferev, and N. Ida, *Surface Impedance Boundary Conditions. A Comprehensive Approach*, (NY: CRC Press, 2009).

[43] E. M. Hamham, A. Zugari, and A. Benali, "Calculating radar cross section of lossy targets using the surface impedance approach," Prog. Electromagn. Res. M, **55**, 13-24 (2017). http://dx.doi.org/10.2528/PIERM16101503

[44] M. Niknejad, M. Maddah-Ali, A. Bakhtafrouz, and M. Maddahali, "Self-dual integral equation for scattering analysis from bodies of revolution with multiple impedance boundary conditions," Prog. Electromagn. Res. C, **121**, 207-220 (2022). http://dx.doi.org/10.2528/PIERC22051904

[45] M. V. Nesterenko, S. L. Berdnik, A. V. Gomozov, D. V. Gretskih, and V. A. Katrich, "Approximate boundary conditions for electromagnetic fields in electromagnetics," Radioelectronic and Computer Systems, **103**, 141-160 (2022). http://nti.khai.edu/ojs/index.php/reks/article/view/reks.2022.3.11/1904

[46] D. Li, J. Yang, X. Wang, T. Wang, and R. Gong, "Ultrabroadband Metamaterial Absorber Based on Effectively Coupled Multilayer HIS Loaded Structure With Dallenbach Layer," IEEE Trans. Microwave Theory Tech. **70**, 232-238 (2021). https://doi.org/10.1109/TMTT.2021.3129219

[47] B. Tegowski, T. Jaschke, A. Sienganschin, and A. Jacob, "A Transmission Line Approach for Rough Conductor Surface Impedance Analysis," IEEE Trans. Microwave Theory Tech. **71**, 471-479 (2023). https://doi.org/10.1109/TMTT.2022.3206440

[48] D. Bosman, M. Huynen, D. De Zutter, X. Sun, N. Pantano, G. Van der Plas, E. Beyne, and D. Vande Ginste, "Analysis and Application of a Surface Admittance Operator for Combined Magnetic and Dielectric Contrast in Emerging Interconnect Topologies," IEEE Trans. Microwave Theory Tech. **71**, 2794-2806 (2023). https://doi.org/10.1109/TMTT.2023.3244205

[49] L. A. Weinstein, *The Theory of Diffraction and the Factorization Method*, (Golem Press, NY, 1969).

[50] V. Tabatadze, K. Karacuha, E. Veliyev and E. Karacuha, "The diffraction by two half-planes and wedge with fractional boundary condition," Prog. Electromagn. Res. M, **91**, 1-10 (2020). http://dx.doi.org/10.2528/PIERM20020503

[51] M. Nesterenko, V. Katrich, O. Dumin, and S. Berdnik, "Approximate solution of the field equations for magnetodielectric layer with inhomogeneous permeability on perfectly conducting plane," in: *Proc. XXVIIIth Intern. Seminar on Direct and Inverse Problems of Electromagnetic and Acoustic Wave Theory*, pp. 150-154 (2023).

ВПЛИВ ЕЛЕКТРОФІЗИЧНИХ ПАРАМЕТРІВ МАГНІТОДІЕЛЕКТРИЧНОГО ШАРУ НА ІПП НА ЙОГО ЕЛЕКТРОДИНАМІЧНІ ХАРАКТЕРИСТИКИ

Михайло В. Нестеренко, Віктор О. Катрич, Олександр М. Думін, Наталья К. Блінова

Харківський національний університет імені В.Н. Каразіна, майдан Свободи, 4, Харків, Україна, 61022

У рамках імпедансної концепції отримані наближені аналітичні формули для розподіленого поверхневого імпедансу магнітодіелектричного шару з неоднорідними магнітною та діелектричною проникностями, розташованого на ідеально провідній площині (ІПП) для випадків квадратичного закону зміни електричних параметрів вздовж товщини шару. Проведено порівняльний аналіз коефіцієнта відбиття електромагнітних хвиль від цієї структури для різних законів зміни магнітної проникності та діелектричної проникності.

Ключові слова: *магнітодіелектричний шар; імпедансна концепція; поверхневий імпеданс; неоднорідна магнітна проникність; неоднорідна діелектрична проникність; коефіцієнт відбиття*

POLYACRYLAMIDE'S RHEOLOGICAL AND PHYSICOCHEMICAL PROPERTIES: ANALYSIS AND APPLICATIONS

Ⓘ**Ummatjon A. Asrorov[a,b]***

[a]National University of Uzbekistan named after Mirzo Ulugbek, Tashkent, Uzbekistan,
[b]Tashkent State Pedagogical University named after Nizami, Tashkent, Uzbekistan.
*Corresponding Author e-mail: ummat.asrorov1995@gmail.com

This study presents an in-depth rheological characterization of polyacrylamide polymers produced locally, employing the Anton Paar MCR 92 (Modular Compact Rheometer). The polymer samples were systematically analyzed to understand their response to various external stimuli. Using infrared spectroscopy, the composition of the polymer was meticulously verified, ensuring a robust assessment of its molecular structure and chemical stability under different environmental conditions. Our findings elucidate the significant potential of polyacrylamide in diverse industrial applications, attributable to its adaptable viscoelastic properties and chemical resilience. The implications of this research are profound, suggesting enhanced utility of polyacrylamide in fields requiring precise material behavior modulation under dynamic conditions.

Keywords: *Polyacrylamide; Anton Paar MCR 92 (Modular Compact Rheometer); Rheology; Gel; Gidrogel; IR spectroscopy*
PACS: 81.70.Pg

INTRODUCTION

Polymer materials, owing to their unique molecular structures and substantial sizes, are extensively utilized across various sectors of industry and technology, including construction, pharmaceuticals, and the oil and gas industries [1, 2]. For instance, these materials are employed in coatings, stabilization elements, and water retention systems, where their structural properties and characteristics play a crucial role in solving industry-specific challenges. Research indicates that polymers, particularly macromolecular compounds like polyacrylamide, are capable of participating in complex chemical and physical processes due to their high viscosity and durability. These properties ensure polymers' effective application across diverse environmental conditions [1, 4].

In the oil and gas sectors, the ability to control the cohesiveness of polyacrylamide is critically important for enhancing the efficiency of oil flow. This polymer optimizes the viscosity of liquids, thereby facilitating more effective extraction of oil from subterranean sources. Additionally, in water purification systems, polyacrylamide plays a pivotal role in the effective separation of toxic substances, which is essential for maintaining ecological stability [2, 3].

In the manufacture of pharmaceuticals, polyacrylamide plays a critical role in stabilizing drugs and controlling their dispersal, which extends the effectiveness and duration of the medications [5]. These studies and scientific discoveries delve deeper into the novel properties and practical applications of polymers, driving forward new advancements in the scientific community and the field of technology. The science and applications of polymers are becoming one of the most crucial topics in materials science, serving as a pivotal factor in the development of modern technologies [3, 5].

Rheometry is a scientific method focused on studying the flow and deformation properties of materials. This field provides information about the internal structure of materials by studying their response to flow and deformation, which is essential for understanding and predicting the mechanical behavior of materials [1-3]. Materials, particularly liquids and solids, provide extensive information about their compositional characteristics through rheometric analysis. This information, obtained through parameters such as viscosity and flow capabilities, is typically determined using specialized rheometers [2-5]. This process, known as rheotesting, allows for a precise understanding of how materials respond to dynamic and static loads. This scientific approach opens new avenues for understanding materials and their practical applications, playing a fundamental role in advancing research and developments in materials science. Rheometry creates a solid scientific foundation for accurately and reliably analyzing the physical and mechanical properties of materials [3,4,9].

X-ray analysis, especially X-ray diffraction (XRD), is another crucial method that determines the interatomic or interionic structure of crystalline and amorphous substances. This analysis provides data about the phase composition and lattice dimensions of materials. XRD data are extensively used in materials science, mineralogy, and metallurgy because this method allows for an in-depth study of the microstructural properties of materials [6, 11]. Thus, information obtained from infrared spectroscopy and X-ray analysis deeply enhances our understanding of the chemical and physical structures of materials. These analyses play an important role in defining the properties of materials and the potential applications in which they can be used, thereby laying the groundwork for further research and scientific developments [12].

EXPERIMENTAL
Materials

Polyacrylamide (PAA). Polyacrylamide is an odorless, amorphous solid with a white-yellowish color, the molecular weight of which is 10^4-10^7 (depending on the conditions of preparation). The density of polyacrylamide at room temperature (295-297 K) is about 1.302 g/cm³. The decomposition temperature is about 463 K. Polyacrylamide is a polyelectrolyte with hygroscopic properties, harmless, and forms a soft gel when dissolved in water [4, 5, 11].

Polyacrylamide (PAA) is a polyelectrolyte synthesized through the polymerization of acrylamide, which contains nitrogen, resulting in a structure that is linearly branched. This compound is produced at the Navoi Chemical Plant and complies with the standard TSh 6.1-00203849-64:1997. Polyacrylamide appears as an amorphous solid, typically white to yellowish, and is odorless. It exhibits a molecular weight of approximately $10^4 \times 10^7$, although this can vary based on synthesis conditions. At standard room temperature (around 295-297 K), its density is recorded at 1.302 g/cm³. Polyacrylamide decomposes at a temperature of about 463 K. Due to its hygroscopic nature, polyacrylamide is harmless and capable of forming a soft gel upon dissolution in water, leveraging its polyelectrolyte properties [3-5, 8, 12].
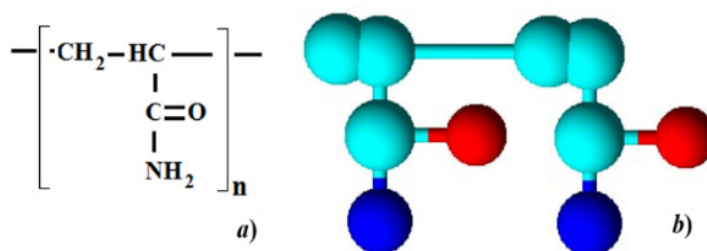

Figure 1. Chemical formula (a) and model structure of PAA (b) [4, 5]

FTIR. The structure of the obtained products was determined using IR spectroscopy and electron microscopy. IR spectra in the range 400–4000 cm^{-1} were recorded on "NIKOLET Magna-560 IR" and "Specord-75IR" spectrophotometers (Carl Zeiss, GDR). The samples for IR spectroscopy were prepared in the form of pellets with KBr, films on a KRS-5 plate, and films 8–12 μm thick. Films on a KRS-5 plate were obtained by evaporation of the solvent (water) at room temperature (295–297 K).

XRD. The device used for X-ray diffraction analysis is an X-ray diffractometer, which operates using X-rays emitted from a copper (Cu) source. It functions at 40 kV voltage and a current of 30 mA, capable of rotating samples within an angular range of 4° to 80°. The sample rotation speed is set at 2° per minute, ensuring accurate and reproducible measurements. The X-rays undergo diffraction within the crystal lattice, adhering to the laws of X-ray diffraction.

$$n\lambda = 2d \sin \varphi \qquad (1)$$

Rheometer. Rheological studies were conducted using the Anton Paar MCR 92 (Modular Compact Rheometer), a device noted for its modernity and high sensitivity. The MCR 92 model can operate continuously for less than one day, generating rotational and oscillatory torques ranging from 1 to 125 mNm. This rheometer's angular velocity ranges from 10^{-4} to 157 rad/s, and its angular frequency spans from 10^{-4} to 628 rad/s. The rotation speed (CSS/CSR) can be adjusted from 0.001 to 1500 rpm. The device can operate within a temperature range of -50°C to +400°C. During the sample examination, relatively flat and slightly conical plates were used. Throughout the rheological tests, the sample temperature was maintained at a constant 25±0.5°C, enhancing the reliability and repeatability of the experimental results. These specifications highlight the device's high precision and versatility, facilitating the accurate and effective study of the rheological properties of various materials.

Sample Preparation. The research sample of polyacrylamide was prepared under controlled conditions at room temperature (25°C). Due to the slow dissolution rate of polyacrylamide in water and to ensure thorough mixing, the 8% concentration of the sample was fully dissolved using a specialized dispenser, facilitating uniform consistency, pH = 7.2.

RESULTS AND DISCUSSION

The average molecular weight of polyacrylamide has been determined to be approximately 3.2·10^6 *g/mol* using an Ubbelohde viscometer in an aqueous medium at 25°C. Furthermore, the dynamic viscosity was quantitatively analyzed as a function of concentration employing the Huggins equation.

Infrared spectroscopy and X-ray fluorescence analyses are also important methods for material analysis. Infrared spectroscopy (IR spectroscopy) is used to study the chemical composition of materials; this method examines the vibrational characteristics of bonds within molecules, thereby identifying the types of chemical bonds between the atoms in the molecules. Through this technique, it is possible to understand the molecular structure of polymers, organic compounds, and other complex materials [5, 7, 9]. An IR spectroscopic image of polyacrylamide polymer is presented below (Fig. 2). The results obtained in the infrared region clearly show all the main bonds present in the structure of the polyacrylamide polymer.
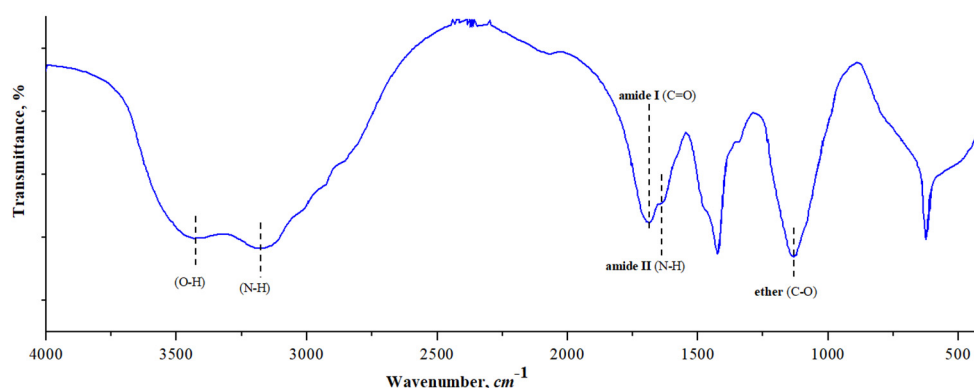
**Figure 2.** Infrared spectroscopic imaging of polyacrylamide polymer.

Polymers are macromolecular compounds that, while exhibiting amorphous characteristics in their dry state, also contain crystalline regions within their structure. The presence of these crystalline areas and the degree of crystallinity can be determined using X-ray diffraction (XRD) analysis.

$$X_c = \frac{I_{criss}}{I_{gen}} \times 100\% \ . \tag{2}$$

From the results, we can also calculate the lattice size formed.

$$D = \frac{K\lambda}{\beta\cos\theta} \ . \tag{3}$$

An XRD analysis of a film formed by drying a polymer solution at room temperature was conducted (Fig. 3).
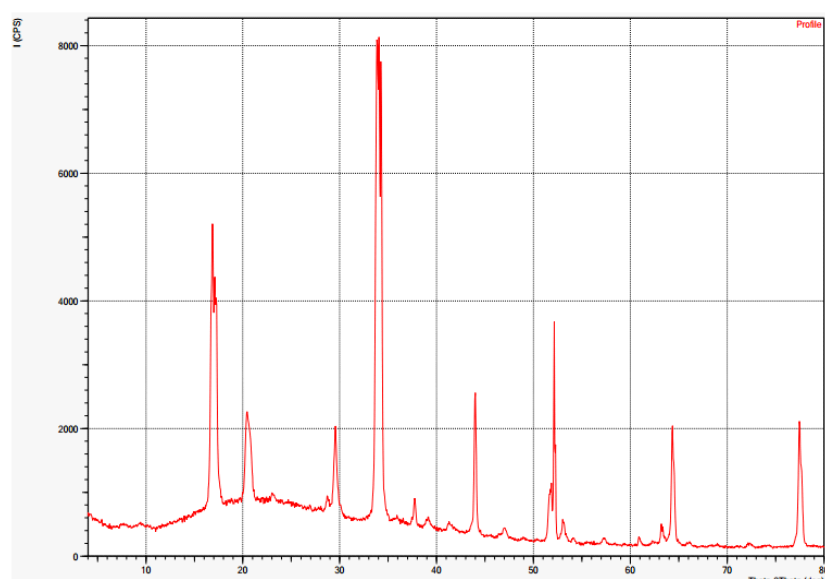
Figure 3. XRD image of polyacrylamide polymer film.

The XRD spectrum of this polyacrylamide provides crucial information about the crystalline structure of the material. Notably, the most intense peak around 30° represents the primary crystalline phase of polyacrylamide. This peak indicates that the distances between the atoms in the material's crystalline lattice are well-defined. Using these peaks, it was determined that the amount of crystalline phase in the polymer content is significant, and the sizes of the lattices were identified (Tab. 1).

Table 1. XRD spectrum analysis of polyacrylamide crystalline structure

| Peak number	2Theta (degrees)	FWHM (degrees)	FWHM (radians)	Crystal size (Å)
1	17.0504	0.7365	0.012854	109.07
6	34.0265	0.7190	0.012549	115.55
14	77.4771	0.4371	0.007629	233.01

The location and intensity of each peak are critical as they provide complete information about the characteristics of the crystalline phases. The overall structure of the graph indicates that the XRD spectrum of polyacrylamide includes not only the crystalline phases but also the material's amorphous characteristics. The amorphous phases are visible in the regions of lower intensity between the peaks, representing the non-uniform amorphous parts of the polymer structure.

Rheology. A solution of polyacrylamide in water was examined using an Anton Paar MCR 92 rheometer, across an angular frequency range from 0 to 700 rad/s. The dependence of shear stress and shear strain on frequency was studied (Table 2).

Table 2. Rheological properties of polyacrylamide solution

Point No	Angular Frequency [rad/s]	Storage Modulus [Pa]	Loss Modulus [Pa]	Loss Factor [1]	Shear Strain [%]	Shear Stress [Pa]	Torque [mN·m]
1	0.314	2.4435	48869	20000	0.00276	1.3476	0.005498
2	0.521	46799	11926	0.255	0.931	449.81	1.8352
3	0.866	19625	10192	0.519	0.208	45.897	0.18725
4	1.44	56971	36551	0.642	0.853	577.62	2.3566
5	2.38	43812	31773	0.725	0.886	479.77	1.9574
6	3.96	77604	58170	0.75	0.961	931.73	3.8013
7	6.57	1.02E+05	79830	0.783	0.977	1264.9	5.1607
8	10.9	1.19E+05	94252	0.794	0.986	1494.2	6.0962
9	18.1	1.37E+05	1.10E+05	0.801	0.997	1747.7	7.1304
10	30	1.52E+05	1.19E+05	0.787	1	1932.2	7.8831
11	49.9	1.62E+05	1.28E+05	0.791	0.976	2013.1	8.213
12	82.8	1.97E+05	1.51E+05	0.767	0.994	2465.4	10.059
13	137	2.25E+05	1.74E+05	0.773	0.995	2833.3	11.56
14	228	2.47E+05	1.96E+05	0.795	0.998	3145.6	12.833
15	379	2.51E+05	2.01E+05	0.801	1	3228.9	13.174
16	628	2.58E+05	2.14E+05	0.829	1	3360.4	13.71

The results graphically depict how the material's stress and deformation change with varying angular velocities. It is evident from the graphs that the behavior of the material's stress and deformation changes according to different laws at various angular frequencies (Fig. 4).
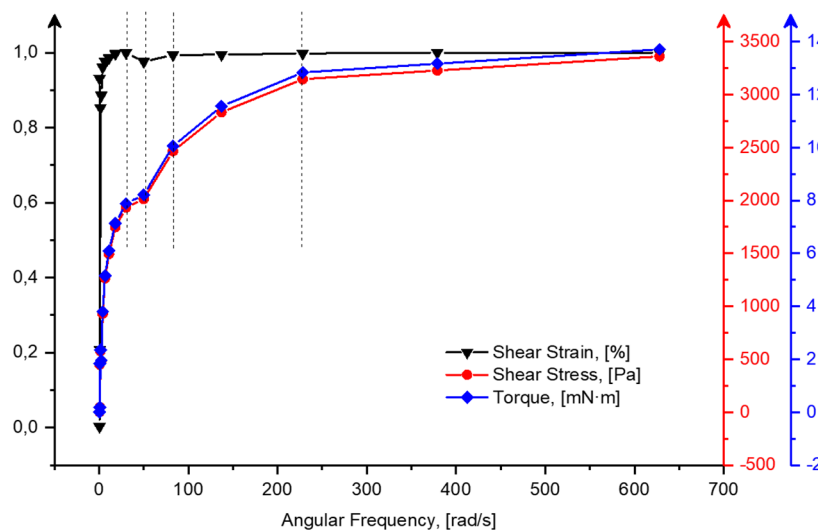
Figure 4. Dependence of rheological parameters on the angular frequency of rotation

At the beginning of the graph, the shear strain rapidly increases, reaching nearly 1.0 (100%) at approximately 100 rad/s, and then remains nearly constant. This indicates that the elastic phase of polyacrylamide quickly saturates and subsequently does not deform further.

The shear stress curve also shows an increase, rising with angular frequency and stabilizing around 3500 Pa. This suggests that polyacrylamide retains its elastic properties even at higher frequencies, and due to the considerable size of polyacrylamide molecules, elasticity becomes more pronounced with increasing frequency due to the ordering of their conformational state.

The dependence of the solution's internal friction coefficient on angular frequency was examined (Fig. 5). Initial viscosity values are very high (≈ 3000 mPa), decreasing almost exponentially with increasing frequency and stabilizing at around 500 mPa. This indicates that in the absence of external influences, the material's molecules form strong cohesion; as external forces increase, elasticity emerges and cohesion decreases. The material maintains its stability even under high strain, which is crucial for determining its application areas.

When we apply a shear stress to the liquid, we impart a pulse, which is transmitted through different layers of the liquid. Due to friction between the layers, the velocity of the liquid and its kinetic energy decrease. The transverse stress and shear velocity are proportionally linked through the coefficient of internal liquid friction. The kinetic energy in the system occurs due to internal cohesion or dynamic viscosity η [3].

$$\eta = \frac{\sigma}{\dot{\gamma}} \tag{4}$$

The viscosity of a liquid depends on pressure and temperature, generally increasing with rising pressure and decreasing temperature. We can observe how the internal friction coefficient changes according to different laws at various angular frequencies. The graph can be divided into areas where the internal friction coefficient changes according to three distinct laws. While the polyacrylamide polymer exhibits high viscosity at low angular frequencies, the viscosity decreases rapidly up to 12-15 s^{-1} as the frequency increases, then decreases linearly between 178-180 s^{-1}, and remains nearly constant at higher frequencies.
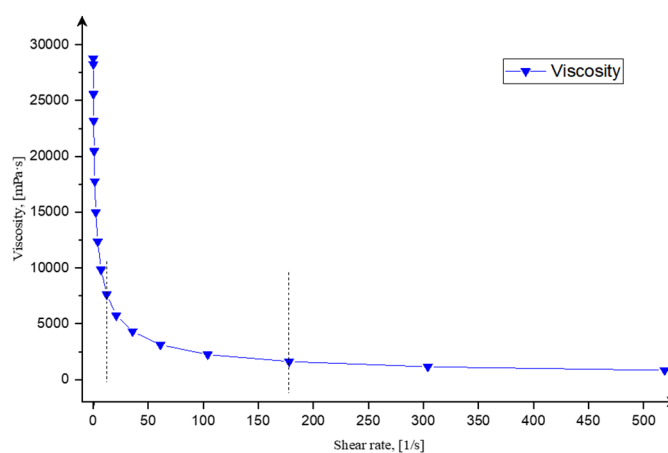

Figure 5. Relationship between sample viscosity and shear rate

The decrease in viscosity at high angular velocities is a characteristic of solutions containing long-chain molecular structures. At high velocities, the molecules' conformation aligns with the flow direction, and they begin to flow as parallel layers.

CONCLUSIONS

The rheological properties of the polyacrylamide polymer are analyzed with high precision using the state-of-the-art Anton Paar MCR 92 across an angular frequency range from 0 to 700 rad/s. The physicochemical properties of polyacrylamide, including its molecular weight, viscosity, and sensitivity to external influences, were studied.

The molecular structure and dimensions of the crystalline lattice of the polymer material were thoroughly investigated using IR spectroscopy and X-ray diffraction (XRD). The XRD spectra indicate that the high quantity of the primary crystalline phase of polyacrylamide aids in understanding the dissolution mechanism in the solvent. The results observed a rapid saturation of the material's elastic phase and a stabilization of shear stress around 3500 Pa, demonstrating polyacrylamide's ability to retain its elastic properties even at high frequencies. In conclusion, these analyses provide significant insights into the rheological properties and molecular structure of polyacrylamide.

Optimizations, including the introduction of various types of additives, are required for the application of polyacrylamide in the oil and gas industry, water purification systems, and pharmaceutical manufacturing. These findings also help in understanding the effective application of polyacrylamide produced by local manufacturers in different environments and contribute to advancing new achievements within the scientific community.

ORCID

Ummatjon Asrorov, https://orcid.org/0009-0009-6800-7392

REFERENCES

[1] L.-Y. Shi, W.-W. Lei, F. Liao, J. Chen, M. Wu, Y.-Y. Zhang, C.-X. Hu, *et al*., "H-bonding tuned phase transitions of a strong microphase-separated polydimethylsiloxane-*b*-poly(2-vinylpyridine) block copolymer," Polymer, **153**, 277-286 (2018). https://doi.org/10.1016/j.polymer.2018.02.003

[2] M. Pühringer, Ch. Paulik, and K. Bretterbauer, "Synthesis and characterization of polyacrylamide-based biomimetic underwater adhesives," Monatshefte fur Chemie-Chemical Monthly, **154**, 503–513 (2023). https://doi.org/10.1007/s00706-023-03057-4

[3] H. Murata, *Rheology – Theory and Application to Biomaterials, Polymerization*, edited by A. De Souza Gomes, (IntechOpen, 2012). http://dx.doi.org/10.5772/48393

[4] Z. Su, Ch. Li, G. Jiang, J. Li, H. Lu, and F. Guo, Rheology and Thixotropy of Cement Pastes Containing Polyacrylamide, Hindawi, Geofluids, 2022, https://doi.org/10.1155/2022/1029984

[5] S.Ya. Inagamov, U.A. Asrorov, N.T. Qodirova, O.T. Yomgirov, and G.I. Mukhamedov, "Development of Interpolymer Complexes Based on Sodium Carboxymethylcellulose and Polyacrylamide," in: *II International Scientific and Practical Conference "Technologies, Materials Science and Engineering, AIP Conf. Proc.* **2999**, 020049, 2023, https://doi.org/10.1063/5.0158621.

[6] S.Ya. Inagamov, U.A. Asrorov, and E.B. Xujanov, "Structure and physico-mechanical properties of polyelectrolyte complexes based on sodium carboxymethylcellulose polysaccharide and polyacrylamide," East European Journal of Physics, (4), 258-266 (2023). https://doi.org/10.26565/2312-4334-2023-4-32.

[7] M.S. Gualdesia, C.I. Alvarez Igarzabalb, J. Varaa, and C.S. Ortiz, "Synthesis and physicochemical properties of polyacrylamide nanoparticles as photosensitizer carriers," International Journal of Pharmaceutics, **512**, 213–218 (2016). http://dx.doi.org/10.1016/j.ijpharm.2016.08.051

[8] C. Du, and R.J. Hill, "Complementary-DNA-Strand Cross-Linked Polyacrylamide Hydrogels," Macromolecules, https://doi.org/10.1021/acs.macromol.9b01338

[9] Y. Liu, L. Liu, Y. Wang, G. Zhu, and W. Tan, "The rheological behavior of graphite oxide/cationic polyacrylamide suspensions," RSC Adv. **6**, 102938 (2016). https://doi.org/10.1039/c6ra18527d

[10] J.S. Oha, A.I. Isayeva, and M.A. Rogunova, "Continuous ultrasonic process for in situ compatibilization of polypropylene/natural rubber blends," Polymer, **44**, 2337–2349 (2003). https://doi.org/10.1016/S0032-3861(03)00080-6

[11] F.Z. Jamoldinov, M.R. Yusupaliyev, and A.U. Asrorov, "Radiation graft copolymerization of vinyl fluoride to cotton, hydrocellulose fiber and fabric," East European Journal of Physics, (2), **422-430** (2024). https://doi.org/10.26565/2312-4334-2024-2-55

[12] Ch. Xiong, F. Wei, W. Li, P. Liu, Y. Wu, M. Dai, and J. Chen, "Mechanism of Polyacrylamide Hydrogel Instability on High Temperature Conditions," ACS Omega, **3**, 10716−10724 (2018). https://doi.org/10.1021/acsomega.8b01205

РЕОЛОГІЧНІ ТА ФІЗИКО-ХІМІЧНІ ВЛАСТИВОСТІ ПОЛІАКРИЛАМІДУ: АНАЛІЗ ТА ЗАСТОСУВАННЯ

Умматджон А. Асроров[a,b]
[a]Національний університет Узбекистану імені Мірзо Улугбека, Ташкент, Узбекистан
[b]Ташкентський державний педагогічний університет імені Нізамі, Ташкент, Узбекистан

У цьому дослідженні представлено поглиблену реологічну характеристику поліакриламідних полімерів, вироблених на місцевому рівні, використовуючи Anton Paar MCR 92 (модульний компактний реометр). Зразки полімерів систематично аналізували, щоб зрозуміти їх реакцію на різні зовнішні подразники. Використовуючи інфрачервону спектроскопію, склад полімеру був ретельно перевірений, забезпечуючи надійну оцінку його молекулярної структури та хімічної стабільності в різних умовах навколишнього середовища. Наші висновки з'ясовують значний потенціал поліакриламіду в різноманітних промислових застосуваннях, що пояснюється його адаптивними в'язкопружними властивостями та хімічною стійкістю. Наслідки цього дослідження є глибокими, що свідчить про збільшення користі поліакриламіду в областях, де потрібна точна модуляція поведінки матеріалу в динамічних умовах.

Ключові слова: *поліакриламід; Anton Paar MCR 92 (модульний компактний реометр); реологія; гель; гідрогель; ІЧ-спектроскопія*

STUDYING THE EFFECT OF TRANSPORT LAYERS ON ZrS2/MEH-PPV SOLAR CELLS: USING SCAPS -1D SOFTWARE

Marwan S. Mousaᵃ, ⓘHmoud Al-Dmourᵇ*, Emad K. Jaradatᶜ, Osama Y. Al-Madanatᵈ, Ahmad M.D. (Assa'd) Jaberᵉ, Beddiaf Zaidiᶠ, Ahmet Sait Alaliᵍ, V. Aravindanʰ

ᵃDepartment of Renewable Energy Engineering, Jadara University, Irbid 21110, Jordan
ᵇDepartment of Physics, Faculty of Science, Mu'tah University, Mu'tah 6170, Jordan
ᶜDepartment of Physics, Faculty of Science. Imam Mohammad Ibn Saud Islamic University, Riyadh 11623, Saudi Arabi
ᵈDepartment of Chemistry, Faculty of Science, Mu'tah University, Mu'tah 6170, Jordan
ᵉDepartment of Basic Humanities and Science, Faculty of Medicine, Aqaba Medical Sciences University, Aqaba 77110, Jordan
ᶠDepartment of Physics, Faculty of Material Sciences, University of Batna 1, Batna, Algeria
ᵍDepartment of Physics, Yıldız Technical University, Istanbul, 34220 Turkey
ʰSmart Materials Lab, Department of Physics, Thiagarajar College of Engineering, Madurai-625015, India
*Correspondence Author e-mail: hmoud79@mutah.edu.jo

This study investigates the effect of charge transport layers on the efficiency of Poly[2-methoxy-5-(2-ethylhexyloxy)-1,4-phenylenevinylene] (MEH_PPV) and Zirconium Disulfide (ZrS2) solar cells using Scaps-1D software. It was found that by increasing the MEH-PPV thickness and decreasing its acceptor doping concentration, the efficiency ($\mu\%$), fill factor (FF), and short-circuit current density (J_{sc}) decreased. Conversely, increasing the thickness of the ZrS2 electron transport layer and decreasing its donor doping density enhanced the efficiency ($\mu\%$) and short-circuit current density (J_{sc}) while maintaining a constant open-circuit voltage (V_{oc}). These results can be attributed to decreased charge separation and collection in MEH-PPV and reduced optical path length in ZrS2. On the other hand, the back contact with work function is below 4.65 eV, the MEH-PPV/ZrS2 solar cells produced the lowest efficiency compared to different types of back contact. Under optimal conditions, MEH-PPV/ZrS2 solar cell shows a high efficiency of 21% when the dopant concentration of MEH-PPV and the value of the neutral defect density at the ZrS2/ MEH-PPV interface are 10^{22} cm^{-3} and 10^9 cm^{-3} respectively.

Keywords: *SCAPS simulation; Solar cells; Doping density; Interface Defect; Work function*
PACS: 28.41.Ak, 88.40.H, 61.72.Vv,71.55.−I, 73.30.+y

1. INTRODUCTION

Over the past decade, scientists working on solar cells have explored various materials and techniques to create solar cells that are both highly efficient and cost-effective [1–4]. One notable development is perovskite solar cells (PSCs), which have garnered significant attention due to their impressive power conversion efficiency (PCE) and their ability to address several existing limitations [1, 2]. In 2009, Tsutomu Miyasaka and his team published an article demonstrating the achievement of 3.8% power conversion efficiency through a perovskite solar cell with a scaffold of mesoporous TiO2 [3]. Since then, the efficiency of PSCs has rapidly increased to reach 25%, providing an alternative solar cell technology to the Si, CdTe, and copper indium gallium commercial solar cells [2]. In general, solar cells are mainly composed of different materials that work as electron and hole transport layers (ETL, HTL). ETL materials can be prepared from different materials, such as transition metal dichalcogenides (TMDCs) [5, 6]. For example, ZrS2 is a two-dimensional (2D) transition metal disulfide synthesized as a thin film for application in flexible transparent devices. It has high electron mobility and a small energy gap. Therefore, they received significant attention due to their potential as candidates for various applications, including solar cells. In our recent publication, zirconium disulfide (ZrS2) has been used in studying the properties of Go/ZrS2 solar cells. The device shows a high efficiency of 15% [6]. For hole transport materials (HTL), organic materials have been widely used as HTL in fabricating organic light-emitting diode OLEDs or flexible and lightweight organic photovoltaics, in addition to their easy fabrication features [7–9]. One example of such materials is MEH PPV (poly[2-methoxy-5-(2-ethylhexyloxy)-1,4-phenylenevinylene]), which has the absorption of light at a wavelength of 450–550 nm and orbital energy at 5.3 eV for the highest occupied molecular orbital (HOMO) and the lowest unoccupied molecular orbital (LUMO) at 3.2 eV [10]. Moreover, the MEH-PPV layer is interesting for light energy harvesting because it absorbs light in the 450–550 nm range, which has relatively high photon energy and converts more sunlight into electricity [11, 12].

The performance of MEH-PPV solar cells is influenced by the characteristics of the MEH-PPV layer, including its thickness, energy band gap, stability, and mobility [12, 13]. Optimizing these conduction properties is crucial for enhancing the efficiency of organic solar cells. For instance, our previous research illustrates how the traits of nc-TiO2 grains impact the performance of organic-inorganic solar cells and how the rigidity of the thiophene ring affects dye-sensitized solar cell efficiency [14]. The findings indicate that the film morphology developed during processing and the structure of the polymeric chain can hinder the pore filling of the mesoporous layer, which in turn significantly impacts

inter-chain hopping and overall device performance. This study intends to explore the elements that may influence the performance of ZrS$_2$/MEH-PPV by utilizing the capacitance simulator (SCAPS-1D) version 3.3.0, a software tool developed by Burgelman et al. [15]. The factors considered include temperature fluctuations, variations in layer thickness, doping levels, and series resistances of the solar cell components.

2. DEVICE SIMULATION

It has been known that numerical simulation can play a vital role in optimizing different structures of solar cells, such as SCPAS. In the beginning, this simulation was used to simulate the efficiency of solar cells whose components are CuInSe2 and the CdTe family [11]. Then, it was applied to identify the parameters that influence the performance of solar cells. These parameters include the thickness, energy band gap, and charge carrier concentration of components of solar cells. On the other hand, the results obtained from both the SCAPS-1D program and experimental measurements are very close to each other. [16]. The SCAPS-1D software is based on solving the fundamental semiconductor equations essential for modelling solar cell behavior. These include the Poisson equation e, the Poisson equation (1), and the continuity equations for electrons and holes (2 and 3). [6.11]

$$\frac{d^2\psi}{dx^2} + \frac{q}{\varepsilon}\left[p(x) - n(x) + N_D - N_A + \rho_p - \rho_n\right] = 0 \tag{1}$$

$$\frac{1}{q}\frac{dJ_P}{dx} = G_{op} - R(x) \tag{2}$$

$$\frac{1}{q}\frac{dJ_n}{dx} = -G_{op} + R(x) \tag{3}$$

Where ε represents the dielectric constant, q denotes the charge of an electron, NA and ND indicate the densities of ionized acceptors and donors, respectively, Ψ refers to the electrostatic potential, Jp is the current density associated with holes, Jn is the current density associated with electrons, G_{op} signifies the rate of carrier generation, R is the overall recombination rate, p represents the density of free holes, n stands for the density of free electrons, while ρ_p and ρ_n are the distributions of holes and electrons, respectively. The following drift-diffusion equations (2) and (3) represent the hole and electron carrier transport properties of the semiconducting material. In this work, the proposed solar cell is composed of zirconium disulfide (ZrS$_2$) and poly[2-methoxy-5-(2-ethylhexyloxy)-1,4-phenylenevinylene] (MEH-PPV) and front contact (fluorine-doped tin dioxide, SnO$_2$;Fn) and back contact (Gold, Au). We studied the dependence of the parameters of solar cells on the properties of charge transport layers. These parameters are power conversion efficiency (μ%), short circuit current density (J$_{sc}$), and fill factor (FF) extracted by drawing the current density versus voltage of solar cells under different conditions and back contact (Gold, Au). Figure 1 shows schematic diagrams of SnO$_2$:F/ZrS$_2$/MEH-PPV/Au solar cells. From previous literature (6,13,17), Tables 1 and 2 present the input parameters used in SCAPS simulators for studying the performance of solar cells.
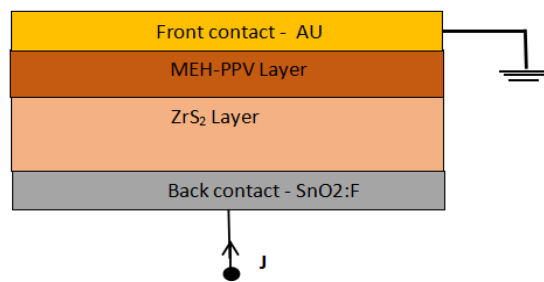

Figure 1. Schematic diagrams of SnO2:F/ZrS$_2$/MEH-PPV/Au solar cells

Table 1. Simulation parameters of components of MEH-PPV/ZrS solar cells

| Material properties	ZrS$_2$	MEH-PPV
Thickness(μm)	Varying	Varying
Bandgap (eV)	1.55	2.1
Electron affinity(eV)	4.7	2.8
Dielectric permittivity(relative)	16.4	3
CB effective density of states (1/cm^3)	2.2 e^{+19}	2e^{+19}
VB effective density of states (1/cm^3)	1.8 e^{+19}	2e^{+19}
Electron mobility (cm^3/Vs)	300	1e^{-5}
Hole mobility (cm^3/Vs)	30	1e^{-6}
Shallow uniform donor density ND (1/cm^3)	1.00 e^{+19}	0
Shallow uniform acceptor density NA (1/cm^3)	0	1e^{18}

Table 2. Simulation parameters of back and front contact of solar cells

Parameters	Back contact (Au electrode)	Front contact (SnO₂:F electrode)
Surface recombination velocity of electrons (cm/s)	$1.00E^{+5}$	$1.00E^{+5}$
Surface recombination velocity of holes (cm/s)	$1.00E^{+7}$	$1.00E^{+7}$
Metal-work function(eV)	5.1	4.5

3. RESULT AND DISCUSSION
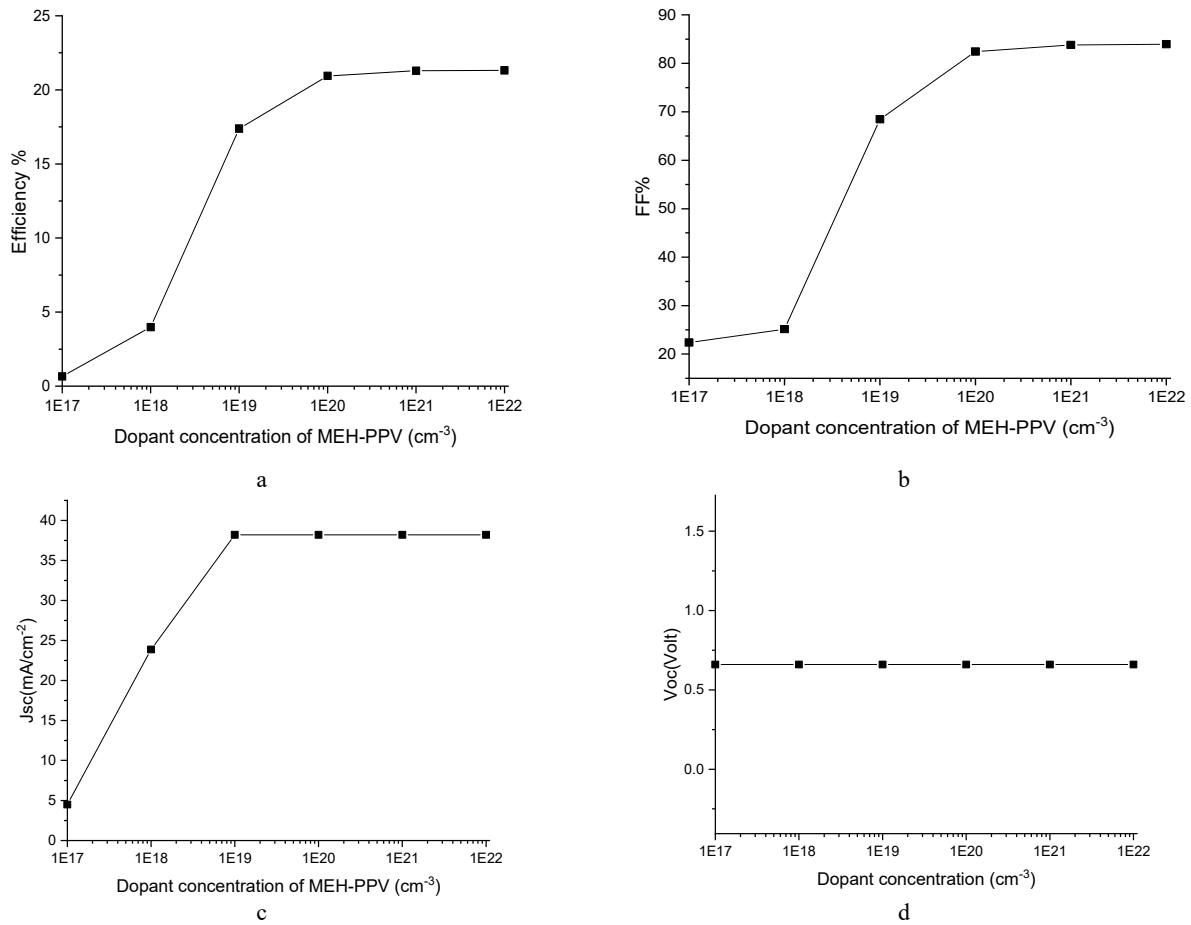### 3.1. Effect properties of MEH-PPV on the performance of solar cells

Figure 2 shows the effect of MEH-PPV thickness on the photovoltaic parameters of MEH-PPV/ZrS$_2$ solar cells. The thickness of the MEH-PPV layer varied from 10 nm to 250 nm.
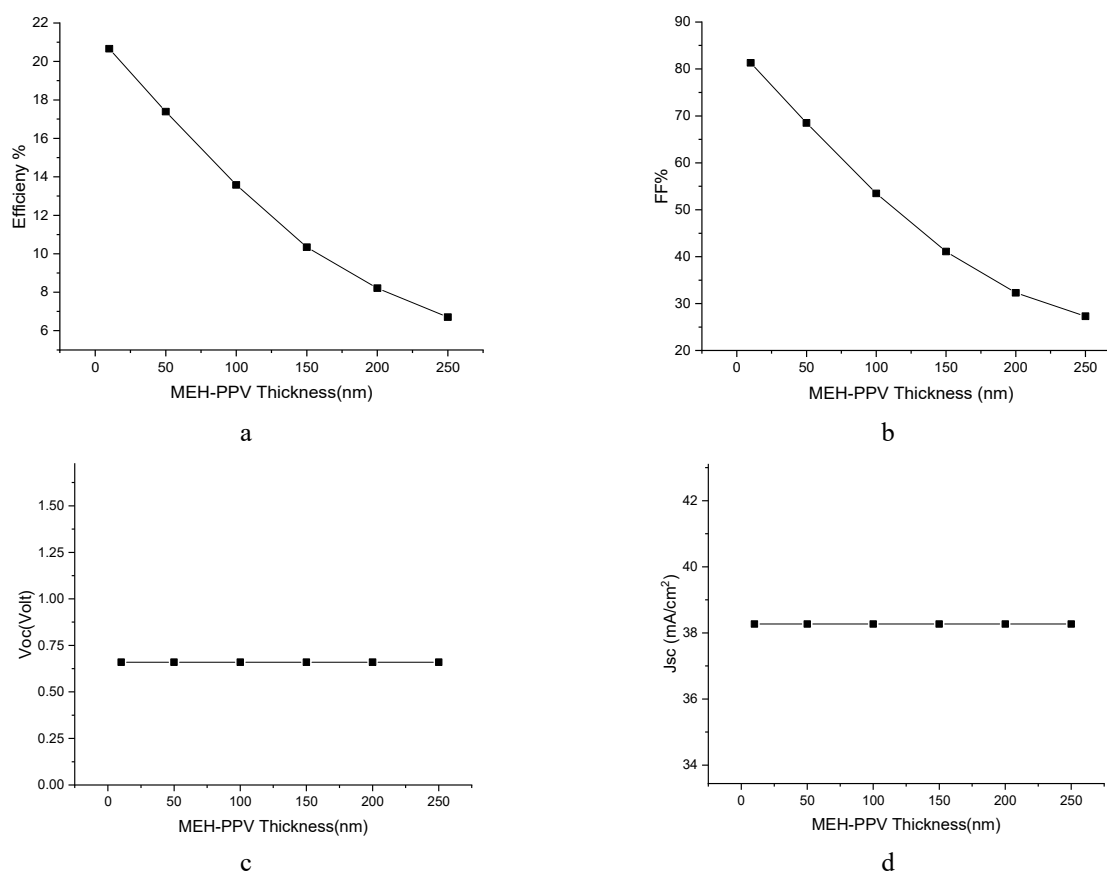
Figure 2. Effect of MEH-PPV thickness on cell performance parameters

Figures 2a and 2b demonstrate that an increase in MEH-PPV thickness from 10 nm to 250 nm results in a decrease in both efficiency and fill factor, from 20.66% to 6.71% and from 81.3% to 27.24%, respectively. This is attributed to reduced charge separation collection at the MEH-PPV and ZrS$_2$ interface due to the bad matching of their atomic orbitals. Besides, thicker HTL in solar cells increases the series resistance in the pathway of positive charge transport additions, which introduces defects and traps, thus, leading to increased charge recombination. These drawbacks cause a decrease in the performance of MEH-PPV solar cells, which agrees with the published work in [18]. On the other hand, Figures 2c and 2d show the open-circuit voltage (V$_{oc}$) and short-circuit current density remain constant at approximately 0.87 V and 32.2 mA/cm², respectively, because the built-in potential is not affected by the increase in thickness.

Figure 3 shows J$_{SC}$, V$_{oc}$, FF, and efficiency of the MEH-PPV /ZrS$_2$ solar cell as functions of the acceptor doping concentration of the MEH-PPPV layer. This concentration was changed over five orders of magnitude from 1×10^{17} to 1×10^{22} cm^{-3}. The results show that the low MEH-PPV doping level produces lower efficiency and fill factor compared to the high MEH-PPV doping level in MEH-PPV/ZrS$_2$ solar cells. Figures 3a and 3b show the efficiency and fill factors were enhanced with an acceptor doping concentration ranging from 0.66% to 21.32% and 22.38% to 83.95%, respectively. Moreover, the open circuit voltage V$_{oc}$ remains constant while the short circuit current density increases and reaches its peak value with an increase in doping density (see Figures 3c and 3d). The JSC gets saturated with small changes when the doping concentration reaches 10^{-20}cm^{-3}. Similar results are reported by Bradeško et al. who emphasized that a high doping level effectively reduces the ohmic losses of the cell and minimizes free carrier recombination by enhancing the electric field in the space charge region [19]. Therefore, increasing the doping level in the active region leads to extra charge carrier generation and also controls the photocarrier transport path, and consequently, it leads to increased

efficiency. A high doping level effectively reduces the ohmic losses of the cell and minimizes free carrier recombination by enhancing the electric field at the space charge region.

Figure 3. Effect of the doping concentration of MEH-PPV on cell performance parameters

3.2. Effect of properties of ZrS₂ on the performance of solar cells

Figure 4 shows the effect of the thickness of the electron transport layer, ZrS_2 on the performance of ZrS_2/MEH PPV solar cells. Its thickness varied from 0.25 μm to 1.5μm and the values of acceptor density and thickness of MEH - PPV are 0.05μm and 10^{+19} cm^{-3} respectively. The enhancement of efficiency is attributed to an increase in short-circuit current density of around 30%, while the decrease in fill factor was approximately 14%. The advantage of having thicker ZrS_2 improves electron-hole pair generation more than their recombination. This can be explained by the high electron mobility in ZrS_2, which minimizes the increase in series resistance in thicker materials [20]. The results present that the increase in thickness of ZrS_2 leads to an increase in Jsc from 30.61 mA/cm^2 to 38.66 mA/cm^2 whereas the V_{oc} remains constant, which in turn enhances efficiency. This can be explained based on the fact that increasing the ZrS_2 layer thickness leads to enhancing the optical path length of the light falling on the device and ionizing more atoms within the materials. This causes the material to produce more electron-hole pairs, corresponding to a large amount of light absorption. Additionally, the narrow bandgaps of the ZrS_2 layer enhance the photo-charge separation and consequently increase the short circuit current density [21]

Figure 5 shows the effect of donor doping concentration in the ZrS_2 layer on the efficiency, V_{oc}, J_{sc}, and FF of the solar cells. The donor density was varied from 1×10^{17} to 1×10^{22} cm^{-3}. At a lower ZrS_2 doping level, the MEH-PPV/ZrS_2 solar cells produced higher short-circuit current density and efficiency compared to a higher ZrS_2 doping level. As shown in Figures 5-a and 5-b, the efficiency and Jsc decrease as the acceptor doping concentration increases, from 38.2 mA/cm^2 to 35.11 mA/cm^2 and from 17.4% to 16.25%, respectively. Moreover, the open-circuit voltage (V_{oc}) remains constant, while the fill factor (FF%) increases and reaches its peak value with increasing doping density (see Figures 5-c and 5-d). The doping concentration influences the electric field and the processes of charge generation, transport, and recombination. For example, a study reported that low dopant concentrations (<10^{20} cm^{-3}) do not significantly affect the parameters of bulk heterojunction cells, whereas higher doping levels decrease efficiency. These results are consistent with our results, which attribute the increased efficiency at low doping concentrations to reduced recombination rates and improved charge carrier mobility, combined with minimized parasitic losses. Additionally, low doping levels enhance the built-in electric field strength, leading to more effective charge separation and collection [22, 23].
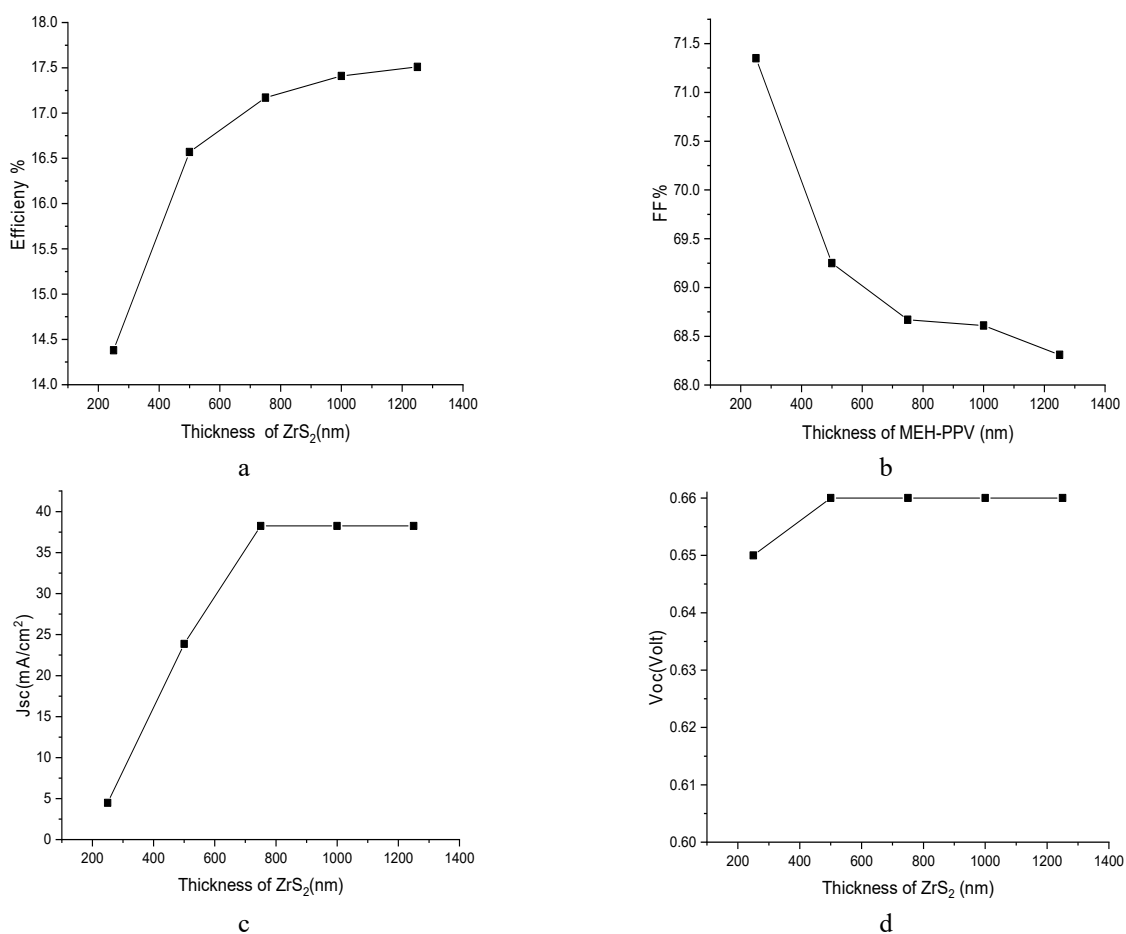
a

b

c

d

Figure 4. Effect of ZrS$_2$ thickness on cell performance parameters
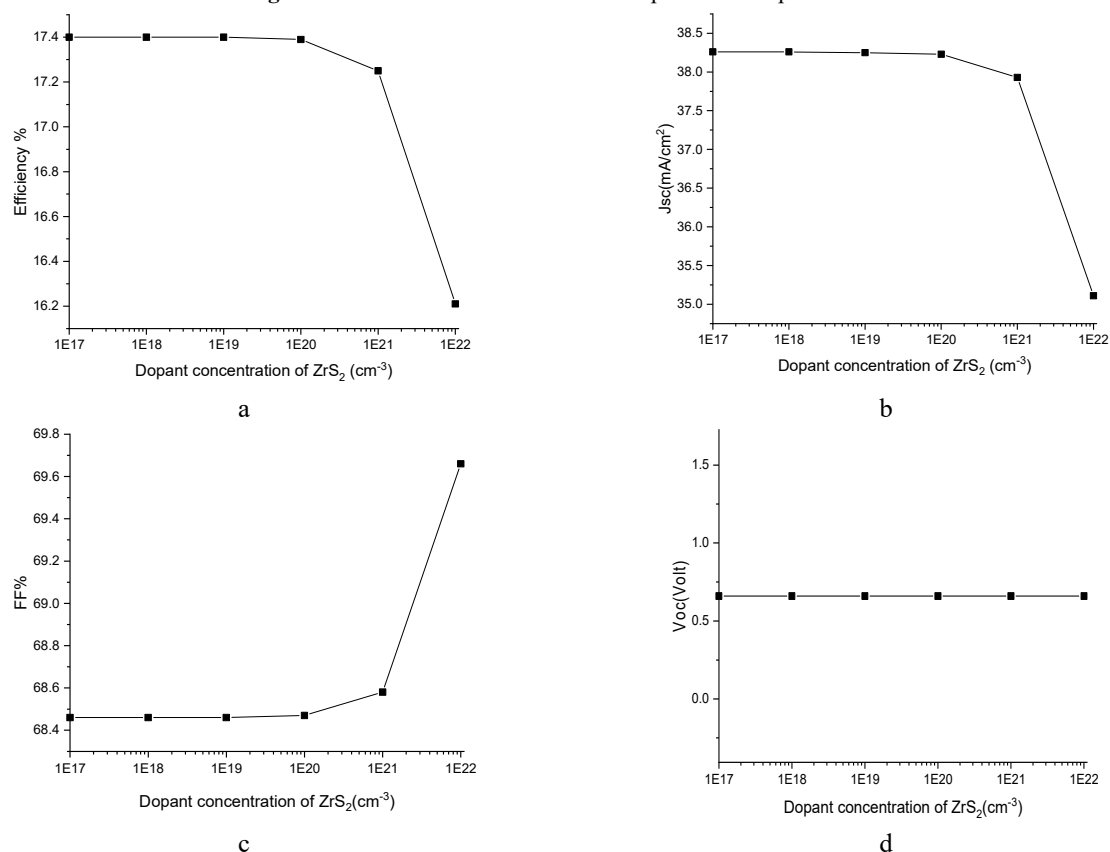

a

b

c

d

Figure 5. Effect of dopin concentration of ZrS$_2$ on cell performance parameters

3.3. Effect of interface defects (N_{ti}) on the performance of solar cells

It has been reported that the properties of interfaces play an important role in the permanence of solar cells [24]. In general, the formation of these defects is related to structural imperfections of the active layer, inconsistent fabrication techniques, mismatched energy levels, poor adhesion between ETL and HTL, and exposure to oxygen. In our solar cells, an interface defect is created between ZrS_2 and MEH-PPV where charge generation and separation occur. Therefore, to study the influence of defects on a solar cell's efficiency, the neutral defect density at this interface was varied from 1×10^9 cm^{-3} to 10^{15} m^{-3}. Figure 6 shows a reduction in μ, FF, and V_{oc}, while J_{sc} remains unaffected by an increase in defect density at the ZrS_2/MEH-PPV interface. These results can be attributed to enhanced recombination losses; J_{SC} remains unaffected as it is more dependent on the generation of charge carriers than recombination, which agrees with some of the previous reports [24]. At low defect density, the carrier diffusion length is high, resulting in lower recombination processes, which contributes to improved photovoltaic performance.
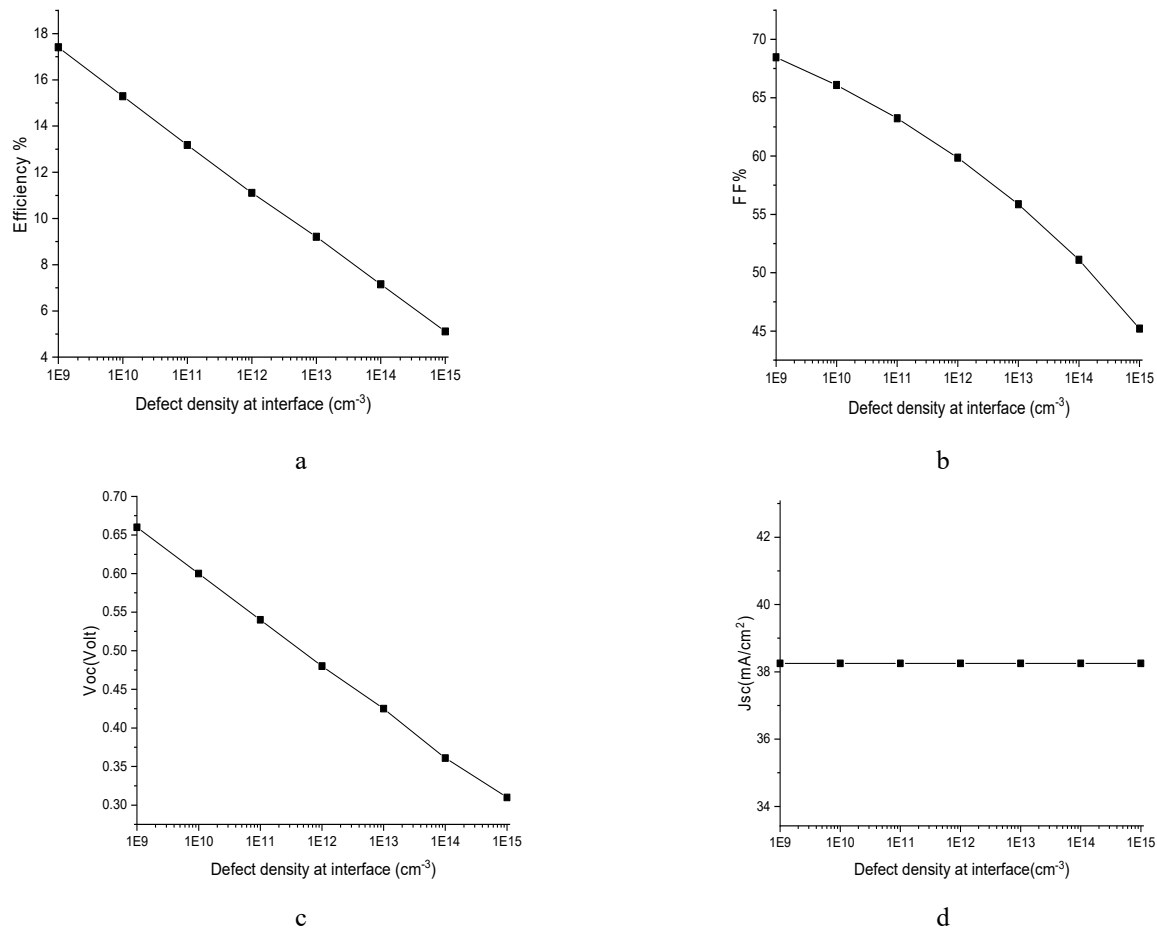

Figure 6. Effect of defect density at ZrS_2/MEH-PPV interface on cell performance parameters

3.4. Effect of back-contact work function

The properties of back contact in MEH-PPV/ZrS_2 solar cells have been studied to enhance their performance and thermal stability. This improvement can be achieved by selecting a suitable work function material as the back contact may yield a reasonable built-in voltage between the metal and active layer. The built-in voltage affects the open-circuit voltage of solar cells, which is accompanied by an increase in electric field. This field within solar cells serves as a driving force for separating and collecting the photogenerated charge carriers from their corresponding electrodes before they recombine and lose. It can also involve selecting appropriate materials with suitable energy levels, modifying the device architecture, or using interfacial layers to adjust the energy level alignment [6]. Table 3 shows the parameters of SnO_2:Fn/ZrS_2/ MEH-PPV/Au solar cells versus different back-contact work functions. It was observed that with the decreasing of the back contact work function from 5.35 eV to 4.5eV, the V_{oc} stayed constant around 0.66 V. While it reduced to 0.5V when the work function decreased below 4.5 eV. However, both μ and FF continued to decrease from 17.4% to 1.54% and 68.47 to 9.81 respectively. The short circuit current (J_{SC}) remained nearly unchanged despite variations in the back contact work function. On the other hand, as the workforce of the back contact decreases, the Schottky barrier at the MEH-PPV/back contact interface increases and impending hole transport from MEH-PPV to the back contact. Consequently, both FF and PCE are also reduced.

Table 3. The parameters of SnO$_2$:Fn/ZrS$_2$/MEH-PPV solar cells versus different back-contact metals.

Back contact work function(eV)	Efficiency μ%	FF%	V$_{oc}$(Volt)	J$_{sc}$(mA/cm^2)
Platinum (Pt) 5.35	17.4	68.47	0.66	38.25
Gold (Au) 5.1	17.4	68.46	0.66	38.25
Copper (Cu) 4.65	12.41	48.85	0.66	38.25
Iron (Fe) 4.5	7.47	29.45	0.66	38.25
Silver (Ag) 4.5	1.54	9.81	0.5	38.1

CONCLUSIONS

This work investigates the effect of properties charge transport layers on performance of MEH-PPV /ZrS$_2$ solar cells using SCAPS software. The results reveal that Increasing MEH-PPV thickness and decreasing its doping concentration reduce efficiency while increasing ZrS$_2$ thickness and decreasing its doping density improve efficiency. The optimal values of the neutral defect density interface and the work function of back contact were is 10^9 cm^{-3} and higher 4.65 eV respectively.

ORCID

Hmoud Al-Dmour, https://orcid.org/0000-0001-5680-5703

REFERENCES

[1] N. Kumar, and K. Chandra, Journal of Materiomics, **7**(5), 940 (2021). https://doi.org/10.1016/j.jmat.2021.04.002
[2] S. Liu, V. Biju, Y. Qi, *et al*., NPG Asia Materials, **15**, 1 (2023). https://doi.org/10.1038/s41427-023-00474-z
[3] A. Kojima, K. Teshima, Y. Shirai, and T. Miyasaka, Journal of the American chemical society, 131, 6050 (2009). https://doi.org/10.1021/ja809598r
[4] H. Al-Dmour, R.H. Alzard, R.H.H. Alblooshi, K. Alhosani, S. AlMadhoob, and N. Saleh, Front Chemistry, **7**, 561 (2019). https://doi.org/10.3389/fchem.2019.00561
[5] R. Ranjanm, A. Nikhi, *et al*., Scientific Report, **13**. 1 (2023). https://doi: 10.1038/s41598-023-44845-6
[6] H. Al-Dmour, East European Journal of Physics, (2), 445 (2024). https://doi.org/10.26565/2312-4334-2024-2-58
[7] S. Lee, J. Li, S. Lee, C. Moon, Y. Kim, J. Cao, and C. Jhun, Molecules, **26**(9), 2512 (2021). https://doi.org/10.3390/molecules26092512
[8] W. Brütting, Nature. Material, **18**, 432 (2019). https://doi.org/10.1038/s41563-019-0329-0
[9] S. Al-Taweel, S. Al-Trawneh, H. Al-Dmour, O. Al-Gzawat, W. Alhalasah, and M. Mousa, Heliyon, **9**(10), 21039 (2023). https://doi.org/10.1016/j.heliyon.2023.e21039
[10] R. Suryana, *et al*., IOP Conference series: Materials Science and Engineering, **333**, 012022 (2018). https://doi:10.1088/1757-899X/333/1/012022.
[11] A. Reshak, M. Shahimin, N. Juhari, R. Vairavan, Current Applied Physics, **13**, 1894 (2013). https://doi.org/10.1016/j.cap.2013.07.023
[12] H. Chen, T. Huang, T. Chang, *et al*., Scientific Report, **6**, 34319 (2016). https://doi.org/10.1038/srep34319
[13] R. Chaymaa, *et al*., Matériaux and Techniques, **111**, 507 (2023). https://doi.org/10.1051/mattech/2024003
[14] H. Al-Dmour, S. Al-Trawneh, and S. Al-Taweel, International Journal of Advanced and Applied Sciences **8**(6), 128 (2021). https://doi.org/10.21833/ijaas.2021.06.015
[15] M. Burgelman, P. Nollet, and S. Degrave, Thin Solid Films, **361**, 527 (2000). https://doi.org/10.1016/S0040-6090(99)00825-1
[16] H. Amina, G. Yigit, M. Begrettin, and K. Hamdi, Optical Materials, **121**, 111544 (2021). https://doi.org/10.1016/j.optmat.2021.111544
[17] M. Abdelfatah, A. El Sayed, W. Ismail, *et al*., Scientific Report, **13** 4553 (2023). https://doi.org/10.1038/s41598-023-31553-4
[18] D. Lee, and K. Kim, Nanomaterials, 13, 1848 (2023). https://doi.org/10.3390/nano13121848
[19] A. Bradesko, *et al*., Journal of Material Chemistry, **9**, 3204 (2021). https://doi.org/10.1039/D0TC05854H
[20] A. Mortadi, E. Hafidi, M. Monkade, R. El Moznine, Materials Science for Energy Technologies, **7**, 158-165 (2024). https://doi.org/10.1016/j.mset.2023.10.001
[21] A. Chowdhur, Acta Physica Polonica A, **145**, 215 (2024). https://doi.org/10.12693/APhysPolA.145.215
[22] A. Trukhanov, V. Bruevich, and Yu. Paraschuk, Physical Review B, **84**, 5318 (2011). https://doi.org/10.1103/PhysRevB.84.205318
[23] H. Al Dmour, AIMS Materials, **8**, 261 (2021). https://doi.org/10.3934/matersci.2021017
[24] R. Priyanka, S. Numeshwar, T. Sanjay, and K. Khare, IOP Conf. Series: Materials Science and Engineering, **798**, 012020 (2020). https://doi.org/10.1088/1757-899X/798/1/012020

**ДОСЛІДЖЕННЯ ВПЛИВУ ТРАНСПОРТНИХ ШАРІВ НА СОНЯЧНІ ЕЛЕМЕНТИ ZrS2/MEH-PPV:
ВИКОРИСТАННЯ ПРОГРАМНОГО ЗАБЕЗПЕЧЕННЯ SCAPS -1D**
**Марван С. Муса^a, Хмуд Аль-Дмур^b, Емад К. Джарадат^c, Усама Є. Аль-Маданат^d, Ахмад M.D. (Асса'д) Джабер^e,
Беддіаф Заїді^f, Ахмет Саїт Алалі^g, В. Аравіндан^h**
^{a}Департамент інженерії відновлюваної енергетики, Університет Джадара, Ірбід 21110, Йорданія
^{b}Департамент фізики, факультет природничих наук, Університет Мута, Мута 6170, Йорданія
^{c}Департамент фізики, природничий факультет. Ісламський університет імама Мохаммада Ібн Сауда,
Ер-Ріяд 11623, Саудівська Аравія
^{d}Департамент хімії, Факультет природничих наук, Університет Мута, Мута 6170, Йорданія
^{e}Департамент фундаментальних гуманітарних наук і природничих наук, медичний факультет, Університет медичних наук
Акаби, Акаба 77110, Йорданія
^{f}Кафедра фізики, факультет матеріальних наук, Університет Батна 1, Батна, Алжир
^{g}Факультет фізики, Технічний університет Йилдиз, Стамбул, 34220 Туреччина
^{h}Лабораторія Smart матеріалів, факультет фізики, Інженерний коледж Тіагараджар, Мадурай-625015, Індія

У цій роботі досліджується вплив шарів транспортування заряду на ефективність сонячних елементів із полі[2-метокси-5-(2-етилгексилокси)-1,4-феніленвінілену] (MEH_PPV) і дисульфіду цирконію (ZrS$_2$) за допомогою програмного забезпечення Scaps-1D. Було встановлено, що при збільшенні товщини MEH-PPV і зменшенні концентрації його акцепторного допування ефективність (μ%), коефіцієнт заповнення (FF) і густина струму короткого замикання (Jsc) зменшуються. І навпаки, збільшення товщини шару транспортування електронів ZrS$_2$ і зменшення його щільності донорного легування підвищило ефективність (μ%) і щільність струму короткого замикання (Jsc), зберігаючи постійну напругу холостого ходу (Voc). Ці результати можна пояснити зниженим розподілом і збором зарядів у MEH-PPV і зменшеною довжиною оптичного шляху в ZrS$_2$. З іншого боку, зворотний контакт із роботою виходу нижче 4,65 eB, сонячні елементи MEH-PPV/ZrS$_2$ показали найнижчу ефективність порівняно з різними типами зворотного контакту. За оптимальних умов сонячна батарея MEH-PPV/ZrS2 показує високу ефективність 21%, коли концентрація допанту MEH-PPV і значення нейтральної щільності дефектів на межі ZrS$_2$/MEH-PPV становлять 10^{22} см-3 і 10^9 см$^{-3}$ відповідно.

Ключові слова: *SCAPS моделювання; сонячні елементи; щільність легування; дефект інтерфейсу; робоча функція*

EFFECT OF ZnS BUFFER LAYER ON PERFORMANCE OF CIGS SOLAR CELL

Laid Abdelali[a], Hamza Abid[a], Ikram Zidani[a], Aissa Meksi[b], Abdellah Bouguenna[c]*, Zaid Bendaoudi[d]

[a]*Applied Material Laboratory, University Djillali Liabes of Sidi Bel Abbes, Algeria*
[b]*Electrical Engineering Department University of Sciences and Technology of Oran, Algeria B.P 1505, El Mnaouer, Oran, Algeria*
[c]*Electrical Engineering Laboratory of Oran, Department of Electronics, Faculty of Electrical Engineering, University of Sciences & Technology of Oran (MB-USTO), 31000, Oran, Algeria*
[d]*Department of Electrotechnical & Automatic Engeneering, University of Relizane, Algeria*
*Corresponding Author e-mail: abdellah.bouguenna@univ-usto.dz
Received July 9, 2024; revised September 18, 2024; accepted September 25, 2024

Cu(In,Ga)Se$_2$ (CIGS)-based thin-film solar cells are currently among the most efficient. Zinc sulfide (ZnS) is the best buffer layer used in CIGS-based solar cells because it is non-toxic and has a wide band gap. In this study, we present a simulation of a CIGS solar cell with a ZnS buffer layer, carried out using the Silvaco-Atlas simulator. We attained an efficiency of 24.13%, short-circuit current of 37.81 mA/cm^2, an open circuit voltage of 740 mV and a fill factor of 78.78% at a bandgap around 1.41 eV, corresponding to an x ratio of 0.5. The photovoltaic performance of the ZnS/CIGS solar cell is improved by optimizing the effects of layer parameters such as thickness, acceptor and donor densities of the CIGS absorber and ZnS buffer layers. For a 0.035 μm thick ZnS acceptor with a density of 6×10^{17} cm^{-3} and a 3 μm thick CIGS donor with a density of 10^{18} cm^{-3}, a maximum efficiency improved to 27.22%.
Keywords: *Buffer layer (ZnS); CIGS; Solar cell; Optimization; Silvaco-Atlas*
PACS: 84.60.Jt; 78.20.Bh; 89.30.Cc; 42.60.Lh.

1. INTRODUCTION

Due to its lower production costs, higher conversion efficiency and enhanced stability, the thin-film solar cell based on the CIGS compound semiconductor has recently grown in popularity. In the visible solar spectrum, the CIGS compound semiconductor offers captivating features, such as a directly controllable bandgap from (1.0 to 1.7 eV) to maximize irradiance, and an absorption factor of 10^6 cm^{-1}. CIGS and CdS solar cells are the most popular thin-film photovoltaic technology, with an energy conversion efficiency of 22.6%. When the 2.4 eV bandgap is unsuitable for solar cells, the CdS buffer layer shows optical absorption losses, particularly in the short-wave range [3, 4]. In addition, because of the hazardous cadmium (Cd) waste produced during deposition, the CdS buffer layer can pose a risk to human health and the environment. Given these factors, the CIGS absorption layer is compatible with other wide-bandgap buffer layers. Zinc sulfide (ZnS) prepared using chemical bath deposition (CBD) offers an attractive alternative to CdS in collaboration with CIGS absorbers [8, 9] due to its wide bandgap of around 3.68 eV and its non-toxicity to the environment. Cell efficiency is enhanced by ZnS/CIGS, Zn$_{1-x}$Sn$_x$O$_y$ and CIGS, In$_x$S$_y$/CIGS, with rates of 21.0% [5], 18.2% [6] and 18.1% [7] respectively.

The energy of zinc sulfide (ZnS) is much higher than that of CdS in the bandgap. The ZnS buffer layer used in CIGS solar cells improves current generation at shorter wavelengths. CIGS solar cells with a ZnS buffer layer perform almost identically to CdS/CIGS solar cells [10-11]. The use of solar cell simulation has become an essential tool for studying their operation and improving the design of high-performance solar cells. In this research, we perform a simulation of both CIGS and ZnO/ZnS/CIGS solar cells to evaluate their performance [12, 14, 15, 16], where ZnS/CIGS solar cells are more promising than CdS/CIGS solar cells [2, 17].

The main parameters of ZnS/CIGS cells have been identified by several numerical studies, such as thickness, bandgap, gradient of the CIGS absorber layer and thickness of the ZnS buffer layer [17, 18, 19, and 20].

In this article, we examine ZnS/CIGS solar cells using simulation studies. Numerical analysis of CIGS solar cells is presented using the Silvaco-Atlas simulator (AM1.5 G, 100 mW/cm², 300 K) to determine basic parameters (Jsc, Voc, FF and η). We use ZnS as a buffer layer to study the performance of CIGS solar cells, and have simulated our structure to study photovoltaic characteristics. We compared the performance of a CIGS solar cell with a ZnS buffer layer with other works [21, 22]. The consequences of the thickness of the absorber layer, the temperature and the impact of the CIGS absorber layer in the band gap. The efficiency of this solar cell is 24.13%, thanks to the use of ZnS and CIGS.

2. Modeling and simulation parameters
2.1. Structure simulated

Figure 1 shows schematically the structure of the CIGS solar cell examined in this study. It consists of a single-junction solar cell based on a CIGS that is both optically and electrically connected, with a layer of ZnO serving as a transparent coating.Figure 1 shows the doping concentrations and thicknesses of the various layers that make up the

simulated structure. The CIGS consists of a transparent n-type ZnO contact layer, an n-type ZnS buffer layer and a p-type CIGS absorber layer. Finally, a layer of Molybdenum (Mo) on a glass substrate is often used as a back contact.
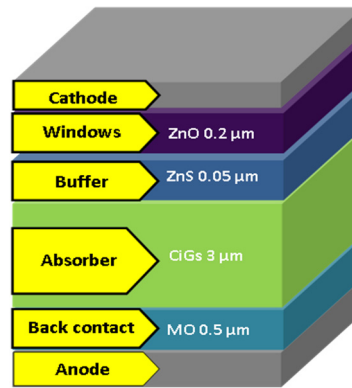

Figure 1. Structure of CIGS solar cell

2.2. Physical models

The Silvaco Atlas simulation software was used in this study. Atlas is a two- and three-dimensional physics-based device simulator that enables us to numerically solve the Poisson's equation coupled to the continuity equations for electrons and holes under stationary conditions. Newton's method is the default method selected for solving the basic semi-conductor equations in the software [23]. The various basic parameters used in this work include band gaps E_g, relative permittivity ε_r, electronic affinity χ_e, charge carrier mobility in the conduction band μ_n, charge carrier mobility in the valence band μ_p, effective density of states in the conduction band N_C, the effective density of states in the valence band N_V, the Gaussian defect density N_{GA}, N_{GD}, the maximum energy position E_{GA}, E_{GD}, the standard energy deviation W_{GA}, W_{GD}, the electron capture cross section σ_n, the hole capture cross section σ_p, and the surface recombination velocity parameters of electrons S_n and holes S_p.

Table 1 [1, 13, 22, 24] shows the parameters for each layer of the solar cell, which serve as input data for the Atlas-Silvaco numerical simulation.

Table 1. Material parameters used in the simulation.

Layer properties	ZnO	ZnS	CIGS
$E_g\,(ev)$	3.3	3.68	Varied
ε_r	4.1	4.5	4.8
$\chi_e\,(ev)$	9	8.32	13.9
$\mu_n\,(cm^2\,/\,Vs)$	100	250	100
$\mu_p\,(cm^2\,/\,Vs)$	25	40	25
$N_c\,(cm^{-3})$	2.2×10^{18}	1.5×10^{18}	2.2×10^{18}
$N_v\,(cm^{-3})$	1.8×10^{19}	1.8×10^{19}	1.8×10^{19}
Gaussian defect states			
$N_{DG},N_{VG}\,(1\,/\,cm^3)$	$D:10^{17}$	$A:10^{15}$	$D:10^{15}$
$E_A,E_D\,(eV)$	Mid gap	Mid gap	Mid gap
$W_G\,(eV)$	0.1	0.1	0.1
$\sigma_e\,(cm^2)$	10^{-12}	10^{-17}	10^{-13}
$\sigma_h\,(cm^2)$	10^{-15}	10^{-13}	10^{-15}

In this simulation, we use the illumination conditions of the AM1.5 G solar spectrum at one sun, with an incident power density of 100 mW/cm^2 and an ambient temperature of 300°K. The bandgap of CuIn$_{1-x}$Ga$_x$Se$_2$ was calculated using the empirical expression:

$$Eg[eV] = 1.010 + 0.626 \cdot x - 0.167x(1-x) \tag{1}$$

Where Eg varies from 1.0692 eV to 1.7609 eV for x=0 (CIS) and x=1 (CGS), respectively [25].

Ga composition was set at 0.30, corresponding to a bandgap energy of 1.27 eV.

ATLAS offers a variety of models that can be used to simulate devices. We have used the Density of States (DOS) model to represent the defect density in CIGS and ZnS layers. The data provide two deep-level bands, modeled using a Gaussian distribution.

$$g_{GA}(E) = N_{GA} \exp\left[-\left[\frac{E_{GA} - E}{W_{GA}}\right]^2\right] \tag{2}$$

$$g_{GD}(E) = N_{GD} \exp\left[-\left[\frac{E - E_{GD}}{W_{GD}}\right]^2\right] \tag{3}$$

In this situation, E corresponds to the fault energy, while the indices (G, A, D) correspond to Gaussian fault states, acceptors and donors respectively. Density states are defined by their effective density N_{GA} or N_{GD}, their standard energy gap W_{GA} or W_{GD}, and their maximum energy position E_{GA} or E_{GD} [23].

In the standard model, the Gaussian defect distribution is used to describe the defect states of semiconductor materials with defects. Shockley-Read-Hall recombination is modeled as follows:

$$R_{SRH} = \frac{pn - n_i^2}{\tau_p \left(n + n_i \exp^{\frac{E_i - E_T}{KTL}}\right) + \tau_n \left(p + n_i \exp^{\frac{-(E_i - E_T)}{KTL}}\right)} \tag{4}$$

$$\tau_n = \frac{1}{\sigma_n v_{th} N_t} \text{ and } \tau_p = \frac{1}{\sigma_p v_{th} N_t}$$

Where τ_n and τ_p are the electrons and holes lifetime parameters (TAUN0 and TAUP0 in Silvaco Atlas), σ_n and σ_p are the capture cross sections for electrons and holes, respectively, v_{th} is the thermal velocity, and N_t is the trap density by volume. n_i is a spatially varying intrinsic concentration level, E_i is the intrinsic Fermi energy level, E_T is the trap energy level, (E_i - E_T is ETRAP in Silvaco Atlas), and T_L is the lattice temperature in Kelvin [23,26].

A general expression for surface recombination is:

$$R_{surf} = \frac{pn - n_i^2}{\tau_p^{eff} \left(n + n_i \exp^{\frac{E_i - E_T}{KTL}}\right) + \tau_n^{eff} \left(p + n_i \exp^{\frac{-(E_i - E_T)}{KTL}}\right)} \tag{5}$$

$$\frac{1}{\tau_n^{eff}} = \frac{1}{\tau_n^i} + \frac{d_i}{A_i} S.N \text{ and } \frac{1}{\tau_p^{eff}} = \frac{1}{\tau_p^i} + \frac{d_i}{A_i} S.P$$

where τ_p^i and τ_n^i are the volume lifetimes calculated at node i along the interface, which may also be a function of impurity concentration. Parameters d_i and A_i are the interface length and area for node i. Parameters S.N and S.P are the recombination velocities for electrons and holes respectively [27].

3. Simulation Results and Discussion
3.1. Optimal CIGS absorbing layer bandgap

The electrical parameters of the CIGS cell were calculated for different values of the bandgap of the CIGS absorber layer to determine the optimum efficiency-enhancing bandgap. We set the thickness of the CIGS absorber layer at 3 μm and varied the bandgap by changing the X ratio from 0 to 1.
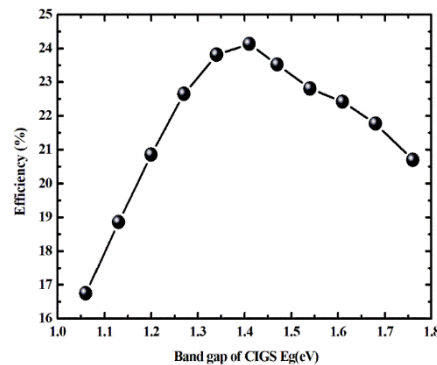
Figure 2. The variation band gap energy of CIGS as function of efficiency

The characteristics of the CIGS cell for different band gaps as a function of efficiency are shown in Figure 2. It can be seen that increasing the band gap of the CIGS absorber layer, and hence increasing the x-ratio, leads to a proportional increase in efficiency up to a value of 1.4 and then the efficiency starts to decrease, the efficiency increase starts from

16.75% to 24.13%. The excellent efficiency obtained for the CIGS solar cell is 24.13%. The optimum efficiency of the CIGS cell was achieved when the optical bandgap was around 1.41 eV, corresponding to an x ratio of 0.5.

3.2. Influence of absorber layer thickness

The CIGS solar cell structure, obtained using Silvaco-Atlas, is shown in Figure 3.
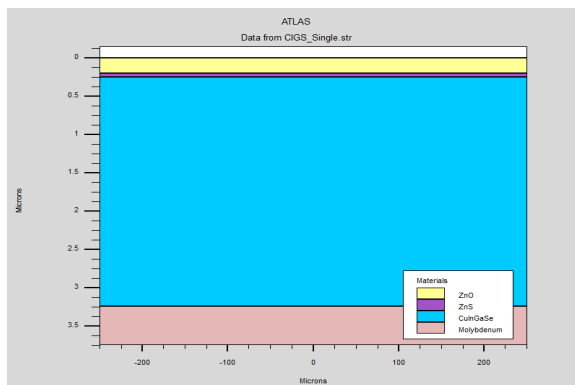

Figure 3. Silvaco-Atlas structure file of the CIGS solar cell

In this section of the simulation, we first opted for a CIGS layer thickness of 2 μm, then adjusted the thickness of the zinc sulfide (ZnS) buffer layer from 0.1 μm to 0.03 μm.

We observed that the efficiency increases and then decreases with increasing ZnS buffer layer thickness. We also found that the high efficiency of CIGS thin-film solar cells decreases as the thickness of the zinc sulfide buffer layer increases (from 22.45% for 0.035 μm to 20.91% for 0.1 μm). As is obvious, the performance of all solar cells decreases as the buffer layer thickness increases, with the exception of open-circuit voltage, which remains constant. Even if some absorption losses in solar cells are caused by the ZnS buffer layer or emitter thickness, this may explain the profile of this result. The ZnS layer has a thickness ranging from 10 nm to 30 nm, while the CIGS layer varies from 1 μm to 4 μm. Figures 4, 5, 6 and 7 shows the impact of ZnS layer thickness on the performance of CIGS-based solar cells. The short-circuit current density increases from 30.69 to 35.70 mA/cm^2 as the thickness of the ZnS buffer layer increases from 10 to 35 nm.
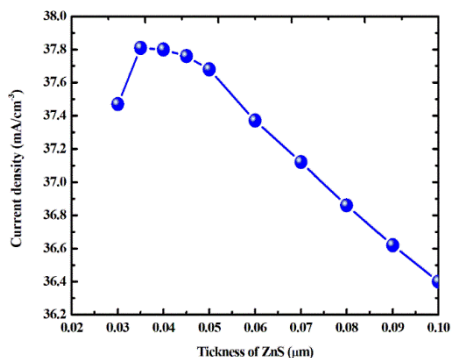

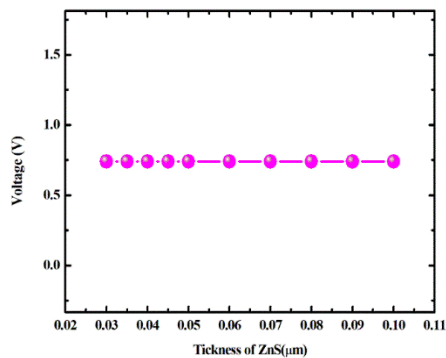**Figure 4.** Effect of ZnS buffer layer thickness on the current density of the CIGS solar cells

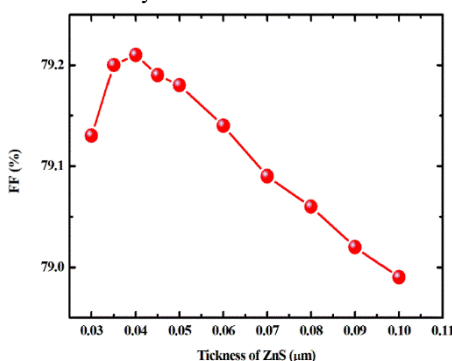**Figure 5.** Effect of ZnS buffer layer thickness on the voltage of the CIGS solar cells

Figure 6. Effect of ZnS buffer layer thickness on the factor form of the CIGS solar cells
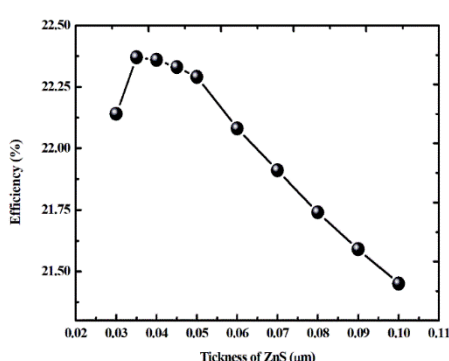

Figure 7. Effect of ZnS buffer layer thickness on the efficiency of the CIGS solar cells

The increase leads to a rise in the solar cell's conversion rate. In physical terms, a very thin absorber layer indicates that the back contact and the depletion zone are very close, which favors electron capture by this contact. This form of recombination process affects cell performance, as it has an impact on conversion efficiency.
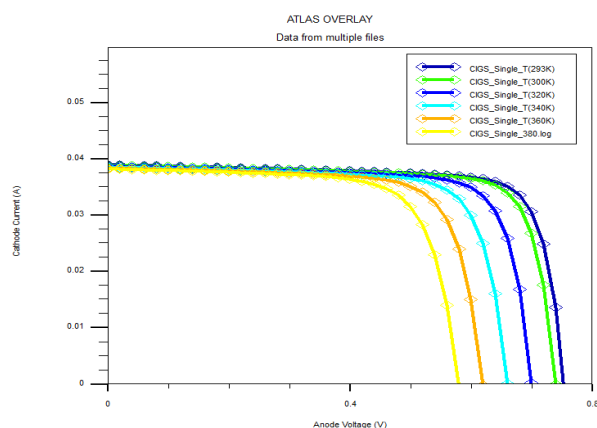
3.3. Effect of temperature on CIGS solar cells using ZnS as buffer layer

One of the most crucial parameter optimizations for thin-film solar cells is operating temperature, which plays an important role in assessing thin-film performance.

We are studying the influence of temperature on CIGS-based solar cells, using ZnS as a buffer layer. As we can see, the performance of thin-film solar cells decreases with increasing operating temperature. The same variation in performance properties with increasing operating temperature. This indicates that ZnS could be a good alternative material for use in photovoltaic applications.

Figure 8 shows the influence of operating temperature on CIGS-based solar cells using ZnS as a buffer layer.

Extracted from the various (J-V) characteristics shown in Figure 9, the electrical parameters of the CIGS cell are summarized in Table 2 and compared with the published data [21, 22], our simulated results represent higher efficiency than them.

Figure 8. Effect of the Temperature on performance of solar cells, using ZnS as Buffer layer
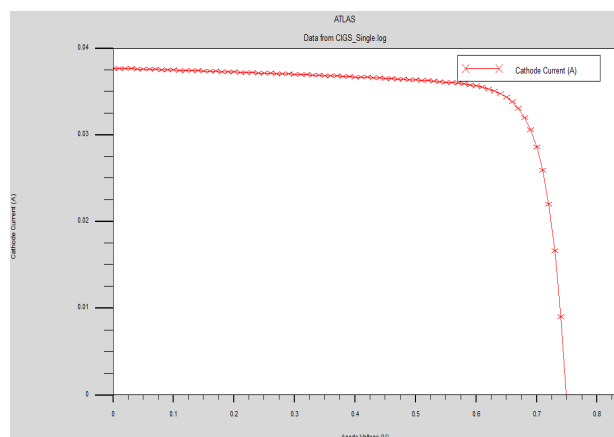
Figure 9. Simulation $J–V$ characteristics of the ZnS/CIGS solar cell

Table 2. Comparison between our model and other works

	Voc (mv)	Jsc (mA/ cm^2)	FF (%)	$\eta(\%)$
Our Simulation ZnS/CIGS (Eg=1.2 eV)	0.74	37.68	79.18	22.29
Simulation of [21] ZnS/CIGS (Eg=1.2 eV)	0.71	37.96	81.24	22.16
Our Simulation ZnS/CIGS (Eg=1.41 eV, x=0.5)	0.74	37.81	78.78	24.13
Simulation of [22] ZnS/CIGS (Eg=1.41 eV, x=0.5)	0.804	35.66	82.14	23.54

It is conceivable that the simulated data will serve as a starting point for modeling the effect of absorber layer thickness, absorber layer bandgap and the use of ZnS as a buffer layer on solar cell performance in our work.

In this study, we aim to obtain the highest current values for the CIGS cell and find an optimum matching efficiency for the simulated structure.

4. CONCLUSION

In this work, we have presented and discussed the results of a numerical simulation study of the electrical characteristics of a CIGS-based thin-film hetero-junction solar cell. Of the electrical characteristics of a CIGS-based thin-film hetero-junction solar cell, generated by the Silvaco Atlas-2D simulation software.

We studied the electrical stimulation of the CIGS cell with the ZnS cell, proving that the ZnS cell is better than the other cells. Then we studied the impact of two layers in ZnS (buffer layer) and CIGS (absorber layer) with the aim of designing an optimal ZnO/ZnS/CIGS hetero-junction structure that gives the best electrical performance. We conclude from this study that the best doping for the ZnS layer is concentration 6×10^{17} cm^{-3} with a thin thickness of 35 nm and the best doping for the CIGS layer of concentration 1×10^{18} cm^{-3} with a thickness of 3 μm to obtain the optimum electrical efficiency of 27.22%.

ORCID
Laid Abdelali, https://orcid.org/0009-0009-9173-3835; **Ikram Zidani**, https://orcid.org/0009-0003-8900-5261
Aissa Meksi, https://orcid.org/0009-0007-1698-5069; **Abdellah Bouguenna**, https://orcid.org/0000-0003-3492-5418

REFERENCES

[1] H. Heriche, Z. Rouabah, and N. Bouarissa, Int. J. Hydrogen Energy, **42**(15), 9524-9532 (2017). https://doi.org/10.1016/j.ijhyden.2017.02.099

[2] P. Jackson, R. Wuerz, D. Hariskos, E. Lotter, W. Witte, and M. Powalla, Rapid Research Letters. **10**(8), 583 (2016). https://doi.org/10.1002/pssr.201600199

[3] D. Hariskos, S. Spiering, and M. Powalla, Thin Solid Films. **480**, 99-109 (2005). https://doi.org/10.1016/j.tsf.2004.11.118

[4] M.A. Green, Y. Hishikawa, E.D. Dunlop, D.H. Levi, J. Hohl- Ebinger, M. Yoshita, and W.Y. Ho-Baillie Anita, Solar cell efficiency tables (Version 53), Prog. Photovolt Res. Appl. **27**, 3–12 (2019). https://doi.org/10.1002/pip.3102

[5] T. M. Friedlmeier, P. Jackson, A. Bauer, D. Hariskos, O. Kiowski, R. Wuerz, and M. Powalla, IEEE Journal of Photovoltaics **5**(5), 1487-1491 (2015). https://doi.org/10.1109/JPHOTOV.2458039

[6] S. Spiering, A. Nowitzki, F. Kessler, M. Igalson, and H. A. Maksoud, Solar Energy Materials and Solar Cells, **144**, 544-550 (2016), https://doi.org/10.1016/j.solmat.2015.09.038

[7] T. Törndahl, A. Hultqvist, C. Platzer-Björkman, and M. Edoff, in: *Proceedings Volume 7603, Oxide-based Materials and Devices International Society for Optics and Photonics*, (San Francisco, California, United States, 2010), p. 76030D https://doi.org/10.1117/12.846351

[8] M.A. Olopade, O.O. Oyebola, and B.S. Adeleke, Adv. Appl. Sci. Res. **3**, 3396 (2012).

[9] T. Kobayashi, T. Kumazawa, Z.J.L. Kao, and T. Nakada, Energy Mater. Sol. Cells, **119**, 129 (2013). https://doi.org/10.1016/solmat.2013.05.052

[10] M. Fedawy, S.M. Ali, and T. Abdolkader, Journal of Advanced Research in Materials Science, **42**(1), 1 (2018).

[11] M.A. Green, K. Emery, Y. Hishikawa, W. Warta, E.D. Dunlop, D.H. Levi, and H. Baillie, Solar cell efficiency tables (version 49), Prog. Photovolt: Res. Appl. **25**(1), 3 (2017), https://doi.org/10.1002/pip2855

[12] N. Khoshsirat, N.A. Yunus, M.N. Hamidon, S. Shafie, and N. Amin, Optik, **126**(7-8), 681 (2015). https://doi.org/10.1016/j.ijleo.2015.02.037

[13] M. Mostefaoui, H. Mazari, S. Khelifi, A. Bouraiou, and R. Dabou, Energy Procedia, **74**, 736 (2015). https://doi.org/10.1016/j.egpro.2015.07.809

[14] F. Za'Abar, A.W. Zuhdi, M.S. Bahrudin, S.F. Abdullah, M.N. Harif, and A.H. Hasani, in: *2018 IEEE International Conference on Semiconductor Electronics (ICSE)*, (IEEE, Kuala Lumpur, Malaysia, 2018), pp. 209-213. https://doi.org/10.1109/SMELEC.2018.8481289

[15] J. Park, and M. Shin, Energies, **11**(7), 1785 (2018). https://doi.org/10.3390/en11071785

[16] M.B. Hosen, A.N. Bahar, M.K. Ali, and M. Asaduzzaman, Data Brief. **14**, 246 (2017). https://doi.org/10.1016/j.dib.2017.07.054

[17] T. Shawky, M.H. Aly, and M. Fedawy, IEEE Access, **9**, 75283 (2021). https://doi.org/10.1109/ACCESS.2021.3080391

[18] A. Sylla, S. Touré, and J.P. Vilcot, Int. J. Sci. Res. **6**(11), 855 (2017). https://doi.org/10.4236/ampc.2011.13014

[19] K. Luo, Y. Sun, L. Zhou, F. Wang, and F. Wu, Journal of Semiconductors, **38**(8), 084006 (2018). https://doi.org/10.1088/1674-4926/38/8/084006

[20] J. Park, and M. Shin, Energies, **11**(7), 1785 (2018). https://doi.org/10.3390/en11071785

[21] H.I. Abdalmageed, M. Fedawy, and M.H. Aly, Journal of Physics: Conference Series, **2128**(1), 012009 (2021). https://doi.org/10.1088/1742-6596/2128/1/012009

[22] S. Tobbeche, S. Kalache, M. Elbar, M.N. Kateb, and M.R. Serdouk, Optical and Quantum Electronics, **51**(8), 1 (2019). https://doi.org/10.1007/s11082-019-2000-z

[23] SILVACO, Inc. ATLAS User's Manual device simulation software. 701 Patrick Henry Drive, Bldg. 2 March 20, (2012).

[24] N. Khoshsirat, and N.A. Yunus, in: *2013 IEEE Conference on Sustainable Utilization and Development in Engineering and Technology (CSUDET)*, (IEEE, Selangor, Malaysia, 2013) pp. 63-67. https://doi.org/10.1109/CSUDET.2013.6670987

[25] J.M. Olson, D.J. Friedman, S. Kurtz, Handbook of Photovoltaic Science and Engineering, West Sussex, first ed. (John Wiley and Sons, 2003), pp. 567-616. https://doi.org/10.1002/0470014008

[26] J. Raymond, and I. Kilway. Thesis; Five- Junction Solar Cell Optimization Using Silvaco-Atlas, in: *Naval Postgraduate School*, (Monterey, California, 2017). https://doi.org/NSN 7540-01- 280-5500

[27] SILVACO, solarex12, Thin Film Tandem Solar Cell, (2015). https://doi.org/NSN 7540-01-280-5500

ВПЛИВ БУФЕРНОГО ШАРУ ZnS НА ЕФЕКТИВНІСТЬ СОНЯЧНИХ ЕЛЕМЕНТІВ CIGS

Лаїд Абделалі[a], Хамза Абід[a], Ікрам Зідані[a], Аісса Мексі[b], Абделлах Бугенна[c], Заїд Бендауді[d]

[a]Лабораторія прикладних матеріалів, Університет Джиллалі Ліабес Сіді-Бель-Аббес, Алжир
[b]Відділ електротехніки Університет наук і технологій Орану, Алжир B.P 1505, Ель Мнауер, Оран, Алжир
[c]Лабораторія електротехніки Орана, Департамент електроніки, Факультет електротехніки, Університет наук і технологій Орана (MB-USTO), 31000, Оран, Алжир
[d]Відділ електротехніки та автоматики, Університет Релізану, Алжир

Тонкоплівкові сонячні елементи на основі Cu(In,Ga)Se2 (CIGS) наразі є одними з найефективніших. Сульфід цинку (ZnS) є найкращим буферним шаром, який використовується в сонячних елементах на основі CIGS, оскільки він нетоксичний і має широку заборонену зону. У цьому дослідженні ми представляємо моделювання сонячної батареї CIGS з буферним шаром ZnS, виконане за допомогою симулятора Silvaco-Atlas. Ми досягли ефективності 24,13%, струму короткого замикання 37,81 мА/см2, напруги холостого ходу 740 мВ і коефіцієнта заповнення 78,78% при ширині забороненої зони близько 1,41 еВ, що відповідає відношенню x 0,5. Фотоелектричні характеристики сонячної батареї ZnS/CIGS покращуються шляхом оптимізації впливу параметрів шару, таких як товщина, щільність акцепторів і донорів поглинача CIGS і буферного шару ZnS. Для акцептора ZnS товщиною 0,035 мкм з щільністю 6 × 1017 см-3 і донора CIGS товщиною 3 мкм з щільністю 1018 см-3 максимальна ефективність покращилася до 27,22%.

Ключові слова: *буферний шар (ZnS); CIGS; сонячна батарея; оптимізація; Silvaco-Atlas*

STRUCTURAL FEATURES OF REVERSE AOT MICELLES IN WATER/CYCLOHEXANE: MOLECULAR DYNAMICS STUDY

Dilbar Bozorova[a]*, Shukur Gofurov[b], Mavlonbek Ziyaev[c], Oksana Ismailova[a,d,e]*

[a]Ion-plasma and laser technologies Institute, AS Uzbekistan, 100125, Tashkent, Dorman Yoli 33 Uzbekistan,
[b]University of Tsukuba, 1 Chome-1-1 Tennodai, Tsukuba, - Ibaraki 3058577, Japan
[c]Namangan State University, 160107, Namangan, Boburshokh 161, Uzbekistan
[d]Turin Polytechnic University in Tashkent, 100195, Kichik khalka Yoli 17, Uzbekistan
[e]Uzbek-Japan Innovation Center of Youth, Tashkent, 100195, University 2b, Uzbekistan
*Corresponding Author e-mail: bozorova191@gmail.com

A study of the structural features of reverse micelles of Na AOT (sodium bis(2-ethylhexyl) sulfosuccinate) molecules in cyclohexane with an aqueous core was carried out using the molecular dynamics method. Reverse AOT micelles are formed in three-component systems containing a non-polar solvent, water, and AOT molecules at certain concentration ratios, expressed as $w = [H_2O]/[AOT]$. A strong hydrogen bond between water molecules and AOT was found at the concentration $w=6$. For the first time, a sharp decrease in hydrogen bonding between water molecules and AOT at $w=7$ was shown, caused by a difference in the packing of AOT molecules and the collective dynamics of water molecules in the micelle core. The calculated results are in good agreement with experimental data from other authors. It is shown that, along with the methods of vibrational spectroscopy and dynamic light scattering, the molecular dynamics method is also informative for determining the structural characteristics of supramolecular structures and analyzing the collective dynamics of water molecules.

Keywords: *Molecular dynamics method; Reverse micelles; Hydrogen bonding*
PACS: 82.70.Uv; 47.11.Mn; GROMACS 5.1.3

INTRODUCTION

The formation of reverse AOT micelles with an aqueous nano-core [1] is of particular interest, as these systems serve as a medium for the growth of nanoparticles of various types [2, 3], organic molecules [4-6], biomolecules [7], and metal nanoparticles [8, 9]. Information on the stability of reverse micelle solutions, the shape of reverse micelles, their size distribution, and the properties of water in the core of reverse micelles has been obtained using small-angle X-ray [9] and neutron scattering [10], nuclear magnetic resonance [6], infrared spectroscopy [3, 6, 11], UV-vis spectroscopy [4], Raman spectroscopy, dielectric spectroscopy [12], methods of dynamic [13] and static light scattering [14], ultrafiltration [15], conductivity [16], and density measurements [17-19], as well as other physical methods. The difficulty of obtaining detailed molecular-level information on the structure of reverse micelles is that, unlike other complex organic structures, reverse micelles are self-assembled exclusively in solutions, which does not allow for X-ray analysis or the use of high-resolution microscopy [20]. Therefore, molecular dynamics is one of the main methods for studying supramolecular systems with a large number of degrees of freedom.

The aim of this work is the molecular dynamics investigation of the self-organization of reverse micelles of AOT molecules in the cyclohexane + water system and the study of structural properties and types of interactions depending on the variation of parameter w.

METHOD OF MOLECULAR DYNAMICS

The self-organization of reverse AOT micelles with a change in the molar ratio of water and surfactant $(w = [H_2O]/[AOT]$ (Fig. 1) was studied using the GROMACS (Groningen Machine for Chemical Simulations) software package [21], version 5.1.3.

To describe water, the SPC/E (Extended Single Point Charge) interaction potential was used [22], which was successfully applied in other studies [23-31]. TIP3P water model is used in these molecular dynamics simulations to accurately capture hydrogen bonding behavior in this micellar system.


Figure 1. Chemical structure AOT

Systems were chosen in such way that the number of AOT and cyclohexane molecules were constant, and the number of water molecules corresponded to the concentration range w=0.25÷11 presented in Table 1. For cyclohexane and AOT (Figure 1), the all-atom force field potential CHARMM27 [32] was chosen, as it describes well the formation of reverse micelles in other solutions [33] and clusters [34]. A cubic cell with periodic boundary conditions and a cut off radius of 1.2 nm were applied. Other parameters and detail procedure of NPT ensemble are presented in our previous work [24]. The equilibrium systems were prepared for 30 ns with a time step of

2 fs (Figure 2). Only the last 5 ns of the runs were used for data analysis. For the velocity autocorrelation function, the equilibrium system was rerun for the next 15 ps.

Table 1. Number of molecules in the system as a function of w = [H$_2$O]/[AOT] concentration.

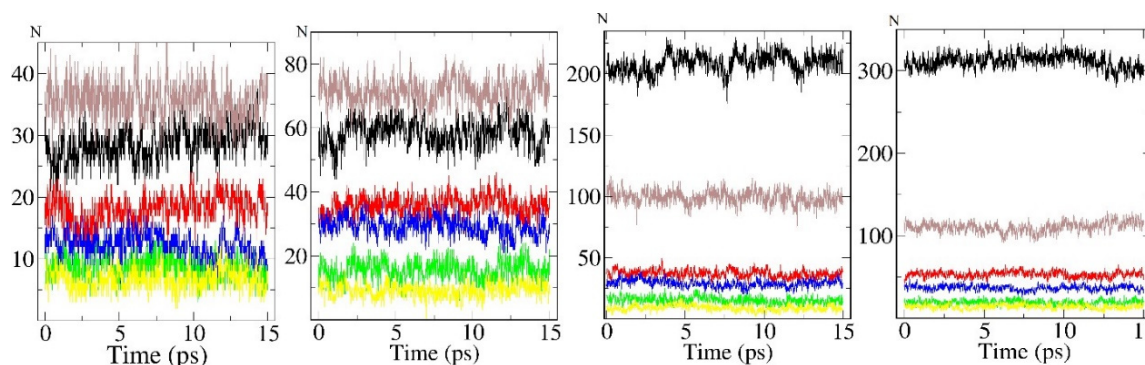|	Number of molecules		
w	cyclohexane	water	AOT
0	1000	0	95
0.25	1000	24	95
0.5	1000	47	95
1.0	1000	95	95
2.0	1000	189	95
3.0	1000	284	95
4.0	1000	379	95
5.0	1000	473	95
6.0	1000	568	95
7.0	1000	662	95
8.0	1000	757	95
9.0	1000	852	95
10.0	1000	946	95
11.0	1000	1041	95

a)

b)

w=6	w=7	w=8	w=9	w=10	w=11
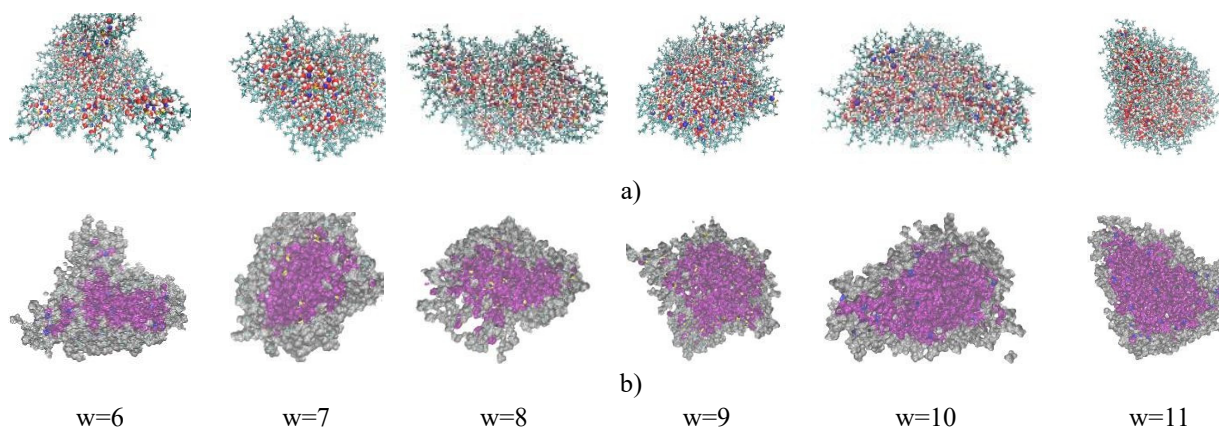
**Figure 2.** Formed micelles in concentration range 6÷11 of w = [H$_2$O]/[AOT]

RESULTS AND DISCUSSION

Figure 3 presents the number of hydrogen bonds at various water/AOT concentrations (w), illustrating two main types of interactions: between the SO$^-$ anionic group of AOT and water molecules, and between water molecules themselves. At low concentrations (w=1 and w=2), these two interaction types are roughly equal in number, suggesting a balance between AOT-water and water-water bonding. However, starting at w=3, a shift occurs with water molecules forming significantly more hydrogen bonds with each other than with AOT, at a ratio of approximately 2.5:1. This shift indicates the formation of a more cohesive water network within the micellar core, as the available water molecules begin interacting primarily with each other rather than with the surfactant. This structural change suggests that, as the water content grows, water molecules cluster into a stable pool, altering the micelle's internal arrangement.


Figure 3. Number of hydrogen bonds in the system as a function of water/AOT concentration, shown from left to right: w=1, w=2, w=3, w=4. Different types of hydrogen bonds are presented: between water molecules and: molecules calculated as the centre of mass of molecules (black); hydrophilic part of SO$^-$ (brown); O1 atom of AOT molecule (red); O2 atom of AOT molecule (green); O3 atom of AOT molecule (green); O4 atom of AOT molecule (yellow)

As shown in Figure 4, at higher concentrations (w=6 and w=7), the number of hydrogen bonds between the SO$^-$ group and water remains stable, but a sharp increase in water-water interactions occurs. This increase enhances the internal hydrogen-bonded network among water molecules, contributing to a more robust water framework within the micelle and impacting the overall structure. Additionally, for higher concentrations (w≥7), we observe a distinct pattern where interactions between specific oxygen atoms on AOT (O1 and O3) and water increase, while those involving O2 and O4 decrease. This pattern suggests a reorganization of the surfactant layer around the expanding water core. The repacking of AOT molecules likely facilitates this structural shift, helping to stabilize the enlarged core. These findings support a mechanism of micelle elongation under high hydration, as previously reported in studies describing the transition from spherical to cylindrical shapes in micelles at elevated water content.
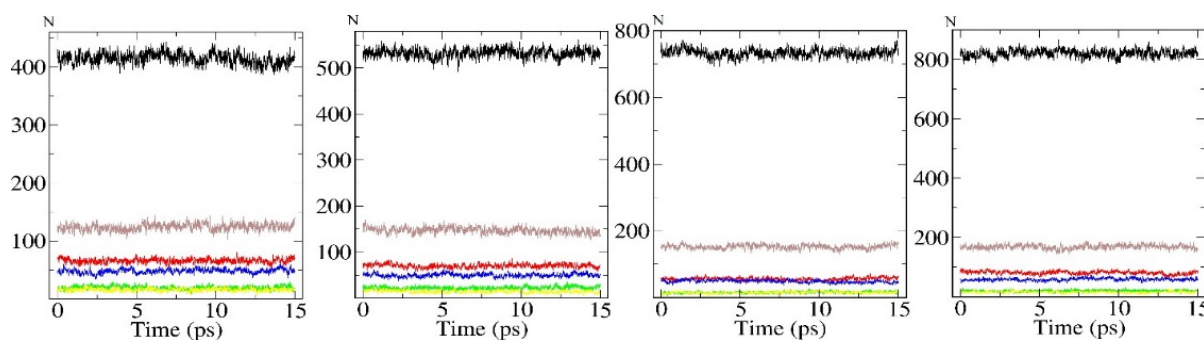

Figure 4. Number of hydrogen bonds in the system as a function of water/AOT concentration, shown from left to right: w=5, w=6, w=7, w=8. The types of hydrogen bond are shown in Figure 2.
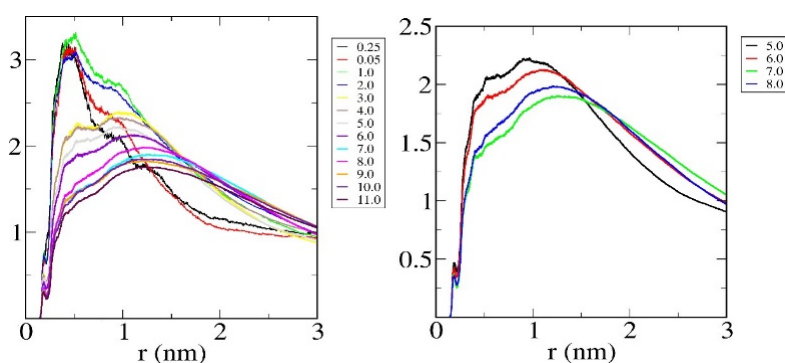
Figure 5. Radial distribution function between water molecules and AOT (calculated as the centre of mass of molecules).

Figure 5 provides further structural insight through the radial distribution function (RDF) between water and AOT molecules. At low water content (w=0.25÷2), RDF peaks are observed at 0.5 nm and 1.2 nm, indicating that water molecules are closely associated with AOT, suggesting a compact micellar core. However, as concentration increases to w=3÷6, the intensity of the first RDF peak diminishes, reflecting the shift toward water-water hydrogen bonding within the growing core. For concentrations w=7 and above, the peaks shift further towards longer distances, indicating that the micelle is adjusting to a larger, less compact core. This structural adaptation results in a looser AOT packing, consistent with the formation of elongated micelles as the water pool expands.
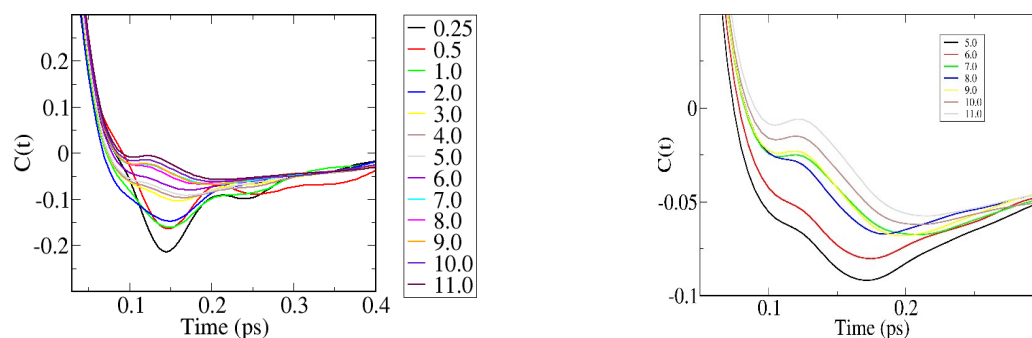
Figure 6. Autocorrelation velocity function for the water oxygen atom

The autocorrelation velocity function of the water oxygen atom (Figure 6) highlights dynamic changes across concentrations. At low concentrations (w=0.25÷2), we observe a distinct minimum around 0.15 picoseconds and a slight maximum at approximately 0.2 picoseconds, indicating restricted motion of water molecules due to strong interactions

with the AOT head groups. With increasing concentration (w=3÷6), this minimum becomes blurred, signaling that the water core has become more stable and continuous, allowing for greater water mobility. At higher concentrations (w≥7), the velocity function shifts, with the minimum appearing at around 0.1 picoseconds and the maximum at about 0.12 picoseconds. This shift signifies increased fluidity and longer-range interactions within the water core, consistent with structural elongation of the micelle [35].

In summary, at low water concentrations, hydrogen bonding is primarily between AOT and isolated water molecules, supporting a compact micellar core. As water content rises, the formation of a stable hydrogen-bonded water network within the core prompts a structural shift in the micelle, with AOT molecules rearranging around the expanded core. This progression from isolated water molecules to a cohesive water network causes the micelle to elongate, consistent with experimental observations of shape transitions in AOT micelles as hydration increases [35]. These findings illustrate how hydrogen bonding dynamics drive structural adaptations within reverse AOT micelles, influencing both the shape and internal dynamics of the micellar system as water concentration changes.

CONCLUSIONS

The study of the structural characteristics of reverse micelles in cyclohexane solution with an aqueous core has been carried out using the method of molecular dynamics. In micelles, there is a strong interaction between surfactant molecules and water, which leads to the rearrangement of water molecules and changes in micelle shape. It was shown that during the transition from w=5.6 to w=7, a difference in the packing of surfactant molecules and the water core is observed, which is related to the dynamics of water molecules. The calculation of hydrogen bonds in the system, the radial distribution function between surfactant molecules and water, as well as the autocorrelation velocity function for the water oxygen atom, showed a deviation for w=7. This deviation is related to the minimal interaction of surfactant molecules with water and compensation of Coulomb and Van der Waals forces, as well as the dielectric susceptibility of water observed in similar systems [15, 19]. The results based on data analyses reveal that at w=6, a strong hydrogen bond appears between the hydrophilic group of AOT and water, and at w=7, the strength of the hydrogen bond changes drastically, indicating that the micelle changes its shape. This fact is also confirmed by other authors [14, 35]. Thus, there is a significant increase in the interaction of water with the polar groups of AOT, leading to structural changes in micelles. With a further increase in www, the content of the aqueous pseudophase and the interaction of polar groups of surfactant molecules with water molecules determine the size of nanoparticles obtained in micelles.

ORCID

Dilbar Bozorova, https://orcid.org/0000-0001-5525-2676; **Shukur Gofurov,** https://orcid.org/0000-0002-5456-8182
Ziyayev Mavlonbek, https://orcid.org/0000-0002-9496-1210; **Oksana Ismailova,** https://orcid.org/0000-0001-8972-546X

REFERENCES

[1] S. Abel, M. Waks, W. Urbach, and M. Marchi, "Structure, "Stability, and Hydration of a Polypeptide in AOT Reverse Micelles", J. Am. Chem. Soc. **128**(2), 382–383 (2006). https://doi.org/10.1021/ja053043u

[2] R.E. Ridley, H. Fathi-Kelly, J.P. Kelly, V.R. Vasquez, and O.A. Graeve, "Predicting Destabilization in Salt- Containing Aqueous Reverse Micellar Colloidal Systems," ACS Earth Space Chem. **586**, 830-835 (2021). https://doi.org/10.1021/acsearthspacechem.1c00148

[3] B. Sinha, A. Dan, A. Wongkamlue, A. Chanakul, T. Charinpanitkul, S.P. Moulik, and A.K. Panda, "Synthesis and characterization of dispersions of ZnCrO4 prepared in AOT stabilized water/heptane microemulsion", J. Mol. Liq, **164**(3), 171-177 (2011). https://doi.org/10.1016/j.molliq.2011.09.004

[4] M. Mal, and D. Mandal, "Double proton transfer in a polar nano-droplet: Phototautomerization of alloxazine in AOT/alkane reverse micelles containing water or glycerol," Spectrochimica Acta Part A Molecular and Biomolecular Spectroscopy, **255**, 119708 (2021). https://doi.org/10.1016/j.saa.2021.119708

[5] A.E.L. Aferni, M. Guettari, T. Tajouri, and A. Rahdar, "The confinement of PVP in AOT microemulsions: Effect of water content and PVP concentration regime on electrical percolation phenomenon", J. Mol. Liq, **318**, 114012 (2020). https://doi.org/10.1016/j.molliq.2020.114012

[6] T. Butkhuzi, M. Kurtanidze, R. Chaladze, M. Gvaramia, M. Rukhadze, G. Bezarashvili, and P. Pradhan, "Investigation of influence of nonionic additives on structural changes of water droplets encapsulated in AOT reverse micelles by instrumental methods. Colloids and Surfaces A: Physicochemical and Engineering Aspects", **460**, 123–129 (2014). https://doi.org/10.1016/j.colsurfa.2014.03.067

[7] F. Zou, L. Xue, X. Yu, Y. Li, Y. Zhao, L. Lu, and Y. Qu, "One step biosynthesis of chiral, conducting and water-soluble polyaniline in AOT micellar solution", Colloids and Surfaces A: Physicochemical and Engineering Aspects, **429**, 38–43 (2013).

[8] R.F. Martín, C. Prietzel, and J. Koetz, "Template-mediated self-assembly of magnetite-gold nanoparticle superstructures at the water-oil interface of AOT reverse microemulsions", J. Colloid Interface Sci. **581**, 44-55 (2021). https://doi.org/10.1016/j.jcis.2020.07.079

[9] M. Harada, K. Saijo, N. Sakamoto, and K. Ito, "Characterization of water/AOT/benzene microemulsions during photoreduction to produce silver particles", J. Colloid Interface Sci. **343**(2), 423–432 (2010). https://doi.org/10.1016/j.jcis.2009.12.006

[10] Y. Sueishi, D. Yoshioka, M. Negi, and Kotake, "High static pressure alters water-pool properties in reversed micelles formed by aerosol OT (sodium bis(2-ethylhexyl) sulfosuccinate): A high pressure ESR study," Chemical Physics Letters, **415**(4-6), 261-264 (2005). https://doi.org/10.1016/j.cplett.2005.08.15

[11] Z. Lai, and P. Wu, "Investigation on the conformations of AOT in water-in-oil microemulsions using 2D-ATR- FTIR correlation spectroscopy," J. Mol. Struct. **883-884**, 236-241 (2008). https://doi.org/10.1016/j.molstruc.2008.01.017

[12] K. Małycha, A. Burakowski, J. Gliński, H. Niu, S.-L. Bai, and K. Orzechowski, "Characterization of isooctane/AOT/water reverse micelles by dielectric spectroscopy, dynamic light scattering and acoustic methods," J. Mol. Liq. **330**, 115335 (2021). https://doi.org/10.1016/j.molliq.2021.115335

[13] R.E. Ridley, Fathi-Kelly, H., Kelly, J.P., Vasquez, V.R., and Graeve, O.A., "Predicting Destabilization in Salt- Containing Aqueous Reverse Micellar Colloidal Systems", ACS Earth and Space Chemistry, **586**, 830-835 (2021). https://doi.org/10.1021/acsearthspacechem.1c00148

[14] I.V. Plastinin, S.A. Burikov, and T.A. Dolenko, "Laser diagnostics of reverse microemulsions: Influence of the size and shape of reverse micelles on the Raman spectrum on the example of water/AOT/cyclohexane system", J. Mol. Liq. **325**, 115153 (2021). https://doi.org/10.1016/j.molliq.2020.115153

[15] D. Fan, Z. Hao, P. Zheng, J. Zhao, and W. Shen, "The effect of polyethylene glycols on the interaction and stability of AOT/water/isooctane microemulsions. Arabian Journal of Chemistry, **13**(1), 2925-2933 (2018). https://doi.org/10.1016/j.arabjc.2018.08.002

[16] B. Shau, and R.A. Bhattarai, "Study of conductivity, contact angle and surface free energy of anionic (SDS, AOT) and cationic (CTAB) surfactants in water and isopropanol mixture", J. Mol. Liq. **323**, 114604 (2021). https://doi.org/10.1016/j.molliq.2020.114604

[17] A.E.L. Aferni, M. Guettari, T. Tajouri, and A. Rahdar, "The confinement of PVP in AOT microemulsions: Effect of water content and PVP concentration regime on electrical percolation phenomenon", J. Mol. Liq. **318**, 114012 (2020). https://doi.org/10.1016/j.molliq.2020.114012

[18] X. Wang, Z. Chen, and W. Shen., "The volumetric properties of water/AOT/isooctane microemulsions with larger-size droplets," J. Chem. Thermodynamics, **130**, 129-139 (2019). https://doi.org/10.1016/j.jct.2018.09.034

[19] Xue Wanga, Zhiyun Chena, Weiguo Shena, "The volumetric properties of water/AOT/isooctane microemulsions with small-size droplets," Colloids and Surfaces A, **529**, 893–900 (2017). https://doi.org/10.1016/j.colsurfa.2017.06.076

[20] G. Eskici, and P.H. Axelsen, "The Size of AOT Reverse Micelles", J. Phys. Chem. B, **120**(44), 1337–11347 (2016). https://doi.org/10.1021/acs.jpcb.6b06420

[21] B. Hess, C. Kutzner, D. van der Spoel, and E. Lindahl, "GROMACS 4: Algorithms for Highly Efficient, Load- Balanced, and Scalable Molecular Simulation," J. Chem. Theory Comput. **4**(3), 435–447 (2008). https://doi.org/10.1021/ct700301q

[22] H.J.C. Berendsen, J.R. Grigera, and T.P., Straatsma, "The missing term in effective pair potentials," J. Phys. Chem. A, **91**(24), 6269–6271 (1987).

[23] D. Bozorova, Sh. Gofurov, A. Kokhkharov, and O. Ismailova, "Terahertz spectroscopy of aqueous solutions of acetic acid", J. Appl. Spectrosc. **88**(4), 719-722 (2021). https://doi.org/10.1007/s10812-021-01230-3

[24] I. Plastinin, S. Burikov, Sh. Gofurov, O. Ismailova, Yu. Mirgorod, and T. Dolenko, "Features of Self-Organization of Sodium Dodecyl-Sulfate in Water-Ethanol solutions: Theory and Vibrational Spectroscopy", J. Mol. Liq. **298**, 112053 (2020). https://doi.org/10.1016/j.molliq.2019.112053

[25] Sh. Gofurov, U.K. Makhmanov, A. Kokhkharov, and O.B. Ismailova, "Structural and Optical Characteristics of Aqueous Solutions of Acetic Acid", Appl. Spectrosc. **73**(5), 503-510 (2019). https://doi.org/10.1177/0003702819831325

[26] Sh. Gofurov, O. Ismailova, U. Makhmanov, and A. Kokhkharov, "Heteromolecular Structure Formation in Aqueous Solutions of Ethanol, Tetrahydrofuran and Dimethylformamide," World Academy of Science, Engineering and Technology, Int. J. Chem. Eng. **11**(4), 330-333 (2017).

[27] J. Razzokov, O. Ismailova, S. Mamatkulov, O. Trunilina, and A. Kokhkharov, "Heteromolecular Structures in Aqueous Solutions of Dimethylformamide and Tetrahydrofuran, According to Molecular Dynamics Data," Russ. J. Phys. Chem. B, **88**(88), 1500-1506 (2014).

[28] A. Kaiser, O. Ismailova, A. Koskela, S. Huber, M. Ritterd, B. Cosenza, W. Benger, et al., "Ethylene glycol revisited: molecular dynamics simulations and visualization of the liquid and its hydrogen-bond network," J. Mol. Liquids, **189**(100), 20-29 (2013). https://doi.org/10.1016/j.molliq.2013.05.033

[29] O. Ismailova, A. Berezin, M. Probst, and R. Nazmutdinov, "Interfacial Bond-Breaking Electron Transfer in Mixed Water-Ethylene Glycol Solutions: Reorganization Energy and Interplay between Different Solvent Modes," The J. Phys. Chem. B, **117**(29), 8793-8801 (2013). https://doi.org/10.1021/jp405097c

[30] D. Bozorova, Sh. Gofurov, M. Ziyayev, D. Mirtojiyeva, O. Ismanova, and O. Ismailova, "The role of hydrogen bonds in diluted ethanol solutions of cyclohexane and dimethylformamide," Chemistry and chemical engineering, **2021**(1), 44-47 (2021).

[31] D. Bozorova, Sh. Gofurov, A. Kokhkharov, M. Ziyayev, and O. Ismailova, "Spectral features and hydrogen bond structure of aqueous solutions", Chemistry and chemical engineering, **2021**(4), 30-33 (2021).

[32] N. Foloppe, and A.D. MacKerell, Jr., "All-atom empirical force field for nucleic acids: I. Parameter optimization based on small molecule and condensed phase macromolecular target data," J. Comput. Chem. **21**(2), 86-104 (2000). https://doi.org/10.1002/(SICI)1096-987X(20000130)21:2%3C86::AID-JCC2%3E3.0.CO;2-G

[33] S. Abel, F. Sterpone, S. Bandyopadhyay, and M. Marchi, "Molecular Modeling and Simulations of AOT−Water Reverse Micelles in Isooctane: Structural and Dynamic Properties," J. Phys. Chem. B, **108**(50), 19458–19466 (2004).

[34] V. Monje-Galvan, and J. Klauda, "Interfacial properties of aqueous solutions of butanol isomers and cyclohexane," Fluid Phase Equilib. **513**, 112551 (2020). https://doi.org/10.1016/j.fluid.2020.112551

[35] T. Hellweg, and W. Eimer, "The micro-structures formed by Ni2+-AOT/cyclohexane/water microemulsions: a light scattering study," Colloids and Surfaces A", Physicochem. Eng. Asp. **136**, 97–107 (1998). https://doi.org/10.1021/jp711932h

[36] Y. Yoshimura, I. Abe, M. Ueda, K. Kajiwara, T. Hori, and Z.A. Schelly, "Apparent Molar Volume of Solubilized Water in AOT/Isooctane/Water Reverse Micellar Aggregates", Langmuir, **16**(8), 3633–3635 (2000). https://doi.org/10.1021/la981209h

СТРУКТУРНІ ОСОБЛИВОСТІ ОБРОТНИХ МІЦЕЛ AOT У ВОДІ/ЦИКЛОГЕКСАНІ: МОЛЕКУЛЯРНО-ДИНАМІЧНЕ ДОСЛІДЖЕННЯ

Дільбар Бозорова[a], Шукур Гофуров[b], Мавлонбек Зіяєв[c], Оксана Ісмаїлова[a,d,e]

[a]*Інститут іонно-плазмових і лазерних технологій, AS Узбекистан, 100125, Ташкент, Дорман Йолі 33, Узбекистан*
[b]*Університет Цукуби, 1 Чоме-1-1 Тенодай, Цукуба, - Ібаракі 3058577, Японія*
[c]*Наманганський державний університет, 160107, Наманган, Бобуршох 161, Узбекистан*
[d]*Туринський політехнічний університет в Ташкенті, 100195, Кічік Халка Йолі 17, Узбекистан*
[e]*Узбецько-японський інноваційний молодіжний центр, Ташкент, 100195, Університет 2б, Узбекистан*

Методом молекулярної динаміки проведено дослідження структурних особливостей зворотних міцел молекул Na AOT (біс(2-етилгексил)сульфосукцинат натрію) у циклогексані з водним ядром. Зворотні міцели AOT утворюються в трикомпонентних системах, що містять неполярний розчинник, воду та молекули AOT при певних співвідношеннях концентрацій, виражених як w = [H2O]/[AOT]. Виявлено сильний водневий зв'язок між молекулами води та AOT при концентрації w=6. Вперше було показано різке зменшення водневих зв'язків між молекулами води та AOT при w=7, викликане різницею в упаковці молекул AOT та колективною динамікою молекул води в ядрі міцели. Результати розрахунків добре узгоджуються з експериментальними даними інших авторів. Показано, що поряд з методами коливальної спектроскопії та динамічного розсіювання світла метод молекулярної динаміки також є інформативним для визначення структурних характеристик супрамолекулярних структур та аналізу колективної динаміки молекул води.

Ключові слова: *метод молекулярної динаміки; зворотні міцели; водневий зв'язок*